Frequency-Stabilized Cavity Ring-Down Spectroscopy of O_2 and CO_2 to Support Atmospheric Remote Sensing

Thesis by

David Alexander Long

In Partial Fulfillment of the Requirements

for the Degree of

Doctor of Philosophy

California Institute of Technology

Pasadena, California

2012

(Defended August 8 2011)

Acknowledgements

This dissertation is dedicated first and foremost to my family. Without their love and support, this certainly would not have been possible. I would like to especially thank my parents and my brother; you have made the past 26 years truly wonderful.

Scientifically I will always be indebted to Mitchio Okumura, Joe Hodges, and Chip Miller; I have learned so much from each of you. Mitchio, thank you for allowing me the freedom to explore the physical chemistry world, but still always being there for discussion and guidance. You taught me how to develop an idea and carry it through. Chip, your enthusiasm is truly infectious and your ability to convey the importance of fundamental science to a broad audience is inspiring. I hope that my collaborations with both of you will span well into the future.

Joe, your impact on this work cannot be overestimated. I am so grateful to you for the time you have spent with me. You were never too busy for a conversation or a little help. In four years you transformed me from an undergraduate with no physical chemistry lab experience into the scientist I am today. I am absolutely thrilled to have the opportunity to continue to work with you once I arrive at NIST.

Further I would like to note the contributions of my collaborators on this work: Dan Havey, Linda Brown, Herb Pickett, Pin Chen, David Robichaud, Laurence Yeung, Daniel Lisak, Kasia Bielska, Shanshan Yu, Roger van Zee, Jeremie Courtois, Keith Gillis and the entire OCO/OCO-2 science team. The work in this thesis could not have been completed without your great assistance. As well as my committee, Mitchio, Chip, Geoff Blake, Tom Miller, and Vince McKoy, for their insight and advice.

And of course, the entire Okumura group, past and present: Kana Takematsu, Matt Sprague, Nathan Eddingsaas, Aaron Noell, David Robichaud, Laurence Yeung, Kathryn Perez, Thinh Bui, Leah Dodson, Kathleen Spencer, Aileen Hui, and Sigrid Barklund. You

guys made the office a fun place to be and were always around for a non-blueberry coffee, softball, or a little Ernie's. I will miss Noyes 101, despite the tight confines and mysterious green carpeting.

I'd also like to thank my undergraduate collaborators: Mo Hunsen, Jim Anderson, Jim Hedrick, Jane Frommer, Russell Pratt, and Sheryl Hemkin as well as all of my professors at Kenyon College for the excellent preparation. This work would not have been possible without the education and insight you provided. I arrived at Caltech with an very solid foundation, thank you.

Liz, this thesis is for you. You were there for unwavering support, friendship, and love. I couldn't have done this without you. Your wit, sense of humor, intelligence, and compassion are an inspiration. Thank you for putting up with me. I can't wait to walk across the stage with you come June. See you in DC!

Abstract

Recent remote-sensing satellite missions have aimed to measure global greenhouse gas concentrations with precisions as demanding as 0.25%. These high-resolution measurements should allow for the quantification of carbon sources and sinks, thus, allowing for a considerable reduction in present carbon cycle uncertainties. To achieve these unprecedented measurement goals will require the most precise body of spectroscopic reference data (i.e., laboratory measurements) ever assembled. In order to aid these missions, we have measured ultraprecise spectroscopic parameters for the (30012)←(00001) CO_2 band at 1.57 μm and the O_2 *A*-band at 0.76 μm. These near-infrared transitions are utilized in recent greenhouse gas monitoring missions, with the *A*-band being employed to derive pressure and temperature profiles. In these investigations we have employed frequency-stabilized cavity ring-down spectroscopy (FS-CRDS), a novel ultrasensitive spectroscopic technique. In the O_2 *A*-band we have measured magnetic dipole line parameters for $^{16}O_2$ as well as each of the rare isotopologues and have produced calculated, HITRAN-style line lists. Due to the clear presence of collisional narrowing in the spectra, we have utilized the Galatry line profile in these studies and have reported narrowing parameters under self- and air-broadened conditions. We anticipate that the use of these spectral parameters will greatly reduce the uncertainties of atmospheric remote-sensing retrievals. In addition, the spectral fidelity of FS-CRDS allowed us to observe and quantify unresolved hyperfine structure for the ^{17}O-containing isotopologues. Furthermore, the high sensitivity of FS-CRDS enabled measurements of ultraweak (S~10^{-30} cm molec.$^{-1}$) electric quadrupole transitions in the *A*-band, many of which had not previously been observed. Recently we have begun a series of studies of the near-infrared CO_2 transitions. Measurements at low pressures (<40 kPa) have revealed the simultaneous presence of Dicke narrowing and speed dependence of collisional broadening and shifting. In addition, we have demonstrated that the use of the simple Voigt profile (which neglects these effects) in the pressure range will lead to several percent biases in the retrieved Lorentzian width and spectral area.

Contents

List of Tables

List of Figures

CHAPTER 1

Introduction

Motivation

Carbon dioxide (CO_2) is the dominant anthropogenic greenhouse gas in the Earth's atmosphere. During the industrial era the CO_2 mixing ratio has risen from 280 ppm (parts per million) to greater than 390 ppm, contributing a radiative forcing of 1.66(17) W m^{-2} [1]. Fortunately, only about fifty percent of the emitted CO_2 has contributed to this increase, with the remainder being absorbed by the oceans and biosphere. Due to the great complexity of the global carbon cycle, the precise identity and location of these carbon sinks is not well known. As a result, it is poorly understood how these carbon sinks will respond to rising temperatures and elevated CO_2 mixing ratios and thus, the Earth's susceptibility to further perturbation.

Finding answers to these pressing questions will require extremely precise measurements of CO_2 mixing ratios (at or below the 1 ppm level, 0.3%) which assesses variations across a wide range of spatial and temporal scales [2]. To meet this challenging measurement target NASA is presently developing two satellite-based remote sensing missions: the Orbiting Carbon Observatory (OCO-2) [3] and Active Sensing of CO_2 Emissions over Nights Days and Seasons (ASCENDS). These satellite missions are ideally suited for this challenge, allowing for uninterrupted measurements with global coverage including oceanic and difficult-to-reach sites where ground-based stations are infeasible. In addition, they will have a high measurement precision (<0.3%) and spatial resolution, thus allowing for identification and quantification of present CO_2 sources and sinks.

Achieving this daunting measurement target will require the most precise spectroscopic reference data (i.e., laboratory measurements) ever assembled [4]. When this measurement goal was set, in many cases the needed, metrology-level spectroscopic precision was in excess of any reported measurement. In order to achieve its precision targets, OCO must employ entire spectral bands, not just the strongest rovibrational transitions as in earlier missions, thus, ultraprecise reference data are required for

thousands of transitions across the three utilized bands (the 1.61 and 2.06 μm bands of CO_2 and the 0.76 μm band or *A*-band of O_2).[1] In addition, all weak interfering transitions (e.g. hot bands, combination bands, and rare isotopologue transitions) whose intensities are >0.1% of the weakest main band transitions must be measured and quantified. Thus, a laboratory-based spectroscopic technique is required that is not only extremely sensitive but also exhibits very high resolution and spectral resolution.

While discussing the OCO measurement goals in 2005, Dr. Charles Miller of NASA's Jet Propulsion Laboratory (JPL) outlined three fundamental challenges these daunting targets pose to the spectroscopy community [4]:

Can absolute (or even relative) intensities and line shape parameters be measured to the required 0.3% accuracy for a polyatomic molecule? Are there new, unanticipated aspects of the typical line position/line intensity/line shape problem that are revealed at this level of scrutiny? Will these investigations reveal new physics or demonstrate a new paradigm for the spectroscopic parameters needed to reproduce atmospheric remote sensing data quantitatively?

These challenges motivated this dissertation.

Herein we will present our efforts to address these pressing spectroscopic needs through a series of investigations of near-infrared O_2 and CO_2 transitions. We have employed frequency-stabilized cavity ring-down spectroscopy (FS-CRDS), a novel ultrasensitive technique which is ideally suited for high precision measurements of spectral line shapes. These studies have produced ultraprecise line lists for the O_2 *A*-band (for both the dominant and rare isotopologues) and have quantified subtle line shape effects in both the *A*-band and the near-infrared CO_2 bands including Dicke narrowing and speed dependence. In addition, we have measured hyperfine structure in the ^{17}O-containing isotopologues of O_2, previously unobserved electric quadrupole transitions, and preformed precision measurements of rare CO_2 isotopologues.

[1] Detailed discussion of these bands and their role in remote sensing will follow.

Background

Frequency-stabilized cavity ring-down spectroscopy (FS-CRDS) is an ultrasensitive variant of traditional *cw*-cavity ring-down spectroscopy which was developed in the laboratory of Dr. Joseph Hodges at the National Institute of Standards and Technology (NIST) in Gaithersburg, MD [5,6].

1.1. Cavity Ring-Down Spectroscopy

Cavity ring-down spectroscopy (CRDS) is an established absorbance technique whereby a gas sample is placed within a high finesse optical cavity [7]. Laser radiation is injected into the cavity until the intracavity power reaches a desired level. The light is then turned off (for *cw*-CRDS this is generally achieved through the use of an acousto-optic modulator, AOM) and the power within the cavity decays in an exponential fashion. Since the transmission is proportional to the intracavity power, the resulting exponential decay can be recorded by a photodiode located after the rear cavity mirror. The time constant of this decay is related to the intracavity losses due to mirror losses and sample absorbance (i.e., a large absorbance leads to a short time constant):

$$\tau = \frac{t_r}{2[(1-R)+\alpha L]} \tag{1}$$

where R is the mirror reflectivity (assuming a symmetric cavity with two identical mirrors), α is the absorption coefficient, L in the length of the optical cavity, and t_r is the round trip time for light in the cavity (i.e., $2L/c$). The resulting decay is only a pure, single exponential if a lone cavity mode is excited by the probe laser. Therefore, for high precision, quantitative CRDS it is important that the probe laser be actively mode-matched to the optical cavity through a servo.

Generally, extremely high reflectivity mirrors are utilized (99.9% reflectivity or higher), which results in an enormous increase in effective path length and a complimentary increase in the signal-to-noise ratio. CRDS possesses two fundamental

advantages over traditional long path length direct absorbance techniques. Firstly, since we are measuring the time constant of the decay rather than absolute light intensity, laser power fluctuations have a minimal impact. In addition, the use of an optical cavity allows for a very small gas sample volume (~0.2 L in our case), a feature which will be important for isotopic analyses where expensive, isotopically enriched samples are utilized.

1.2. Frequency-Stabilized Cavity Ring-Down Spectroscopy

Frequency-stabilized cavity ring-down spectroscopy (FS-CRDS) differs from traditional CRDS in two fundamental aspects [5]. Firstly, FS-CRDS is a single-mode technique, so individual cavity modes are selectively excited, thus ensuring quantitative absorption measurements. Secondly, the optical cavity length is actively stabilized with respect to an external frequency reference (see Figure 1a).

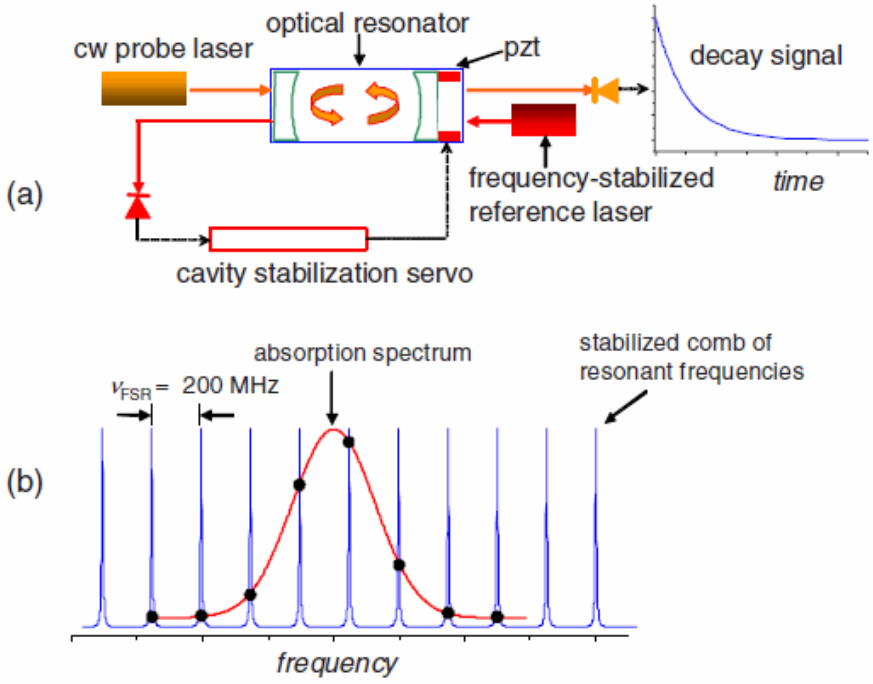

FIG. 1. Frequency-stabilized cavity ring-down spectroscopy (FS-CRDS). (a) Schematic of the FS-CRDS instrument. (b) Spectral acquisition scheme. During a scan, the probe laser is locked to successive TEM_{00} modes of the optical cavity. The stabilized comb of resonant frequencies thus serves as an extremely linear, stable, and accurate frequency axis for the measured spectra. Figure reprinted from [8] with permission of the American Physical Society (2009).

During a scan the probe laser is actively locked to a given TEM_{00} cavity mode. After ring-down measurements have been made, the probe laser frequency is then stepped a distance in frequency space given by the free-spectral range (in our case ~200 MHz) to the next TEM_{00} mode and relocked. This procedure ensures single-mode operation and due to the locked optical cavity length provides an extremely linear, accurate, and stable frequency axis for our spectra. Detailed descriptions of the locking procedures can be found in Refs. [5,6,9]. Note that the entire system has been automated, allowing for spectra to be collected for several days without user intervention [6].

The high sensitivity and spectral fidelity of FS-CRDS make it ideal for ultraprecise line shape studies. Recent FS-CRDS studies have measured line intensities with relative combined uncertainties less than 0.3% [10], Doppler widths to better than 1 part in 6,000 [8], and transition frequencies with uncertainties less than 0.5 MHz (1.5×10^{-5} cm^{-1}) [11]. Spectral signal-to-noise ratios as high as 28,000:1 have been achieved for relatively weak near-infrared transitions (S~3×10^{-26} cm molec. $^{-1}$, or ~8 orders of magnitude weaker than a typical mid-infrared vibrational transition) [12]. In addition, ultraweak transitions [8] (S<4×10^{-29} cm molec.$^{-1}$) and unresolved hyperfine structure [13] have been observed and quantitatively measured.

References

[1] S. Solomon, D. Qin, M. Manning, Z. Chen, M. Marquis, K. B. Averyt, M. Tignor, H. L. Miller (Ed.), Climate Change 2007: The Physical Science Basis. Contribution of Working Group I to the Fourth Assessment Report of the Intergovernmental Panel on Climate Change. (Cambridge University Press, Cambridge, UK and New York, NY, 2007).

[2] P. J. Rayner, D. M. O'Brien, Geophys. Res. Lett. **28,** 175-178 (2001).

[3] D. Crisp, R. M. Atlas, F. M. Breon, L. R. Brown, J. P. Burrows, P. Ciais, B. J. Connor, S. C. Doney, I. Y. Fung, D. J. Jacob, C. E. Miller, D. O'Brien, S. Pawson, J. T. Randerson, P. Rayner, R. J. Salawitch, S. P. Sander, B. Sen, G. L. Stephens, P. P. Tans, G. C. Toon, P. O. Wennberg, S. C. Wofsy, Y. L. Yung, Z. Kuang, B. Chudasama, G. Sprague, B. Weiss, R. Pollock, D. Kenyon, S. Schroll, In: *Trace Constituents in the Troposphere and Lower Stratosphere*, (Pergamon-Elsevier Science Ltd, Kidlington, 2004).

[4] C. E. Miller, L. R. Brown, R. A. Toth, D. C. Benner, V. M. Devi, C. R. Phys. **6,** 876-887 (2005).

[5] J. T. Hodges, H. P. Layer, W. W. Miller, G. E. Scace, Rev. Sci. Instrum. **75,** 849-863 (2004).

[6] J. T. Hodges, R. Ciurylo, Rev. Sci. Instrum. **76,** 023112 (2005).

[7] A. O'Keefe, D. A. G. Deacon, Rev. Sci. Instrum. **59,** 2544-2551 (1988).

[8] D. A. Long, D. K. Havey, M. Okumura, H. M. Pickett, C. E. Miller, J. T. Hodges, Phys. Rev. A **80,** 042513 (2009).

[9] D. J. Robichaud, Dissertation (Ph. D.), California Institute of Technology, 2008.

[10] D. A. Long, D. K. Havey, M. Okumura, C. E. Miller, J. T. Hodges, J. Quant. Spectrosc. Radiat. Transfer **111,** 2021-2036 (2010).

[11] D. J. Robichaud, J. T. Hodges, P. Maslowski, L. Y. Yeung, M. Okumura, C. E. Miller, L. R. Brown, J. Mol. Spectrosc. **251,** 27-37 (2008).

[12] D. A. Long, M. Okumura, C. E. Miller, J. T. Hodges, Appl. Phys. B**,** In press (2011).

[13] D. A. Long, D. K. Havey, M. Okumura, C. E. Miller, J. T. Hodges, Phys. Rev. A **81,** 064502 (2010).

CHAPTER 2

O_2 *A*-Band Line Parameters to Support Atmospheric Remote Sensing

This chapter was published as

D. A. Long, D. K. Havey, M. Okumura, C. E. Miller, and J. T. Hodges, *J. Quant. Spectrosc. Radiat. Transfer*, **111**, 2021–2036 (2010).

Abstract

Numerous satellite and ground-based remote sensing measurements rely on the ability to calculate O_2 *A*-band $[b^1\Sigma_g^+ \leftarrow X^3\Sigma_g^-(0,0)]$ spectra from line parameters, with combined relative uncertainties below 0.5% required for the most demanding applications. In this work, we combine new $^{16}O_2$ *A*-band *R*-branch measurements with our previous *P*-branch observations, both of which are based on frequency-stabilized cavity ring-down spectroscopy. The combined set of data spans angular momentum quantum number, J' up to 46. For these measurements, we quantify a *J*-dependent quadratic deviation from a standard model of the rotational distribution of the line intensities. We provide calculated transition wave numbers, and intensities for J' up to 60. The calculated line intensities are derived from a weighted fit of the generalized model to an ensemble of measured data and agree with our measured values to within 0.1% on average, with a relative standard deviation of ~0.3%. We identify an error in the calculated frequency dependence of the O_2 *A*-band line intensities in existing spectroscopic databases. Other reported line shape parameters include a revised set of lower-state energies, self- and air-pressure-broadening coefficients and self- and air-Dicke-narrowing coefficients. We also report a band-integrated intensity at 296 K of $2.231(7)\times10^{-22}$ cm molec.$^{-1}$ and Einstein-*A* coefficient of 0.0869(3) s^{-1}.

Note that Dr. Joseph Hodges of NIST assisted greatly in the preparation of this publication. His contributions were especially significant in sections 2.3.5–2.3.7.

2.1. Introduction

For fifty years the O_2 *A*-band [$b^1\Sigma_g^+ \leftarrow X^3\Sigma_g^-(0,0)$] has been used extensively in atmospheric remote sensing. The *A*-band has been utilized in the SCIAMACHY [1,2], GOME [3], SAGE III [4], ACE-MAESTRO [5], and GOSAT [6] satellite missions to determine pressure and temperature profiles. In addition, the *A*-band has been applied to remote measurements of cloud-top heights [7], cloud optical properties [8], surface pressure [9,10], and aerosol optical properties [11]. This band is ideally suited to these remote sensing applications for several reasons: O_2 in the atmosphere is uniformly distributed with a well-known mixing ratio, many relatively weak *A*-band transitions are not saturated for long path lengths, and the band is centered at 762 nm (13,125 cm^{-1}) in a window region largely free of spectral interferences.

Due to the importance of O_2 spectral parameters to remote sensing applications, there have been numerous laboratory studies of the *A*-band. Thorough literature summaries can be found in Brown and Plymate [12] and Robichaud et al. [13], and as a result we will only discuss a few relevant studies in detail. In 1987, Ritter and Wilkerson [14] measured 54 transitions with a spectrometer comprising a continuous-wave tunable dye laser ($<10^{-4}$ cm^{-1} resolution) in a multipass configuration. They reported line strengths, half-widths, and lineshape parameters which formed the basis for the 1996 edition of the HITRAN database [15]. In 2000, Brown and Plymate [12] used the McMath Fourier-transform infrared spectrometer (FT-IR) at Kitt Peak to measure *A*-band transitions up to $J' = 22$ (see Section 3 for notation) with a wave number resolution of 0.02 cm^{-1}. Line intensities were reported with a relative uncertainty of 2%. Also reported were half-widths and their corresponding temperature dependence. These measurements were utilized in HITRAN 2000 [16] and 2004 [17], with the half-width temperature dependence being preserved in the current edition [18]. Schermaul and Learner [19] used FT-IR with a resolution of 0.0069–0.029 cm^{-1} to measure intensities and lineshape parameters at room temperature and at 198 K. The resulting spectra were fit using a collisionally narrowed Voigt profile, with line intensities reported having uncertainties of ~0.3%. A comparison of these intensity measurements to calculations showed evidence

of a *J*-dependent slope which was attributed to a rotation-vibration, or Herman-Wallis (HW) effect [20]. Predoi-Cross et al. employed FT-IR and a multispectrum fitting procedure to report intensities and lineshape parameters of N_2- [21] and self-broadened [22] transitions. The effects of chosen lineshape profile and line mixing were also examined.

In recent years, the *A*-band has been utilized in measurements with demanding precision requirements. In particular, high-resolution measurements have aimed to determine surface pressure to 0.1% [9,10] and CO_2 concentration to 0.3% [23,24,25]. These increasingly precise remote sensing measurements, however, have shown that the present uncertainty in O_2 spectroscopic reference data ultimately limits the accuracy of the resulting retrievals [9,26]. To address this problem, Robichaud et al. utilized frequency-stabilized cavity ring-down spectroscopy (FS-CRDS) to measure lineshape parameters [13], positions [27], and pressure-shifting coefficients [28] for many transitions up to $J' = 32$ in the *P*-branch of the *A*-band. The measured positions were tied to the D_1 and D_2 atomic transitions of ^{39}K, yielding uncertainties less than 1 MHz (3×10^{-5} cm^{-1}). Transition line shapes were fit using Galatry line profiles, resulting in line intensity relative uncertainties of ~0.1%-0.5%. It was shown in that study and by Yang et al. [29] that the air- and self-broadening coefficients found in HITRAN 2004, which were based on extrapolations of low-*J* measurements, were inaccurate at higher-*J*. In addition, FS-CRDS was utilized to probe $b^1\Sigma_g^+ \leftarrow X^3\Sigma_g^-(0,0)$ transitions of rare O_2 isotopologues [30]. This collection of FS-CRDS measurements presently forms the basis for HITRAN 2008 for the band intensities of all listed isotopologues, although the rotational dependences were unchanged from HITRAN 2004. In addition, the air- and self-broadening coefficients, transition frequencies, and pressure-shifting coefficients found in HITRAN 2008 are based on FS-CRDS measurements of Robichaud et al. [13].

Most recently, we have pushed the absolute detection limit of FS-CRDS to enable quantitative measurements of ultraweak absorption features, including electric quadrupole transitions [31] and high-*J* [32] magnetic dipole transitions of the $^{16}O_2$ *A*-band. In these experiments the ring-down cavity length stabilization enabled long-term

averaging of spectra, which reduced the detection limit to ~1.8×10^{-11} cm^{-1}. The electric quadrupole transitions were measured and their rotational intensity distribution was modeled. As reported in Long et al., the measured intensities, which had relative uncertainties of <9%, were in agreement with the calculations [31]. The high-*J* magnetic dipole measurements of Havey et al. extended the range of *A*-band line parameters to $J' = 50$ [32]. The intensities of the ultraweak electric quadrupole and high-*J* magnetic dipole transitions are more than 5 orders of magnitude weaker than the strongest magnetic dipole transitions discussed herein. The success of these high-sensitivity studies enabled the intensity measurements over the relatively wide range of *J* reported here. Additionally, in our high-*J* measurements [32], we noted a *J*-dependent deviation in the line intensities (from a standard model) consistent with that reported by Schermaul and Learner [19] which was assigned to a HW interaction.

The preceding FS-CRDS measurements have reduced the uncertainties associated with present *A*-band spectroscopic parameters. Unfortunately, in these earlier studies the tuning range of the probe laser limited measurements to the *P*-branch of the O_2 *A*-band. In this work, we present new FS-CRDS measurements of 34 transitions in the *R*-branch which are combined with our previous *P*-branch measurements. Intensity data are fit using a standard model which includes a HW effect for the rotational dependence of the intensities. Thus, we confirm and quantify the HW effect and demonstrate its importance with regard to an accurate description of O_2 *A*-band line intensities. Also, we present data illustrating the *J*- and branch-dependence of the narrowing parameter. This information is intended to enable the remote sensing community to incorporate more realistic line shape profiles that capture narrowing effects. We provide correlations which are based on fits to our measured line shape parameters for line positions, intensities, collisional narrowing parameters, air- and self-broadening coefficients, and pressure-shifting coefficients. These results are summarized in a new list of calculated line parameters up to $J = 60$.

2.2. Experiment

Measurements were made using the frequency-stabilized cavity ring-down spectrometer located at the National Institute of Standards and Technology (NIST) in Gaithersburg, MD. The FS-CRDS technique has been previously described in considerable detail [33,34], and thus we will only briefly summarize the technique here.

FS-CRDS is similar to traditional CW-CRDS techniques in that both methods utilize a narrow linewidth continuous wave (CW) laser to excite individual optical resonances (modes) of the ring-down cavity. Both enable the determination of sample absorption coefficient from the measured intensity decay rate and avoid the complexities of multiexponential decays caused by broadband laser excitation [35,36,37]. However, the FS-CRDS and CW-CRDS techniques differ in an important way. In the former, the comb of resonant frequencies and thus cavity length are actively locked against a frequency-stabilized reference laser, whereas in the latter, the cavity modes are unlocked and subject to drift as a result of nanometer-scale changes in the cavity length (see Fig. 1). In CW-CRDS, the cavity length or probe laser frequency is typically modulated by an amount slightly more than the free-spectral range (FSR), thus forcing spectral overlap of the narrowband probe laser with the cavity resonant frequencies [38,39,40], and in other CW-CRDS implementations, the cavity length is modulated with a smaller amplitude and servoed to track frequency tuning of the probe laser [41,42]. For FS-CRDS, the probe laser selectively excites the TEM_{q00} transverse mode (where q is a specific longitudinal mode order), and sub-FSR frequency steps are realized by frequency shifting the reference laser (and hence cavity frequency comb) with an acousto-optic modulator. The result is a high-resolution (<1 MHz) and linear spectrum frequency-axis for FS-CRDS that is immune to frequency drift in the probe laser.

For the measurements described herein, the reference laser was a frequency-stabilized HeNe laser with a long-term (8 h) frequency uncertainty of less than 1 MHz. The probe laser was an external cavity diode laser (ECDL) with a wavelength range of 759-771 nm and an output power of 6-10 mW. Two separate pairs of custom-made dichroic ring-down mirrors were employed for these measurements. Both pairs of mirrors

had reflectivity R = 95% at the reference laser wavelength (633 nm). The higher loss mirrors had a nominal reflectivity for the probe wavelength of 99.98%, which corresponds to an effective path length of 3.5 km, given our 0.74 m cavity (finesse ≈ 15,000). While using these mirrors, the noise equivalent absorption coefficient (NEA) was 6×10^{-10} cm^{-1} Hz$^{-1/2}$. For the measurement of weaker transitions, lower-loss mirrors for the probe beam were utilized having a nominal reflectivity of R = 99.997%. The use of these mirrors reduced the NEA to 2.5×10^{-10} cm^{-1} Hz$^{-1/2}$. We measured the cavity free-spectral range to be 201.970(10) MHz for the higher-loss mirrors and 202.495(12) MHz for the lower-loss mirrors using the technique described by Lisak and Hodges [43].

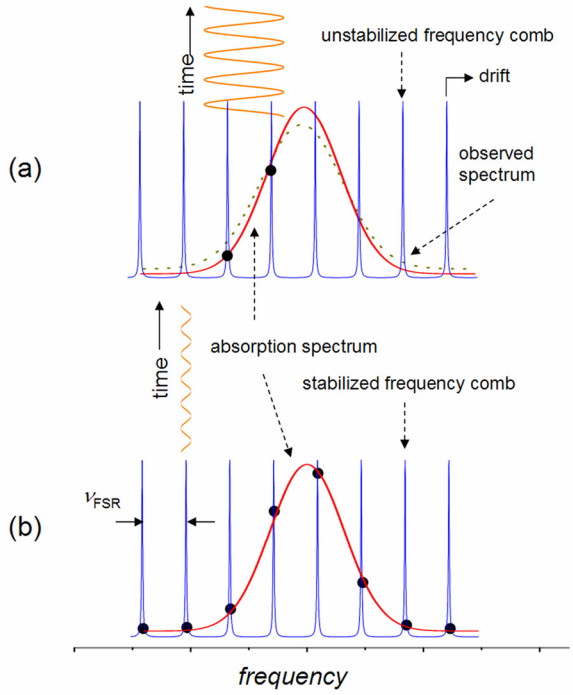

FIG. 1. Comparison of cavity ring-down spectroscopy techniques. (a) CW-CRDS method using an unstabilized cavity and modulation of the laser frequency through one cavity free-spectral range (FSR). Alternatively, the laser frequency is step scanned and the cavity length is modulated to force spectral overlap at each mean frequency step. In the former case, the observed spectrum is instrumentally broadened by the mode spacing. In the latter case, transverse mode competition, laser frequency drift and nonlinearity in the laser frequency tuning can distort the observed spectrum. (b) FS-CRDS method using a stabilized resonator. The probe laser is step-scanned through successive TEM_{q00} modes. The frequency resolution is given by the stability of the cavity resonances, the step size is equal to the cavity FSR (or smaller using an AOM) and the observed spectrum is subject to minimal instrumental broadening.

Spectral scans were made over 10 GHz wide windows centered at an individual transition (note that the Doppler width of $^{16}O_2$ (full-width half-maximum) in the *A*-band at 296 K is ~0.85 GHz). For measurements with the higher-loss (2×10^{-4}) mirrors, 50 MHz frequency steps were made, while 200 MHz steps were used with the lower-loss (3×10^{-5}) mirrors. Note that the uncertainty in the frequency axis is limited by the frequency-stabilized HeNe reference laser and is therefore less than 1 MHz. Further details on this frequency stability and the experimental scanning procedure can be found elsewhere [13,33,34].

Temperature measurements were made with a NIST-calibrated 2.4 kΩ thermistor in good thermal contact with the ring-down cavity. The uncertainty in the gas temperature was examined in detail by Havey et al. [32]. It was shown that the combined uncertainty is less than 28 mK (15 mK uncertainty in the measurement and 23 mK uncertainty from the presence of a thermal gradient along the cavity). All measurements were made over the temperature range 299 to 300 K. Pressure was measured by two NIST-calibrated capacitance diaphragm gauges having full-scale responses of 13.3 kPa (100 Torr) and 133 kPa (1,000 Torr). We estimate the relative combined standard uncertainty of this pressure measurement to be less than 0.1%.

Measurements were made on static samples of either pure O_2, synthetic air (mixture of N_2 and O_2), or a synthetic air mixture having ~2% O_2. The pure O_2 had >99.9% purity. The synthetic air was a NIST standard reference material (SRM 2659a, hereafter referred to as "NIST standard air") having a molar composition of 79.28% N_2, 20.720 ± 0.043% O_2, 0.0029% Ar, 0.00015% H_2O, and 0.001% other compounds. The 2% O_2 mixture was also a NIST SRM (2657a, hereafter referred to at "NIST 2% O_2") which had a molar composition of 98.05% N_2, 1.9734 ± 0.0053% O_2, 0.004% Ar, 0.00011% H_2O, and 0.001% other compounds. All samples contained O_2 at natural terrestrial isotopic abundance (I_a = 0.995262 for $^{16}O_2$ [18]). Table 1 summarizes the experimental conditions. For our analysis, we calculate the number density, n, of O_2 to be $n = (x_{O2}p)/(k_BT)$, where x_{O2} is the mole fraction of O_2, T is temperature, p is total pressure, and k_B is the Boltzmann constant.

TABLE 1. Experimental Conditions for the O_2 *A*-band *R*-branch FS-CRDS measurements.

J'	sample[a]	mirror losses (10^{-6})	finesse	step size (MHz)
2-22	NIST 2%	200	15,000	50
24,26,32	NIST Air	200	15,000	50
34-42	NIST Air	30	105,000	202
34, 38-42	Pure O_2	30	105,000	202

[a]All measurements were made over the temperatures range of 299 to 300 K and then corrected to T_{ref} = 296 K. Sample pressure was transition dependent [see Tables A1(a-c)]. The ring-down cavity finesse is based on the measured time constant under empty cavity conditions.

We modeled the measured FS-CRDS spectra, denoted by $[c\tau(\tilde{\nu})]^{-1}$ as the sum of absorption line shape profiles superimposed on a linear baseline, $[c\tau(\tilde{\nu})]^{-1} = \alpha(\tilde{\nu}) + L_b(\tilde{\nu})\ell^{-1}$. Here, *c* is the speed of light, $\tilde{\nu}$ is wave number of the probe laser, τ is the measured ring-down time constant, ℓ is the ring-down cavity length, and L_b is the effective base cavity loss comprising all losses other than local line absorption by the gas sample. We determined the line area A_l by evaluating $\int d\tilde{\nu}\alpha(\tilde{\nu} - \tilde{\nu}_0)$ in which α is the absorption coefficient found by fitting the line shape to the observed spectrum centered at $\tilde{\nu}_0$. Measured values of *n* and A_l gave the line intensity as $S = A_l/(cn)$.

Reported results were obtained by fitting the Galatry line profile [44] to our measured spectra. This lineshape is based on a soft-collision model which includes the effects of collisional (Dicke) narrowing [45]. Line areas, Lorentzian full-width at half-maximum frequency ($\Delta\nu_L$), the narrowing frequency (ν_{opt}) [45,46], and a linear baseline were treated as fitted parameters while the Doppler width was constrained to its theoretical value. The narrowing frequency is also referred to as the optical frequency of velocity-changing collisions. Generally, the collisional narrowing parameter $\eta = \nu_{opt}/p$ was calculated from the slope of ν_{opt} vs. *p*. However, it was not possible for some transitions to determine ν_{opt} with sufficient accuracy. For some blended transitions ν_{opt}

was constrained based on a previously established J-dependence for η [13,32] while ν_{opt} for a few lower pressure spectra was fixed to a value determined by a linear fit to the higher pressure measurements.

2.3. Results and Discussion

The O_2 A-band [$b^1\Sigma_g^+ \leftarrow X^3\Sigma_g^-$ (0,0)] is forbidden by quantum mechanical electric dipole selection rules, but is allowed as a magnetic dipole transition [47]. The rotational levels of O_2 are fully described by three quantum numbers: N, the rotational angular momentum, S, the spin angular momentum, and J, the total angular momentum ($J = N + S$). The $X^3\Sigma_g^-$ ground state of O_2 is split into three energy levels having $J'' = N'' - 1$, N'' + 1, N''. The $b^1\Sigma_g^+$ upper state has only one level whereby $J' = N'$. For $^{16}O_2$, N' must be even and N'' must be odd due to spin statistics.

The A-band transitions can be described as ΔN N'' ΔJ J'' and occur in four branches: PP, PQ, RR, and RQ. Both the P- ($\Delta N = -1$) and R- ($\Delta N = 1$) branches are made up of pairs of transitions which are separated by ~2 cm^{-1}. The P-branch transitions (i.e., PP, PQ) begin at 13,120 cm^{-1} (762 nm) and decrease in wave number with increasing J'. The spacing between sets of pairs increases with increasing J', whereas, the distance between sets of pairs decreases in the R-branch, forming a bandhead at 13,165 cm^{-1}. Each transition in the four branches can be specified by an angular momentum index, m, where $m = -J''$ (PP- and PQ-branches) and, $m = J''+1$ (RR- and RQ-branches).

2.3.1. Measured Line Intensities

Measured line intensities are given at natural terrestrial isotopic abundance and were corrected to $T_{\text{ref}} = 296$ K using $S(T_{ref}) = S(T)[Q(T)/Q(T_{ref})]e^{-hcE''/k_B(1/T_{ref}-1/T)}$, where E'' is the lower state energy expressed as a wave number and $Q(T)$ is the total internal partition function of $^{16}O_2$ for which $Q(T_{\text{ref}}) = 215.7739$. The resulting intensities and other measured line parameters can be found in Tables A1(a-c).

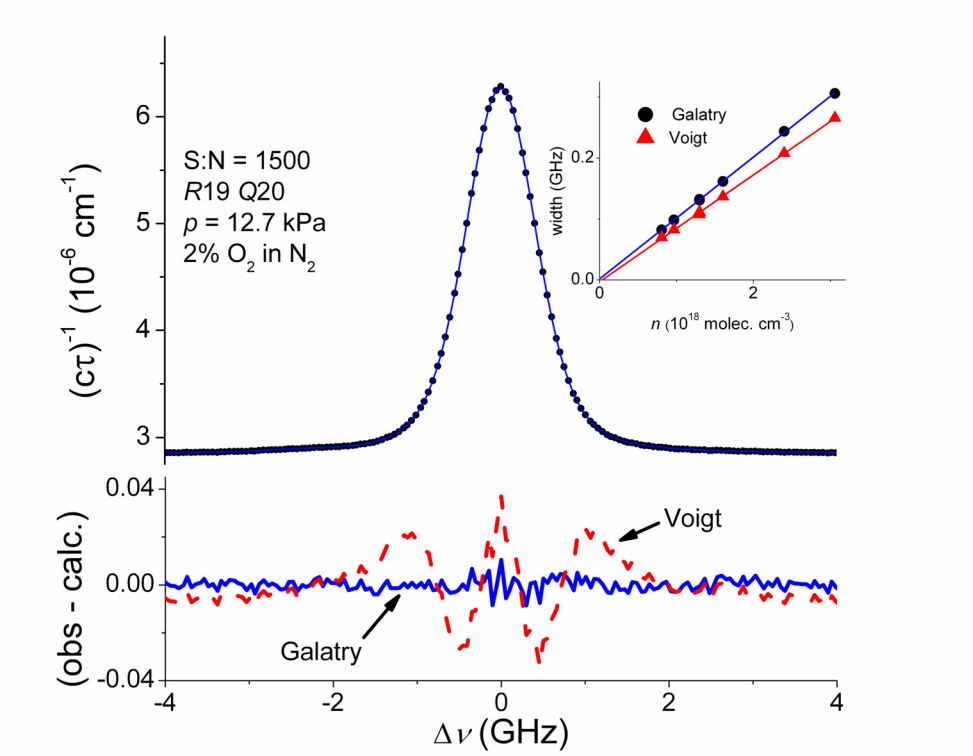

FIG. 2. Top panel: Measured absorption spectrum (symbols) and Galatry fit (line) for the *R*19*Q*20 O_2 *A*-band transition. The abscissa represents frequency detuning about line center. The gas mixture was NIST 2% O_2, and the total pressure, p = 12.7 kPa. Bottom panel: Fit residuals for Galatry and Voigt profiles. The inset of the top panel shows the Lorentzian width (FWHM) vs. total gas concentration, n. The Voigt fit gives a slope (broadening coefficient) 15.4% lower and spectrum area 1.35% greater in comparison to those values obtained from fitting the Galatry profile.

Figure 2 gives a typical measured absorption spectrum and Galatry fit, as well as fit residuals for the Galatry and Voigt profiles. The sample conditions correspond to the NIST 2% O_2 sample at a total pressure of 12.7 kPa. The ratio of peak absorption losses to root-mean-square baseline variations is ~1,500:1 for this spectrum, making it possible to clearly distinguish between the two fitted lineshapes. Unlike the Galatry profile, which essentially captures the measured line shape at the baseline noise level, the Voigt profile exhibits relatively large symmetric residuals. We attribute these residuals in the Voigt fit to collisional narrowing effects. This phenomenon also leads to an underestimation of the Lorentzian width shown in the inset of Fig. 2 and which is discussed below. The fitted Voigt profile in Fig. 2 yields a spectrum area which is 1.35% greater than that obtained from fits of the Galatry profile. Similar results were found in a

FS-CRDS study of six O_2 $b^1\Sigma_g^+(1)\leftarrow X^3\Sigma_g^-(0)$ transitions (B-band) where Lisak et al. [48] showed that the Voigt profile gave spectrum areas differing from 0.3% to 1% in comparison to those based on the Galatry profile. They showed that the Voigt profile induced a decrease in fitted area for all but one transition.

The uncertainty in our measured line intensities is obtained from a quadrature sum of the Type A and Type B uncertainties which arise from random effects and systematic effects, respectively. For measured transitions with $J' \leq 26$, the estimated uncertainties are similar to those found in Robichaud et al. [13]. For each of these transitions the relative combined standard uncertainty was between 0.2% and 0.4%. For these transitions below the bandhead, the dominant uncertainties were fit reproducibility and sample composition. Choice of line profile [48], temperature [32], and pressure uncertainties contributed a small amount (less than 0.1%) to the overall reported uncertainty. For weaker transitions near the bandhead (i.e., those with $J' > 26$) the uncertainties are much larger than those found in Robichaud et al. [13] and Havey et al. [32] for similar J'. For these transitions, the measurement accuracy was not limited by the signal-to-noise ratio, but rather by the presence of interfering transitions (including many rare isotopologue transitions). These transitions were often blended with the target transition, thus making quantitative fitting difficult. For the rare isotopologue lines, lineshape parameters found in HITRAN 2008 [18] (which are based upon the measurements of Robichaud et al. [30]) were utilized and were not floated in the fitting procedure. Uncertainties in these rare isotopologue line shape parameters were incorporated into the combined standard uncertainties for the bandhead $^{16}O_2$ transitions. These fitting challenges ultimately led to relative combined standard uncertainties as large as 4%. In these cases, the fitting uncertainties were dominant and contributions from n, P, T, were negligible.

2.3.2. Standard Intensity Model

A physical model for the distribution of line intensities within a given band is a valuable tool for predicting and interpreting molecular spectra. The intensity of absorption for a dipole transition in a band of intensity S_b is given by [49]

$$S_m = \frac{C_b\, S_b g \tilde{\nu}_m L_m e^{-E_m'' hc/k_B T_{ref}} (1 - e^{-\tilde{\nu}_m hc/k_B T_{ref}})}{Q(T_{ref})\tilde{\nu}_b}. \quad (1)$$

In this expression, g is a degeneracy factor (in this case equal to three given the triplet ground state), L_m is the Hönl-London factor (the transition-dependent factor which captures the non-Boltzmann, J-dependence of the intensities), $\tilde{\nu}_m$ is the transition wave number, $\tilde{\nu}_b$ is the band center wave number, and C_b is a dimensionless normalization constant close to unity which ensures that $\Sigma\ S_m = S_b$. The temperature-independent Einstein-A coefficients, $A_m(J')$, can also be calculated as [49]

$$A_m(J') = \frac{8\pi c\, Q(T_{ref})\, \tilde{\nu}_m^2 S_m}{(2J'+1) e^{-E_m'' hc/k_B T_{ref}} (1 - e^{-\tilde{\nu}_m hc/k_B T_{ref}})}. \quad (2)$$

In the present case, the set of L_m are the Hönl-London factors are given by Watson [50] and were calculated using the $^{16}O_2$ molecular parameters of Long et al. [31]. Henceforth, we refer to the preceding two expressions as the standard intensity model. Below, we compare experimentally measured intensities, corrected to the reference temperature, to the standard intensity model.

2.3.3. Comparison of Standard Intensity Model to Existing Databases

In principle, the O_2 A-band line intensities in HITRAN (since the 1996 edition) are based upon the standard intensity model [49] and the Einstein A-coefficient of 0.0887 s^{-1} measured by Ritter and Wilkerson [14]. For HITRAN 2008, this value was reduced by ≈1% [18] based on the measurements of Robichaud et al. [13]. This recent modification had no effect on the J-dependence of the tabulated intensities.

Previously, we identified a discrepancy between J-dependent line intensities predicted by the standard intensity model and those found in the HITRAN 2008 database [32]. Here we confirm that the O_2 A-band line intensities in HITRAN 2008 do not follow the standard model given by Eq. 1. Further, our analysis indicates that the frequency dependence of the HITRAN 2008 intensities can be reconciled with Eq. 1 provided one introduces the extra factor, $\tilde{\nu}_\mathrm{m}^{\,3}$. Denoting the corresponding database intensities by S_HT,

we empirically find that $(\tilde{\nu}_m / \tilde{\nu}_b)^3 S_{HT} / S_m$ is essentially a transition-independent constant. See Figure 3. It appears that a mistake was made in calculating the *J*-dependence of the HITRAN line intensities for the O_2 *A*-band. We conclude that the wave number dependence of the HITRAN 2008 O_2 *A*-band line intensities is unphysical, and consequently with regard to the *J*-dependence of the line intensities, this error masks physical departures from the standard intensity model. Finally, we emphasize that this discrepancy applies to multiple rovibronic bands of $^{16}O_2$ and other isotopologues in both the HITRAN and GEISA [51,52] databases.

2.3.4. Comparison of Measurements to Standard Intensity Model

For the O_2 *A*-band, *J*-dependent deviations of the intensities from the standard intensity model have been previously observed by Miller et al. [53], Ritter and Wilkerson [14], and Schermaul and Learner [19]. Schermaul and Learner ascribed this to a Herman-Wallis (HW) rotation-vibration interaction [20], while Balasubramanian and Narayanan [54] have attributed these deviations to a series of rotational perturbations (spin uncoupling, orbit rotation interaction and spin-orbit perturbation). Unfortunately, a HW theory applicable to transitions between electronic states is not presently available. Further, by comparison of their rotational perturbation theory to the measurements of Miller et al., Balasubramanian and Narayanan noted only marginal improvement over the standard model [54]. Therefore, the present theoretical basis for this effect is incomplete. In the following we will denote observed deviations from the standard intensity model as HW-like, while acknowledging that other perturbations are likely present.

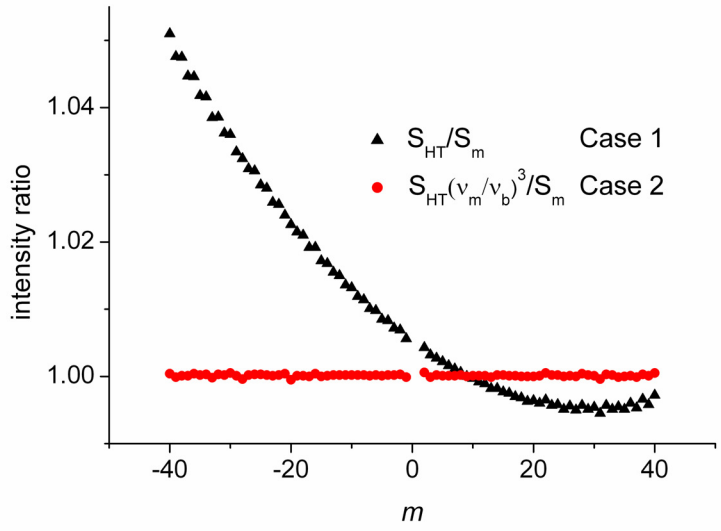

FIG. 3. Comparison of m-dependence of the intensities given by HITRAN 2008, S_{HT}, to those given by the standard intensity model, S_{m}. Triangles (Case 1) correspond to the ratio $S_{\mathrm{HT}} / S_{\mathrm{m}}$ and circles (Case 2) are for the ratio, $S_{\mathrm{HT}}(\tilde{\nu}_m / \tilde{\nu}_b)^3 / S_{\mathrm{m}}$. The average absolute deviation from unity for Case 2 is 2×10^{-4}, which we assign to round-off error.

In Fig. 4 we present a comparison of the standard intensity model to the present measurements and those of Robichaud et al. [13], Havey et al. [32], Brown and Plymate [12], Ritter and Wilkerson [14], and Schermaul and Learner [19]. In our previous work [32], all data was for $m < 0$ (P-branch) for which the intensity deviations over this range appear linear. We note that the experimentally determined HW-like slope elucidated by comparison to the HITRAN 2008 intensities [32] had the opposite sign and a smaller magnitude than that obtained in comparison to the standard intensity model. This discrepancy is now attributed to the extra wave number factor discussed above. In the present work, we provide new line intensity measurements for $m > 0$ (R-branch). Below, all of the NIST FS-CRDS O_2 A-band data, which includes the present measurements and those of Robichaud et al. [13] and Havey et al. [32], are treated as a single data set spanning $m = -46$ to 43. After combining this data, it is apparent that the deviation between the measurements and the standard intensity model varies nonlinearly with m.

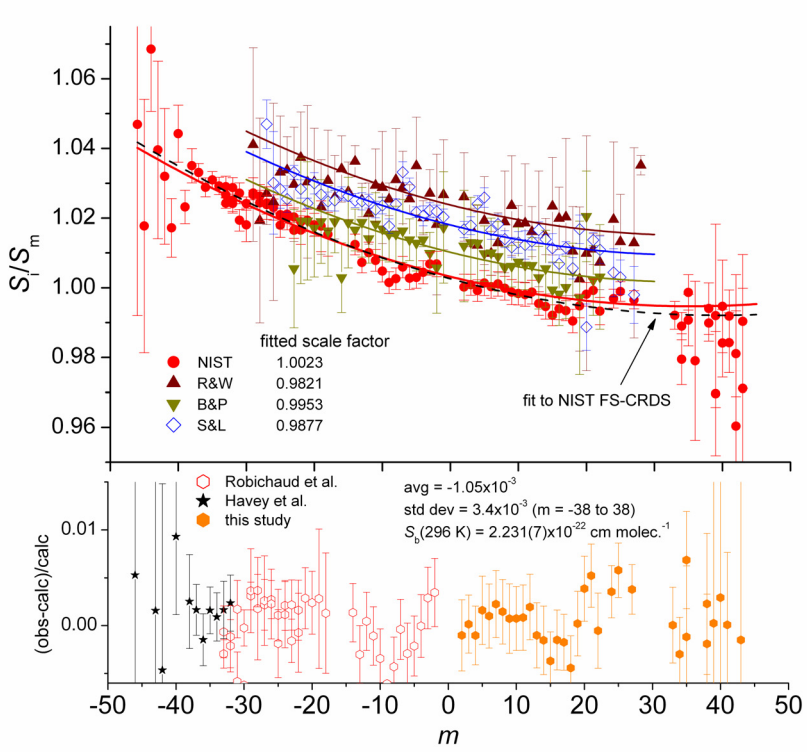

FIG. 4. Comparison of experimental intensities to calculations performed using Eq. 2 with the Watson [50] Hönl-London factors. Note that the Ritter and Wilkerson measurements (R&W) [14] were corrected to 296 K (from 294 K), the Schermaul and Learner measurements (S&L) [19] were corrected to natural isotopic abundance, while the Brown and Plymate measurements (B&P) correspond directly to those reported in the literature [12]. In addition, the NIST and R&W studies employed Galatry line profiles, while the B&P and S&L studies utilized Voigt line profiles. Top panel: The indicated data sets (symbols), and fitted values (lines) for the global fit of the quadratic HW-like functions $f_i^{-1}(1 + a_1 m + a_2 m^2)^2$, where f_i^{-1} is the fitted scale factor for set i, (i= 1 to 4). The dashed line represents another HW-like fit to previous NIST FS-CRDS data [13,32] combined with the present work yielding, $a_1 = -2.6580\times10^{-4}$ and $a_2 = 3.3622\times10^{-6}$. Bottom panel: The relative difference between the NIST FS-CRDS measurements and the latter fit. The error bars for the NIST FS-CRDS data correspond to ±1 standard deviation and include the quadrature sum of random (Type A) and systematic (Type B) uncertainties.

We empirically used the general quadratic formula of Watson [55],

$$F_{HW} = (1 + a_1 m + a_2 m^2)^2, \tag{3}$$

which was derived for HW corrections to the intensities of rotation-vibration transitions of linear molecules. We did a global, weighted least-squares fit of the ratio $S_{meas,i}/S_m = f_i F_{HW}$, using this model and including all four sets of measurements shown in Fig. 4. Here, $S_{meas,i}$ represents the observed intensities for measurement set i. The coefficients a_1

and a_2 were common fitted parameters, and each measurement set was independently scaled by the fitted parameter, f_i, to account for systematic deviations between the experiments. The results are given by the solid curves in the upper panel of Fig. 4. As previously shown [19,32], all of the data exhibit a HW-like effect. Also, the global fit reveals a spread of ~2% in the scaling factors which is indicative of systematic differences between the measured the line intensities. We repeated the fit of the quadratic F_{HW} function to the ratio S_{meas}/S_m, using only the NIST FS-CRDS data. This result, which is shown in Fig. 4 as the dashed line, differs only slightly from the global fit, yielding $a_1 = -2.658(88)\times10^{-4}$ and $a_2 = 3.36(44)\times10^{-6}$.

Tipping and Bouanich [56] discussed how for dipole transitions, F_{HW} can be expressed as an expansion in powers of m given by

$$F_{HW} = 1 + \sum_{j=1}^{\infty} e_j m^j , \tag{4}$$

where the jth order coefficient e_j is of order ε^j . Here, ε is the ratio of rotational to vibrational spacing equal to $(2B_e/\omega_e)$. We calculate $\varepsilon = 1.82\times10^{-3}$, using $B_e = 1.4377\ \text{cm}^{-1}$ and $\omega_e = 1580.19\ \text{cm}^{-1}$ [57] for the $X^3\Sigma_g^-$ lower state of $^{16}O_2$. Expanding Eq. 4 and using our fitted values for a_1 and a_2 gives the measured expansion coefficients, $e_1 = 2a_1 = -5.3\times10^{-4}$, $e_2 = (a_1^2 + 2a_2) = 6.8\times10^{-6}$, $e_3 = 2a_1a_2 = -1.8\times10^{-9}$ and $e_4 = a_2^2 = 1.1\times10^{-11}$, which are of order ε , ε^2 , ε^3 , and ε^4 , respectively. This order-of-magnitude analysis leads us to conclude that our measured HW-like J-dependent correction factor is consistent with the spectroscopic constants of O_2 and the expansion given by Eq. 4. However, when we employ the rotationally perturbed Hönl-London factors of Balasubramanian and Narayanan [54] the observed intensity deviations of the FS-CRDS data are reduced by roughly a factor of 2, suggesting that this mechanism also plays an important role. Therefore, we conclude that a more comprehensive theoretical analysis of the relative contributions of various perturbations is warranted.

The precision of the quadratic fit to the FS-CRDS O_2 A-band intensity data is illustrated in the bottom panel of Fig. 4, where the standard deviation of the relative difference between the measurements and the theoretical values (over the range m = -38

to 38) is 0.34%, with a mean value of –0.1% (m = –46 to 43). In this figure, the three sets of data which comprise the FS-CRDS intensity measurements are delineated and are self-consistent at the 0.3% level. We note that the FS-CRDS intensity measurements reported by Havey et al. [32] comprising the five O_2 A-band transitions $P47P47$ through $P51P51$, the weakest of which has a measured intensity of $1.10(31)\times10^{-30}$ cm molec.$^{-1}$ were not included in the above analysis because of their relatively high uncertainties. Nevertheless, these measured intensities agree with the calculated values given in Table A2 to within their measurement uncertainty, thus confirming the extrapolation of the intensity calculation out to at least $J \approx 50$.

The fit described above yielded a band intensity of $S_b(296\ \text{K}) = 2.231(7)\times10^{-22}$ cm molec.$^{-1}$, from which we obtained the band-integrated Einstein-A coefficient, $A_b = 0.0869(3)\ \text{s}^{-1}$. This band intensity is lower than those calculated for the previous experimental studies, with Brown and Plymate's [12] and Schermaul and Learner's [19] measurements resulting in band intensities ~0.7%-1.5% higher than the present study, and Ritter and Wilkerson's [14] temperature-corrected value being ~2% higher than our present measurements. See Table 4 of Ref. [22] for a complete collection of earlier measurements of the band-integrated Einstein-A coefficient.

Line intensities calculated using the above model, with the HW-like correction described above, can be found below in Table A2 up to J' = 60 for all four branches. This table also contains line positions and lower state energies calculated using the molecular parameters of Long et al. [31] as well as the Einstein-A coefficients calculated using Eq. 2 and the Hönl-London factors of Watson [50]. Table A2 also includes other line parameters including the broadening coefficients, narrowing parameters, and pressure-shifting coefficients which are discussed below.

2.3.5. Broadening Coefficients

The air- and self-broadening coefficients, γ_{air} and γ_{self}, found in HITRAN 2008 [18] are based upon the FS-CRDS measurements of Robichaud et al. [13], which were fit using the empirical correlation of Yang et al. [26]:

$$\gamma = A_\gamma + \frac{B_\gamma}{1 + c_1 J' + c_2 J'^2 + c_3 J'^4}, \tag{5}$$

in which A_γ and B_γ have units of MHz/Pa, c_1, c_2, and c_3 are dimensionless constants, and where the broadening coefficient is defined as $\gamma = \Delta\nu_L/(2p)$. It has been noted in the literature [13,26,32] that the air- and self-broadening correlations found in HITRAN 2004 [17] which were based upon the extrapolation of low-*J* data, are not accurate at high-*J* (with deviations of up to 40% at some high-*J* values). Recently, Havey et al. [32] examined the accuracy of the HITRAN 2008 correlation at high-*J* (up to J' = 50) in the *P*-branch using FS-CRDS. Excellent agreement was seen between these new measurements and HITRAN 2008 in the overlap region. In addition, new correlations for air- and self-broadening coefficients were proposed; although these new results are only slightly altered from those of HITRAN 2008. Coefficients for air- [13] and self- [32] broadening correlations given by Eq. 5 are given in Table 2.

Tables A1(a-c) give the measured broadening coefficients for the NIST 2% O_2, NIST air and pure O_2, gas mixtures respectively. Each of these γ values was based on fitting the Galatry profile to measured spectra and an average of measurements made at several different pressures, *p*. We corrected the broadening coefficients to T_{ref} = 296 K according to the temperature dependence found in HITRAN 2008 [18] which is based upon the measurements of Brown and Plymate [12]. The uncertainty in this temperature correction was negligible compared to the fit uncertainties.

TABLE 2. Factors used to calculate air- and self-pressure broadening coefficients (γ_{air} and γ_{self}) and air- and self- narrowing parameters (η_{air} and η_{self}) given in Table A2. The former were given by $\gamma = A_\gamma + B_\gamma /(1 + c_1 J' + c_2 J'^2 + c_3 J'^4)$ and the latter by $\eta = \eta_\infty - \kappa\gamma(J')$. The pressure shifting coefficient was calculated from $\delta = b_0 + b_1 J' + b_2 J'^2$.

	A_γ (MHz Pa^{-1})	B_γ (MHz Pa^{-1})	c_1	c_2	c_3
γ_{air}	6.018E-03	1.217E-02	7.806E-02	–3.270E-03	4.184E-06
γ_{self}	7.186E-03	1.021E-02	7.180E-02	–2.334E-03	3.025E-06

branch	sample	η_∞ (MHz Pa^{-1})	κ
PP	air	0.00992	0.43011
PQ	air	0.00900	0.37063
RQ	air	0.00550	0.05684
RR	air	0.00601	0.08725
PP,PQ,RQ,RR	O_2	0.00883	0.39532

branch	sample	b_0 (MHz Pa^{-1})	b_1 (MHz Pa^{-1})	b_2 (MHz Pa^{-1})
PP,PQ,RQ,RR	air,O_2	-1.7195E-03	-4.5947E-05	3.3747E-07

In all cases, a plot of $\Delta\nu_L$ as a function of p exhibited good linearity and roughly zero intercept, as would be expected for physical parameters. Linearity was also observed for spectra fit with the Voigt profile. However, the slope and hence broadening coefficient was generally smaller than for the Galatry profile case. This difference in fitted line width between the Galatry and Voigt profiles is a consequence of collisional narrowing effects. In this case, the best-fit Voigt profile compensates for line narrowing by reducing the Lorentzian width and consequently fails to capture the actual line shape. We refer again to Fig. 2 where this effect is illustrated. Here fitting the Voigt profile gave a broadening coefficient 15.4% smaller than that obtained by fitting the Galatry profile. These results are also consistent with the O_2 *B*-band observations of Lisak et al. [48], who showed that use of the Voigt profile can reduce the fitted Lorentzian width by as much as 50% compared to those obtained with the Galatry profile or other line shapes that incorporate line narrowing effects.

2.3.5.1. Air-Broadening Coefficients

Our O_2 *A*-band *R*-branch γ values for air-broadening, given in Table A1(b), agree in general with the earlier FS-CRDS *P*-branch measurements to within their combined uncertainties (see Fig. 5). In addition, these present measurements show excellent agreement with HITRAN 2008, with a mean absolute relative deviation of 4% and values typically agreeing to within the experimental uncertainty. Therefore, these present *R*-branch measurements serve as an independent validation of the broadening coefficients found in HITRAN 2008.

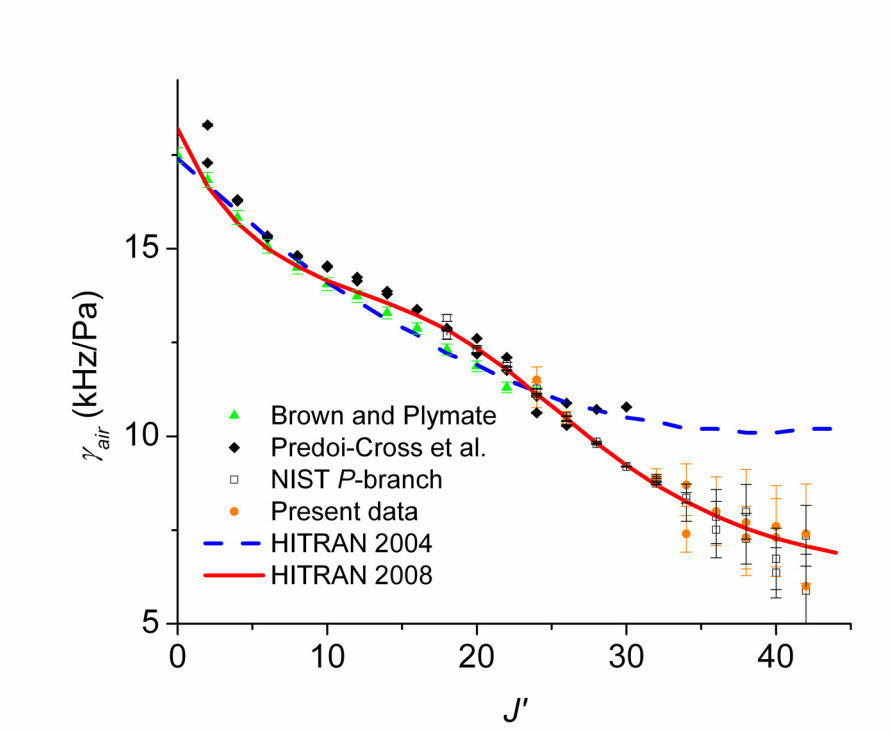

FIG. 5. Air-broadening coefficients as a function of J' for *P*- and *R*-branch transitions in the O_2 *A*-band. All coefficients have been corrected to T_{ref} = 296 K. Lines show correlations from the HITRAN 2004 [17] and 2008 [18] databases. Also, shown are the earlier FS-CRDS *P*-branch measurements [13,32] and the measurements of Brown and Plymate [12] and Predoi-Cross et al. [21,22]. Note that the present study and the NIST *P*-branch measurements utilized Galatry line profiles, while the Brown and Plymate and Predoi-Cross et al. studies employed Voigt line profiles.

Differences in air-broadening coefficients for a given J' were largely due to the presence of interfering lines. Unfortunately, these interferences led to uncertainties that were too large to enable us to differentiate between the correlation found in HITRAN

2008 and that of Havey et al. [32]. As a result, this study finds no evidence that the air-broadening coefficients for the O_2 *A*-band *R*-branch found in HITRAN 2008 need to be revised. Furthermore, these overlapping lines greatly complicated the fitting procedure and limited the number of transitions we were able to quantitatively measure.

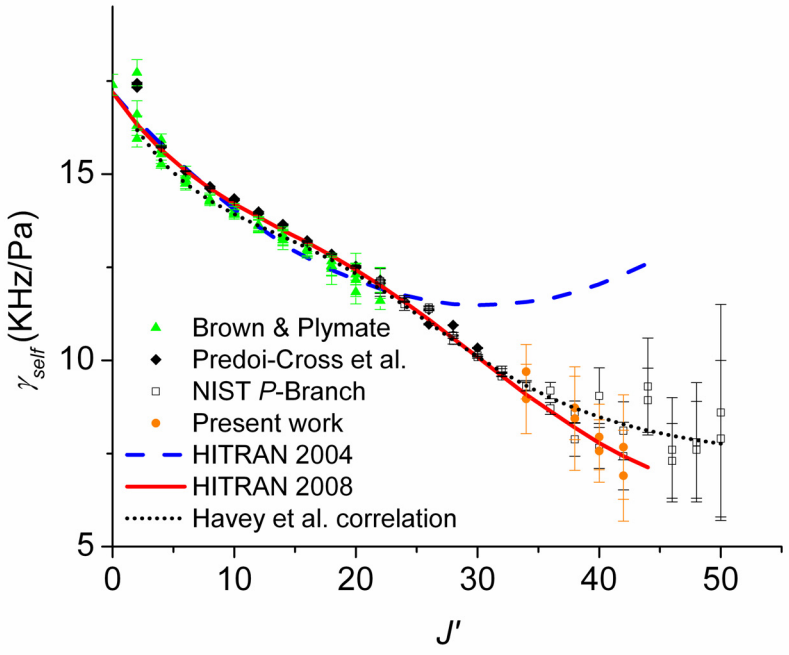

FIG. 6. Self-broadening coefficients as a function of J' for *P*- and *R*-branch transitions in the O_2 *A*-band. All coefficients have been corrected to T_{ref} = 296 K. The outer two lines show the correlations found in the HITRAN 2004 [17] and 2008 [18] databases. The dotted inner line is the correlation given by Havey et al. [32]. Also, shown are the earlier FS-CRDS *P*-branch measurements [13,32] and the measurements of Brown and Plymate [12] and Predoi-Cross et al. [21,22]. Note that the present study, the NIST *P*-branch measurements, and the Predoi-Cross et al. study utilized Galatry line profiles, while the Brown and Plymate study employed Voigt line profiles.

2.3.5.2. Self-Broadening Coefficients

Over the range of J' probed in this study, the self-broadening coefficients given in Table A1(c) were on average 10% larger than the corresponding air-broadening coefficients. As can be seen in Fig. 6, the present *R*-branch measurements agreed with the earlier FS-CRDS *P*-branch measurements to within their combined uncertainties [13,32]. In addition, for J' up to ~34 the measured self-broadening coefficients showed excellent agreement with the self-broadening coefficients found in HITRAN 2008, with a mean

absolute relative deviation of 4%. The high-J study of Havey et al. [32], however, provide an extended range over which the correlation of Eq. 5 was fit to the data. Compared to the HITRAN 2008 self-broadening values, the resulting correlation begins to differ for $J' > 30$, and approaches a value 20% greater for $J' = 50$.

2.3.6. Collisional Narrowing Parameters for the Galatry Profile

Molecular spectroscopy line lists typically assume Voigt profiles for which the only shape parameters are the Doppler and Lorentzian widths. In recent years it has become apparent that more general line profiles, such as the Galatry profile, are required for demanding atmospheric applications [21,22,26,58]. Although the Galatry profile may not completely account for all physical mechanisms influencing the lineshape, unlike the Voigt profile it provides an additional fit parameter to model collisional narrowing effects, which is important for the O_2 A-band (see Figure 2). In particular, the choice of a Galatry over a Voigt profile will affect the fitted line parameters, especially the Lorentzian width. However, when compared to more complex models, (e.g., speed-dependent profiles, which require at least two more adjustable parameters), the Galatry profile provides a reasonable compromise between accuracy and computational complexity. Unfortunately, accurately measuring the narrowing parameter, η, requires both high spectral resolution with low instrumental broadening and a high signal-to-noise ratio. As a result a typical approach is to assume that η is a constant independent of rotational quantum number and either measure a mean value [14,59] or calculate it as discussed below. As a result, compiled lists of η vs. J are uncommon. Here, we provide data which establish the branch- and J-dependence of the narrowing parameter for the O_2 A-band.

The Galatry profile [44] was derived in terms of Dicke narrowing effects which are caused by elastic velocity-changing (VC) collisions between the absorber and perturber [45]. Dicke narrowing is a consequence of a reduction in the root-mean-square velocity of the absorber with increasing density [60], which decreases the effective Doppler width. For VC-only collisions, it can be argued from gas kinetic theory that the

narrowing parameter $\eta = \nu_{opt}/p$ is $\eta_{diff} = k_B T/(2\pi m_a D p)$ where D and m_a are the absorber's mass diffusion coefficient and mass, respectively. This is the basis for assuming a J-independent narrowing parameter. With regard to mixtures of O_2 and N_2 considered here, the O_2 diffusion coefficient is nearly independent of composition because both constituents have similar molecular weights and diffusion coefficients. We find D(100 kPa, 296K) ≈0.2 cm^2 s^{-1} [61], and for all three gas mixtures used in this study, we calculate η_{diff} = 0.0062 MHz Pa^{-1}. Consequently, η would be constant for all cases considered here (i.e., all branches and gas mixtures) under the VC-only collision assumption. However, inelastic velocity-changing and dephasing (VCD) collisions, which affect both the velocity and the internal state of the absorber, were not considered by Dicke and can result in values for ν_{opt} that differ from those predicted by kinetic theory.

To the extent that there are significant VCD collisions, the collisional narrowing will depend on the internal states of the absorber and perturber. Wehr et al. measured variations in η with J' with $\eta < \eta_{diff}$ for CO absorption broadened by Ar [62,63]. They argued that only rotationally elastic VC collisions contribute to the Dicke narrowing of an isolated transition, whereas internal-state-changing VCD collisions do not contribute to this effect. Thus, when rotationally inelastic VCD collisions are concurrent with Dicke narrowing, η_{diff} should tend to overestimate η. Furthermore as discussed by Wehr et al. [62,63], correlation between η and γ may occur when such VCD collisions dominate collisional broadening. With this assumption, mutual dependency on J' of our measured narrowing parameter and broadening coefficients could lead to a correlation of the form,

$$\eta = \eta_\infty - \kappa\gamma(J'), \tag{6}$$

where κ is an empirical coefficient [62,63] and η_∞ is the narrowing parameter in the limit of high J' where collisional broadening effects are minimized. Note, that we have neglected the effect of pressure shifting which makes the above relation complex valued. As in references [64,65], we have also relaxed the original constraint, $\eta_\infty = \eta_{diff}$, which assumes Dicke narrowing as the only narrowing effect. As reported by Casa et al. [66] in

measurements of self-broadened CO_2 lineshapes, other mechanisms such as speed-dependent effects may introduce additional narrowing which could cause η to differ from or exceed $\eta_{diff.}$

Our new experimental narrowing parameters for the O_2 *A*-band *R*-branch are given in Tables A1(a-c). These data are combined with our previous *P*-branch measurements to form the data set shown in Fig. 7, where the results and fits to the data are grouped by branch and plotted vs. J' for the air-broadened (also including the NIST 2% O_2) mixtures. For each branch, we fit Eq. 6 to the narrowing parameter data by floating η_∞ and κ and using the γ_{air} (J') correlation given by Eq. 5. The fitted values of η_∞ and κ coefficients for each branch are given in Table 2. As can be seen in Fig. 7, although the η values have a relatively high uncertainty and exhibit scatter when plotted against J', these measurements reveal that η cannot be treated as a constant. These data show a relatively strong ΔN-branch dependence of η, with the $\Delta N = -1$ case showing much more variation in η with J' than that of the $\Delta N = 1$. For the $\Delta N = -1$ branch, the $\Delta J = 0$ case generally has a smaller value of η for a given J' than the $\Delta J = -1$. However, for the $\Delta N = 1$ branch a slight reduction of the $\Delta J = 0$ measurements of η relative to those of the $\Delta J = 1$ can barely be resolved. We note furthermore, that for the $\Delta N = -1$ measurements, both *P*- and *Q*- branches (in ΔJ) have η values exceeding η_{diff} at high J', unlike the $\Delta N = 1$ results in which the measured η at high J' are generally less than $\eta_{diff.}$ For all branches and low J', the measured η are close to the constant value of 0.00429 MHz Pa^{-1} reported by Ritter and Wilkerson [14] for the O_2 *A*-band.

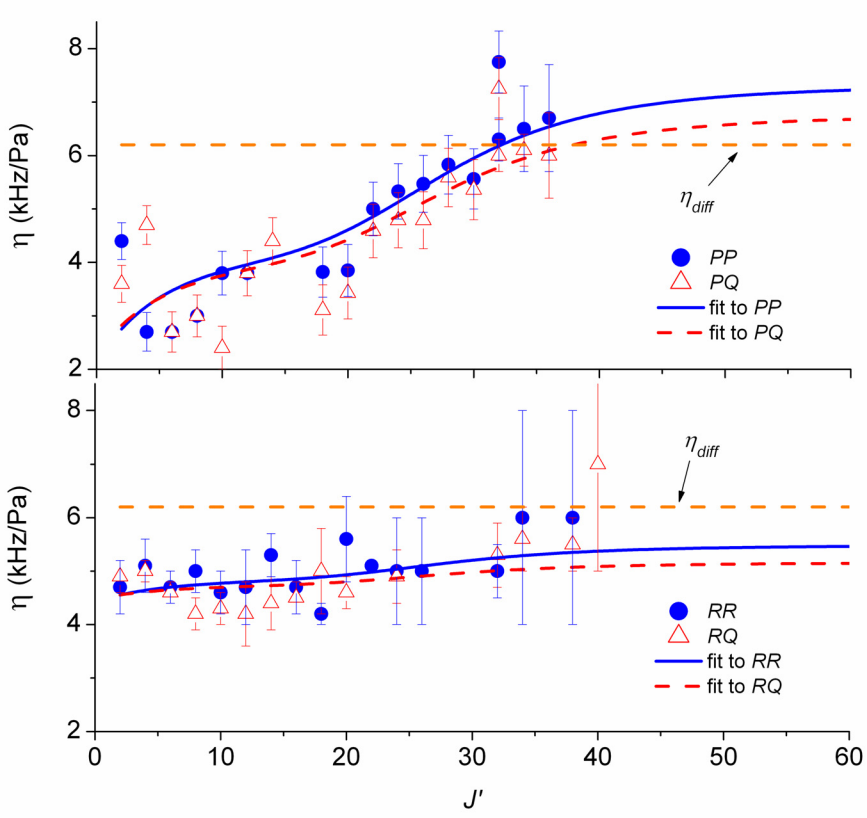

FIG. 7. Measured air-narrowing parameter, η_{air} vs. J', for O_2 *A*-band. Data include *P*-branch measurements of Robichaud et al. [13], and Havey et al. [32], as well as the *R*-branch results obtained here. Gas mixtures correspond to NIST standard air and NIST 2% O_2. Temperature was nominally equal to 296 K for all cases. Data for each branch were fit using the correlation function $\eta = \eta_\infty - \kappa\gamma_{air}(J')$ based on the air-broadening coefficient. The horizontal dashed line in each panel corresponds to η_{diff} = 0.0062 MHz Pa^{-1}. Fit coefficients, η_∞ and κ, for each case are given in Table 2.

The measurements of η for the self-broadened case are shown in Fig. 8. These results include our previous *P*-branch measurements of Robichaud et al. [13] and Havey et al. [32]. Because of the relatively high scatter and small range in J', we are unable to distinguish between data from the various branches, although the data reveal a tendency for η to increase with J'. We fit Eq. 6 to all the self-broadened data, yielding $\kappa = 0.3953$ and $\eta_\infty = 0.00883$ (MHz Pa^{-1}).

Lisak et al. [48] showed that the line narrowing effect in the O_2 *B*-band can be modeled equally well using profiles based on Dicke-narrowing (e.g., Galatry profile) or those that incorporate the speed dependence of collisional broadening. These models

give similar line areas and Lorentzian widths. In practice, they found that it is difficult to distinguish between Dicke-narrowing and speed-dependent contributions because of practical limitations in the signal-to-noise ratio of measured spectra and the concomitant uncertainty in the fitted value of ν_{opt}. They also measured relatively symmetric line shapes and small pressure shifting and therefore concluded that the speed dependence of collisional shifting for spectra in this band was insignificant. Similarly, the present measurements (see Fig. 2) show little evidence of asymmetry in the *A*-band line shapes. Thus, Galatry profiles that incorporate measured narrowing parameters are expected to provide an accurate representation for O_2 *A*-band spectra.

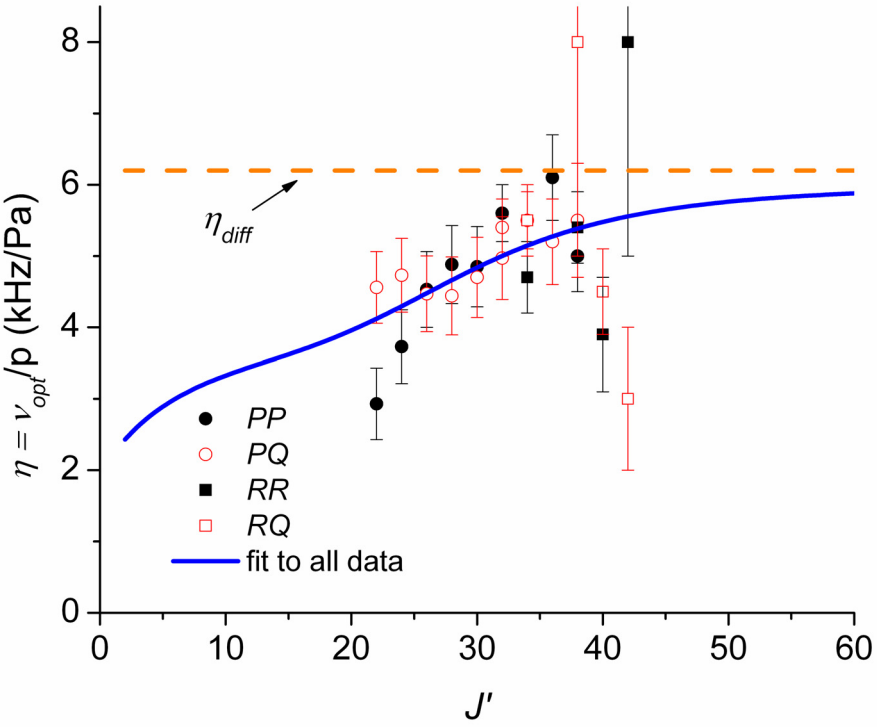

FIG. 8. Measured self-narrowing parameter, η vs. J', for O_2 *A*-band. Data include *P*-branch measurements of Robichaud et al. [13], and Havey et al. [32], as well as the *R*-branch results obtained here. Gas mixtures correspond to pure O_2. Temperature was nominally equal to 296 K for all cases. Data for all branches were fit together using the correlation function $\eta = \eta_\infty - \kappa\gamma_{self}(J')$ based on the self-broadening coefficient. The horizontal dashed line corresponds to $\eta_{diff} = 0.0062$ MHz Pa^{-1}. Fit coefficients are given in Table 2.

2.3.7. Pressure-Shifting Coefficients

Achieving the necessary precision and/or range of pressure required to resolve changes in line peak position makes the measurement of pressure-shifting coefficient, δ, challenging. Nevertheless, numerous groups have measured this line parameter in the O_2 *A*-band [12,13,28,67,68] for various mixtures of O_2 and N_2. The O_2 *A*-band *P*-branch data from these groups were compared in Robichaud et al. [13] and exhibit relatively wide variation. However, all measurements support a general trend of increasingly negative δ as a function of J'. Recently, the high frequency stability of the FS-CRDS method was exploited to measure δ with uncertainties up to 5 times lower than previous measurements [13,28]. These *P*-branch data were fit to a second-order polynomial in J'. This empirical correlation given in Table 2 was used to generate the list of δ values for the *P*- and *R*- branches given in Table A2.

2.4. Conclusions

We used frequency-stabilized cavity ring-down spectroscopy to measure 34 transitions in the *R*-branch of the O_2 *A*-band and determined line parameters from fits of Galatry profiles to the measured spectra. These measurements complement our previous *P*-branch studies and provide a more complete body of data that allows us to formulate a line list up to $J' = 60$. We report calculated line positions, intensities, air- and self-broadening coefficients, narrowing parameters, and pressure-shifting coefficients for the $^{16}O_2$ *A*-band. Low relative standard uncertainties in the line intensity measurements enabled the quantification of a quadratic *J*-dependent deviation from a standard intensity model. Over the range $m = -38$ to 38, this calculated line list reproduces the FS-CRDS-measured line intensities on average to less than 0.1% with a relative standard deviation of ~0.3%. It is anticipated that this new line list will allow for significantly improved remote sensing atmospheric retrievals.

Acknowledgements

We thank Piotr Masłowski of Nicolaus Copernicus University in Toruń, Poland for useful discussions regarding line shape analysis. David A. Long was supported by the National Defense Science and Engineering Graduate Fellowship. We acknowledge the National Research Council for awarding Daniel Havey a postdoctoral fellowship at the National Institute of Standards and Technology (NIST), Gaithersburg, MD. Part of the research described in this paper was performed at the Jet Propulsion Laboratory, California Institute of Technology, under contract with the National Aeronautics and Space Administration (NASA). Additional support was provided by the Orbiting Carbon Observatory (OCO) project, a NASA Earth System Science Pathfinder (ESSP) mission; the NASA Upper Atmospheric Research Program grant NNG06GD88G and NNX09AE21G; and the NIST Office of Microelectronics Programs.

References

[1] S. Corradini, M. Cervino, J. Quant. Spectrosc. Radiat. Transfer **97,** 354-380 (2006).

[2] B. van Diedenhoven, O. P. Hasekamp, I. Aben, Atmos. Chem. Phys. **5,** 2109-2120 (2005).

[3] K. Chance, J. Quant. Spectrosc. Radiat. Transfer **58,** 375-378 (1997).

[4] L. W. Thomason, G. Taha, Geophys. Res. Lett. **30,** 1631 (2003).

[5] C. R. Nowlan, C. T. McElroy, J. R. Drummond, J. Quant. Spectrosc. Radiat. Transfer **108,** 371-388 (2007).

[6] M. Yokomizo, Fujitsu Sci. Tech. J. **44,** 410-417 (2008).

[7] D. M. O'Brien, R. M. Mitchell, J. Appl. Meteorol. **31,** 1179-1192 (1992).

[8] A. K. Heidinger, G. L. Stephens, J. Atmos. Sci. **57,** 1615-1634 (2000).

[9] D. M. O'Brien, S. A. English, G. DaCosta, J. Atmos. Ocean. Technol. **14,** 105-119 (1997).

[10] D. M. O'Brien, R. M. Mitchell, S. A. English, G. A. Da Costa, J. Atmos. Ocean. Technol. **15,** 1272-1286 (1998).

[11] V. V. Badayev, M. S. Malkevich, Izv. Atmos. Oceanic Phys. **14,** 722–727 (1978).

[12] L. R. Brown, C. Plymate, J. Mol. Spectrosc. **199,** 166-179 (2000).

[13] D. J. Robichaud, J. T. Hodges, L. R. Brown, D. Lisak, P. Maslowski, L. Y. Yeung, M. Okumura, C. E. Miller, J. Mol. Spectrosc. **248,** 1-13 (2008).

[14] K. J. Ritter, T. D. Wilkerson, J. Mol. Spectrosc. **121,** 1-19 (1987).

[15] L. S. Rothman, C. P. Rinsland, A. Goldman, S. T. Massie, D. P. Edwards, J. M. Flaud, A. Perrin, C. Camy-Peyret, V. Dana, J. Y. Mandin, J. Schroeder, A. McCann, R. R. Gamache, R. B. Wattson, K. Yoshino, K. V. Chance, K. W. Jucks, L. R. Brown, V. Nemtchinov, P. Varanasi, J. Quant. Spectrosc. Radiat. Transfer **60,** 665-710 (1998).

[16] L. S. Rothman, A. Barbe, D. C. Benner, L. R. Brown, C. Camy-Peyret, M. R. Carleer, K. Chance, C. Clerbaux, V. Dana, V. M. Devi, A. Fayt, J. M. Flaud, R. R. Gamache, A. Goldman, D. Jacquemart, K. W. Jucks, W. J. Lafferty, J. Y. Mandin, S. T. Massie, V. Nemtchinov, D. A. Newnham, A. Perrin, C. P. Rinsland, J. Schroeder, K. M. Smith, M. A. H. Smith, K. Tang, R. A. Toth, J. Vander Auwera, P. Varanasi, K. Yoshino, J. Quant. Spectrosc. Radiat. Transfer **82,** 5-44 (2003).

[17] L. S. Rothman, D. Jacquemart, A. Barbe, D. C. Benner, M. Birk, L. R. Brown, M. R. Carleer, C. Chackerian, K. Chance, L. H. Coudert, V. Dana, V. M. Devi, J. M. Flaud, R. R. Gamache, A. Goldman, J. M. Hartmann, K. W. Jucks, A. G. Maki, J. Y. Mandin, S. T. Massie, J. Orphal, A. Perrin, C. P. Rinsland, M. A. H. Smith, J. Tennyson, R. N. Tolchenov, R. A. Toth, J. Vander Auwera, P. Varanasi, G. Wagner, J. Quant. Spectrosc. Radiat. Transfer **96,** 139-204 (2005).

[18] L. S. Rothman, I. E. Gordon, A. Barbe, D. C. Benner, P. F. Bernath, M. Birk, V. Boudon, L. R. Brown, A. Campargue, J. P. Champion, K. Chance, L. H. Coudert, V. Dana, V. M. Devi, S. Fally, J. M. Flaud, R. R. Gamache, A. Goldman, D.

Jacquemart, I. Kleiner, N. Lacome, W. J. Lafferty, J. Y. Mandin, S. T. Massie, S. N. Mikhailenko, C. E. Miller, N. Moazzen-Ahmadi, O. V. Naumenko, A. V. Nikitin, J. Orphal, V. I. Perevalov, A. Perrin, A. Predoi-Cross, C. P. Rinsland, M. Rotger, M. Simecková, M. A. H. Smith, K. Sung, S. A. Tashkun, J. Tennyson, R. A. Toth, A. C. Vandaele, J. Vander Auwera, J. Quant. Spectrosc. Radiat. Transfer **110,** 533-572 (2009).

[19] R. Schermaul, R. C. M. Learner, J. Quant. Spectrosc. Radiat. Transfer **61,** 781-794 (1999).

[20] R. Herman, R. F. Wallis, J. Chem. Phys. **23,** 637-646 (1955).

[21] A. Predoi-Cross, C. Holladay, H. Heung, J. P. Bouanich, G. C. Mellau, R. Keller, D. R. Hurtmans, J. Mol. Spectrosc. **251,** 159-175 (2008).

[22] A. Predoi-Cross, K. Harnbrook, R. Keller, C. Povey, I. Schofield, D. Hurtmans, H. Over, G. C. Mellau, J. Mol. Spectrosc. **248,** 85-110 (2008).

[23] D. Crisp, R. M. Atlas, F. M. Breon, L. R. Brown, J. P. Burrows, P. Ciais, B. J. Connor, S. C. Doney, I. Y. Fung, D. J. Jacob, C. E. Miller, D. O'Brien, S. Pawson, J. T. Randerson, P. Rayner, R. J. Salawitch, S. P. Sander, B. Sen, G. L. Stephens, P. P. Tans, G. C. Toon, P. O. Wennberg, S. C. Wofsy, Y. L. Yung, Z. Kuang, B. Chudasama, G. Sprague, B. Weiss, R. Pollock, D. Kenyon, S. Schroll, *Trace constituents in the troposphere and lower stratosphere* (Pergamon-Elsevier Science Ltd, Kidlington, 2004, 700-709).

[24] C. E. Miller, L. R. Brown, R. A. Toth, D. C. Benner, V. M. Devi, C. R. Phys. **6,** 876-887 (2005).

[25] C. E. Miller, D. Crisp, P. L. DeCola, S. C. Olsen, J. T. Randerson, A. M. Michalak, A. Alkhaled, P. Rayner, D. J. Jacob, P. Suntharalingam, D. B. A. Jones, A. S. Denning, M. E. Nicholls, S. C. Doney, S. Pawson, H. Boesch, B. J. Connor, I. Y. Fung, D. O'Brien, R. J. Salawitch, S. P. Sander, B. Sen, P. Tans, G. C. Toon, P. O. Wennberg, S. C. Wofsy, Y. L. Yung, R. M. Law, J. Geophys. Res.-Atmos. **112,** D10314 (2007).

[26] Z. Yang, P. O. Wennberg, R. P. Cageao, T. J. Pongetti, G. C. Toon, S. P. Sander, J. Quant. Spectrosc. Radiat. Transfer **90,** 309-321 (2005).

[27] D. J. Robichaud, J. T. Hodges, P. Maslowski, L. Y. Yeung, M. Okumura, C. E. Miller, L. R. Brown, J. Mol. Spectrosc. **251,** 27-37 (2008).

[28] D. J. Robichaud, J. T. Hodges, D. Lisak, C. E. Miller, M. Okumura, J. Quant. Spectrosc. Radiat. Transfer **109,** 435-444 (2008).

[29] S. F. Yang, M. R. Canagaratna, S. K. Witonsky, S. L. Coy, J. I. Steinfeld, R. W. Field, A. A. Kachanov, J. Mol. Spectrosc. **201,** 188-197 (2000).

[30] D. J. Robichaud, L. Y. Yeung, D. A. Long, M. Okumura, D. K. Havey, J. T. Hodges, C. E. Miller, L. R. Brown, J. Phys. Chem. A **113,** 13089-13099 (2009).

[31] D. A. Long, D. K. Havey, M. Okumura, H. M. Pickett, C. E. Miller, J. T. Hodges, Phys. Rev. A **80,** 042513 (2009).

[32] D. K. Havey, D. A. Long, M. Okumura, C. E. Miller, J. T. Hodges, Chem. Phys. Lett. **483,** 49-54 (2009).

[33] J. T. Hodges, R. Ciurylo, Rev. Sci. Instrum. **76,** 023112 (2005).

[34] J. T. Hodges, H. P. Layer, W. W. Miller, G. E. Scace, Rev. Sci. Instrum. **75,** 849-863 (2004).
[35] J. T. Hodges, J. P. Looney, R. D. van Zee, Appl. Opt. **35,** 4112-4116 (1996).
[36] J. T. Hodges, J. P. Looney, R. D. van Zee, J. Chem. Phys. **105,** 10278-10288 (1996).
[37] K. K. Lehmann, D. Romanini, J. Chem. Phys. **105,** 10263-10277 (1996).
[38] A. R. Awtry, J. H. Miller, Appl. Phys. B **75,** 255-260 (2002).
[39] M. Hippler, M. Quack, J. Chem. Phys. **116,** 6045-6055 (2002).
[40] P. Macko, D. Romanini, S. N. Mikhailenko, O. V. Naumenko, S. Kassi, A. Jenouvrier, V. G. Tyuterev, A. Campargue, J. Mol. Spectrosc. **227,** 90-108 (2004).
[41] D. Romanini, A. A. Kachanov, N. Sadeghi, F. Stoeckel, Chem. Phys. Lett. **264,** 316-322 (1997).
[42] D. Romanini, A. A. Kachanov, F. Stoeckel, Chem. Phys. Lett. **270,** 538-545 (1997).
[43] D. Lisak, J. T. Hodges, Appl. Phys. B **88,** 317-325 (2007).
[44] L. Galatry, Phys. Rev. **122,** 1218-1223 (1961).
[45] R. H. Dicke, Phys. Rev. **89,** 472-473 (1953).
[46] D. Lisak, J. T. Hodges, R. Ciurylo, Phys. Rev. A **73,** 052507 (2006).
[47] H. D. Babcock, L. Herzberg, Astrophys. J. **108,** 167-190 (1948).
[48] D. Lisak, P. Maslowski, A. Cygan, K. Bielska, S. Wojtewicz, M. Piwinski, J. T. Hodges, R. S. Trawinski, R. Ciurylo, Phys. Rev. A **81,** 042504 (2010).
[49] R. R. Gamache, A. Goldman, L. S. Rothman, J. Quant. Spectrosc. Radiat. Transfer **59,** 495-509 (1998).
[50] J. K. G. Watson, Can. J. Phys. **46,** 1637-1643 (1968).
[51] N. Jacquinet-Husson, N. A. Scott, A. Chedina, L. Crepeau, R. Armante, V. Capelle, J. Orphal, A. Coustenis, C. Boonne, N. Poulet-Crovisier, A. Barbee, M. Birk, L. R. Brown, C. Camy-Peyret, C. Claveau, K. Chance, N. Christidis, C. Clerbaux, P. F. Coheur, V. Dana, L. Daumont, M. R. De Backer-Barilly, G. Di Lonardo, J. M. Flaud, A. Goldman, A. Hamdouni, M. Hess, M. D. Hurley, D. Jacquemart, I. Kleiner, P. Kopke, J. Y. Mandin, S. Massie, S. Mikhailenko, V. Nemtchinov, A. Nikitin, D. Newnham, A. Perrin, V. I. Perevalov, S. Pinnock, L. Regalia-Jarlot, C. P. Rinsland, A. Rublev, F. Schreier, L. Schult, K. M. Smith, S. A. Tashkun, J. L. Teffo, R. A. Toth, V. G. Tyuterev, J. V. Auwera, P. Varanasi, G. Wagner, J. Quant. Spectrosc. Radiat. Transfer **109,** 1043-1059 (2008).
[52] N. Jacquinet-Husson, N. A. Scott, A. Chedin, K. Garceran, R. Armante, A. A. Chursin, A. Barbe, M. Birk, L. R. Brown, C. Camy-Peyret, C. Claveau, C. Clerbaux, P. F. Coheur, V. Dana, L. Daumont, M. R. Debacker-Barilly, J. M. Flaud, A. Goldman, A. Hamdouni, M. Hess, D. Jacquemart, P. Kopke, J. Y. Mandin, S. Massie, S. Mikhailenko, V. Nemtchinov, A. Nikitin, D. Newnham, A. Perrin, V. I. Perevalov, L. Regalia-Jarlot, A. Rublev, F. Schreier, I. Schult, K. M. Smith, S. A. Tashkun, J. L. Teffo, R. A. Toth, V. G. Tyuterev, J. V. Auwera, P. Varanasi, G. Wagner, J. Quant. Spectrosc. Radiat. Transfer **95,** 429-467 (2005).

[53] J. H. Miller, R. W. Boese, L. P. Giver, J. Quant. Spectrosc. Radiat. Transfer **9,** 1507-1517 (1969).
[54] T. K. Balasubramanian, O. Narayanan, Acta. Phys. Hung. **74,** 341-353 (1994).
[55] J. K. G. Watson, J. Mol. Spectrosc. **125,** 428-441 (1987).
[56] R. H. Tipping, J. P. Bouanich, J. Quant. Spectrosc. Radiat. Transfer **71,** 99-103 (2001).
[57] NIST Chemistry WebBook.
[58] C. D. Boone, K. A. Walker, P. F. Bernath, J. Quant. Spectrosc. Radiat. Transfer **105,** 525-532 (2007).
[59] P. L. Varghese, R. K. Hanson, Appl. Opt. **23,** 2376-2385 (1984).
[60] P. Duggan, P. M. Sinclair, R. Berman, A. D. May, J. R. Drummond, J. Mol. Spectrosc. **186,** 90-98 (1997).
[61] J. O. Hirschfelder, C. F. Curtiss, R. B. Bird, *Molecular Theory of Gases and Liquids* (Wiley, New York, 1954,).
[62] R. Wehr, R. Ciurylo, A. Vitcu, F. Thibault, D. A. Shapiro, W. K. Liu, F. R. W. McCourt, J. R. Drummond, A. D. May, In: *Spectral Line Shapes*, E. Oks, M. Pindzola (AIP, 2006).
[63] R. Wehr, R. Ciurylo, A. Vitcu, F. Thibault, J. R. Drummond, A. D. May, J. Mol. Spectrosc. **235,** 54-68 (2006).
[64] F. Chaussard, X. Michaut, R. Saint-Loup, H. Berger, P. Joubert, B. Lance, J. Bonamy, D. Robert, J. Chem. Phys. **112,** 158-166 (2000).
[65] A. S. Pine, R. Ciurylo, J. Mol. Spectrosc. **208,** 180-187 (2001).
[66] G. Casa, R. Wehr, A. Castrillo, E. Fasci, L. Gianfrani, J. Chem. Phys. **130,** 184306 (2009).
[67] C. Hill, D. A. Newnham, J. M. Brown, J. Mol. Spectrosc. **219,** 65-69 (2003).
[68] A. J. Phillips, P. A. Hamilton, J. Mol. Spectrosc. **174,** 587-594 (1995).
[69] G. Rouillé, G. Millot, R. Saintloup, H. Berger, J. Mol. Spectrosc. **154,** 372-382 (1992).

Appendix

TABLE A1. Measured line parameters for the $^{16}O_2$ *A*-band. Positions from HITRAN 2008 [18], intensities, *S*, at T_{ref} = 296 K, broadening coefficients, γ in (MHz Pa^{-1}) corrected to 296 K using the temperature dependence given in HITRAN 2008. Pressure broadening corresponds to half-width at half-maximum. For the line intensities and broadening coefficients, the values in parenthesis are the combined (Type A and Type B) standard uncertainties in the last digit. For the narrowing parameters the values in parenthesis correspond to the fit uncertainty.

(a) sample: NIST 2% O_2

transition	$\tilde{\nu}$ (cm^{-1})	S (10^{-24}cm molec.$^{-1}$)	γ (MHz Pa^{-1})	η (MHz Pa^{-1})	pressure range (kPa)	# scans	# pressures
R1R1	13126.392003	1.530(6)	0.0183(1)	0.0047(5)	4.0-20.0	8	4
R1Q2	13128.268803	3.57(1)	0.0174(1)	0.0049(3)	2.7-8.0	10	4
R3R3	13131.491440	4.28(1)	0.0167(1)	0.0051(5)	1.3-5.6	9	4
R3Q4	13133.441040	6.22(2)	0.0166(1)	0.0050(2)	1.3-3.3	5	4
R5R5	13136.217103	6.30(2)	0.0158(1)	0.0047(3)	1.3-3.3	5	4
R5Q6	13138.204803	8.03(3)	0.0158(1)	0.0046(2)	1.3-3.3	5	4
R7R7	13140.567420	7.35(2)	0.0152(1)	0.0050(4)	1.3-3.3	5	4
R7Q8	13142.583320	8.80(3)	0.0148(2)	0.0042(3)	1.3-3.3	5	4
R9R9	13144.540760	7.44(2)	0.0147(1)	0.0046(4)	1.3-3.3	5	4
R9Q10	13146.580460	8.61(3)	0.0146(1)	0.0043(3)	1.3-3.3	5	4
R11R11	13148.135226	6.79(2)	0.0144(2)	0.0047(7)	1.3-3.3	5	4
R11Q12	13150.196626	7.65(3)	0.0139(2)	0.0042(6)	1.3-3.3	5	4
R13R13	13151.348659	5.64(2)	0.0142(2)	0.0053(4)	1.3-3.3	6	4
R13Q14	13153.430459	6.25(2)	0.0135(2)	0.0044(5)	1.3-3.3	6	4
R15R15	13154.178835	4.34(1)	0.0133(2)	0.0047(5)	1.3-5.6	9	4
R15Q16	13156.280235	4.76(1)	0.0133(1)	0.0045(3)	1.3-5.6	9	4
R17R17	13156.623169	3.09(1)	0.0122(1)	0.0042(2)	5.6-8.0	6	3
R17Q18	13158.743569	3.38(1)	0.0131(2)	0.0050(8)	2.7-8.0	9	4
R19R19	13158.679005	2.079(7)	0.0126(2)	0.0056(8)	2.7-8.0	9	4
R19Q20	13160.818105	2.249(7)	0.0123(1)	0.0046(3)	3.3-13.3	8	6
R21R21	13160.343426	1.292(5)	0.0117(1)	0.0051(1)	4.0-20.0	6	4

(b) sample: NIST standard air

transition	$\tilde{\nu}$ (cm^{-1})	S (10^{-26} cm $molec^{-1}$)	γ (MHz Pa^{-1})	η (MHz Pa^{-1})	pressure range (kPa)	# scans	# pressures
R23R23	13161.613145	75.9(2)	0.0111(3)	0.005(1)	1.3-3.3	4	4
R23Q24	13163.788745	81.2(2)	0.0115(3)	0.0049(5)	1.3-2.7	4	4
R25Q26	13164.678607	44.3(1)	0.0105(2)	0.005(1)	1.3-3.3	5	4
R31Q32	13164.922553	5.04(2)	0.0089(2)	0.0053(6)	10.0-12.0	7	2
R33R33	13161.917130	2.057(8)	0.0074(5)	0.0050(5)	3.3-13.3	3	3
R33Q34	13164.182130	2.18(1)	0.0087(6)	0.0056(6)	3.3-13.3	6	3
R35R35	13160.740806	0.83(2)	0.0080(9)	0.006(2)	1.7-6.7	3	3
R37R37	13159.141488	0.324(2)	0.0073(8)	0.0055(5)	3.3-13.3	4	3
R37Q38	13161.441788	0.339(9)	0.008(1)	0.006(2)	3.3-13.3	3	3
R39R39	13157.114405	0.118(2)	0.007(1)	0.007(2)	3.3-13.3	4	3
R39Q40	13159.432305	0.1227(9)	0.008(1)	Eq. 6	3.3-13.3	3	2
R41R41	13154.654303	0.0398(5)	0.007(1)	Eq. 6	3.3-13.3	20	3
R41Q42	13156.989803	0.0420(8)	0.006(1)	Eq. 6	3.3-13.3	20	3

(c) sample: pure O_2

transition	$\tilde{\nu}$ (cm^{-1})	S (10^{-27} cm $molec^{-1}$)	γ (MHz Pa^{-1})	η (MHz Pa^{-1})	pressure range (kPa)	# scans	# pressures
R33R33	13161.917130	20.4(1)	0.0090(9)	0.0047(5)	3.3-13.3	3	3
R33Q34	13164.182130	21.7(2)	0.0097(7)	0.0055(5)	3.3-13.3	3	3
R37R37	13159.141488	3.23(2)	0.0087(9)	0.0054(5)	3.3-13.3	3	3
R37Q38	13161.441788	3.31(6)	0.008(1)	0.008(3)	3.3-13.3	3	3
R39R39	13157.114405	1.17(1)	0.0076(8)	0.0039(8)	3.3-13.3	3	3
R39Q40	13159.432305	1.22(1)	0.0079(9)	0.0045(6)	3.3-13.3	3	3
R41R41	13154.654303	0.39(2)	0.008(1)	0.008(3)	3.3-13.3	3	3
R41Q42	13156.989803	0.41(1)	0.007(1)	0.003(1)	3.3-13.3	3	3

Table A2. Line parameters for magnetic dipole transitions of the $^{16}O_2$ *A*-band. Lower state energies and positions were calculated using the lower and upper state molecular constants found in Long et al. [31] and the definitions found in Rouillé et al. [69]. The intensities, *S*, which correspond to T_{ref} = 296 K and natural terrestrial isotopic abundance of $^{16}O_2$, were calculated using Eq. 2 with the Hönl-London factors, *L*, of Watson [50], a band intensity of 2.2314×10^{-22} cm molec.$^{-1}$ and the positions and lower state energies shown. We estimate $u_r(S) < 0.4\%$ for $m = -38$ to 38. Note that the intensities were weighted by the HW-like quadratic term, given by $(1+a_1m+a_2m^2)^2$ with $a_1 = -2.658\times10^{-4}$ and $a_2 = 3.3622\times10^{-6}$, as described in the text. Einstein-*A* coefficients were calculated from the corresponding intensities using Eq. 4. The broadening coefficients, γ_{air} and γ_{self}, the narrowing parameters, η_{air} and η_{self}, and the pressure-shifting coefficients, δ, were calculated using the correlations and coefficients given in Table 2. Uncertainties for the broadening and narrowing parameters are comparable to those given in Table A1. Note 1 cm^{-1} atm^{-1} = 0.295872 MHz Pa^{-1}.

transition	*L*	$\tilde{\nu}$ (cm^{-1})	*S* (cm molec^{-1})	*A* (s^{-1})	*E"* (cm^{-1})	γ_{air} (MHz Pa^{-1})	γ_{self} (MHz Pa^{-1})	δ (MHz Pa^{-1})	η_{air} (MHz Pa^{-1})	η_{self} (MHz Pa^{-1})
P61Q60	30.3441	12774.178997	4.547E-34	0.02139	5367.87752	6.27E-03	7.47E-03	-3.26E-03	6.68E-03	5.88E-03
P59P59	30.0000	12790.010354	2.323E-33	0.02192	5029.97839	6.31E-03	7.51E-03	-3.25E-03	7.21E-03	5.86E-03
P59Q58	29.3441	12791.508287	2.286E-33	0.02142	5028.48046	6.31E-03	7.51E-03	-3.25E-03	6.66E-03	5.86E-03
P57P57	29.0000	12806.885855	1.108E-32	0.02197	4701.28301	6.35E-03	7.56E-03	-3.23E-03	7.19E-03	5.84E-03
P57Q56	28.3441	12808.400536	1.090E-32	0.02146	4699.76833	6.35E-03	7.56E-03	-3.23E-03	6.65E-03	5.84E-03
P55P55	28.0000	12823.330010	5.013E-32	0.02202	4383.32615	6.41E-03	7.62E-03	-3.22E-03	7.16E-03	5.82E-03
P55Q54	27.3441	12824.861458	4.926E-32	0.02149	4381.79470	6.41E-03	7.62E-03	-3.22E-03	6.63E-03	5.82E-03
P53P53	27.0000	12839.348247	2.149E-31	0.02207	4076.15958	6.47E-03	7.68E-03	-3.20E-03	7.14E-03	5.79E-03
P53Q52	26.3441	12840.896484	2.110E-31	0.02152	4074.61134	6.47E-03	7.68E-03	-3.20E-03	6.60E-03	5.79E-03
P51P51	26.0000	12854.945718	8.726E-31	0.02212	3779.83330	6.55E-03	7.76E-03	-3.17E-03	7.10E-03	5.76E-03
P51Q50	25.3441	12856.510765	8.562E-31	0.02155	3778.26826	6.55E-03	7.76E-03	-3.17E-03	6.57E-03	5.76E-03
P49P49	25.0000	12870.127299	3.356E-30	0.02218	3494.39554	6.64E-03	7.86E-03	-3.15E-03	7.06E-03	5.72E-03
P49Q48	24.3441	12871.709183	3.290E-30	0.02158	3492.81365	6.64E-03	7.86E-03	-3.15E-03	6.54E-03	5.72E-03
P47P47	24.0000	12884.897600	1.222E-29	0.02223	3219.89269	6.76E-03	7.98E-03	-3.12E-03	7.01E-03	5.68E-03
P47Q46	23.3441	12886.496349	1.197E-29	0.02161	3218.29394	6.76E-03	7.98E-03	-3.12E-03	6.50E-03	5.68E-03
P45P45	23.0000	12899.260968	4.211E-29	0.02229	2956.36938	6.90E-03	8.12E-03	-3.09E-03	6.95E-03	5.62E-03
P45Q44	22.3441	12900.876614	4.119E-29	0.02164	2954.75373	6.90E-03	8.12E-03	-3.09E-03	6.44E-03	5.62E-03
P43P43	22.0000	12913.221492	1.373E-28	0.02234	2703.86842	7.07E-03	8.28E-03	-3.05E-03	6.88E-03	5.56E-03
P43Q42	21.3441	12914.854071	1.341E-28	0.02166	2702.23585	7.07E-03	8.28E-03	-3.05E-03	6.38E-03	5.56E-03
P41P41	21.0000	12926.783009	4.233E-28	0.02240	2462.43083	7.29E-03	8.48E-03	-3.02E-03	6.79E-03	5.48E-03
P41Q40	20.3441	12928.432561	4.130E-28	0.02169	2460.78127	7.29E-03	8.48E-03	-3.02E-03	6.30E-03	5.48E-03
P39P39	20.0000	12939.949105	1.234E-27	0.02247	2232.09578	7.55E-03	8.72E-03	-2.98E-03	6.67E-03	5.38E-03
P39Q38	19.3441	12941.615675	1.202E-27	0.02172	2230.42921	7.55E-03	8.72E-03	-2.98E-03	6.20E-03	5.38E-03
P37P37	19.0000	12952.723123	3.397E-27	0.02253	2012.90065	7.86E-03	9.00E-03	-2.94E-03	6.54E-03	5.27E-03
P37Q36	18.3441	12954.406761	3.304E-27	0.02174	2011.21702	7.86E-03	9.00E-03	-2.94E-03	6.09E-03	5.27E-03
P35P35	18.0000	12965.108162	8.838E-27	0.02260	1804.88101	8.24E-03	9.32E-03	-2.89E-03	6.37E-03	5.15E-03
P35Q34	17.3441	12966.808930	8.579E-27	0.02177	1803.18025	8.24E-03	9.32E-03	-2.89E-03	5.95E-03	5.15E-03
P33P33	17.0000	12977.107088	2.170E-26	0.02268	1608.07059	8.70E-03	9.69E-03	-2.84E-03	6.18E-03	5.00E-03
P33Q32	16.3441	12978.825055	2.102E-26	0.02179	1606.35262	8.70E-03	9.69E-03	-2.84E-03	5.78E-03	5.00E-03
P31P31	16.0000	12988.722531	5.029E-26	0.02276	1422.50128	9.23E-03	1.01E-02	-2.79E-03	5.95E-03	4.84E-03
P31Q30	15.3441	12990.457779	4.860E-26	0.02182	1420.76603	9.23E-03	1.01E-02	-2.79E-03	5.58E-03	4.84E-03

P29P29	15.0000	12999.956891	1.099E-25	0.02286	1248.20315	9.83E-03	1.05E-02	-2.74E-03	5.69E-03	4.66E-03
P29Q28	14.3441	13001.709517	1.059E-25	0.02185	1246.45053	9.83E-03	1.05E-02	-2.74E-03	5.36E-03	4.66E-03
P27P27	14.0000	13010.812342	2.263E-25	0.02296	1085.20445	1.05E-02	1.10E-02	-2.69E-03	5.41E-03	4.48E-03
P27Q26	13.3441	13012.582464	2.174E-25	0.02187	1083.43433	1.05E-02	1.10E-02	-2.69E-03	5.12E-03	4.48E-03
P25P25	13.0000	13021.290834	4.388E-25	0.02307	933.53157	1.11E-02	1.15E-02	-2.63E-03	5.13E-03	4.30E-03
P25Q24	12.3441	13023.078597	4.200E-25	0.02190	931.74381	1.11E-02	1.15E-02	-2.63E-03	4.87E-03	4.30E-03
P23P23	12.0000	13031.394096	8.005E-25	0.02321	793.20908	1.18E-02	1.19E-02	-2.57E-03	4.86E-03	4.12E-03
P23Q22	11.3441	13033.199679	7.629E-25	0.02193	791.40349	1.18E-02	1.19E-02	-2.57E-03	4.64E-03	4.12E-03
P21P21	11.0000	13041.123637	1.372E-24	0.02336	664.25967	1.23E-02	1.23E-02	-2.50E-03	4.61E-03	3.96E-03
P21Q20	10.3441	13042.947271	1.301E-24	0.02196	662.43604	1.23E-02	1.23E-02	-2.50E-03	4.42E-03	3.96E-03
P19P19	10.0000	13050.480752	2.207E-24	0.02355	546.70424	1.28E-02	1.27E-02	-2.44E-03	4.40E-03	3.81E-03
P19Q18	9.3442	13052.322739	2.079E-24	0.02200	544.86225	1.28E-02	1.27E-02	-2.44E-03	4.24E-03	3.81E-03
P17P17	9.0000	13059.466520	3.324E-24	0.02377	440.56179	1.32E-02	1.30E-02	-2.37E-03	4.23E-03	3.68E-03
P17Q16	8.3442	13061.327268	3.108E-24	0.02204	438.70104	1.32E-02	1.30E-02	-2.37E-03	4.10E-03	3.68E-03
P15P15	8.0000	13068.081811	4.679E-24	0.02406	345.84949	1.36E-02	1.33E-02	-2.30E-03	4.09E-03	3.56E-03
P15Q14	7.3442	13069.961892	4.332E-24	0.02208	343.96941	1.36E-02	1.33E-02	-2.30E-03	3.97E-03	3.56E-03
P13P13	7.0000	13076.327282	6.131E-24	0.02443	262.58268	1.39E-02	1.36E-02	-2.22E-03	3.96E-03	3.45E-03
P13Q12	6.3442	13078.227537	5.605E-24	0.02214	260.68242	1.39E-02	1.36E-02	-2.22E-03	3.87E-03	3.45E-03
P11P11	6.0000	13084.203384	7.445E-24	0.02494	190.77481	1.42E-02	1.39E-02	-2.15E-03	3.83E-03	3.33E-03
P11Q10	5.3442	13086.125129	6.690E-24	0.02221	188.85306	1.42E-02	1.39E-02	-2.15E-03	3.75E-03	3.33E-03
P9P9	5.0000	13091.710358	8.312E-24	0.02569	130.43750	1.45E-02	1.43E-02	-2.07E-03	3.68E-03	3.18E-03
P9Q8	4.3443	13093.655833	7.287E-24	0.02231	128.49202	1.45E-02	1.43E-02	-2.07E-03	3.62E-03	3.18E-03
P7P7	4.0000	13098.848243	8.426E-24	0.02688	81.58050	1.50E-02	1.47E-02	-1.98E-03	3.47E-03	3.00E-03
P7Q6	3.3444	13100.821748	7.110E-24	0.02247	79.60699	1.50E-02	1.47E-02	-1.98E-03	3.44E-03	3.00E-03
P5P5	3.0000	13105.616870	7.573E-24	0.02913	44.21171	1.57E-02	1.53E-02	-1.90E-03	3.18E-03	2.76E-03
P5Q4	2.3446	13107.628463	5.974E-24	0.02276	42.20012	1.57E-02	1.53E-02	-1.90E-03	3.19E-03	2.76E-03
P3P3	2.0000	13112.015868	5.721E-24	0.03497	18.33718	1.67E-02	1.62E-02	-1.81E-03	2.75E-03	2.43E-03
P3Q2	1.3458	13114.100185	3.888E-24	0.02353	16.25286	1.67E-02	1.62E-02	-1.81E-03	2.82E-03	2.43E-03
P1P1	1.0000	13118.044661	3.066E-24	0.08744	3.96108	1.82E-02	1.74E-02	-1.72E-03	2.10E-03	1.95E-03
R1R1	0.5000	13126.391964	1.531E-24	0.00875	3.96108	1.67E-02	1.62E-02	-1.81E-03	4.55E-03	2.43E-03
R1Q2	1.1542	13128.268754	3.566E-24	0.02019	2.08429	1.67E-02	1.62E-02	-1.81E-03	4.55E-03	2.43E-03
R3R3	1.5000	13131.491402	4.282E-24	0.01458	18.33718	1.57E-02	1.53E-02	-1.90E-03	4.64E-03	2.76E-03
R3Q4	2.1554	13133.440971	6.209E-24	0.02095	16.38761	1.57E-02	1.53E-02	-1.90E-03	4.61E-03	2.76E-03
R5R5	2.5000	13136.217029	6.289E-24	0.01683	44.21171	1.50E-02	1.47E-02	-1.98E-03	4.70E-03	3.00E-03
R5Q6	3.1556	13138.204770	8.013E-24	0.02124	42.22397	1.50E-02	1.47E-02	-1.98E-03	4.65E-03	3.00E-03
R7R7	3.5000	13140.567357	7.338E-24	0.01802	81.58050	1.45E-02	1.43E-02	-2.07E-03	4.74E-03	3.18E-03
R7Q8	4.1557	13142.583244	8.797E-24	0.02139	79.56461	1.45E-02	1.43E-02	-2.07E-03	4.68E-03	3.18E-03
R9R9	4.5000	13144.540696	7.437E-24	0.01875	130.43750	1.42E-02	1.39E-02	-2.15E-03	4.77E-03	3.33E-03
R9Q10	5.1558	13146.580459	8.603E-24	0.02149	128.39773	1.42E-02	1.39E-02	-2.15E-03	4.70E-03	3.33E-03
R11R11	5.5000	13148.135152	6.776E-24	0.01925	190.77481	1.39E-02	1.36E-02	-2.22E-03	4.80E-03	3.45E-03
R11Q12	6.1558	13150.196583	7.658E-24	0.02155	188.71338	1.39E-02	1.36E-02	-2.22E-03	4.71E-03	3.45E-03
R13R13	6.5000	13151.348626	5.646E-24	0.01962	262.58268	1.36E-02	1.33E-02	-2.30E-03	4.83E-03	3.56E-03
R13Q14	7.1558	13153.430440	6.277E-24	0.02160	260.50087	1.36E-02	1.33E-02	-2.30E-03	4.73E-03	3.56E-03
R15R15	7.5000	13154.178813	4.344E-24	0.01989	345.84949	1.32E-02	1.30E-02	-2.37E-03	4.85E-03	3.68E-03
R15Q16	8.1558	13156.280200	4.772E-24	0.02163	343.74811	1.32E-02	1.30E-02	-2.37E-03	4.75E-03	3.68E-03
R17R17	8.5000	13156.623203	3.105E-24	0.02010	440.56179	1.28E-02	1.27E-02	-2.44E-03	4.89E-03	3.81E-03
R17Q18	9.1558	13158.743620	3.379E-24	0.02166	438.44137	1.28E-02	1.27E-02	-2.44E-03	4.77E-03	3.81E-03
R19R19	9.5000	13158.679074	2.071E-24	0.02028	546.70424	1.23E-02	1.23E-02	-2.50E-03	4.93E-03	3.96E-03

R19Q20	10.1559	13160.818147	2.237E-24	0.02168	544.56517	1.23E-02	1.23E-02	-2.50E-03	4.80E-03	3.96E-03
R21R21	10.5000	13160.343498	1.292E-24	0.02042	664.25967	1.18E-02	1.19E-02	-2.57E-03	4.98E-03	4.12E-03
R21Q22	11.1559	13162.500954	1.387E-24	0.02170	662.10222	1.18E-02	1.19E-02	-2.57E-03	4.83E-03	4.12E-03
R23R23	11.5000	13161.613332	7.559E-25	0.02053	793.20908	1.11E-02	1.15E-02	-2.63E-03	5.04E-03	4.30E-03
R23Q24	12.1559	13163.788973	8.075E-25	0.02171	791.03344	1.11E-02	1.15E-02	-2.63E-03	4.87E-03	4.30E-03
R25R25	12.5000	13162.485220	4.153E-25	0.02063	933.53157	1.05E-02	1.10E-02	-2.69E-03	5.09E-03	4.48E-03
R25Q26	13.1559	13164.678897	4.417E-25	0.02172	931.33790	1.05E-02	1.10E-02	-2.69E-03	4.91E-03	4.48E-03
R27R27	13.5000	13162.955591	2.145E-25	0.02071	1085.20445	9.83E-03	1.05E-02	-2.74E-03	5.15E-03	4.66E-03
R27Q28	14.1559	13165.167191	2.274E-25	0.02172	1082.99285	9.83E-03	1.05E-02	-2.74E-03	4.94E-03	4.66E-03
R29R29	14.5000	13163.020655	1.043E-25	0.02078	1248.20315	9.23E-03	1.01E-02	-2.79E-03	5.20E-03	4.84E-03
R29Q30	15.1559	13165.250091	1.102E-25	0.02173	1245.97372	9.23E-03	1.01E-02	-2.79E-03	4.98E-03	4.84E-03
R31R31	15.5000	13162.676399	4.777E-26	0.02084	1422.50128	8.70E-03	9.69E-03	-2.84E-03	5.25E-03	5.00E-03
R31Q32	16.1559	13164.923607	5.035E-26	0.02173	1420.25407	8.70E-03	9.69E-03	-2.84E-03	5.01E-03	5.00E-03
R33R33	16.5000	13161.918589	2.063E-26	0.02089	1608.07059	8.24E-03	9.32E-03	-2.89E-03	5.29E-03	5.15E-03
R33Q34	17.1559	13164.183518	2.169E-26	0.02173	1605.80566	8.24E-03	9.32E-03	-2.89E-03	5.03E-03	5.15E-03
R35R35	17.5000	13160.742763	8.404E-27	0.02094	1804.88101	7.86E-03	9.00E-03	-2.94E-03	5.32E-03	5.27E-03
R35Q36	18.1559	13163.025375	8.818E-27	0.02173	1802.59840	7.86E-03	9.00E-03	-2.94E-03	5.05E-03	5.27E-03
R37R37	18.5000	13159.144227	3.232E-27	0.02097	2012.90065	7.55E-03	8.72E-03	-2.98E-03	5.35E-03	5.38E-03
R37Q38	19.1559	13161.444496	3.384E-27	0.02173	2010.60039	7.55E-03	8.72E-03	-2.98E-03	5.07E-03	5.38E-03
R39R39	19.5000	13157.118058	1.174E-27	0.02100	2232.09578	7.29E-03	8.48E-03	-3.02E-03	5.37E-03	5.48E-03
R39Q40	20.1559	13159.435962	1.227E-27	0.02172	2229.77787	7.29E-03	8.48E-03	-3.02E-03	5.09E-03	5.48E-03
R41R41	20.5000	13154.659092	4.026E-28	0.02103	2462.43083	7.07E-03	8.28E-03	-3.05E-03	5.39E-03	5.56E-03
R41Q42	21.1559	13156.994619	4.204E-28	0.02172	2460.09530	7.07E-03	8.28E-03	-3.05E-03	5.10E-03	5.56E-03
R43R43	21.5000	13151.761924	1.306E-28	0.02105	2703.86842	6.90E-03	8.12E-03	-3.09E-03	5.41E-03	5.62E-03
R43Q44	22.1559	13154.115067	1.361E-28	0.02171	2701.51528	6.90E-03	8.12E-03	-3.09E-03	5.11E-03	5.62E-03
R45R45	22.5000	13148.420908	4.004E-29	0.02107	2956.36938	6.76E-03	7.98E-03	-3.12E-03	5.42E-03	5.68E-03
R45Q46	23.1559	13150.791663	4.170E-29	0.02170	2953.99863	6.76E-03	7.98E-03	-3.12E-03	5.12E-03	5.68E-03
R47R47	23.5000	13144.630146	1.162E-29	0.02109	3219.89269	6.64E-03	7.86E-03	-3.15E-03	5.43E-03	5.72E-03
R47Q48	24.1559	13147.018515	1.208E-29	0.02169	3217.50432	6.64E-03	7.86E-03	-3.15E-03	5.12E-03	5.72E-03
R49R49	24.5000	13140.383486	3.189E-30	0.02110	3494.39554	6.55E-03	7.76E-03	-3.17E-03	5.44E-03	5.76E-03
R49Q50	25.1559	13142.789473	3.314E-30	0.02168	3491.98955	6.55E-03	7.76E-03	-3.17E-03	5.13E-03	5.76E-03
R51R51	25.5000	13135.674520	8.289E-31	0.02111	3779.83330	6.47E-03	7.68E-03	-3.20E-03	5.44E-03	5.79E-03
R51Q52	26.1559	13138.098134	8.606E-31	0.02167	3777.40969	6.47E-03	7.68E-03	-3.20E-03	5.13E-03	5.79E-03
R53R53	26.5000	13130.496578	2.040E-31	0.02111	4076.15958	6.41E-03	7.62E-03	-3.22E-03	5.45E-03	5.82E-03
R53Q54	27.1559	13132.937827	2.116E-31	0.02165	4073.71833	6.41E-03	7.62E-03	-3.22E-03	5.14E-03	5.82E-03
R55R55	27.5000	13124.842719	4.757E-32	0.02112	4383.32615	6.35E-03	7.56E-03	-3.23E-03	5.45E-03	5.84E-03
R55Q56	28.1559	13127.301617	4.931E-32	0.02164	4380.86725	6.35E-03	7.56E-03	-3.23E-03	5.14E-03	5.84E-03
R57R57	28.5000	13118.705733	1.051E-32	0.02112	4701.28301	6.31E-03	7.51E-03	-3.25E-03	5.46E-03	5.86E-03
R57Q58	29.1559	13121.182295	1.089E-32	0.02162	4698.80645	6.31E-03	7.51E-03	-3.25E-03	5.14E-03	5.86E-03
R59R59	29.5000	13112.078129	2.202E-33	0.02111	5029.97839	6.27E-03	7.47E-03	-3.26E-03	5.46E-03	5.88E-03
R59Q60	30.1559	13114.572371	2.279E-33	0.02160	5027.48415	6.27E-03	7.47E-03	-3.26E-03	5.14E-03	5.88E-03

CHAPTER 3

O_2 *A*-band Line Parameters to Support Atmospheric Remote Sensing. Part II: The Rare Isotopologues

This chapter was submitted for publication as

D. A. Long, D. K. Havey, S. S. Yu, M. Okumura, C. E. Miller, and J. T. Hodges, *J. Quant. Spectrosc. Radiat. Transfer*, (2011).

Abstract

Frequency-stabilized cavity ring-down spectroscopy (FS-CRDS) was employed to measure over 100 transitions in the *R*-branch of the $b^1\Sigma_g^+ \leftarrow X^3\Sigma_g^-(0,0)$ band for the rare O_2 isotopologues. The use of ^{17}O- and ^{18}O-enriched mixtures allowed for line positions to be measured for the $^{16}O^{17}O$, $^{16}O^{18}O$, $^{17}O_2$, $^{17}O^{18}O$, and $^{18}O_2$ isotopologues. Simultaneous fits to the upper and lower states were performed for each isotopologue using the FS-CRDS positions supplemented by microwave, millimeter, submillimeter, terahertz, and Raman ground state positions from the literature. Positions, line intensities, pressure broadening parameters, and collisional narrowing parameters are reported for the $^{16}O^{18}O$ and $^{16}O^{17}O$ isotopologues which are based upon the present study and our earlier FS-CRDS work [Long et al., JQSRT, 111, 2021(2010) and Robichaud et al., JPCA, 113, 13089(2009)]. The calculated line intensities include a term for the observed Herman-Wallis-like interaction and correct a frequency-dependent error which is present in existing spectroscopic databases.

3.1. Introduction

The O_2 *A*-band [$b^1\Sigma_g^+ \leftarrow X^3\Sigma_g^-(0,0)$] is utilized extensively in remote sensing to determine surface pressure [1-2], aerosol and cloud optical properties [3-4], cloud-top heights [5], and optical path length. Recent remote sensing measurements have demonstrated high precision (e.g., surface pressure determinations with a reproducibility better than 0.1% [1-2] and optical path length to better than 0.3% [6-7]), requiring spectroscopic parameters with even higher precision. Additionally, many *A*-band transitions from the dominant $^{16}O_2$ isotopologue are heavily saturated under atmospheric observing conditions. Also, transitions from rare O_2 isotopologues have significant absorption strengths, requiring high-precision spectroscopic parameters for these transitions [8]. Despite the importance of O_2 rare isotopologues to remote sensing applications, only a few high resolution studies have measured rare isotopologue spectroscopic parameters.

Babcock and Herzberg performed the first quantitative analysis of $^{16}O^{17}O$ and $^{16}O^{18}O$ spectroscopic parameters using high-resolution atmospheric spectra [9]. Since these early measurements, a variety of techniques including Fourier-transform spectroscopy (FTS) [10-11], cavity ring-down spectroscopy (CRDS) [12], frequency-modulation spectroscopy (FMS) [13], and noise-immune cavity-enhanced optical heterodyne molecular spectroscopy (NICE-OHMS) [14] have been employed to measure rare isotopologue spectroscopic parameters. A major experimental challenge in these studies has been to obtain sufficient signal-to-noise in the high resolution spectra to retrieve accurate spectroscopic parameters for the rare isotopologues of O_2. See Robichaud et al. for a complete literature summary [15].

Recently, Robichaud et al. [15] used frequency-stabilized cavity ring-down spectroscopy (FS-CRDS) to perform the most precise rare isotopologue measurements of O_2 to date. These measurements were the first comprehensive study of line intensities and lineshape parameters for the $^{17}O^{18}O$ and $^{18}O_2$ isotopologues. These FS-CRDS measurements presently form the basis for the $^{16}O^{18}O$ and $^{16}O^{17}O$ transitions found in the

HITRAN 2008 database [16].[1] The tuning range of the external-cavity diode laser, which was used in the Robichaud et al. FS-CRDS study [15], unfortunately limited our earlier measurements to the *P*-branch of the $b^1\Sigma_g^+ \leftarrow X^3\Sigma_g^-(0,0)$ band. The present study extends FS-CRDS measurements to the *R*-branch transitions and uses a ^{17}O-enriched sample to significantly improve the spectroscopic parameters determined for the ^{17}O isotopologues (see Figure 1 for a survey scan). We combine our present results with those of our earlier FS-CRDS studies [15,18] to generate a spectroscopic database for the $b^1\Sigma_g^+ \leftarrow X^3\Sigma_g^-(0,0)$ transitions of $^{16}O^{18}O$ and $^{16}O^{17}O$.

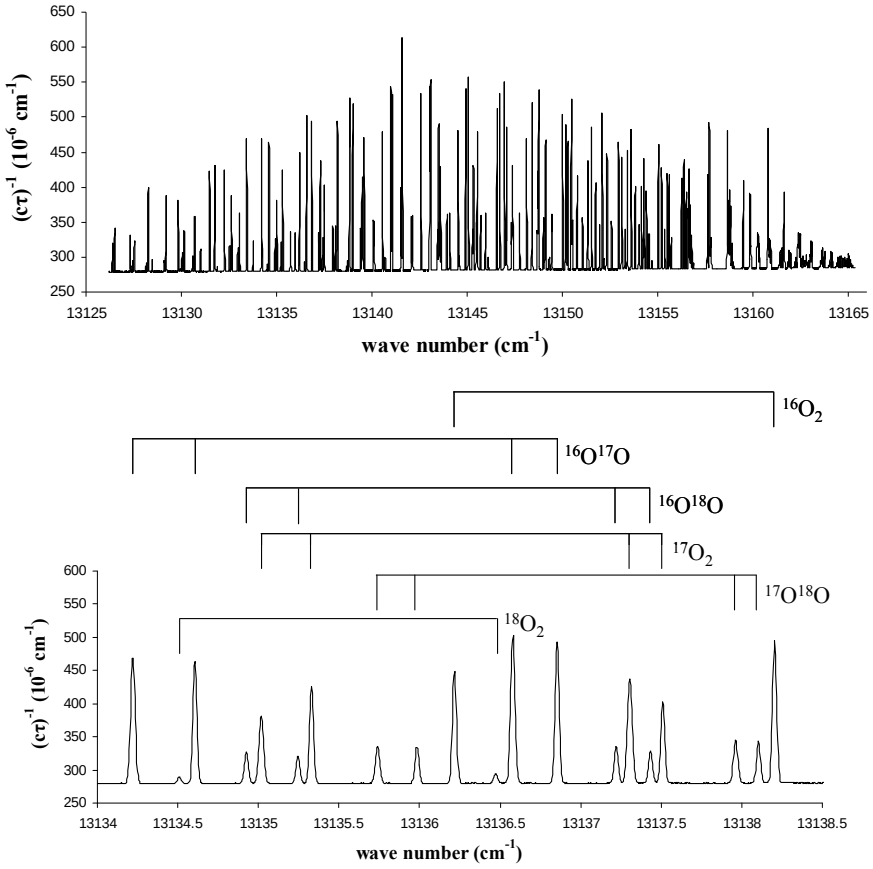

FIG. 1. Upper panel: Recorded absorption spectrum of the *R*-branch of the O_2 *A*-band at 0.234 kPa (1.75 Torr) ^{17}O-enriched gas (see Table 1 for composition) at 299.5 K. Lower panel: The above scan between 13134.0 and 13138.5 cm^{-1} with isotopologue assignments shown.

[1] Contrary to the description found in the HITRAN 2008 publication [16] (which states that the given transition frequencies were taken from Robichaud et al. [15]), the $^{16}O^{17}O$ transition frequencies found in HITRAN 2008 are identical to those found in HITRAN 2004 [17].

3.2. Experiment

The frequency-stabilized cavity ring-down spectrometer utilized for these measurements is located at the National Institute of Standards and Technology (NIST) Gaithersburg, MD and has been described in detail previously [19-20]. Briefly, FS-CRDS differs from traditional *cw*-CRDS techniques by actively stabilizing the intracavity length to an external frequency reference (in our case a co-resonant frequency-stabilized HeNe laser), which in turn eliminates drift in the cavity's comb of transmission modes. The probe laser frequency is then stepped from one TEM_{00} cavity mode to the next, resulting in an extremely linear and stable frequency axis [21]. Each of these modes is separated by the cavity free spectral range (FSR), which is typically determined to better than 1 part in 10^4. Sub-FSR frequency steps are made by shifting the HeNe laser frequency with an acousto-optic modulator in a double-pass alignment. In the present study, we used this procedure to take ½ FSR frequency steps (~100 MHz) to increase the sampling density of our measured spectra.

The probe laser used in the present study was an external cavity diode laser with an output power of 6-10 mW, a wavelength tuning range of 759-771 nm, and a linewidth of 300 kHz (1 s averaging time). Cavity mirrors with reflectivities of 99.98% were employed (cavity finesse ~15,000), leading to a noise-equivalent absorption coefficient of 6×10^{-10} cm^{-1} $Hz^{-1/2}$ for an acquisition rate of 20 Hz and relative uncertainty in the measured decay time of 0.1%. The reference laser was a frequency-stabilized HeNe laser with a long-term frequency uncertainty of 1 MHz (over 8 h). The cavity FSR was determined to be 201.970(10) MHz through the procedure of Lisak and Hodges [22].

Two isotopically enriched O_2 samples were employed for these measurements. The first was an ^{18}O-enriched sample (nominally 50% ^{18}O) which had been previously utilized in our measurements of the *P*-branch O_2 isotopologue transitions [15]. The supplier of this sample was unable to measure the isotopologue composition with sufficient accuracy for the present study. Therefore, we performed a mass spectral analysis of this sample using a double-focusing magnetic-sector mass spectrometer with electron impact ionization [15]. A ^{17}O-enriched sample (nominally 50% ^{17}O) was

supplied with a mass spectral analysis and isotopologue fractions; nevertheless, we performed an independent mass spectral analysis in order to verify the given composition and assess the relevant uncertainties. For the mass 34 species (i.e. $^{16}O^{18}O$ and $^{17}O_2$) the manufacturer atomic composition was utilized to constrain the subsequent fit. The analyses for both samples are given in Table 1.

TABLE 1. Composition of isotopically enriched samples

Iso.	Natural Abundance[a]	^{18}O-Enriched Sample[b]	^{17}O-Enriched Sample[c]	Calculated Band Intensity[d] (cm molec.$^{-1}$)	Measured Band Intensity[e] (cm molec.$^{-1}$)
$^{16}O_2$	0.995262	0.2784 (51)	0.1523(57)	2.231E-22	2.231(7)E-22
$^{16}O^{17}O$	0.000742	0.0099 (4)	0.3816(28)	1.663E-25	1.77(7)E-25
$^{16}O^{18}O$	0.00399141	0.3672 (18)	0.0828(29)	8.947E-25	9.13(5)E-25
$^{17}O_2$	1.38×10^{-7}	not determined	0.2593(49)	3.093E-29	not determined
$^{17}O^{18}O$	1.49×10^{-6}	0.0174 (4)	0.1115(80)	3.340E-28	3.37(8)E-28
$^{18}O_2$	4.00178×10^{-6}	0.3271 (32)	0.0125(26)	8.970E-28	8.66(9)E-28

[a]Based upon the HITRAN 2004 recommended values [17]. [b]Composition determined by mass spectrometer. Values in parentheses are standard uncertainties (1σ). Note that $^{16}O^{18}O$ abundance is actually $^{16}O^{18}O + {}^{17}O_2$ (i.e. mass 34). The uncertainty due to this assumption should be less than 0.01%. [c]Supplier provided composition data. We performed an independent mass spectral analysis in order to assess the uncertainty in the given composition. [d]Band intensities at T_{ref} = 296 K and natural terrestrial abundance as determined by scaling the FS-CRDS determined $^{16}O_2$ band intensity by the natural abundance [17]. [e]Band intensities at T_{ref} = 296 K and natural terrestrial isotopic abundance as determined by a fit to the FS-CRDS rare isotopologue measurements. This fit employed the Gamache et al. intensity model [23] with the Hönl-London factors of Watson [24] and a quadratic Herman-Wallis-like correction [25] as described in the text.

Spectral scans of each of the isotopically enriched samples were performed over the *R*-branch (13125-13165 cm^{-1}) with a nominal 100 MHz (~0.003 cm^{-1}) step size (see Figure 1 for an example survey spectrum).The ^{18}O-enriched sample and ^{17}O-enriched sample were scanned at 0.214 kPa (1.60 Torr) and 0.234 kPa (1.75 Torr), respectively. Pressure was measured with a NIST-calibrated capacitance diaphragm gauge having a full-scale response of 1.33 kPa (10 Torr) and a relative combined standard uncertainty less than 0.1%. The sample cell was placed within an insulated box to mitigate temperature variations. During these scans, temperatures ranged from 299.5 to 300.0 K as measured by a NIST-calibrated 2.4 kΩ thermistor. The temperature uncertainty in these

experiments was examined in detail by Havey et al. [26] and shown to be less than 28 mK.

The importance of using a Galatry profile [27] (which accounts for collisional narrowing [28]) as opposed to a Voigt profile in quantitative measurements of line intensities and lineshape parameters of the $b^1\Sigma_g^+ \leftarrow X^3\Sigma_g^-(0,0)$ band has been demonstrated by our group and others [18,29-30]. However, for the purposes of determining the line center of isolated transitions, symmetric profiles, such as the Voigt or Galatry, yield identical positions when fit to a given set of data. Therefore, since the primary goal of the present study was to experimentally determine transition frequencies, for computational efficiency all transitions were fit with a Voigt profile.[2] Moreover, for the present case (<0.234 kPa), collisional narrowing should be negligible (<1 MHz) compared to the Doppler width (~850 MHz FWHM), thus ensuring effective equivalence between the Voigt and Galatry profiles. Importantly, our earlier FS-CRDS measurements [15,18,30] retrieved line intensities and lineshape parameters, and therefore, it was necessary to utilize the Galatry profile in those studies.

Line intensity, position, and pressure broadening coefficient were fit by least-squares minimization. For the isotopologues which did not contain ^{17}O, the Gaussian width was constrained to the theoretical Doppler width, whereas for the ^{17}O-containing isotopologues, the Gaussian width was floated to account for unresolved hyperfine splitting. Note that the observed hyperfine structure was the subject of a separate publication [31]. . As was shown in that publication, the unresolved hyperfine structure does not alter the center of mass of the transition and therefore, does not alter the measured transition frequency.

3.3. Results and Discussion

The $b^1\Sigma_g^+ \leftarrow X^3\Sigma_g^-(0,0)$ band is triply forbidden as an electric dipole transition but occurs as a magnetic dipole transition [9]. The rotational energy levels of O_2 are commonly described by three quantum numbers: N, the orbital angular momentum; S, the spin; and

[2] No other spectroscopic line parameters determined in the present study (e.g., intensity, pressure broadening parameter) were reported or utilized in the generation of the line lists (Tables 4-5) given below.

J, the total angular momentum (i.e., $J = N+S$). The $X^3\Sigma_g^-$ ground state of O_2 (for $N''>0$) is split into three levels having $J'' = N''-1$, N'', $N''+1$; while the upper state has only one level with $J' = N'$. The $^{16}O_2$ and $^{18}O_2$ isotopologues follow Bose-Einstein statistics and only odd levels of N'' have non-zero spin-statistical weights, whereas the other isotopologues can have any value of N''. The $b^1\Sigma_g^+ \leftarrow X^3\Sigma_g^-(0,0)$ band magnetic dipole transitions occur as doublets designated as ΔN (N'') ΔJ (J''), leading to four branches: *PP*, *PQ*, *RR*, and *RQ*.

Our previous FS-CRDS study [15] focused upon the *P*-branch (i.e., *PP*- and *PQ*-branches), while this study measured the *R*-branch. The *R*-branch of each isotopologue exhibits dense, overlapping rotational structure with a bandhead near 13,165 cm^{-1}. Near the bandhead, the isotopologue transitions become heavily blended (especially in isotopically enriched mixtures); thus limiting the range of transitions we can measure quantitatively.

3.3.1. Line Positions

Frequencies for the rare isotopologue transitions were measured relative to the $^{16}O_2$ positions which we recently have measured with FS-CRDS [21]. Those earlier measurements were referenced to the hyperfine components of ^{39}K; thus allowing for combined uncertainties below 1 MHz (~3×10^{-5} cm^{-1}). Each rare isotopologue transition was referenced to the frequency of the nearest spectrally isolated $^{16}O_2$ transition. Rare isotopologue transition frequencies were corrected for pressure shifting using the *J*-dependent $^{16}O_2$ pressure shifts [32] since accurate pressure-shifting parameters for the rare isotopologues are not known and could not be accurately determined from the present data. This approximation should introduce negligible uncertainty since the pressure shift was only ~0.5 MHz (1.5×10^{-5} cm^{-1}) at the low pressures used in the present study. The estimated zero-pressure transition frequencies are given in the Supplementary Information (Tables A1-A5). In some cases the presence of interfering transitions limited the precision with which we could measure transition frequencies. This

was included in the experimental uncertainties given in Table A1-A5 and leads to some strong transitions to have larger uncertainties than relatively weak transitions.

3.3.2 Line Position Calculations

Molecular constants for each of the rare isotopologues were then determined through a simultaneous fit to the lower ($X^3\Sigma_g^-$) and upper ($b^1\Sigma_g^+$) states using SPFIT [33] and the formalism of Rouillé et al. [34]. FS-CRDS measurements (the present study and Robichaud et al. [15]) were used for the $b^1\Sigma_g^+ \leftarrow X^3\Sigma_g^-(0,0)$ band transition frequencies while lower state transition energies were further constrained by including microwave [35-39], millimeter [40-41], submillimeter [41-42], terahertz [43], and Raman [44] measurements. These global fits included a total of 127 [15,35], 203 [15,36-38,42-44], 539 [40] 98 [15,35], and 135 [15,39,41,43-44] transitions for the $^{16}O^{17}O$, $^{16}O^{18}O$, $^{17}O_2$, $^{17}O^{18}O$, and $^{18}O_2$ isotopologues, respectively.[3] The resulting lower and upper state molecular constants and their corresponding uncertainties are given in Tables 2-3. Following HITRAN convention, lower state energies for the $^{16}O_2$ and $^{18}O_2$ are set relative to the $N'' = 1$, $J'' = 0$ level, whereas for the remaining isotopologues they are relative to the $N'' = 0$, $J'' = 1$ level. For comparison molecular constants determined in previous studies have been presented in Tables 8 and 9 of Robichaud et al. [15].

It is interesting to compare these lower state molecular constants to those recently determined by Leshchishina et al. [42-43]. In that study CRDS measurements of the $a^1\Delta_g \leftarrow X^3\Sigma_g^-(0,0)$ were employed in combination with a similar collection of microwave and Raman studies. The FS-CRDS measurements described herein are more precise than those described by Leshchishina et al. [42-43], but a significantly more transitions were measured in that study. Therefore, a comparison allows us to assess the importance of these two separate attributes. In general, the lower state molecular constants agree to within their given uncertainties. The only significant departures are seen for $^{16}O_2$, whereby the B_0 and D_0 parameters differ by three and nine times the quadrature sum of the given uncertainties, respectively. In addition, the two sets of parameters generally

[3] For the rare isotopologues, the terms H and H_0 are not well constrained, resulting in the large uncertainties given. Global fits performed with these parameters fixed to zero led to similar fit residuals.

have very similar reported uncertainties. The Leshchishina et al. studies [42-43] report significantly lower uncertainties for a few of the $^{17}O_2$ parameters, largely due to the very limited number of $^{17}O_2$ FS-CRDS measurements.

TABLE 2. Lower state ($X^3\Sigma_g^-$) molecular constants determined through the described global fit for each of the O_2 isotopologues (Iso.). All values are in cm^{-1}. Lower state energy levels are defined by Rouillé et al. [34]. Values in parentheses are standard uncertainties in the final digit. $^{16}O_2$ parameters were determined through a global fit as described in Long et al. [47].

Iso.	B_0	D_0 (10^{-6})	H_0 (10^{-12})	λ_0	λ_0' (10^{-6})	λ_0'' (10^{-12})	μ_0 (10^{-3})	μ_0' (10^{-9})	μ_0'' (10^{-14})	Zero level (cm^{-1})
1616	1.437676078(29)	4.84178(14)	4.28(19)	1.98475118(5)	1.9470(3)	9.70(3)	-8.4253696(58)	-8.136(22)	-4.04(15)	-0.24584
1617	1.3953309(28)	4.541(12)		1.98471099(30)	1.8887(38)		-8.176541(78)	-7.13(59)		-0.46452
1618	1.357852204(61)	4.3141(22)	-28(22)	1.98467434(16)	1.83330(86)	9.57(81)	-7.956002(11)	-7.275(39)		-0.47795
1717	1.3529812(23)	3.9(10)		1.98466937(57)	1.82776(88)		-7.9278(11)	-7.194(90)		-0.47975
1718	1.3154968(23)	4.0485(84)		1.98463263(69)	1.7847(96)		-7.70718(12)	-7.0(1)		-0.49403
1818	1.278008487(57)	3.82340(42)	3.8(11)	1.984595545(42)	1.72139(23)	7.73(24)	-7.4866992(46)	-6.418(16)	-3.8(1)	-0.07513

TABLE 3. Upper state ($b^1\Sigma_g^+$) molecular constants determined through the described global fit for each of the O_2 isotopologues (Iso.). All values are in cm^{-1}. Upper state energy levels are given by $T+BJ(J+1)-DJ^2(J+1)^2+HJ^3(J+1)^3$. Values in parentheses are standard uncertainties in the final digit. $^{16}O_2$ parameters were determined through a global fit as described in Long et al. [47].

Iso.	T	B	D (10^{-6})	H (10^{-12})
1616	13122.0057456(89)	1.39124922(11)	5.36909(28)	0.0165(33)
1617	13123.803741(92)	1.3502891(32)	5.028(31)	
1618	13124.793138(23)	1.31404418(43)	4.7858(18)	-36(25)
1717	13124.92252(26)	1.309331(24)	4.43(88)	
1718	13125.92895(11)	1.2730753(29)	4.487(11)	
1818	13126.516194(33)	1.27800849(41)	4.2381(13)	

3.3.3 Line Intensities

As was previously noted for the $^{16}O_2$ *A*-band [18], the calculated line intensities found in the HITRAN 2008 [16] and GEISA [48] databases contain an erroneous frequency dependence (note that the two databases have identical values for all included [$b^1\Sigma_g^+ \leftarrow X^3\Sigma_g^-(0,0)$] isotopologue transitions). This error masked a quadratic Herman-

Wallis (HW)-like rotation-vibration interaction [25,49] which is present in numerous high-resolution studies [18,26,29-30,50-51]. An identical error is present in the $^{16}O^{18}O$ databases. The $^{16}O^{17}O$ line intensities in the databases exhibit a different, but still erroneous, frequency dependence.

Once the line intensities for the rare isotopologues are correctly calculated using the standard model of Gamache et al. [23] with the Hönl-London factors of Watson [24] and compared to the FS-CRDS measurements [15] there is evidence of a quadratic HW-like deviation. This effect, which is described by the term F_{HW}, is given by Watson [25] as

$$F_{HW} = (1 + a_1 m + a_2 m^2)^2, \qquad (1)$$

where m = -J'' (P-branch) and m = J''+1 (R-branch). As seen in Figure 2, the HW-like interaction for the rare isotopologues is nearly identical to that observed for the $^{16}O_2$ isotopologue. It should be expected that the HW coefficients for the different isotopologues would be very similar. To first order the linear HW coefficient has a $\mu^{-1/2}$-dependence (where μ is the reduced mass), while the quadratic HW coefficient has a μ^{-1}-dependence [52-53]. As a result, in the most extreme case (i.e., $^{16}O_2$ vs. $^{18}O_2$), these coefficients would only differ by ~5% and ~12%, respectively. This subtle effect is below our instrumental sensitivity limit. Therefore, the HW coefficients determined for $^{16}O_2$ were utilized for all isotopologues when calculating intensities for our line list.

Band intensities were determined by a new fit of the measurements of Robichaud et al. [15] using the standard intensity model of Gamache et al. [23] with the quadratic HW like correction given in Eq. 1. These fitted band intensities differ by as much as 7% from those given in Robichaud et al. [15], because those were based on the erroneous J-dependent intensities given in HITRAN 2004 [17]. The present measured band intensities were compared to those calculated based upon the $^{16}O_2$ measurements, and as can be seen in Table 1 there are no significant differences. As a result, calculated band intensities were utilized in the line list calculations (as described subsequently) instead of those based on the Robichaud et al. measurements [15].

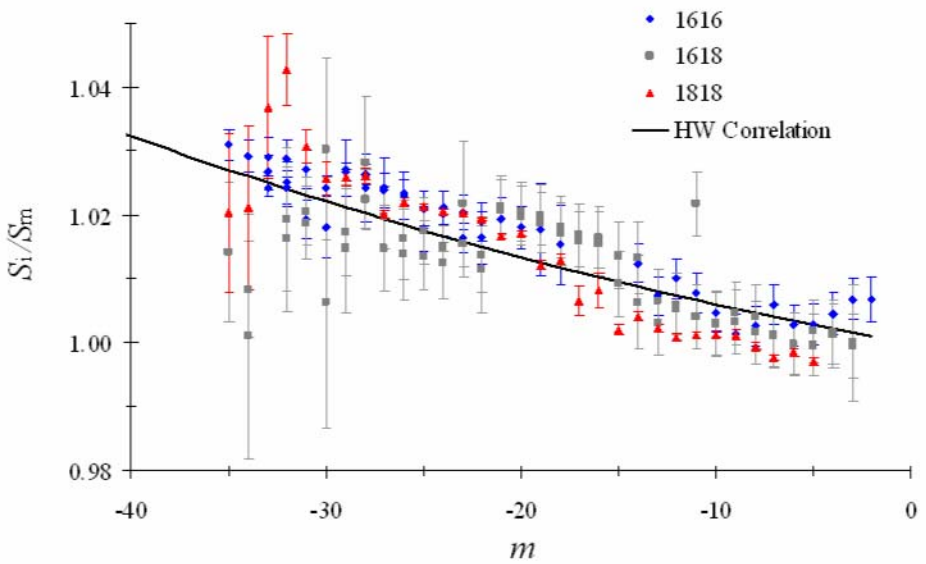

FIG. 2. Comparison of measured FS-CRDS intensities (S_i) to intensities calculated using the standard model of Gamache et al. [23] with the Hönl-London factors of Watson [24] (S_m) for the $^{16}O_2$, $^{16}O^{18}O$, and $^{18}O_2$ isotopologues. Also shown is a quadratic Herman-Wallis (HW) correlation [25] of the form $F=(1+a_1m+a_2m^2)^2$ where a_1 and a_2 were determined via a fit to the $^{16}O_2$ measurements to be -2.6580×10^{-4} and 3.3622×10^{-6}, respectively. As can be seen, this correlation matches the $^{16}O^{18}O$ and $^{18}O_2$ measurements to within the experimental uncertainty. The uncertainties shown for the 16-16 isotopologue are relative combined standard uncertainties which include Type A random uncertainties (due to fit precision) and Type B systematic uncertainties (including those uncertainties due to choice of line shape, temperature, pressure, and ring-down cavity free-spectral range). For the rare isotopologues (16-17 and 16-18) the shown uncertainties are relative standard Type A uncertainties which only include uncertainty due to fit precision.

3.3.4. Calculated Line Parameters for the $^{16}O^{18}O$ and $^{16}O^{17}O$ Isotopologues

We calculated HITRAN-style line parameters for the $^{16}O^{18}O$ and $^{16}O^{17}O$ isotopologues using our collected FS-CRDS measurements [15,18,26,30,32]. The results are presented in Tables A6 and A7. Transition frequencies ($\tilde{\nu}$) and lower state energies (E'') were calculated using the lower and upper state molecular constants given in Tables 2 and 3. Lower state energies are reported relative to the $N'' = 0$, $J'' = 1$ level in accordance with HITRAN convention. Hönl-London factors (L) were also calculated using these molecular constants and the formalism of Watson [24].

Band intensities were then determined by scaling the $^{16}O_2$ band intensity determined in Long et al. [18] by the natural isotopic abundance [17] as shown in Table 1 (see Calculated Band Intensities). Line intensities were then calculated using these band intensities and the standard intensity model of Gamache et al. [23] with the quadratic

HW-like correction as described in Long et al. [18]. As was shown above, the rare isotopologues exhibited a similar HW deviation, thus, the HW coefficients previously determined for $^{16}O_2$ [18] were used for all of the isotopologues. Additionally, Tables A6 and A7 give calculated intensities for transitions up to $J'' = 41$ for the $^{16}O^{18}O$ and $^{16}O^{17}O$ isotopologues at T_{ref} = 296 K and natural terrestrial isotopic abundance [17]. Uncertainties for these calculated intensities can be estimated based upon the experimental uncertainties given in Robichaud et al. [15]. Einstein-A coefficients were then calculated through the formalism of Gamache et al. [23] (see Eq. 2 of Long et al. [18]).

The earlier FS-CRDS study [15] revealed no discernible difference in pressure broadening for the different isotopologues. Therefore, self- and air-broadening parameters (γ) were calculated based upon the correlations recently determined for the $^{16}O_2$ isotopologue [18]. The J-dependent correlations for the collisional narrowing parameters (η) of $^{16}O_2$ [18] were mass-corrected for the rare isotopologues based on the gas kinetic theory formulation: $\eta_{diff} = k_B T/(2\pi m_a D p)$, where m_a and D are the absorber's mass and diffusion coefficient, respectively. Note that this mass correction is in agreement with the experimentally determined mass-dependence of the collisional narrowing parameter determined by Ritter and Wilkerson [29] and Robichaud et al. [15]. The pressure-shifting parameters (δ) for the rare isotopologues were constrained to the $^{16}O_2$ correlation [18,32] since we did not measure precise pressure shifts under the limited pressure range of the present experiment.

3.4 Conclusions

Frequency-stabilized cavity ring-down spectroscopy (FS-CRDS) has been used to measure R-branch transitions in the $b^1\Sigma_g^+ \leftarrow X^3\Sigma_g^-(0,0)$ band for all five rare O_2 isotopologues. This study complements our earlier work which focused on the P-branch. The combined FS-CRDS data set was employed to produce a recommended Galatry line list for the $^{16}O^{18}O$ and $^{16}O^{17}O$ isotopologues out to $J' = 40$ and includes line positions, intensities, pressure broadening parameters, and collisional narrowing parameters. The

reported line positions and molecular constants are based upon a simultaneous fit to the upper and lower states which included FS-CRDS measurements and a variety of earlier lower state measurements. The line intensity calculations included a Herman-Wallis-like interaction and correct a frequency-dependent error which is found in present spectroscopic databases. We anticipate that the use of the reported line parameters will significantly reduce remote sensing residuals for these rare isotopologues.

Acknowledgements

David A. Long was supported by the National Defense Science and Engineering Graduate Fellowship and the National Science Foundation Graduate Fellowship. Daniel K. Havey acknowledges the support of the National Research Council as a postdoctoral fellow at the National Institute of Science and Technology (NIST), Gaithersburg, MD. Part of the research described in this chapter was performed at the Jet Propulsion Laboratory, California Institute of Technology, under contract with the National Aeronautics and Space Administration (NASA). Additional support was provided by the Orbiting Carbon Observatory (OCO) project, a NASA Earth System Science Pathfinder (ESSP) mission; the NASA Upper Atmospheric Research Program grant NNG06GD88G and NNX09AE21G; and the NIST Greenhouse Gas Measurements and Climate Research Program. We would also like to acknowledge Dr. Mona Shahgholi for performing the described mass spectral analysis.

References

[1] D. M. O'Brien, S. A. English, G. DaCosta, J. Atmos. Ocean. Technol. **14,** 105-119 (1997).

[2] D. M. O'Brien, R. M. Mitchell, S. A. English, G. A. Da Costa, J. Atmos. Ocean. Technol. **15,** 1272-1286 (1998).

[3] V. V. Badayev, M. S. Malkevich, Izv. Atmos. Oceanic Phys. **14,** 722–727 (1978).

[4] A. K. Heidinger, G. L. Stephens, J. Atmos. Sci. **57,** 1615-1634 (2000).

[5] D. M. O'Brien, R. M. Mitchell, J. Appl. Meteorol. **31,** 1179-1192 (1992).

[6] C. E. Miller, L. R. Brown, R. A. Toth, D. C. Benner, V. M. Devi, C. R. Phys. **6,** 876-887 (2005).

[7] C. E. Miller, D. Crisp, P. L. DeCola, S. C. Olsen, J. T. Randerson, A. M. Michalak, A. Alkhaled, P. Rayner, D. J. Jacob, P. Suntharalingam, D. B. A. Jones, A. S. Denning, M. E. Nicholls, S. C. Doney, S. Pawson, H. Boesch, B. J. Connor, I. Y. Fung, D. O'Brien, R. J. Salawitch, S. P. Sander, B. Sen, P. Tans, G. C. Toon, P. O. Wennberg, S. C. Wofsy, Y. L. Yung, R. M. Law, J. Geophys. Res.-Atmos. **112,** D10314 (2007).

[8] Z. Yang, P. O. Wennberg, R. P. Cageao, T. J. Pongetti, G. C. Toon, S. P. Sander, J. Quant. Spectrosc. Radiat. Transfer **90,** 309-321 (2005).

[9] H. D. Babcock, L. Herzberg, Astrophys. J. **108,** 167-190 (1948).

[10] R. Schermaul, J. Quant. Spectrosc. Radiat. Transfer **62,** 181-191 (1999).

[11] C. Camy-Peyret, S. Payan, P. Jeseck, Y. Te, T. Hawat, Proc. Int. Radiat. Symp., Saint Petersburg, Russia**,** Paper E4 (2000).

[12] H. Naus, A. deLange, W. Ubachs, Phys. Rev. A **56,** 4755-4763 (1997).

[13] G. Gagliardi, L. Gianfrani, G. M. Tino, Phys. Rev. A **55,** 4597-4600 (1997).

[14] N. J. van Leeuwen, H. G. Kjaergaard, D. L. Howard, A. C. Wilson, J. Mol. Spectrosc. **228,** 83-91 (2004).

[15] D. J. Robichaud, L. Y. Yeung, D. A. Long, M. Okumura, D. K. Havey, J. T. Hodges, C. E. Miller, L. R. Brown, J. Phys. Chem. A **113,** 13089-13099 (2009).

[16] L. S. Rothman, I. E. Gordon, A. Barbe, D. C. Benner, P. F. Bernath, M. Birk, V. Boudon, L. R. Brown, A. Campargue, J. P. Champion, K. Chance, L. H. Coudert, V. Dana, V. M. Devi, S. Fally, J. M. Flaud, R. R. Gamache, A. Goldman, D. Jacquemart, I. Kleiner, N. Lacome, W. J. Lafferty, J. Y. Mandin, S. T. Massie, S. N. Mikhailenko, C. E. Miller, N. Moazzen-Ahmadi, O. V. Naumenko, A. V. Nikitin, J. Orphal, V. I. Perevalov, A. Perrin, A. Predoi-Cross, C. P. Rinsland, M. Rotger, M. Simecková, M. A. H. Smith, K. Sung, S. A. Tashkun, J. Tennyson, R. A. Toth, A. C. Vandaele, J. Vander Auwera, J. Quant. Spectrosc. Radiat. Transfer **110,** 533-572 (2009).

[17] L. S. Rothman, D. Jacquemart, A. Barbe, D. C. Benner, M. Birk, L. R. Brown, M. R. Carleer, C. Chackerian, K. Chance, L. H. Coudert, V. Dana, V. M. Devi, J. M. Flaud, R. R. Gamache, A. Goldman, J. M. Hartmann, K. W. Jucks, A. G. Maki, J. Y. Mandin, S. T. Massie, J. Orphal, A. Perrin, C. P. Rinsland, M. A. H. Smith, J. Tennyson, R. N. Tolchenov, R. A. Toth, J. Vander Auwera, P. Varanasi, G. Wagner, J. Quant. Spectrosc. Radiat. Transfer **96,** 139-204 (2005).

[18] D. A. Long, D. K. Havey, M. Okumura, C. E. Miller, J. T. Hodges, J. Quant. Spectrosc. Radiat. Transfer **111,** 2021-2036 (2010).
[19] J. T. Hodges, H. P. Layer, W. W. Miller, G. E. Scace, Rev. Sci. Instrum. **75,** 849-863 (2004).
[20] J. T. Hodges, R. Ciurylo, Rev. Sci. Instrum. **76,** 023112 (2005).
[21] D. J. Robichaud, J. T. Hodges, P. Maslowski, L. Y. Yeung, M. Okumura, C. E. Miller, L. R. Brown, J. Mol. Spectrosc. **251,** 27-37 (2008).
[22] D. Lisak, J. T. Hodges, Appl. Phys. B **88,** 317-325 (2007).
[23] R. R. Gamache, A. Goldman, L. S. Rothman, J. Quant. Spectrosc. Radiat. Transfer **59,** 495-509 (1998).
[24] J. K. G. Watson, Can. J. Phys. **46,** 1637-1643 (1968).
[25] J. K. G. Watson, J. Mol. Spectrosc. **125,** 428-441 (1987).
[26] D. K. Havey, D. A. Long, M. Okumura, C. E. Miller, J. T. Hodges, Chem. Phys. Lett. **483,** 49-54 (2009).
[27] L. Galatry, Phys. Rev. **122,** 1218-1223 (1961).
[28] R. H. Dicke, Phys. Rev. **89,** 472-473 (1953).
[29] K. J. Ritter, T. D. Wilkerson, J. Mol. Spectrosc. **121,** 1-19 (1987).
[30] D. J. Robichaud, J. T. Hodges, L. R. Brown, D. Lisak, P. Maslowski, L. Y. Yeung, M. Okumura, C. E. Miller, J. Mol. Spectrosc. **248,** 1-13 (2008).
[31] D. A. Long, D. K. Havey, M. Okumura, C. E. Miller, J. T. Hodges, Phys. Rev. A **81,** 064502 (2010).
[32] D. J. Robichaud, J. T. Hodges, D. Lisak, C. E. Miller, M. Okumura, J. Quant. Spectrosc. Radiat. Transfer **109,** 435-444 (2008).
[33] H. M. Pickett, J. Mol. Spectrosc. **148,** 371-377 (1991).
[34] G. Rouillé, G. Millot, R. Saintloup, H. Berger, J. Mol. Spectrosc. **154,** 372-382 (1992).
[35] G. Cazzoli, C. D. Esposti, P. G. Favero, G. Severi, Nouvo Cimento B **62,** 243-254 (1981).
[36] M. Mizushima, S. Yamamoto, J. Mol. Spectrosc. **148,** 447-452 (1991).
[37] T. Amano, E. Hirota, J. Mol. Spectrosc. **53,** 346-363 (1974).
[38] W. Steinbach, W. Gordy, Phys. Rev. A **11,** 729-731 (1975).
[39] Y. Endo, M. Mizushima, Jpn. J. Appl. Phys., Part 2 **22,** L534-L536 (1983).
[40] G. Cazzoli, C. D. Esposti, B. M. Landsberg, Nuovo Cimento D **3,** 341-360 (1984).
[41] W. Steinbach, W. Gordy, Phys. Rev. A **8,** 1753-1758 (1973).
[42] R. L. Crownover, F. C. Delucia, E. Herbst, Astrophys. J. **349,** L29-L31 (1990).
[43] B. J. Drouin, S. S. Yu, C. E. Miller, H. S. P. Muller, F. Lewen, S. Bruenken, H. Habara, J. Quant. Spectrosc. Radiat. Transfer **111,** 1167-1173 (2010).
[44] H. G. M. Edwards, E. A. M. Good, D. A. Long, J. Chem. Soc., Faraday Trans. 2 **72,** 865-870 (1976).
[45] O. Leshchishina, S. Kassi, I. E. Gordon, L. S. Rothman, L. Wang, A. Campargue, J. Quant. Spectrosc. Radiat. Transfer **111,** 2236-2245 (2010).
[46] O. Leshchishina, S. Kassi, I. E. Gordon, S. Yu, A. Campargue, J. Quant. Spectrosc. Radiat. Transfer **112,** 1257-1265 (2011).

[47] D. A. Long, D. K. Havey, M. Okumura, H. M. Pickett, C. E. Miller, J. T. Hodges, Phys. Rev. A **80,** 042513 (2009).
[48] N. Jacquinet-Husson, N. A. Scott, A. Chedina, L. Crepeau, R. Armante, V. Capelle, J. Orphal, A. Coustenis, C. Boonne, N. Poulet-Crovisier, A. Barbee, M. Birk, L. R. Brown, C. Camy-Peyret, C. Claveau, K. Chance, N. Christidis, C. Clerbaux, P. F. Coheur, V. Dana, L. Daumont, M. R. De Backer-Barilly, G. Di Lonardo, J. M. Flaud, A. Goldman, A. Hamdouni, M. Hess, M. D. Hurley, D. Jacquemart, I. Kleiner, P. Kopke, J. Y. Mandin, S. Massie, S. Mikhailenko, V. Nemtchinov, A. Nikitin, D. Newnham, A. Perrin, V. I. Perevalov, S. Pinnock, L. Regalia-Jarlot, C. P. Rinsland, A. Rublev, F. Schreier, L. Schult, K. M. Smith, S. A. Tashkun, J. L. Teffo, R. A. Toth, V. G. Tyuterev, J. V. Auwera, P. Varanasi, G. Wagner, J. Quant. Spectrosc. Radiat. Transfer **109,** 1043-1059 (2008).
[49] R. Herman, R. F. Wallis, J. Chem. Phys. **23,** 637-646 (1955).
[50] R. Schermaul, R. C. M. Learner, J. Quant. Spectrosc. Radiat. Transfer **61,** 781-794 (1999).
[51] L. R. Brown, C. Plymate, J. Mol. Spectrosc. **199,** 166-179 (2000).
[52] C. Chackerian, R. H. Tipping, J. Mol. Spectrosc. **99,** 431-449 (1983).
[53] S. J. Singh, J. Mol. Struct. **127,** 203-208 (1985).

Appendix

TABLE A1. Measured $^{16}O^{17}O$ (1617) line positions, uncertainties (Unc), and the difference between observed line positions (Obs) and those calculated (Calc) using the parameters found in Tables 2 and 3. All measurements were made on the ^{17}O-enriched sample (see Table 1 for isotopic composition).

Assignment $\Delta N\, N''\, \Delta J\, J''$	Position (cm^{-1})	Unc (10^{-5} cm^{-1})	Obs-Calc (10^{-5} cm^{-1})	Sample
R0Q1	13126.50416	25	-14	17
R1R1	13127.31879	25	-2	17
R1Q2	13129.20387	25	41	17
R2R2	13129.83936	25	54	17
R3Q4	13134.22093	24	-57	17
R4R4	13134.60675	24	-48	17
R4Q5	13136.58025	24	-6	17
R5R5	13136.85489	24	-41	17
R5Q6	13138.84470	24	1	17
R6R6	13139.01246	24	7	17
R6Q7	13141.01599	48	7	17
R7R7	13141.07838	48	9	17
R8R8	13143.05334	48	52	17
R7Q8	13143.09510	48	52	17
R9R9	13144.93589	24	14	17
R8Q9	13145.08106	24	16	17
R10R10	13146.72690	24	4	17
R9Q10	13146.97505	24	11	17
R11R11	13148.42558	24	-33	17
R10Q11	13148.77642	72	-25	17
R12R12	13150.03266	24	1	17
R11Q12	13150.48610	48	15	17
R13R13	13151.54712	24	30	17
R12Q13	13152.10239	24	-25	17
R14R14	13152.96802	24	-13	17
R13Q14	13153.62646	24	-6	17
R15R15	13154.29624	48	-12	17
R14Q15	13155.05754	24	16	17
R16R16	13155.53118	24	4	17
R15Q16	13156.39490	24	-5	17

TABLE A2. Measured $^{16}O^{18}O$ (1618) line positions, uncertainties (Unc), and the difference between observed line positions (Obs) and those calculated (Calc) using the parameters found in Tables 2 and 3. Measurements were made on either the ^{17}O-enriched (17) or ^{18}O-enriched (18) sample (see Table 1 for isotopic compositions).

Assignment $\Delta N\ N''\ \Delta J\ J''$	Position (cm^{-1})	Unc (10^{-5} cm^{-1})	Obs-Calc (10^{-5} cm^{-1})	Sample
R0Q1	13127.42102	24	-19	18
R1R1	13128.15250	24	-2	18
R1Q2	13130.04493	24	37	18
R2R2	13130.60487	24	-12	18
R2Q3	13132.53661	24	28	18
R3R3	13132.96980	24	34	18
R3Q4	13134.92577	24	-26	18
R4R4	13135.24562	24	-17	18
R4Q5	13137.22106	24	-22	18
R5R5	13137.43362	24	-19	18
R5Q6	13139.42508	24	24	18
R6R6	13139.53362	24	28	18
R8R8	13143.46604	48	-19	17
R7Q8	13143.56077	72	-22	17
R9R9	13145.29942	47	25	17
R8Q9	13145.49450	48	16	17
R10R10	13147.04291	72	7	17
R9Q10	13147.33810	72	12	17
R11R11	13148.69669	72	-29	17
R10Q11	13149.09159	72	-29	17

TABLE A3. Measured $^{17}O^{17}O$ (1717) line positions, uncertainties (Unc), and the difference between observed line positions (Obs) and those calculated (Calc) using the parameters found in Tables 2 and 3. All measurements were made on the ^{17}O-enriched sample (see Table 1 for isotopic composition).

Assignment $\Delta N\ N''\ \Delta J\ J''$	Position (cm^{-1})	Unc (10^{-5} cm^{-1})	Obs-Calc (10^{-5} cm^{-1})	Sample
R1Q2	13130.15582	25	118	17
R2R2	13130.70447	24	-84	17
R2Q3	13132.63690	24	-40	17
R3R3	13133.06098	24	-37	17
R3Q4	13135.01845	24	8	17
R4R4	13135.32964	24	6	17
R4Q5	13137.30543	24	4	17
R5R5	13137.50982	24	-2	17
R5Q6	13139.50152	72	43	17
R6R6	13139.60232	24	36	17
R8R8	13143.52076	48	-26	17
R7Q8	13143.62248	48	-12	17
R9R9	13145.34761	24	6	17
R8Q9	13145.54933	24	20	17
R10R10	13147.08496	48	-15	17
R9Q10	13147.38627	72	-4	17
R11R11	13148.73287	72	-61	17
R10Q11	13149.13360	48	-46	17
R11Q12	13150.79213	72	-13	17
R12Q13	13152.36039	72	-34	17
R14R14	13153.14054	72	-25	17
R13Q14	13153.83907	72	-20	17
R14Q15	13155.22859	73	94	17

TABLE A4. Measured $^{17}O^{18}O$ (1718) line positions, uncertainties (Unc), and the difference between observed line positions (Obs) and those calculated (Calc) using the parameters found in Tables 2 and 3. All measurements were made on the ^{17}O-enriched sample (see Table 1 for isotopic composition).

Assignment $\Delta N\ N''\ \Delta J\ J''$	Position (cm^{-1})	Unc (10^{-5} cm^{-1})	Obs-Calc (10^{-5} cm^{-1})	Sample
R0Q1	13128.47552	26	44	17
R1R1	13129.11188	26	45	17
R1Q2	13131.01134	25	-103	17
R2Q3	13133.42487	101	10	17
R3R3	13133.77793	24	-52	17
R3Q4	13135.73912	24	-4	17
R4R4	13135.98394	24	-7	17
R4Q5	13137.96239	24	-5	17
R5R5	13138.10400	24	-8	17
R5Q6	13140.09715	48	0	17
R6R6	13140.13850	48	0	17
R7R7	13142.08746	48	36	17
R6Q7	13142.14478	48	41	17
R8R8	13143.94964	24	-5	17
R7Q8	13144.10457	24	0	17
R9R9	13145.72637	24	28	17
R8Q9	13145.97833	24	37	17
R9Q10	13147.76485	24	28	17
R11R11	13149.01928	24	-20	17
R10Q11	13149.46426	24	-11	17
R12R12	13150.53621	72	17	17
R11Q12	13151.07750	24	28	17
R13R13	13151.96521	24	-32	17
R12Q13	13152.60288	24	-12	17
R14R14	13153.30771	24	0	17
R13Q14	13154.04153	24	2	17
R15R15	13154.56239	24	6	17
R14Q15	13155.39282	24	27	17
R16R16	13155.72892	24	-19	17

TABLE A5. Measured $^{18}O^{18}O$ (1818) line positions, uncertainties (Unc), and the difference between observed line positions (Obs) and those calculated (Calc) using the parameters found in Tables 2 and 3. Measurements were made on either the ^{17}O-enriched (17) or ^{18}O-enriched (18) sample (see Table 1 for isotopic compositions).

Assignment $\Delta N\ N''\ \Delta J\ J''$	Position (cm^{-1})	Unc (10^{-5} cm^{-1})	Obs-Calc (10^{-5} cm^{-1})	Sample
R1R1	13129.97558	24	33	18
R1Q2	13131.88468	24	11	18
R3R3	13134.50922	24	-35	18
R3Q4	13136.47434	24	9	18
R5R5	13138.71252	24	7	18
R5Q6	13140.70756	24	2	18
R7Q8	13144.60107	49	10	17
R9R9	13146.11954	26	49	17
R11R11	13149.31970	26	-25	17
R13R13	13152.18353	26	-23	17
R13Q14	13154.25810	73	-2	17
R15R15	13154.70863	28	-4	17
R17R17	13156.89267	29	-3	17

TABLE A6. Line parameters of $b^1\Sigma_g^+ \leftarrow X^3\Sigma_g^-(0,0)$ magnetic dipole transitions for $^{16}O^{18}O$ (1618). Transition frequencies ($\tilde{\nu}$) and lower state energies (E'') were calculated using the molecular parameters determined during the global fit (see Tables 2 and 3) and the formalism of Rouillé et al. [34]. Line intensities (S) at T_{ref} = 296 K and natural terrestrial isotopic abundance [17] were calculated using the standard model of Gamache et al. [23] with the Hönl-London factors (L, also calculated with the molecular parameters of Tables 2 and 3) of Watson [24] and a band intensity $S_b = 8.947\times10^{-25}$ cm molec.$^{-1}$. These intensities included a quadratic Herman-Wallis-like correction [25], given by $(1+a_1m+a_2m^2)^2$ where $a_1 = -2.6580\times10^{-4}$ and $a_2 = 3.3622\times10^{-6}$. Einstein-$A$ coefficients were calculated based upon these intensities as described in the text. Note 1 cm^{-1} atm^{-1} = 0.295872 MHz Pa^{-1}. Uncertainties are comparable to those given in Table 4 of Robichaud et al. [15].

Transition	L	$\tilde{\nu}$ (cm^{-1})	S (cm molec.$^{-1}$)	A (s^{-1})	E'' (cm^{-1})	γ_{air} (MHz Pa^{-1})	γ_{self} (MHz Pa^{-1})	δ (MHz Pa^{-1})	η_{air} (MHz Pa^{-1})	η_{self} (MHz Pa^{-1})
P41Q40	20.3643	12941.361526	1.487E-30	0.02142	2325.43140	7.29E-03	8.48E-03	-3.02E-03	5.93E-03	5.15E-03
P40P40	20.5000	12945.953401	2.538E-30	0.02213	2216.96355	7.41E-03	8.59E-03	-3.00E-03	6.34E-03	5.11E-03
P40Q39	19.8643	12947.629006	2.478E-30	0.02143	2215.28795	7.41E-03	8.59E-03	-3.00E-03	5.89E-03	5.11E-03
P39P39	20.0000	12952.120128	4.174E-30	0.02216	2109.45667	7.55E-03	8.72E-03	-2.98E-03	6.28E-03	5.07E-03
P39Q38	19.3643	12953.803756	4.071E-30	0.02144	2107.77304	7.55E-03	8.72E-03	-2.98E-03	5.84E-03	5.07E-03
P38P38	19.5000	12958.194499	6.772E-30	0.02219	2004.58270	7.70E-03	8.85E-03	-2.96E-03	6.22E-03	5.02E-03
P38Q37	18.8643	12959.886163	6.599E-30	0.02145	2002.89103	7.70E-03	8.85E-03	-2.96E-03	5.79E-03	5.02E-03
P37P37	19.0000	12964.176885	1.084E-29	0.02222	1902.34587	7.86E-03	9.00E-03	-2.94E-03	6.15E-03	4.96E-03
P37Q36	18.3643	12965.876597	1.055E-29	0.02146	1900.64616	7.86E-03	9.00E-03	-2.94E-03	5.73E-03	4.96E-03
P36P36	18.5000	12970.067641	1.711E-29	0.02225	1802.75031	8.04E-03	9.15E-03	-2.91E-03	6.08E-03	4.91E-03
P36Q35	17.8643	12971.775414	1.665E-29	0.02147	1801.04253	8.04E-03	9.15E-03	-2.91E-03	5.66E-03	4.91E-03
P35P35	18.0000	12975.867106	2.666E-29	0.02228	1705.80000	8.24E-03	9.32E-03	-2.89E-03	6.00E-03	4.84E-03
P35Q34	17.3643	12977.582955	2.591E-29	0.02148	1704.08415	8.24E-03	9.32E-03	-2.89E-03	5.59E-03	4.84E-03
P34P34	17.5000	12981.575607	4.098E-29	0.02232	1611.49884	8.46E-03	9.50E-03	-2.87E-03	5.91E-03	4.78E-03
P34Q33	16.8643	12983.299546	3.979E-29	0.02149	1609.77490	8.46E-03	9.50E-03	-2.87E-03	5.52E-03	4.78E-03
P33P33	17.0000	12987.193454	6.211E-29	0.02236	1519.85059	8.70E-03	9.69E-03	-2.84E-03	5.81E-03	4.71E-03
P33Q32	16.3644	12988.925501	6.024E-29	0.02151	1518.11854	8.70E-03	9.69E-03	-2.84E-03	5.44E-03	4.71E-03
P32P32	16.5000	12992.720944	9.286E-29	0.02240	1430.85890	8.96E-03	9.89E-03	-2.82E-03	5.71E-03	4.63E-03
P32Q31	15.8644	12994.461116	8.997E-29	0.02152	1429.11872	8.96E-03	9.89E-03	-2.82E-03	5.35E-03	4.63E-03
P31P31	16.0000	12998.158360	1.369E-28	0.02243	1344.52730	9.23E-03	1.01E-02	-2.79E-03	5.60E-03	4.55E-03
P31Q30	15.3644	12999.906677	1.325E-28	0.02153	1342.77898	9.23E-03	1.01E-02	-2.79E-03	5.25E-03	4.55E-03
P30P30	15.5000	13003.505971	1.991E-28	0.02248	1260.85922	9.52E-03	1.03E-02	-2.77E-03	5.48E-03	4.47E-03
P30Q29	14.8644	13005.262455	1.924E-28	0.02154	1259.10274	9.52E-03	1.03E-02	-2.77E-03	5.15E-03	4.47E-03
P29P29	15.0000	13008.764033	2.856E-28	0.02252	1179.85797	9.83E-03	1.05E-02	-2.74E-03	5.36E-03	4.39E-03
P29Q28	14.3644	13010.528707	2.756E-28	0.02156	1178.09330	9.83E-03	1.05E-02	-2.74E-03	5.04E-03	4.39E-03
P28P28	14.5000	13013.932787	4.036E-28	0.02257	1101.52674	1.01E-02	1.08E-02	-2.71E-03	5.23E-03	4.30E-03
P28Q27	13.8644	13015.705676	3.890E-28	0.02157	1099.75385	1.01E-02	1.08E-02	-2.71E-03	4.93E-03	4.30E-03
P27P27	14.0000	13019.012462	5.627E-28	0.02262	1025.86861	1.05E-02	1.10E-02	-2.69E-03	5.10E-03	4.21E-03
P27Q26	13.3644	13020.793595	5.414E-28	0.02158	1024.08748	1.05E-02	1.10E-02	-2.69E-03	4.82E-03	4.21E-03
P26P26	13.5000	13024.003273	7.733E-28	0.02268	952.88657	1.08E-02	1.12E-02	-2.66E-03	4.96E-03	4.13E-03
P26Q25	12.8644	13025.792682	7.428E-28	0.02160	951.09716	1.08E-02	1.12E-02	-2.66E-03	4.70E-03	4.13E-03
P25P25	13.0000	13028.905423	1.047E-27	0.02273	882.58346	1.11E-02	1.15E-02	-2.63E-03	4.83E-03	4.04E-03
P25Q24	12.3644	13030.703143	1.004E-27	0.02161	880.78574	1.11E-02	1.15E-02	-2.63E-03	4.59E-03	4.04E-03
P24P24	12.5000	13033.719101	1.398E-27	0.02279	814.96204	1.15E-02	1.17E-02	-2.60E-03	4.70E-03	3.96E-03

P24Q23	11.8644	13035.525171	1.338E-27	0.02163	813.15597	1.15E-02	1.17E-02	-2.60E-03	4.47E-03	3.96E-03
P23P23	12.0000	13038.444484	1.840E-27	0.02286	750.02495	1.18E-02	1.19E-02	-2.57E-03	4.57E-03	3.88E-03
P23Q22	11.3644	13040.258949	1.756E-27	0.02164	748.21048	1.18E-02	1.19E-02	-2.57E-03	4.36E-03	3.88E-03
P22P22	11.5000	13043.081737	2.385E-27	0.02293	687.77471	1.21E-02	1.21E-02	-2.54E-03	4.45E-03	3.80E-03
P22Q21	10.8644	13044.904646	2.271E-27	0.02166	685.95181	1.21E-02	1.21E-02	-2.54E-03	4.26E-03	3.80E-03
P21P21	11.0000	13047.631011	3.046E-27	0.02301	628.21376	1.23E-02	1.23E-02	-2.50E-03	4.34E-03	3.72E-03
P21Q20	10.3644	13049.462421	2.894E-27	0.02168	626.38235	1.23E-02	1.23E-02	-2.50E-03	4.16E-03	3.72E-03
P20P20	10.5000	13052.092445	3.832E-27	0.02310	571.34441	1.26E-02	1.25E-02	-2.47E-03	4.23E-03	3.65E-03
P20Q19	9.8644	13053.932422	3.630E-27	0.02169	569.50443	1.26E-02	1.25E-02	-2.47E-03	4.07E-03	3.65E-03
P19P19	10.0000	13056.466167	4.746E-27	0.02319	517.16885	1.28E-02	1.27E-02	-2.44E-03	4.14E-03	3.59E-03
P19Q18	9.3644	13058.314787	4.482E-27	0.02170	515.32023	1.28E-02	1.27E-02	-2.44E-03	3.99E-03	3.59E-03
P18P18	9.5000	13060.752291	5.789E-27	0.02329	465.68920	1.30E-02	1.29E-02	-2.40E-03	4.05E-03	3.52E-03
P18Q17	8.8644	13062.609642	5.447E-27	0.02172	463.83185	1.30E-02	1.29E-02	-2.40E-03	3.92E-03	3.52E-03
P17P17	9.0000	13064.950922	6.949E-27	0.02341	416.90743	1.32E-02	1.30E-02	-2.37E-03	3.98E-03	3.47E-03
P17Q16	8.3644	13066.817107	6.512E-27	0.02175	415.04124	1.32E-02	1.30E-02	-2.37E-03	3.85E-03	3.47E-03
P16P16	8.5000	13069.062149	8.206E-27	0.02354	370.82543	1.34E-02	1.32E-02	-2.33E-03	3.91E-03	3.41E-03
P16Q15	7.8644	13070.937292	7.658E-27	0.02177	368.95028	1.34E-02	1.32E-02	-2.33E-03	3.79E-03	3.41E-03
P15P15	8.0000	13073.086052	9.532E-27	0.02368	327.44497	1.36E-02	1.33E-02	-2.30E-03	3.85E-03	3.35E-03
P15Q14	7.3644	13074.970302	8.851E-27	0.02180	325.56072	1.36E-02	1.33E-02	-2.30E-03	3.74E-03	3.35E-03
P14P14	7.5000	13077.022698	1.089E-26	0.02386	286.76774	1.37E-02	1.35E-02	-2.26E-03	3.79E-03	3.30E-03
P14Q13	6.8644	13078.916235	1.005E-26	0.02183	284.87420	1.37E-02	1.35E-02	-2.26E-03	3.69E-03	3.30E-03
P13P13	7.0000	13080.872144	1.221E-26	0.02405	248.79528	1.39E-02	1.36E-02	-2.22E-03	3.73E-03	3.25E-03
P13Q12	6.3644	13082.775192	1.120E-26	0.02186	246.89223	1.39E-02	1.36E-02	-2.22E-03	3.64E-03	3.25E-03
P12P12	6.5000	13084.634433	1.346E-26	0.02428	213.52906	1.40E-02	1.38E-02	-2.18E-03	3.67E-03	3.19E-03
P12Q11	5.8644	13086.547273	1.225E-26	0.02190	211.61622	1.40E-02	1.38E-02	-2.18E-03	3.59E-03	3.19E-03
P11P11	6.0000	13088.309598	1.455E-26	0.02455	180.97044	1.42E-02	1.39E-02	-2.15E-03	3.61E-03	3.13E-03
P11Q10	5.3644	13090.232590	1.312E-26	0.02194	179.04745	1.42E-02	1.39E-02	-2.15E-03	3.53E-03	3.13E-03
P10P10	5.5000	13091.897660	1.541E-26	0.02488	151.12066	1.43E-02	1.41E-02	-2.11E-03	3.54E-03	3.06E-03
P10Q9	4.8645	13093.831279	1.375E-26	0.02200	149.18704	1.43E-02	1.41E-02	-2.11E-03	3.47E-03	3.06E-03
P9P9	5.0000	13095.398629	1.598E-26	0.02528	123.98087	1.45E-02	1.43E-02	-2.07E-03	3.46E-03	2.99E-03
P9Q8	4.3645	13097.343514	1.408E-26	0.02206	122.03598	1.45E-02	1.43E-02	-2.07E-03	3.41E-03	2.99E-03
P8P8	4.5000	13098.812502	1.619E-26	0.02579	99.55209	1.47E-02	1.45E-02	-2.02E-03	3.37E-03	2.91E-03
P8Q7	3.8645	13100.769551	1.403E-26	0.02215	97.59505	1.47E-02	1.45E-02	-2.02E-03	3.33E-03	2.91E-03
P7P7	4.0000	13102.139268	1.599E-26	0.02645	77.83528	1.50E-02	1.47E-02	-1.98E-03	3.27E-03	2.82E-03
P7Q6	3.3646	13104.109789	1.357E-26	0.02225	75.86476	1.50E-02	1.47E-02	-1.98E-03	3.24E-03	2.82E-03
P6P6	3.5000	13105.378901	1.533E-26	0.02736	58.83125	1.53E-02	1.50E-02	-1.94E-03	3.14E-03	2.72E-03
P6Q5	2.8647	13107.364921	1.266E-26	0.02239	56.84523	1.53E-02	1.50E-02	-1.94E-03	3.13E-03	2.72E-03
P5P5	3.0000	13108.531365	1.422E-26	0.02867	42.54074	1.57E-02	1.53E-02	-1.90E-03	2.99E-03	2.60E-03
P5Q4	2.3649	13110.536270	1.132E-26	0.02260	40.53584	1.57E-02	1.53E-02	-1.90E-03	3.00E-03	2.60E-03
P4P4	2.5000	13111.596614	1.265E-26	0.03072	28.96436	1.61E-02	1.57E-02	-1.85E-03	2.81E-03	2.46E-03
P4Q3	1.8653	13113.626722	9.532E-27	0.02292	26.93426	1.61E-02	1.57E-02	-1.85E-03	2.85E-03	2.46E-03
P3P3	2.0000	13114.574588	1.066E-26	0.03441	18.10264	1.67E-02	1.62E-02	-1.81E-03	2.59E-03	2.29E-03
P3Q2	1.3662	13116.643966	7.359E-27	0.02350	16.03326	1.67E-02	1.62E-02	-1.81E-03	2.66E-03	2.29E-03
P2P2	1.5000	13117.465220	8.323E-27	0.04302	9.95599	1.73E-02	1.67E-02	-1.77E-03	2.32E-03	2.08E-03
P2Q1	0.8697	13119.617605	4.874E-27	0.02494	7.80360	1.73E-02	1.67E-02	-1.77E-03	2.42E-03	2.08E-03
P1P1	1.0000	13120.268426	5.695E-27	0.08603	4.52471	1.82E-02	1.74E-02	-1.72E-03	1.97E-03	1.84E-03
R0Q1	0.6303	13127.421207	3.665E-27	0.01807	0.00000	1.73E-02	1.67E-02	-1.77E-03	4.25E-03	2.08E-03
R1R1	0.5000	13128.152519	2.845E-27	0.00861	4.52471	1.67E-02	1.62E-02	-1.81E-03	4.29E-03	2.29E-03

R1Q2	1.1338	13130.044563	6.508E-27	0.01951	2.63267	1.67E-02	1.62E-02	-1.81E-03	4.28E-03	2.29E-03
R2R2	1.0000	13130.604991	5.539E-27	0.01230	9.95599	1.61E-02	1.57E-02	-1.85E-03	4.33E-03	2.46E-03
R2Q3	1.6347	13132.536326	9.137E-27	0.02010	8.02465	1.61E-02	1.57E-02	-1.85E-03	4.31E-03	2.46E-03
R3R3	1.5000	13132.969465	7.984E-27	0.01434	18.10264	1.57E-02	1.53E-02	-1.90E-03	4.37E-03	2.60E-03
R3Q4	2.1351	13134.926032	1.147E-26	0.02042	16.14607	1.57E-02	1.53E-02	-1.90E-03	4.34E-03	2.60E-03
R4R4	2.0000	13135.245790	1.010E-26	0.01565	28.96436	1.53E-02	1.50E-02	-1.94E-03	4.40E-03	2.72E-03
R4Q5	2.6353	13137.221279	1.342E-26	0.02062	26.98888	1.53E-02	1.50E-02	-1.94E-03	4.36E-03	2.72E-03
R5R5	2.5000	13137.433807	1.181E-26	0.01655	42.54074	1.50E-02	1.47E-02	-1.98E-03	4.43E-03	2.82E-03
R5Q6	3.1354	13139.424838	1.495E-26	0.02076	40.54971	1.50E-02	1.47E-02	-1.98E-03	4.37E-03	2.82E-03
R6R6	3.0000	13139.533343	1.309E-26	0.01722	58.83125	1.47E-02	1.45E-02	-2.02E-03	4.45E-03	2.91E-03
R6Q7	3.6355	13141.537898	1.601E-26	0.02086	56.82670	1.47E-02	1.45E-02	-2.02E-03	4.39E-03	2.91E-03
R7R7	3.5000	13141.544215	1.392E-26	0.01772	77.83528	1.45E-02	1.43E-02	-2.07E-03	4.46E-03	2.99E-03
R7Q8	4.1355	13143.560991	1.660E-26	0.02094	75.81850	1.45E-02	1.43E-02	-2.07E-03	4.40E-03	2.99E-03
R8R8	4.0000	13143.466228	1.431E-26	0.01812	99.55209	1.43E-02	1.41E-02	-2.11E-03	4.48E-03	3.06E-03
R8Q9	4.6355	13145.494336	1.675E-26	0.02100	97.52399	1.43E-02	1.41E-02	-2.11E-03	4.41E-03	3.06E-03
R9R9	4.5000	13145.299174	1.429E-26	0.01845	123.98087	1.42E-02	1.39E-02	-2.15E-03	4.49E-03	3.13E-03
R9Q10	5.1356	13147.337981	1.647E-26	0.02105	121.94206	1.42E-02	1.39E-02	-2.15E-03	4.42E-03	3.13E-03
R10R10	5.0000	13147.042835	1.391E-26	0.01872	151.12066	1.40E-02	1.38E-02	-2.18E-03	4.51E-03	3.19E-03
R10Q11	5.6356	13149.091875	1.583E-26	0.02109	149.07162	1.40E-02	1.38E-02	-2.18E-03	4.43E-03	3.19E-03
R11R11	5.5000	13148.696981	1.323E-26	0.01894	180.97044	1.39E-02	1.36E-02	-2.22E-03	4.52E-03	3.25E-03
R11Q12	6.1356	13150.755900	1.491E-26	0.02113	178.91152	1.39E-02	1.36E-02	-2.22E-03	4.44E-03	3.25E-03
R12R12	6.0000	13150.261369	1.232E-26	0.01913	213.52906	1.37E-02	1.35E-02	-2.26E-03	4.53E-03	3.30E-03
R12Q13	6.6356	13152.329893	1.376E-26	0.02116	211.46054	1.37E-02	1.35E-02	-2.26E-03	4.44E-03	3.30E-03
R13R13	6.5000	13151.735743	1.124E-26	0.01929	248.79528	1.36E-02	1.33E-02	-2.30E-03	4.54E-03	3.35E-03
R13Q14	7.1356	13153.813656	1.246E-26	0.02119	246.71737	1.36E-02	1.33E-02	-2.30E-03	4.45E-03	3.35E-03
R14R14	7.0000	13153.119839	1.007E-26	0.01944	286.76774	1.34E-02	1.32E-02	-2.33E-03	4.56E-03	3.41E-03
R14Q15	7.6356	13155.206967	1.109E-26	0.02121	284.68061	1.34E-02	1.32E-02	-2.33E-03	4.46E-03	3.41E-03
R15R15	7.5000	13154.413376	8.847E-27	0.01956	327.44497	1.32E-02	1.30E-02	-2.37E-03	4.57E-03	3.47E-03
R15Q16	8.1356	13156.509579	9.695E-27	0.02122	325.34877	1.32E-02	1.30E-02	-2.37E-03	4.47E-03	3.47E-03
R16R16	8.0000	13155.616062	7.641E-27	0.01968	370.82543	1.30E-02	1.29E-02	-2.40E-03	4.59E-03	3.52E-03
R16Q17	8.6356	13157.721224	8.332E-27	0.02124	368.72026	1.30E-02	1.29E-02	-2.40E-03	4.48E-03	3.52E-03
R17R17	8.5000	13156.727595	6.488E-27	0.01977	416.90743	1.28E-02	1.27E-02	-2.44E-03	4.60E-03	3.59E-03
R17Q18	9.1356	13158.841619	7.045E-27	0.02125	414.79340	1.28E-02	1.27E-02	-2.44E-03	4.49E-03	3.59E-03
R18R18	9.0000	13157.747658	5.418E-27	0.01986	465.68920	1.26E-02	1.25E-02	-2.47E-03	4.62E-03	3.65E-03
R18Q19	9.6356	13159.870463	5.861E-27	0.02127	463.56639	1.26E-02	1.25E-02	-2.47E-03	4.50E-03	3.65E-03
R19R19	9.5000	13158.675921	4.452E-27	0.01994	517.16885	1.23E-02	1.23E-02	-2.50E-03	4.64E-03	3.72E-03
R19Q20	10.1356	13160.807439	4.799E-27	0.02128	515.03734	1.23E-02	1.23E-02	-2.50E-03	4.52E-03	3.72E-03
R20R20	10.0000	13159.512042	3.601E-27	0.02001	571.34441	1.21E-02	1.21E-02	-2.54E-03	4.67E-03	3.80E-03
R20Q21	10.6356	13161.652214	3.869E-27	0.02129	569.20424	1.21E-02	1.21E-02	-2.54E-03	4.53E-03	3.80E-03
R21R21	10.5000	13160.255666	2.867E-27	0.02008	628.21376	1.18E-02	1.19E-02	-2.57E-03	4.69E-03	3.88E-03
R21Q22	11.1356	13162.404443	3.073E-27	0.02130	626.06499	1.18E-02	1.19E-02	-2.57E-03	4.55E-03	3.88E-03
R22R22	11.0000	13160.906424	2.248E-27	0.02014	687.77471	1.15E-02	1.17E-02	-2.60E-03	4.72E-03	3.96E-03
R22Q23	11.6356	13163.063763	2.403E-27	0.02131	685.61737	1.15E-02	1.17E-02	-2.60E-03	4.56E-03	3.96E-03
R23R23	11.5000	13161.463934	1.736E-27	0.02019	750.02495	1.11E-02	1.15E-02	-2.63E-03	4.74E-03	4.04E-03
R23Q24	12.1356	13163.629799	1.851E-27	0.02131	747.85908	1.11E-02	1.15E-02	-2.63E-03	4.58E-03	4.04E-03
R24R24	12.0000	13161.927802	1.321E-27	0.02024	814.96204	1.08E-02	1.12E-02	-2.66E-03	4.77E-03	4.13E-03
R24Q25	12.6356	13164.102161	1.406E-27	0.02132	812.78768	1.08E-02	1.12E-02	-2.66E-03	4.60E-03	4.13E-03
R25R25	12.5000	13162.297618	9.906E-28	0.02028	882.58346	1.05E-02	1.10E-02	-2.69E-03	4.80E-03	4.21E-03

R25Q26	13.1356	13164.480442	1.052E-27	0.02132	880.40063	1.05E-02	1.10E-02	-2.69E-03	4.62E-03	4.21E-03
R26R26	13.0000	13162.572959	7.319E-28	0.02033	952.88657	1.01E-02	1.08E-02	-2.71E-03	4.82E-03	4.30E-03
R26Q27	13.6356	13164.764225	7.759E-28	0.02133	950.69530	1.01E-02	1.08E-02	-2.71E-03	4.63E-03	4.30E-03
R27R27	13.5000	13162.753388	5.331E-28	0.02037	1025.86861	9.83E-03	1.05E-02	-2.74E-03	4.85E-03	4.39E-03
R27Q28	14.1356	13164.953075	5.641E-28	0.02133	1023.66893	9.83E-03	1.05E-02	-2.74E-03	4.65E-03	4.39E-03
R28R28	14.0000	13162.838454	3.826E-28	0.02040	1101.52674	9.52E-03	1.03E-02	-2.77E-03	4.87E-03	4.47E-03
R28Q29	14.6356	13165.046543	4.043E-28	0.02134	1099.31865	9.52E-03	1.03E-02	-2.77E-03	4.67E-03	4.47E-03
R29R29	14.5000	13162.827691	2.708E-28	0.02044	1179.85797	9.23E-03	1.01E-02	-2.79E-03	4.90E-03	4.55E-03
R29Q30	15.1356	13165.044166	2.857E-28	0.02134	1177.64149	9.23E-03	1.01E-02	-2.79E-03	4.68E-03	4.55E-03
R30R30	15.0000	13162.720619	1.889E-28	0.02047	1260.85922	8.96E-03	9.89E-03	-2.82E-03	4.92E-03	4.63E-03
R30Q31	15.6356	13164.945467	1.991E-28	0.02134	1258.63437	8.96E-03	9.89E-03	-2.82E-03	4.70E-03	4.63E-03
R31R31	15.5000	13162.516742	1.300E-28	0.02049	1344.52730	8.70E-03	9.69E-03	-2.84E-03	4.94E-03	4.71E-03
R31Q32	16.1356	13164.749950	1.368E-28	0.02134	1342.29409	8.70E-03	9.69E-03	-2.84E-03	4.71E-03	4.71E-03
R32R32	16.0000	13162.215551	8.817E-29	0.02052	1430.85890	8.46E-03	9.50E-03	-2.87E-03	4.96E-03	4.78E-03
R32Q33	16.6357	13164.457109	9.269E-29	0.02135	1428.61734	8.46E-03	9.50E-03	-2.87E-03	4.72E-03	4.78E-03
R33R33	16.5000	13161.816519	5.899E-29	0.02054	1519.85059	8.24E-03	9.32E-03	-2.89E-03	4.98E-03	4.84E-03
R33Q34	17.1357	13164.066417	6.194E-29	0.02135	1517.60069	8.24E-03	9.32E-03	-2.89E-03	4.74E-03	4.84E-03
R34R34	17.0000	13161.319105	3.892E-29	0.02057	1611.49884	8.04E-03	9.15E-03	-2.91E-03	5.00E-03	4.91E-03
R34Q35	17.6357	13163.577337	4.083E-29	0.02135	1609.24061	8.04E-03	9.15E-03	-2.91E-03	4.75E-03	4.91E-03
R35R35	17.5000	13160.722753	2.534E-29	0.02059	1705.80000	7.86E-03	9.00E-03	-2.94E-03	5.01E-03	4.96E-03
R35Q36	18.1357	13162.989311	2.655E-29	0.02135	1703.53344	7.86E-03	9.00E-03	-2.94E-03	4.76E-03	4.96E-03
R36R36	18.0000	13160.026890	1.627E-29	0.02061	1802.75031	7.70E-03	8.85E-03	-2.96E-03	5.02E-03	5.02E-03
R36Q37	18.6357	13162.301768	1.703E-29	0.02135	1800.47543	7.70E-03	8.85E-03	-2.96E-03	4.76E-03	5.02E-03
R37R37	18.5000	13159.230925	1.030E-29	0.02063	1902.34587	7.55E-03	8.72E-03	-2.98E-03	5.04E-03	5.07E-03
R37Q38	19.1357	13161.514119	1.077E-29	0.02135	1900.06268	7.55E-03	8.72E-03	-2.98E-03	4.77E-03	5.07E-03
R38R38	19.0000	13158.334255	6.435E-30	0.02064	2004.58270	7.41E-03	8.59E-03	-3.00E-03	5.05E-03	5.11E-03
R38Q39	19.6357	13160.625760	6.727E-30	0.02134	2002.29119	7.41E-03	8.59E-03	-3.00E-03	4.78E-03	5.11E-03
R39R39	19.5000	13157.336255	3.967E-30	0.02066	2109.45667	7.29E-03	8.48E-03	-3.02E-03	5.06E-03	5.15E-03
R39Q40	20.1357	13159.636069	4.143E-30	0.02134	2107.15685	7.29E-03	8.48E-03	-3.02E-03	4.79E-03	5.15E-03
R40R40	20.0000	13156.236287	2.413E-30	0.02068	2216.96355	7.17E-03	8.38E-03	-3.04E-03	5.07E-03	5.19E-03
R40Q41	20.6357	13158.544406	2.517E-30	0.02134	2214.65543	7.17E-03	8.38E-03	-3.04E-03	4.79E-03	5.19E-03

TABLE A7. Line parameters of $b^1\Sigma_g^+ \leftarrow X^3\Sigma_g^-(0,0)$ magnetic dipole transitions for $^{16}O^{17}O$ (1617). Transition frequencies ($\tilde{\nu}$) and lower state energies (E'') were calculated using the molecular parameters determined during the global fit (see Tables 2 and 3) and the formalism of Rouillé et al. [34]. Line intensities (S) at T_{ref} = 296 K and natural terrestrial isotopic abundance [17] were calculated using the standard model of Gamache et al. [23] with the Hönl-London factors (L, also calculated with the molecular parameters of Tables 2 and 3) of Watson [24] and a band intensity $S_b = 1.663\times10^{-25}$ cm molec.$^{-1}$. These intensities included a quadratic Herman-Wallis-like correction [25], given by $(1+a_1m+a_2m^2)^2$ where $a_1 = -2.6580\times10^{-4}$ and $a_2 = 3.3622\times10^{-6}$. Einstein-$A$ coefficients were calculated based upon these intensities as described in the text. Note 1 cm^{-1} atm^{-1} = 0.295872 MHz Pa^{-1}. Uncertainties are comparable to those given in Table 6 of Robichaud et al. [15].

Transition	L	$\tilde{\nu}$ (cm^{-1})	S (cm molec.$^{-1}$)	A (s^{-1})	E'' (cm^{-1})	γ_{air} (MHz Pa^{-1})	γ_{self} (MHz Pa^{-1})	δ (MHz Pa^{-1})	η_{air} (MHz Pa^{-1})	η_{self} (MHz Pa^{-1})
P41Q40	20.3546	12935.320248	2.260E-31	0.02323	2389.43349	7.29E-03	8.48E-03	-3.02E-03	6.11E-03	5.31E-03
P40P40	20.5000	12940.090586	3.916E-31	0.02401	2277.92727	7.41E-03	8.59E-03	-3.00E-03	6.53E-03	5.27E-03
P40Q39	19.8546	12941.757977	3.820E-31	0.02324	2276.25988	7.41E-03	8.59E-03	-3.00E-03	6.06E-03	5.27E-03
P39P39	20.0000	12946.425220	6.532E-31	0.02405	2167.46318	7.55E-03	8.72E-03	-2.98E-03	6.47E-03	5.22E-03
P39Q38	19.3546	12948.100865	6.367E-31	0.02326	2165.78753	7.55E-03	8.72E-03	-2.98E-03	6.02E-03	5.22E-03
P38P38	19.5000	12952.665349	1.075E-30	0.02408	2059.70473	7.70E-03	8.85E-03	-2.96E-03	6.41E-03	5.17E-03
P38Q37	18.8546	12954.349261	1.047E-30	0.02327	2058.02082	7.70E-03	8.85E-03	-2.96E-03	5.96E-03	5.17E-03
P37P37	19.0000	12958.811310	1.744E-30	0.02412	1954.65617	7.86E-03	9.00E-03	-2.94E-03	6.34E-03	5.11E-03
P37Q36	18.3546	12960.503501	1.697E-30	0.02328	1952.96397	7.86E-03	9.00E-03	-2.94E-03	5.90E-03	5.11E-03
P36P36	18.5000	12964.863425	2.791E-30	0.02415	1852.32164	8.04E-03	9.15E-03	-2.91E-03	6.26E-03	5.05E-03
P36Q35	17.8546	12966.563910	2.713E-30	0.02330	1850.62115	8.04E-03	9.15E-03	-2.91E-03	5.84E-03	5.05E-03
P35P35	18.0000	12970.822007	4.404E-30	0.02419	1752.70517	8.24E-03	9.32E-03	-2.89E-03	6.18E-03	4.99E-03
P35Q34	17.3546	12972.530801	4.278E-30	0.02331	1750.99638	8.24E-03	9.32E-03	-2.89E-03	5.76E-03	4.99E-03
P34P34	17.5000	12976.687356	6.854E-30	0.02423	1655.81069	8.46E-03	9.50E-03	-2.87E-03	6.09E-03	4.92E-03
P34Q33	16.8546	12978.404475	6.651E-30	0.02332	1654.09357	8.46E-03	9.50E-03	-2.87E-03	5.69E-03	4.92E-03
P33P33	17.0000	12982.459761	1.052E-29	0.02427	1561.64201	8.70E-03	9.69E-03	-2.84E-03	5.99E-03	4.85E-03
P33Q32	16.3546	12984.185223	1.020E-29	0.02334	1559.91655	8.70E-03	9.69E-03	-2.84E-03	5.60E-03	4.85E-03
P32P32	16.5000	12988.139499	1.591E-29	0.02431	1470.20284	8.96E-03	9.89E-03	-2.82E-03	5.88E-03	4.77E-03
P32Q31	15.8546	12989.873323	1.541E-29	0.02335	1468.46902	8.96E-03	9.89E-03	-2.82E-03	5.51E-03	4.77E-03
P31P31	16.0000	12993.726835	2.374E-29	0.02436	1381.49677	9.23E-03	1.01E-02	-2.79E-03	5.77E-03	4.69E-03
P31Q30	15.3546	12995.469042	2.296E-29	0.02336	1379.75457	9.23E-03	1.01E-02	-2.79E-03	5.41E-03	4.69E-03
P30P30	15.5000	12999.222023	3.491E-29	0.02440	1295.52730	9.52E-03	1.03E-02	-2.77E-03	5.65E-03	4.61E-03
P30Q29	14.8546	13000.972635	3.371E-29	0.02338	1293.77668	9.52E-03	1.03E-02	-2.77E-03	5.30E-03	4.61E-03
P29P29	15.0000	13004.625304	5.060E-29	0.02445	1212.29779	9.83E-03	1.05E-02	-2.74E-03	5.52E-03	4.52E-03
P29Q28	14.3546	13006.384347	4.880E-29	0.02339	1210.53874	9.83E-03	1.05E-02	-2.74E-03	5.19E-03	4.52E-03
P28P28	14.5000	13009.936909	7.230E-29	0.02451	1131.81152	1.01E-02	1.08E-02	-2.71E-03	5.39E-03	4.43E-03
P28Q27	13.8546	13011.704410	6.962E-29	0.02340	1130.04402	1.01E-02	1.08E-02	-2.71E-03	5.08E-03	4.43E-03
P27P27	14.0000	13015.157057	1.018E-28	0.02456	1054.07165	1.05E-02	1.10E-02	-2.69E-03	5.25E-03	4.34E-03
P27Q26	13.3546	13016.933046	9.788E-29	0.02342	1052.29566	1.05E-02	1.10E-02	-2.69E-03	4.96E-03	4.34E-03
P26P26	13.5000	13020.285953	1.413E-28	0.02462	979.08123	1.08E-02	1.12E-02	-2.66E-03	5.11E-03	4.25E-03
P26Q25	12.8546	13022.070465	1.356E-28	0.02343	977.29672	1.08E-02	1.12E-02	-2.66E-03	4.84E-03	4.25E-03
P25P25	13.0000	13025.323794	1.932E-28	0.02468	906.84320	1.11E-02	1.15E-02	-2.63E-03	4.98E-03	4.16E-03
P25Q24	12.3546	13027.116866	1.851E-28	0.02345	905.05013	1.11E-02	1.15E-02	-2.63E-03	4.73E-03	4.16E-03

P24P24	12.5000	13030.270762	2.603E-28	0.02475	837.36040	1.15E-02	1.17E-02	-2.60E-03	4.84E-03	4.08E-03
P24Q23	11.8546	13032.072436	2.488E-28	0.02346	835.55873	1.15E-02	1.17E-02	-2.60E-03	4.61E-03	4.08E-03
P23P23	12.0000	13035.127030	3.454E-28	0.02482	770.63555	1.18E-02	1.19E-02	-2.57E-03	4.71E-03	3.99E-03
P23Q22	11.3546	13036.937353	3.295E-28	0.02348	768.82523	1.18E-02	1.19E-02	-2.57E-03	4.50E-03	3.99E-03
P22P22	11.5000	13039.892757	4.515E-28	0.02490	706.67127	1.21E-02	1.21E-02	-2.54E-03	4.59E-03	3.91E-03
P22Q21	10.8546	13041.711783	4.297E-28	0.02350	704.85225	1.21E-02	1.21E-02	-2.54E-03	4.39E-03	3.91E-03
P21P21	11.0000	13044.568092	5.812E-28	0.02499	645.47007	1.23E-02	1.23E-02	-2.50E-03	4.47E-03	3.84E-03
P21Q20	10.3546	13046.395881	5.517E-28	0.02351	643.64228	1.23E-02	1.23E-02	-2.50E-03	4.29E-03	3.84E-03
P20P20	10.5000	13049.153171	7.367E-28	0.02508	587.03433	1.26E-02	1.25E-02	-2.47E-03	4.36E-03	3.76E-03
P20Q19	9.8546	13050.989794	6.972E-28	0.02353	585.19771	1.26E-02	1.25E-02	-2.47E-03	4.20E-03	3.76E-03
P19P19	10.0000	13053.648120	9.193E-28	0.02519	531.36635	1.28E-02	1.27E-02	-2.44E-03	4.27E-03	3.70E-03
P19Q18	9.3546	13055.493658	8.671E-28	0.02355	529.52081	1.28E-02	1.27E-02	-2.44E-03	4.11E-03	3.70E-03
P18P18	9.5000	13058.053050	1.129E-27	0.02530	478.46832	1.30E-02	1.29E-02	-2.40E-03	4.18E-03	3.63E-03
P18Q17	8.8546	13059.907598	1.061E-27	0.02357	476.61377	1.30E-02	1.29E-02	-2.40E-03	4.04E-03	3.63E-03
P17P17	9.0000	13062.368065	1.364E-27	0.02543	428.34229	1.32E-02	1.30E-02	-2.37E-03	4.10E-03	3.57E-03
P17Q16	8.3546	13064.231733	1.277E-27	0.02360	426.47862	1.32E-02	1.30E-02	-2.37E-03	3.97E-03	3.57E-03
P16P16	8.5000	13066.593254	1.621E-27	0.02557	380.99023	1.34E-02	1.32E-02	-2.33E-03	4.03E-03	3.51E-03
P16Q15	7.8546	13068.466175	1.511E-27	0.02362	379.11731	1.34E-02	1.32E-02	-2.33E-03	3.91E-03	3.51E-03
P15P15	8.0000	13070.728695	1.894E-27	0.02573	336.41400	1.36E-02	1.33E-02	-2.30E-03	3.96E-03	3.46E-03
P15Q14	7.3546	13072.611027	1.756E-27	0.02365	334.53167	1.36E-02	1.33E-02	-2.30E-03	3.85E-03	3.46E-03
P14P14	7.5000	13074.774454	2.174E-27	0.02591	294.61534	1.37E-02	1.35E-02	-2.26E-03	3.90E-03	3.40E-03
P14Q13	6.8546	13076.666392	2.005E-27	0.02368	292.72340	1.37E-02	1.35E-02	-2.26E-03	3.80E-03	3.40E-03
P13P13	7.0000	13078.730587	2.452E-27	0.02613	255.59588	1.39E-02	1.36E-02	-2.22E-03	3.84E-03	3.34E-03
P13Q12	6.3546	13080.632369	2.246E-27	0.02371	253.69410	1.39E-02	1.36E-02	-2.22E-03	3.75E-03	3.34E-03
P12P12	6.5000	13082.597136	2.715E-27	0.02637	219.35715	1.40E-02	1.38E-02	-2.18E-03	3.78E-03	3.29E-03
P12Q11	5.8546	13084.509064	2.467E-27	0.02375	217.44522	1.40E-02	1.38E-02	-2.18E-03	3.69E-03	3.29E-03
P11P11	6.0000	13086.374132	2.947E-27	0.02667	185.90056	1.42E-02	1.39E-02	-2.15E-03	3.72E-03	3.22E-03
P11Q10	5.3547	13088.296594	2.654E-27	0.02380	183.97810	1.42E-02	1.39E-02	-2.15E-03	3.64E-03	3.22E-03
P10P10	5.5000	13090.061596	3.135E-27	0.02702	155.22743	1.43E-02	1.41E-02	-2.11E-03	3.64E-03	3.16E-03
P10Q9	4.8547	13091.995098	2.792E-27	0.02385	153.29393	1.43E-02	1.41E-02	-2.11E-03	3.58E-03	3.16E-03
P9P9	5.0000	13093.659535	3.262E-27	0.02746	127.33895	1.45E-02	1.43E-02	-2.07E-03	3.57E-03	3.08E-03
P9Q8	4.3547	13095.604765	2.867E-27	0.02391	125.39372	1.45E-02	1.43E-02	-2.07E-03	3.51E-03	3.08E-03
P8P8	4.5000	13097.167946	3.316E-27	0.02802	102.23621	1.47E-02	1.45E-02	-2.02E-03	3.47E-03	3.00E-03
P8Q7	3.8548	13099.125864	2.866E-27	0.02399	100.27830	1.47E-02	1.45E-02	-2.02E-03	3.43E-03	3.00E-03
P7P7	4.0000	13100.586813	3.284E-27	0.02874	79.92020	1.50E-02	1.47E-02	-1.98E-03	3.37E-03	2.91E-03
P7Q6	3.3548	13102.558824	2.779E-27	0.02410	77.94819	1.50E-02	1.47E-02	-1.98E-03	3.34E-03	2.91E-03
P6P6	3.5000	13103.916109	3.158E-27	0.02972	60.39178	1.53E-02	1.50E-02	-1.94E-03	3.24E-03	2.80E-03
P6Q5	2.8549	13105.904385	2.600E-27	0.02424	58.40350	1.53E-02	1.50E-02	-1.94E-03	3.23E-03	2.80E-03
P5P5	3.0000	13107.155796	2.936E-27	0.03114	43.65172	1.57E-02	1.53E-02	-1.90E-03	3.08E-03	2.68E-03
P5Q4	2.3551	13109.163968	2.326E-27	0.02444	41.64354	1.57E-02	1.53E-02	-1.90E-03	3.10E-03	2.68E-03
P4P4	2.5000	13110.305822	2.617E-27	0.03337	29.70066	1.61E-02	1.57E-02	-1.85E-03	2.90E-03	2.53E-03
P4Q3	1.8555	13112.340671	1.961E-27	0.02477	27.66582	1.61E-02	1.57E-02	-1.85E-03	2.93E-03	2.53E-03
P3P3	2.0000	13113.366126	2.210E-27	0.03738	18.53917	1.67E-02	1.62E-02	-1.81E-03	2.67E-03	2.36E-03
P3Q2	1.3563	13115.442748	1.513E-27	0.02535	16.46255	1.67E-02	1.62E-02	-1.81E-03	2.74E-03	2.36E-03
P2P2	1.5000	13116.336633	1.725E-27	0.04673	10.16767	1.73E-02	1.67E-02	-1.77E-03	2.39E-03	2.15E-03

P2Q1	0.8597	13118.502056	9.990E-28	0.02678	8.00224	1.73E-02	1.67E-02	-1.77E-03	2.49E-03	2.15E-03
P1P1	1.0000	13119.217258	1.182E-27	0.09347	4.58648	1.82E-02	1.74E-02	-1.72E-03	2.03E-03	1.89E-03
R0Q1	0.6403	13126.504300	7.728E-28	0.01995	0.00000	1.73E-02	1.67E-02	-1.77E-03	4.38E-03	2.15E-03
R1R1	0.5000	13127.318812	5.902E-28	0.00935	4.58648	1.67E-02	1.62E-02	-1.81E-03	4.42E-03	2.36E-03
R1Q2	1.1437	13129.203464	1.362E-27	0.02138	2.70183	1.67E-02	1.62E-02	-1.81E-03	4.41E-03	2.36E-03
R2R2	1.0000	13129.838819	1.148E-27	0.01336	10.16767	1.61E-02	1.57E-02	-1.85E-03	4.46E-03	2.53E-03
R2Q3	1.6445	13131.765269	1.906E-27	0.02197	8.24122	1.61E-02	1.57E-02	-1.85E-03	4.45E-03	2.53E-03
R3R3	1.5000	13132.268342	1.654E-27	0.01559	18.53917	1.57E-02	1.53E-02	-1.90E-03	4.50E-03	2.68E-03
R3Q4	2.1449	13134.221497	2.386E-27	0.02229	16.58601	1.57E-02	1.53E-02	-1.90E-03	4.47E-03	2.68E-03
R4R4	2.0000	13134.607224	2.088E-27	0.01700	29.70066	1.53E-02	1.50E-02	-1.94E-03	4.53E-03	2.80E-03
R4Q5	2.6451	13136.580313	2.787E-27	0.02249	27.72757	1.53E-02	1.50E-02	-1.94E-03	4.49E-03	2.80E-03
R5R5	2.5000	13136.855296	2.438E-27	0.01799	43.65172	1.50E-02	1.47E-02	-1.98E-03	4.56E-03	2.91E-03
R5Q6	3.1452	13138.844696	3.096E-27	0.02263	41.66232	1.50E-02	1.47E-02	-1.98E-03	4.51E-03	2.91E-03
R6R6	3.0000	13139.012382	2.696E-27	0.01871	60.39178	1.47E-02	1.45E-02	-2.02E-03	4.58E-03	3.00E-03
R6Q7	3.6452	13141.015927	3.307E-27	0.02273	58.38823	1.47E-02	1.45E-02	-2.02E-03	4.52E-03	3.00E-03
R7R7	3.5000	13141.078288	2.860E-27	0.01926	79.92020	1.45E-02	1.43E-02	-2.07E-03	4.60E-03	3.08E-03
R7Q8	4.1453	13143.094581	3.419E-27	0.02281	77.90391	1.45E-02	1.43E-02	-2.07E-03	4.53E-03	3.08E-03
R8R8	4.0000	13143.052814	2.931E-27	0.01969	102.23621	1.43E-02	1.41E-02	-2.11E-03	4.62E-03	3.16E-03
R8Q9	4.6453	13145.080902	3.437E-27	0.02287	100.20813	1.43E-02	1.41E-02	-2.11E-03	4.54E-03	3.16E-03
R9R9	4.5000	13144.935744	2.918E-27	0.02004	127.33895	1.42E-02	1.39E-02	-2.15E-03	4.63E-03	3.22E-03
R9Q10	5.1453	13146.974947	3.369E-27	0.02292	125.29975	1.42E-02	1.39E-02	-2.15E-03	4.55E-03	3.22E-03
R10R10	5.0000	13146.726853	2.831E-27	0.02033	155.22743	1.40E-02	1.38E-02	-2.18E-03	4.64E-03	3.29E-03
R10Q11	5.6454	13148.776671	3.227E-27	0.02296	153.17761	1.40E-02	1.38E-02	-2.18E-03	4.56E-03	3.29E-03
R11R11	5.5000	13148.425903	2.682E-27	0.02058	185.90056	1.39E-02	1.36E-02	-2.22E-03	4.66E-03	3.34E-03
R11Q12	6.1454	13150.485957	3.026E-27	0.02300	183.84051	1.39E-02	1.36E-02	-2.22E-03	4.57E-03	3.34E-03
R12R12	6.0000	13150.032645	2.486E-27	0.02079	219.35715	1.37E-02	1.35E-02	-2.26E-03	4.67E-03	3.40E-03
R12Q13	6.6454	13152.102641	2.781E-27	0.02303	217.28715	1.37E-02	1.35E-02	-2.26E-03	4.58E-03	3.40E-03
R13R13	6.5000	13151.546817	2.258E-27	0.02097	255.59588	1.36E-02	1.33E-02	-2.30E-03	4.68E-03	3.46E-03
R13Q14	7.1454	13153.626524	2.507E-27	0.02305	253.51617	1.36E-02	1.33E-02	-2.30E-03	4.59E-03	3.46E-03
R14R14	7.0000	13152.968148	2.011E-27	0.02112	294.61534	1.34E-02	1.32E-02	-2.33E-03	4.69E-03	3.51E-03
R14Q15	7.6454	13155.057378	2.218E-27	0.02307	292.52611	1.34E-02	1.32E-02	-2.33E-03	4.59E-03	3.51E-03
R15R15	7.5000	13154.296352	1.758E-27	0.02126	336.41400	1.32E-02	1.30E-02	-2.37E-03	4.71E-03	3.57E-03
R15Q16	8.1454	13156.394954	1.929E-27	0.02309	334.31540	1.32E-02	1.30E-02	-2.37E-03	4.60E-03	3.57E-03
R16R16	8.0000	13155.531133	1.510E-27	0.02138	380.99023	1.30E-02	1.29E-02	-2.40E-03	4.72E-03	3.63E-03
R16Q17	8.6454	13157.638984	1.648E-27	0.02311	378.88238	1.30E-02	1.29E-02	-2.40E-03	4.61E-03	3.63E-03
R17R17	8.5000	13156.672184	1.274E-27	0.02149	428.34229	1.28E-02	1.27E-02	-2.44E-03	4.74E-03	3.70E-03
R17Q18	9.1454	13158.789179	1.385E-27	0.02312	426.22529	1.28E-02	1.27E-02	-2.44E-03	4.63E-03	3.70E-03
R18R18	9.0000	13157.719185	1.057E-27	0.02158	478.46832	1.26E-02	1.25E-02	-2.47E-03	4.76E-03	3.76E-03
R18Q19	9.6454	13159.845237	1.144E-27	0.02314	476.34226	1.26E-02	1.25E-02	-2.47E-03	4.64E-03	3.76E-03
R19R19	9.5000	13158.671805	8.625E-28	0.02167	531.36635	1.23E-02	1.23E-02	-2.50E-03	4.78E-03	3.84E-03
R19Q20	10.1454	13160.806841	9.306E-28	0.02315	529.23132	1.23E-02	1.23E-02	-2.50E-03	4.65E-03	3.84E-03
R20R20	10.0000	13159.529702	6.925E-28	0.02175	587.03433	1.21E-02	1.21E-02	-2.54E-03	4.81E-03	3.91E-03
R20Q21	10.6454	13161.673658	7.449E-28	0.02316	584.89037	1.21E-02	1.21E-02	-2.54E-03	4.67E-03	3.91E-03
R21R21	10.5000	13160.292519	5.473E-28	0.02182	645.47007	1.18E-02	1.19E-02	-2.57E-03	4.83E-03	3.99E-03
R21Q22	11.1454	13162.445343	5.870E-28	0.02317	643.31724	1.18E-02	1.19E-02	-2.57E-03	4.68E-03	3.99E-03

R22R22	11.0000	13160.959892	4.257E-28	0.02188	706.67127	1.15E-02	1.17E-02	-2.60E-03	4.86E-03	4.08E-03
R22Q23	11.6454	13163.121537	4.554E-28	0.02317	704.50963	1.15E-02	1.17E-02	-2.60E-03	4.70E-03	4.08E-03
R23R23	11.5000	13161.531442	3.261E-28	0.02194	770.63555	1.11E-02	1.15E-02	-2.63E-03	4.89E-03	4.16E-03
R23Q24	12.1454	13163.701868	3.480E-28	0.02318	768.46513	1.11E-02	1.15E-02	-2.63E-03	4.72E-03	4.16E-03
R24R24	12.0000	13162.006779	2.460E-28	0.02200	837.36040	1.08E-02	1.12E-02	-2.66E-03	4.91E-03	4.25E-03
R24Q25	12.6454	13164.185952	2.620E-28	0.02319	835.18123	1.08E-02	1.12E-02	-2.66E-03	4.74E-03	4.25E-03
R25R25	12.5000	13162.385503	1.828E-28	0.02205	906.84320	1.05E-02	1.10E-02	-2.69E-03	4.94E-03	4.34E-03
R25Q26	13.1454	13164.573392	1.942E-28	0.02319	904.65531	1.05E-02	1.10E-02	-2.69E-03	4.76E-03	4.34E-03
R26R26	13.0000	13162.667199	1.338E-28	0.02209	979.08123	1.01E-02	1.08E-02	-2.71E-03	4.97E-03	4.43E-03
R26Q27	13.6454	13164.863780	1.419E-28	0.02320	976.88465	1.01E-02	1.08E-02	-2.71E-03	4.77E-03	4.43E-03
R27R27	13.5000	13162.851444	9.646E-29	0.02213	1054.07165	9.83E-03	1.05E-02	-2.74E-03	5.00E-03	4.52E-03
R27Q28	14.1454	13165.056692	1.022E-28	0.02320	1051.86640	9.83E-03	1.05E-02	-2.74E-03	4.79E-03	4.52E-03
R28R28	14.0000	13162.937800	6.855E-29	0.02217	1131.81152	9.52E-03	1.03E-02	-2.77E-03	5.02E-03	4.61E-03
R28Q29	14.6454	13165.151696	7.249E-29	0.02320	1129.59762	9.52E-03	1.03E-02	-2.77E-03	4.81E-03	4.61E-03
R29R29	14.5000	13162.925820	4.800E-29	0.02221	1212.29779	9.23E-03	1.01E-02	-2.79E-03	5.05E-03	4.69E-03
R29Q30	15.1454	13165.148346	5.069E-29	0.02321	1210.07526	9.23E-03	1.01E-02	-2.79E-03	4.82E-03	4.69E-03
R30R30	15.0000	13162.815044	3.313E-29	0.02224	1295.52730	8.96E-03	9.89E-03	-2.82E-03	5.07E-03	4.77E-03
R30Q31	15.6454	13165.046185	3.494E-29	0.02321	1293.29615	8.96E-03	9.89E-03	-2.82E-03	4.84E-03	4.77E-03
R31R31	15.5000	13162.605000	2.254E-29	0.02227	1381.49677	8.70E-03	9.69E-03	-2.84E-03	5.09E-03	4.85E-03
R31Q32	16.1454	13164.844743	2.374E-29	0.02321	1379.25703	8.70E-03	9.69E-03	-2.84E-03	4.85E-03	4.85E-03
R32R32	16.0000	13162.295205	1.512E-29	0.02230	1470.20284	8.46E-03	9.50E-03	-2.87E-03	5.11E-03	4.92E-03
R32Q33	16.6454	13164.543538	1.590E-29	0.02321	1467.95451	8.46E-03	9.50E-03	-2.87E-03	4.87E-03	4.92E-03
R33R33	16.5000	13161.885164	9.993E-30	0.02233	1561.64201	8.24E-03	9.32E-03	-2.89E-03	5.13E-03	4.99E-03
R33Q34	17.1454	13164.142076	1.050E-29	0.02321	1559.38510	8.24E-03	9.32E-03	-2.89E-03	4.88E-03	4.99E-03
R34R34	17.0000	13161.374371	6.514E-30	0.02235	1655.81069	8.04E-03	9.15E-03	-2.91E-03	5.15E-03	5.05E-03
R34Q35	17.6454	13163.639853	6.837E-30	0.02321	1653.54521	8.04E-03	9.15E-03	-2.91E-03	4.89E-03	5.05E-03
R35R35	17.5000	13160.762306	4.186E-30	0.02237	1752.70517	7.86E-03	9.00E-03	-2.94E-03	5.16E-03	5.11E-03
R35Q36	18.1454	13163.036352	4.390E-30	0.02321	1750.43112	7.86E-03	9.00E-03	-2.94E-03	4.90E-03	5.11E-03
R36R36	18.0000	13160.048441	2.653E-30	0.02240	1852.32164	7.70E-03	8.85E-03	-2.96E-03	5.18E-03	5.17E-03
R36Q37	18.6454	13162.331043	2.779E-30	0.02321	1850.03903	7.70E-03	8.85E-03	-2.96E-03	4.91E-03	5.17E-03
R37R37	18.5000	13159.232232	1.658E-30	0.02241	1954.65617	7.55E-03	8.72E-03	-2.98E-03	5.19E-03	5.22E-03
R37Q38	19.1454	13161.523386	1.735E-30	0.02321	1952.36501	7.55E-03	8.72E-03	-2.98E-03	4.92E-03	5.22E-03
R38R38	19.0000	13158.313128	1.022E-30	0.02243	2059.70473	7.41E-03	8.59E-03	-3.00E-03	5.20E-03	5.27E-03
R38Q39	19.6454	13160.612828	1.069E-30	0.02321	2057.40503	7.41E-03	8.59E-03	-3.00E-03	4.92E-03	5.27E-03
R39R39	19.5000	13157.290562	6.211E-31	0.02245	2167.46318	7.29E-03	8.48E-03	-3.02E-03	5.21E-03	5.31E-03
R39Q40	20.1454	13159.598804	6.490E-31	0.02320	2165.15494	7.29E-03	8.48E-03	-3.02E-03	4.93E-03	5.31E-03
R40R40	20.0000	13156.163959	3.723E-31	0.02246	2277.92727	7.17E-03	8.38E-03	-3.04E-03	5.22E-03	5.35E-03
R40Q41	20.6454	13158.480739	3.888E-31	0.02320	2275.61049	7.17E-03	8.38E-03	-3.04E-03	4.94E-03	5.35E-03

CHAPTER 4

Cavity Ring-Down Spectroscopy Measurements of Sub-Doppler Hyperfine Structure

This chapter was published as

D. A. Long, D. K. Havey, M. Okumura, C. E. Miller, and J. T. Hodges, *Phys. Rev. A*, **81**, 064502 (2010).

Abstract

Frequency-stabilized cavity ring-down spectroscopy (FS-CRDS) was used to measure magnetic dipole transitions in the $b^1\Sigma_g^+ \leftarrow X\ ^3\Sigma_g^-(0,0)$ band of O_2. The ^{17}O-containing isotopologues show unresolved hyperfine structure due to magnetic hyperfine splitting in the ground state. The sensitivity and stability of FS-CRDS allow for quantitative sub-Doppler measurements of the hyperfine constants, even when the hyperfine splittings are much smaller than the Doppler width. Unlike saturation spectroscopy, this linear absorption technique can be applied to weak transitions and employed to quantitatively measure intensities and line shapes. This method may be an attractive approach for measuring unresolved hyperfine structure in excited electronic states.

4.1. Introduction

Recent advances in near-infrared spectroscopy have enabled measurements with frequency precision previously only possible in the microwave regime [1,2,3]. Unfortunately, large near-infrared Doppler widths often obscure any hyperfine structure. While saturation spectroscopy can resolve individual hyperfine components [2,4], it is by its very nature a nonlinear technique. As a result, saturation spectroscopy leads to distortion of the spectral line shape and cannot be employed to quantitatively measure line-shape parameters [5,6,7]. In addition, saturation spectroscopy is less general than traditional absorption spectroscopy and cannot easily be applied to the study of weak transitions, such as those described herein.

Here we describe an alternate approach to the measurement of hyperfine structure in the near-infrared region: the use of a linear and highly sensitive cavity ring-down spectrometer. In particular, the hyperfine splitting of the ^{17}O-containing isotopologues of O_2 were measured for magnetic dipole transitions in the $b^1\Sigma_g^+ \leftarrow X\,^3\Sigma_g^-(0,0)$ band. While individual hyperfine transitions are unresolved, the spectra exhibit a sufficiently large signal-to-noise ratio to enable quantitative measurements of hyperfine coupling constants. We note that despite the large number of recent studies which have measured spectroscopic parameters of the $b^1\Sigma_g^+ \leftarrow X\,^3\Sigma_g^-(0,0)$ band for $^{16}O_2$ and the rare isotopologues (see Refs. [1],[8] and the references contained therein), observation of hyperfine splitting has not previously been reported.

4.2. Experiment

Measurements were made using the frequency-stabilized cavity ring-down spectrometer (FS-CRDS) located at the National Institute of Standards and Technology (NIST) in Gaithersburg, MD. The FS-CRDS system has been described in detail previously [9,10], and therefore only the most important details are given. FS-CRDS differs from other single-mode cw-CRDS spectroscopies by actively stabilizing the intracavity length to an external frequency reference. This length stabilization in turn stabilizes the cavity's free spectral range (FSR). The probe laser frequency is then stepped between successive

TEM_{00} cavity modes, resulting in an accurate, stable, and linear frequency axis. FS-CRDS has been utilized to measure transition frequencies to better than 0.5 MHz [1] and line intensities to better than 0.3% [11]. Importantly, due to active frequency stabilization, FS-CRDS does not exhibit instrumental broadening and has therefore been able to record O_2 Doppler (Gaussian) widths to 143 kHz, which is 1 part in 6,000 of the room-temperature Doppler width (~850 MHz) for this band [12].

For the described measurements, the probe was an external-cavity diode laser with a tuning range of 759–771 nm, an output power of 6–10 mW, and a line width of <1 MHz (<3 $\times 10^{-5}$ cm^{-1}). The frequency reference was a frequency-stabilized HeNe laser with a frequency uncertainty of less than 1 MHz over 8 h. Mirrors with 99.98% reflectivity were used, corresponding to a finesse of ~15,000. The resulting short-term noise equivalent absorption coefficient was 6 $\times 10^{-10}$ cm^{-1} $Hz^{-1/2}$, and the cavity FSR was determined to be 201.970(10) MHz. A continuous spectrum was measured over the *R*-branch of the $b^1\Sigma_g^+ \leftarrow X\ ^3\Sigma_g^-(0,0)$ band (13,126–13,165 cm^{-1}) with a step size of 100 MHz (~0.003 cm^{-1}). Sub-FSR frequency steps were enabled by frequency shifting the HeNe reference laser through the use of an acousto-optic modulator in a double-pass configuration [9].

A ^{17}O-enriched O_2 sample containing 15.23% $^{16}O_2$, 38.16% $^{16}O^{17}O$, 8.28% $^{16}O^{18}O$, 25.93% $^{17}O_2$, 11.15% $^{17}O^{18}O$, and 1.25% $^{18}O_2$ was used. Measurements were performed at a pressure of 236 Pa (1.77 Torr) and a temperature of 299.5 K. The combined uncertainty (random and systematic) of this temperature measurement is ~28 mK [13]. Spectra were fit using Voigt line-shape profiles, which account for pressure (Lorentzian) and Doppler (Gaussian) broadening. The importance of using the Galatry [14] line profile for high-resolution measurements at higher pressures is well established [15,16]; however, due to the low pressures of this study, Dicke narrowing [17] is less than 1 MHz and was therefore neglected. During the fit, the transition position and intensity were floated while the pressure broadening coefficient was constrained to the $^{16}O_2$ known values [11]. We have recently shown that there is no difference between the pressure broadening parameters for the O_2 isotopologues to within the experimental

uncertainty of 2% [8]; therefore, at the low pressures utilized herein, the use of the $^{16}O_2$ coefficients for all isotopologues should introduce negligible error. Further experimental details will be given in a separate publication [18].

4.3. Results and Discussion

The $b^1\Sigma_g^+ \leftarrow X\,^3\Sigma_g^-(0,0)$ band is triply forbidden by quantum mechanical electric dipole selection rules but occurs as a magnetic dipole transition [19]. Due to this magnetic dipole character and the necessary change in multiplicity, the $b^1\Sigma_g^+ \leftarrow X\,^3\Sigma_g(0,0)$ band of $^{16}O_2$ is very weak with a band intensity of only $2.231(7) \times 10^{-22}$ cm molec.$^{-1}$ at 296 K [11]. The rotational levels of O_2 are described by three quantum numbers: N is the rotational angular momentum, S is the spin, and J is their sum (i.e., $J = N + S$). The O_2 ground state is a good Hund's case (b) and is split into three levels ($J'' = N'' - 1$, N'', $N'' + 1$), while the upper state has only $J'' = N''$. For $^{16}O_2$ and $^{18}O_2$, only odd levels of N'' are allowed due to spin statistics, while all values of N'' are allowed for the remaining isotopologues. We denote the $b^1\Sigma_g^+ \leftarrow X\,^3\Sigma_g^-(0,0)$ transitions by $\Delta N\,N''$, $\Delta J\,J''$ with the band divided into four branches (*PP*, *PQ*, *RR*, and *RQ*).

While ^{16}O and ^{18}O have a nuclear spin of $I = 0$, ^{17}O has $I = 5/2$, and therefore the ^{17}O-containing isotopologues exhibit hyperfine structure. In the $^3\Sigma_g^-$ ground state, this hyperfine splitting is almost entirely magnetic in nature due to the unpaired spins. Miller and Townes demonstrated that any higher order magnetic and nuclear electric quadrupole hyperfine couplings are negligible (i.e., <1 MHz) [20]. This ground-state hyperfine structure has been observed in microwave, millimeter, submillimeter, and electron paramagnetic resonance spectroscopy measurements of the $^{16}O^{17}O$ [20,21,22], $^{17}O_2$ [23], and $^{17}O^{18}O$ [22] isotopologues.

The upper state ($1^1\Sigma_g^+$) is a singlet state and therefore does not exhibit a permanent magnetic dipole. Thus, any magnetic hyperfine coupling is the result of a perturbation and will be extremely weak [24]. Additionally, it can be shown that the electronic structure of this state leads to a weak electric quadrupole coupling (on the order of a few megahertz) [24,25,26]. Thus, we assume that all observed hyperfine

structure is the result of hyperfine splitting within the $^3\Sigma_g^-$ ground state. This assumption will introduce at most an error of a few megahertz to the measured hyperfine coupling constants.

For $^{16}O^{17}O$ and $^{17}O^{18}O$, the hyperfine energies were calculated by Miller and Townes [24] based upon the formalism of Frosch and Foley [27]:

$$E_{J=N+1} = \frac{\mathbf{I}\cdot\mathbf{J}}{N+1}\left(b + \frac{c}{2N+3}\right), \tag{1}$$

$$E_{J=N} = \frac{\mathbf{I}\cdot\mathbf{J}}{N(N+1)}(b+c), \tag{2}$$

$$E_{J=N-1} = \frac{\mathbf{I}\cdot\mathbf{J}}{N}\left(-b + \frac{c}{2N-1}\right), \tag{3}$$

where

$$\mathbf{I}\cdot\mathbf{J} = \frac{F(F+1) - I(I+1) - J(J+1)}{2}, \tag{4}$$

and

$$\mathbf{F} = \mathbf{I} + \mathbf{J}. \tag{5}$$

The experimentally determined values of the hyperfine coupling constants are b = −101.441(5) MHz, c = 139.73(3) MHz for $^{16}O^{17}O$ and b = −101.46(1) MHz, c = 139.68(6) MHz for $^{17}O^{18}O$ [22]. For $^{16}O^{17}O$, the hyperfine coupling constants have been theoretically confirmed using both a simple Slater-type orbital formalism [28] and the multi-configuration self-consistent field method [29].

Our spectra do not show resolved hyperfine transitions; however, we do observe as much as 200 MHz (~1/4 the Doppler width) of line broadening in excess of the Doppler width. We ascribe this broadening to the hyperfine structure. We have previously measured the O_2 Doppler width to within 143 kHz [12]; as a result, the observed broadening cannot be attributed to instrumental broadening.

The R branch of the $b^1\Sigma_g^+ \leftarrow X\,^3\Sigma_g$ (0,0) band consists of RR and RQ transitions. The RR-branch transitions begin in ground-state levels which have $J'' = N''$; thus, their hyperfine splitting is described by Eq. 2. Note that b and c have opposite signs and (b + c) ~ 38 MHz. As a result, minimal hyperfine splitting would be expected for these

transitions, especially for large N''. As can be seen in Fig. 1(a), the *RR* transitions for each isotopologue exhibit minimal broadening, with observed Gaussian widths converging to the Doppler width for $N'' > 2$.

The *RQ* branch begins in ground-state levels having $J'' = N'' + 1$. In this case, b dominates the observed hyperfine splitting for $N'' > 4$. As a result, hyperfine splittings of hundreds of megahertz are expected, with splittings increasing to an asymptotic limit with increasing N''. In Fig. 1(b), it can readily be seen that the expected behavior is observed for each of the isotopologues.

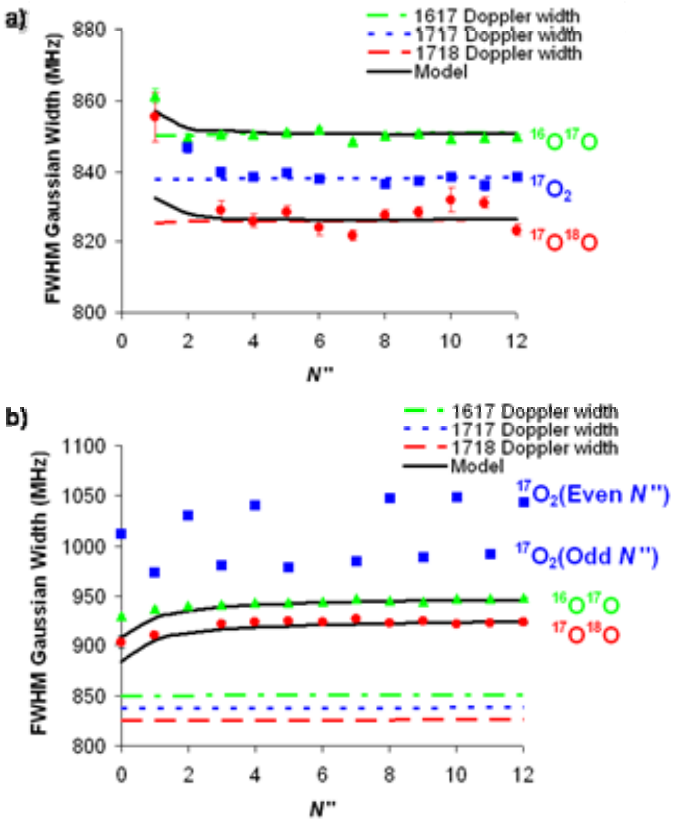

FIG. 1. Experimental Gaussian full width at half-maximum (FWHM) and theoretical Doppler widths (dashed horizontal lines) in megahertz for the ^{17}O-containing isotopologues with fit uncertainties. Each experimental Gaussian width was determined by a Levenberg-Marquardt least-squares fit using a single Voigt line shape with the pressure-broadening parameter constrained to the previously determined $^{16}O_2$ value [11]. Note that collisional narrowing is negligible (i.e., <1 MHz) at the pressure utilized in this study, although it can be very important at higher pressures [15,16]. Also shown are calculated (solid black lines) broadenings for $^{16}O^{17}O$ and $^{17}O^{18}O$ based on the model described in the text. (a) *RR*-branch transitions which exhibit minimal broadening (except for very low-N'' transitions). (b) *RQ*-branch transitions exhibit significant broadening due to the large hyperfine splitting (note the different y-axis scales between the two figures). The hyperfine splitting of the $^{17}O_2$ transitions exhibit a dependence on the parity of N'' due to symmetry constraints. For both branches, the model performs well for transitions with $N'' > 1$.

For $^{17}O_2$, the parity of N'' has a large impact upon the observed splitting. $^{17}O_2$ has two $I = 5/2$ nuclei and therefore has a total nuclear spin of $I_{total} = 5, 4, 3, 2, 1, 0$. The symmetry of $^{17}O_2$ dictates that odd values of N'' can only have even values of I_{total} and even values of N'' can only have odd values of I_{total} [23]. Thus, even values of N'' have

I_{total} = 5, 3, 1, and odd values of N'' have I_{total} =4, 2, 0. Since larger values of I_{total} give rise to larger splitting, we would expect even values of N'' to have a larger splitting [as can be seen in Fig. 1(b)].

The observed broadening can be analyzed with a simple intensity model to determine b and c. In the high-J case, only hyperfine transitions with $\Delta J = \Delta F$ are significant, and the intensities of these transitions are roughly proportional to $(2F + 1)$ [24]. This high-J limit was utilized to calculate the relative intensities of the hyperfine structure components for each of the measured transitions. The hyperfine structure positions were calculated as shown previously. The hyperfine spectrum could then be readily calculated.

It can readily be shown algebraically that for all $J = N \pm 1, 0$,

$$\sum_F (2F+1) E_J(F) = 0, \tag{6}$$

where each sum is over all allowed F quantum numbers (i.e., $F = I + J, I + J - 1, \ldots, |I - J|$) and E_J is defined as in Eqs. 1-3. Thus, the calculated hyperfine structure does not shift the spectral center of mass.

For $^{16}O^{17}O$ and $^{17}O^{18}O$, these calculated frequency splittings and intensities were then utilized to simulate the broadened line shape as a sum of six separate hyperfine profiles whose Gaussian widths were fixed to the theoretical Doppler width for the given isotopologue. As can be seen in Fig. 1, this model reproduces the observed broadening very well for $N'' > 3$. For $N'' \leq 3$, the assumptions made regarding the relative intensities of the hyperfine structure break down and more complicated expressions are required.

Figure 2 shows a measured spectrum which has been fit by a set of six Voigt line profiles (one for each hyperfine component). Each of these hyperfine profiles had its Gaussian width set equal to the theoretical Doppler width and the pressure-broadening parameter fixed to the value determined for $^{16}O_2$ [11]. Thus, the only two fitted parameters were the position of the spectral center of mass and the total integrated area (i.e., all relative hyperfine coupling constants were held fixed). As can be seen in Fig. 2, this model captures the observed behavior to within the baseline noise level.

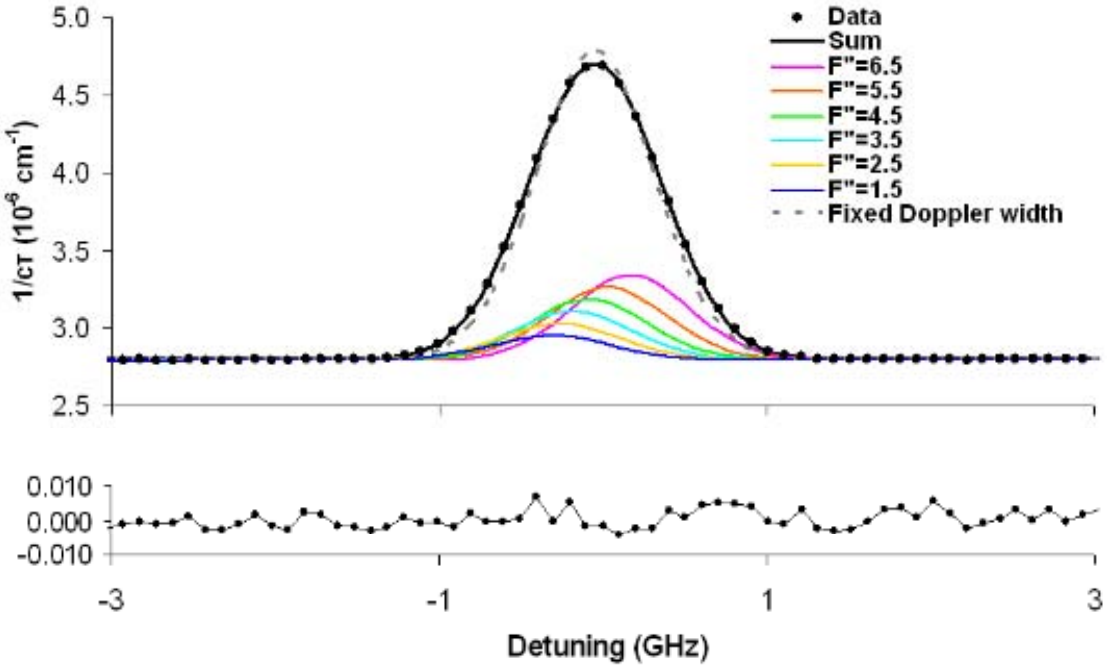

FIG. 2. Upper panel: Measured absorption given by $(c\tau)^{-1}$ where c is the speed of light and τ is the measured ring-down decay time (symbols) and fitted spectrum (solid black line) for the $R3Q4$ $^{16}O^{17}O$ transition, at 236 Pa (1.77 Torr) and 299.5 K. The sum of six Voigt profiles corresponding to the hyperfine structure were fit to the measurements (solid black line) using a Levenberg-Marquardt least-squares fitting algorithm. Each of these Voigt profiles [shown in solid colored (gray) lines with larger values of F'' corresponding to higher intensity hyperfine components] had its relative position and intensity fixed to values calculated using the model described in the text. Each Voigt profile's Gaussian width was constrained to the theoretical Doppler width, and the pressure-broadening parameter was set equal to the measured $^{16}O_2$ value [11]. Thus, only the position of the spectral center of mass and the total integrated area of the composite spectrum were floated. Also shown is a single Voigt profile whose Doppler width was constrained to the theoretical $^{16}O^{17}O$ value (dashed gray line). Lower panel: Fit residual for the sum of hyperfine structure. Based on the peak height and the root-mean-square fit residual, the signal-to-noise ratio of this spectrum is ~825:1.

We were able to determine the b and c hyperfine coupling constants by least-squares fits of the model to our measured spectra. For a fixed value of N'', it is not possible to determine both b and c in this fashion because these two quantities appear as differences in Eqs. 1 and 2, and as a consequence they are completely correlated for a given transition. However, b and c can be determined by a global multispectrum fit of spectra spanning a range of N''. Thus, the hyperfine model presented here was simultaneously fit to five measured spectra with b and c treated as global parameters.

These data correspond to the *R*3*Q*4, *R*4*Q*5, *R*5*Q*6, *R*8*Q*9, and *R*13*Q*14 transitions of $^{16}O^{17}O$. Assuming the individual hyperfine transitions were Voigt profiles having the theoretical Doppler width and *J*-dependent broadening coefficients given in [11], we obtained $b = -100.93(30)$ MHz and $c = 129.8(40)$, which differ from the more accurate microwave measurements of Cazzoli et al. [22] by approximately 0.5 and 10 MHz, respectively. With *c* constrained to the value determined by Cazzoli et al. (139.73 MHz), the multispectrum least-squares fit yielded $b = -101.64(10)$ MHz. This value of *b* is in good agreement (difference < 200 kHz) with that reported by Cazzoli et al. [22]. We attribute this small difference to the finite signal-to-noise ratio of the measured absorption and to variations in the frequency of our reference laser to which the ring-down cavity was locked.

4.4. Conclusions

We emphasize that the hyperfine coupling constants derived from the measured splittings are directly related to important (and often difficult to calculate [29]) electronic structure properties such as the electronic density at the nucleus with nonzero nuclear spin, $|\psi(0)|^2$, and $\left\langle r^{-3} \right\rangle$ [30]. In the $b^1\Sigma_g^+ \leftarrow X^3\Sigma_g(0,0)$ band, the hyperfine structure occurs due to the ground state; however, FS-CRDS can similarly measure hyperfine structure which is dominated by the upper state. As a result, the described technique may provide a new approach to the measurement of hyperfine coupling constants of electronic excited states, measurements which can be difficult by traditional pure rotational spectroscopy.

Acknowledgements

D. A. Long was supported by the National Science Foundation and Department of Defense. D. K. Havey acknowledges the support of the National Research Council as a postdoctoral fellow at NIST, Gaithersburg, MD. Part of the research described in this report was performed at the Jet Propulsion Laboratory, California Institute of Technology, under contract with the National Aeronautics and Space Administration (NASA). Additional support was provided by the Orbiting Carbon Observatory (OCO)

project, a NASA Earth System Science Pathfinder (ESSP) mission, and the NASA Upper Atmospheric Research Program Grants NNG06GD88G and NNX09AE21G.

References

[1] D. J. Robichaud, J. T. Hodges, P. Maslowski, L. Y. Yeung, M. Okumura, C. E. Miller, L. R. Brown, J. Mol. Spectrosc. **251,** 27-37 (2008).

[2] L. S. Chen, J. Ye, Chem. Phys. Lett. **381,** 777-783 (2003).

[3] S. Falke, E. Tiemann, C. Lisdat, H. Schnatz, G. Grosche, Phys. Rev. A **74,** 032503 (2006).

[4] G. Giusfredi, S. Bartalini, S. Borri, P. Cancio, I. Galli, D. Mazzotti, P. De Natale, Phys. Rev. Lett. **104,** 110801 (2010).

[5] D. Lisak, J. T. Hodges, Appl. Phys. B **88,** 317-325 (2007).

[6] J. Y. Lee, J. W. Hahn, Appl. Phys. B **79,** 653-662 (2004).

[7] S. S. Brown, H. Stark, A. R. Ravishankara, Appl. Phys. B **75,** 173-182 (2002).

[8] D. J. Robichaud, L. Y. Yeung, D. A. Long, M. Okumura, D. K. Havey, J. T. Hodges, C. E. Miller, L. R. Brown, J. Phys. Chem. A **113,** 13089-13099 (2009).

[9] J. T. Hodges, H. P. Layer, W. W. Miller, G. E. Scace, Rev. Sci. Instrum. **75,** 849-863 (2004).

[10] J. T. Hodges, R. Ciurylo, Rev. Sci. Instrum. **76,** 023112 (2005).

[11] D. A. Long, D. K. Havey, M. Okumura, C. E. Miller, J. T. Hodges, J. Quant. Spectrosc. Radiat. Transfer **111,** 2021-2036 (2010).

[12] D. A. Long, D. K. Havey, M. Okumura, H. M. Pickett, C. E. Miller, J. T. Hodges, Phys. Rev. A **80,** 042513 (2009).

[13] D. K. Havey, D. A. Long, M. Okumura, C. E. Miller, J. T. Hodges, Chem. Phys. Lett. **483,** 49-54 (2009).

[14] L. Galatry, Phys. Rev. **122,** 1218-1223 (1961).

[15] K. J. Ritter, T. D. Wilkerson, J. Mol. Spectrosc. **121,** 1-19 (1987).

[16] L. R. Brown, C. Plymate, J. Mol. Spectrosc. **199,** 166-179 (2000).

[17] R. H. Dicke, Phys. Rev. **89,** 472-473 (1953).

[18] D. A. Long, D. K. Havey, S. S. Yu, M. Okumura, C. E. Miller, J. T. Hodges, J. Quant. Spectrosc. Radiat. Transfer**,** Submitted. (2011).

[19] H. D. Babcock, L. Herzberg, Astrophys. J. **108,** 167-190 (1948).

[20] S. L. Miller, C. H. Townes, Phys. Rev. **90,** 537-541 (1953).

[21] P. Gerber, Helv. Phys. Acta **45,** 655-682 (1972).

[22] G. Cazzoli, C. D. Esposti, P. G. Favero, G. Severi, Nouvo Cimento B **62,** 243-254 (1981).

[23] G. Cazzoli, C. D. Esposti, B. M. Landsberg, Nuovo Cimento D **3,** 341-360 (1984).

[24] C. H. Townes, A. K. Schawlow, *Microwave Spectroscopy* (Dover Publications, New York, 1975).

[25] C. H. Townes, Phys. Rev. **71,** 909-910 (1947).

[26] C. H. Townes, B. P. Dailey, J. Chem. Phys. **17,** 782-796 (1949).

[27] R. A. Frosch, H. M. Foley, Phys. Rev. **88,** 1337-1349 (1952).

[28] M. Kotani, Y. Mizuno, K. Kayama, E. Ishiguro, J. Phys. Soc. Jpn. **12,** 707-736 (1957).

[29] B. F. Minaev, Spectroc. Acta A **60,** 1027-1041 (2004).

[30] S. L. Miller, C. H. Townes, M. Kotani, Phys. Rev. **90,** 542-543 (1953).

CHAPTER 5

Laboratory Measurements and Theoretical Calculations of O_2 *A*-band Electric Quadrupole Transitions

This chapter was published as

D. A. Long, D. K. Havey, M. Okumura, H. M. Pickett, C. E. Miller, and J. T. Hodges, *Phys. Rev. A*, **80**, 042513 (2009).

Abstract

Frequency-stabilized cavity ring-down spectroscopy was utilized to measure electric quadrupole transitions within the $^{16}O_2$ *A*-band, $b\ ^1\Sigma_g^+ \leftarrow X\ ^3\Sigma_g^-$ (0,0). We report quantitative measurements (relative uncertainties in intensity measurements from 4.4% to 11%) of nine ultraweak transitions in the ^NO, ^PO, ^RS, and ^TS branches with line intensities ranging from 3×10^{-30} to 2×10^{-29} cm molec.$^{-1}$. A thorough discussion of relevant noise sources and uncertainties in this experiment and other cw-cavity ring-down spectrometers is given. For short-term averaging (t < 100 s), we estimate a noise-equivalent absorption of 2.5×10^{-10} cm^{-1} Hz$^{-1/2}$. The detection limit was reduced further by co-adding up to 100 spectra to yield a minimum detectable absorption coefficient equal to 1.8×10^{-11} cm^{-1}, corresponding to a line intensity of ~2.5×10^{-31} cm molec.$^{-1}$. We discuss calculations of electric quadrupole line positions based on a simultaneous fit of the ground and upper electronic state energies which have uncertainties <3 MHz, and we present calculations of electric quadrupole matrix elements and line intensities. The electric quadrupole line intensity calculations and measurements agreed on average to 5%, which is comparable to our average experimental uncertainty. The calculated electric quadrupole band intensity was $1.8(1)\times10^{-27}$ cm molec.$^{-1}$ which is equal to only ~8×10^{-6} of the magnetic dipole band intensity.

Note that Dr. Joseph Hodges of NIST assisted greatly in the preparation of this chapter. His contributions were especially significant in sections 3.3. Also Dr. Herb Pickett performed the line intensity calculations and provided some textual description.

5.1. Introduction

In 1961, Noxon observed the first electric quadrupole transitions of molecular oxygen in the (subsequently named) Noxon band $a\ ^1\Delta_g \leftarrow b\ ^1\Sigma_g^+$ [1]. In 1981, electric quadrupole transitions within the electronic ground state of O_2 were identified by Goldman et al. [2] in the solar spectra of Niple et al. [3] and observed in the laboratory spectra of Reid et al. [4]. Quadrupole transitions within the O_2 *A*-band, $b\ ^1\Sigma_g^+ \leftarrow X\ ^3\Sigma_g^-$ (0,0), were observed in the solar spectra of Brault [5]. Brault was able to produce line positions and intensities for eight transitions (N'' = 5 to 19) within the ^TS branch of the $^{16}O_2$ *A*-band. See Background for notation. The only laboratory observation of an electric quadrupole line within the O_2 *A*-band was performed by Naus et al. who measured the $^TS(9)$ line with a signal-to-noise ratio (SNR) of ~2:1 using pulsed cavity ring-down spectroscopy (CRDS) [6].

The O_2 *A*-band is of special significance due to its extensive use over the past 50 years in remote sensing of the Earth's atmosphere. Measurements of this band have the potential to yield surface pressures to 0.1% [7] and enable accurate CO_2 remote sensing (~0.3%) by constraining surface pressure and photon path length in these retrievals. Use of the O_2 *A*-band has been expanded in recent years to ground-based observations of solar spectra such as those of the TCCON network [8]. Also, solar absorption by this band is used in satellite sensing of atmospheric gases by the GOME [9], SCIAMACHY [10,11], GOSAT [12] missions and was to be used in the OCO [13,14,15] mission.

Although the electric quadrupole transitions of the *A*-band are 10^5 times weaker than the corresponding magnetic dipole transitions, they can be observed in atmospheric spectra [5,16] reaching 1% absorbance at high solar zenith angles. Failure to include electric quadrupole absorptions in O_2 *A*-band remote sensing retrievals will lead to systematic errors in the assessment of photon path lengths, cloud or aerosol optical depths, and atmospheric pressure at the scattering height [7]. The situation is compounded since many of the electric quadrupole transitions occur underneath the much stronger magnetic dipole transitions. For these same reasons, the failure to include electric quadrupole transitions in fits of the line shape and line mixing parameterizations

of the magnetic dipole transitions may result in systematic errors in the representation of the magnetic dipole features.

We present quantitative laboratory-based CRDS measurements which constitute observations of ultraweak (line intensities ranging from 3×10^{-30} to 2×10^{-29} cm molec.$^{-1}$) electric quadrupole transitions in the ${}^{N}O$, ${}^{P}O$, ${}^{R}S$, and ${}^{T}S$ branches of the O_2 *A*-band. We note that Brault [5] measured isolated ${}^{T}S$ lines which lie above the *R*-branch bandhead. Figure 1 shows the calculated positions and intensities of the four electric quadrupole (and magnetic dipole) branches, where the electric quadrupole intensities were calculated as described in Section 4.3. The ${}^{T}S$ lines are relatively easy to observe in comparison with detection of ${}^{N}O$, ${}^{P}O$, and ${}^{R}S$ lines that are nearly degenerate with the magnetic dipole transitions—as are reported in the present study. We also discuss pertinent short- and long-time noise sources in this, and other, cw-CRDS experiments. Line intensities are assigned and combined (absolute) uncertainties in line intensity are estimated by evaluating random and systematic measurement uncertainties. Finally, we present theoretical calculations of line intensities and positions and compare these predictions to our experimental results.

5.2. Background

The O_2 *A*-band, with a band origin at wave number $\tilde{\nu}$ = 13,122 cm^{-1} (λ = 762 nm), is the strongest near-infrared absorption feature in the Earth's atmosphere. Although the transition is triply forbidden by quantum mechanical electric dipole selection rules (*gerade-gerade*, singlet-triplet, and Σ^{+}-Σ^{-}), magnetic dipole and electric quadrupole transitions are allowed [17,18]. The magnetic dipole transitions are 10^7 times weaker than a typical electric dipole transition and the electric quadrupole transitions are a further 10^5 times weaker (see Section 4.3) than the magnetic dipole transitions.

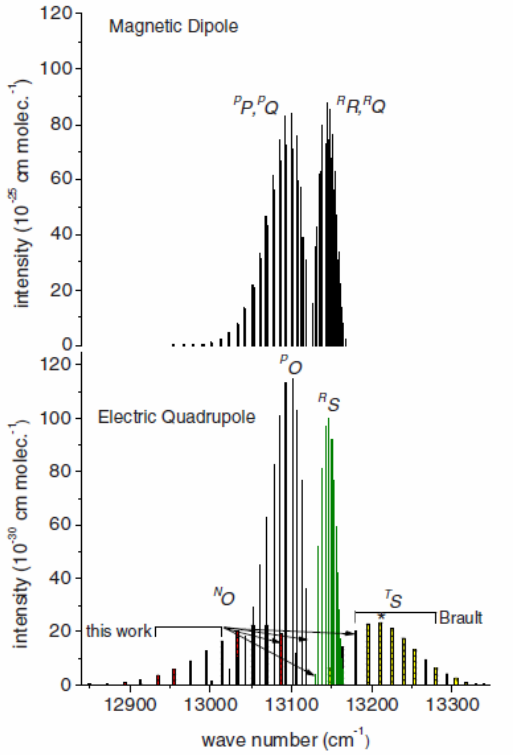

FIG. 1. Stick spectra of magnetic dipole (upper panel) and electric quadrupole (lower panel) $^{16}O_2$ *A* band line intensities at *T*=296 K. Positions for the electric quadrupole lines are given in Table 2. Transitions from the present study and those of Brault [5] as indicated. The symbol * indicates the transition observed by Naus et al. [6]. Note the difference in scales of the vertical axes.

The rotational energy levels of molecular oxygen are described by three quantum numbers: *N*, the rotational angular momentum, *S*, the spin angular momentum, and *J*, the total angular momentum ($J = N+S$). We therefore, describe the *A*-band transitions by $^{\Delta N}\Delta J(N'')$, where the double prime indicates the lower state. An energy level diagram for the O_2 *A*-band is shown in Figure 2, illustrating that there are three *J* levels for every *N* in the triplet ground state. For even values of *N* (in the case of $^{16}O_2$ and $^{18}O_2$) the spin-statistical weight is 0 and hence only odd *N* are allowed. The ^{P}P, ^{P}Q, ^{R}R, and ^{R}Q branches, corresponding to $|\Delta J| = 0,1$ are both magnetic dipole and electric quadrupole allowed. Given the weakness of the electric quadrupole transition moments, we do not expect them to contribute significantly to line intensities in the $|\Delta J| = 0,1$ branches. The $|\Delta J| = 2$ electric quadrupole transitions correspond to four branches: ^{N}O, ^{P}O, ^{R}S, and ^{T}S. The ^{T}S and ^{N}O branches have $|\Delta N| = 3$, whereas the ^{P}O and ^{R}S branches have $|\Delta N| = 1$. As

can be seen in Figure 1, these two $|\Delta N| = 1$ branches are heavily masked by the *P*- and *R*-branches of the magnetic dipole transitions, respectively, with line positions differing, on average, by only 0.2 to 0.3 cm^{-1}. Only the $N'' = 1$ transition for each of these two branches is isolated from its sister magnetic dipole transition and can therefore be feasibly measured in this laboratory experiment.

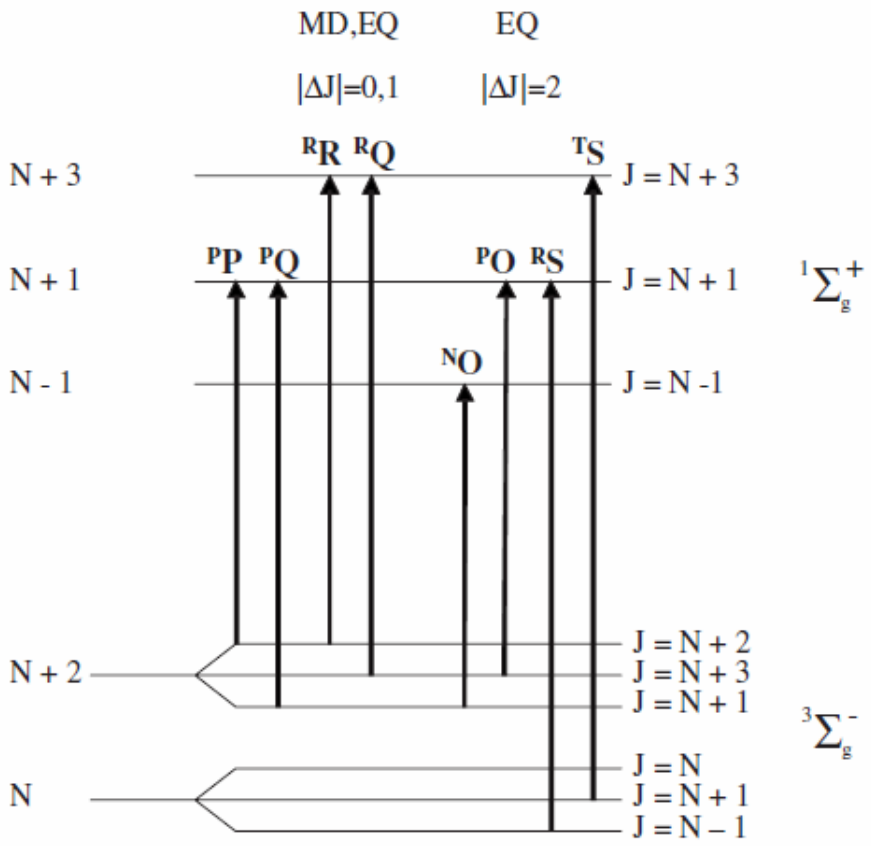

FIG. 2. Energy level diagram of molecular oxygen (only for $^{16}O_2$ and $^{18}O_2$) for the $X\,^3\Sigma_g^-$ ground state and the $b\,^1\Sigma_g^+$ excited state. The $|\Delta J|$=0,1 branches (^PP, ^PQ, ^RR, ^RQ) are shown on the left for ground state rotational angular momentum, *N* (odd), and total angular momentum, *J*. These branches are both magnetic dipole (MD) and electric quadrupole (EQ) symmetry allowed. Similarly, on the right four symmetry-allowed electric quadrupole transition branches measured in this work are shown (^PO, ^NO, ^RS, ^TS).

5.2.1. Line Positions Calculations

The positions of the electric quadrupole transitions were calculated based on a simultaneous fit of the ground $X\ ^3\Sigma_g^-$ and upper $b\ ^1\Sigma_g^+$ states using SPFIT [19]. Microwave [20,21,22,23], far-infrared [24], and Raman [25,26,27,28] positions for the $v = 0$ and $v = 1$ levels of the ground state were taken from the literature and used with their reported uncertainties. The *A*-band positions reported by Robichaud et al. [29] yielded parameters for the upper state and also improved the distortion constants for the ground state compared to fits using only the ground state transitions. The final fit included 327 transitions and yielded a reduced root-mean-square (rms) uncertainty of 0.843, indicating that the relative weighting of the experimental data was slightly conservative. Note that we switched assignments for the (N' ,J'←N'' ,J'') = (11,11←13,13) and (11,10←13,12) transitions at $\tilde{\nu}$ = 1,482.4971 cm^{-1} and 1,482.4739 cm^{-1}, respectively, compared to the assignments reported by Brodersen and Bendtsen [27]. This resulted in a 62% reduction in the reduced rms of the total ground-state-only fit. Our fitted parameters for both lower and upper states as well as those of Rouillé et al. [25] (lower state) and Robichaud et al. [29] (upper state) are given in Table 1, and our predicted electric quadrupole positions are given in Table 2. Uncertainties in our predicted positions of the electric quadrupole transitions are predicted to be less than 3 MHz (10^{-4} cm^{-1}) since these transitions are based on the same energy levels as the magnetic dipole transitions (Figure 2) [29].

However, when we compare our calculated positions to the calculations of Naus et al. [6], we find that their positions are systematically ~300 MHz (0.01 cm^{-1}) lower than ours for both the magnetic dipole and electric quadrupole transitions. We believe that pressure shifting is the root of this discrepancy. Our line positions were calculated based upon laboratory measurements which have been corrected for pressure shifting, while no such correction was applied to the solar observations of Brault [5] and Babcock et al. [17] which formed the basis for the Naus et al. calculations. Brown and co-workers [30] have previously noted a similar discrepancy between the magnetic dipole line positions of several high-resolution laboratory studies [30,31,32] and those of Babcock et al. The direction and magnitude of the observed shift is consistent with the reported pressure

shifting of Robichaud et al. [33] (approximately −0.002 MHz Pa^{-1} or −0.007 cm^{-1} atm^{-1}) for the *P*-branch of the *A*-band magnetic dipole transitions. Thus, we believe that the calculations of Naus et al. [6] would agree with ours if the former were corrected for atmospheric pressure shifting. Additionally, the value reported by Naus et al. for the $^{R}S(1)$ line position is approximately 1 cm^{-1} low compared to both our reported value and our recalculation of this position using their specified spectroscopic constants.

TABLE 1. Spectroscopic constants (cm^{-1}) of the $X\,^3\Sigma_g^-$ and $b^1\Sigma_g+$ states of $^{16}O_2$. Lower state energy levels are defined in Ref. [25] and those of the upper state are given by $\nu_0+B_0J(J+1)-D_0J^2(J+1)^2+H_0J^3(J+1)^3$. Numbers in parentheses represent 1σ uncertainty in units of the least significant digit.

$X^3\Sigma_g^-$ state	This work	Rouillé et al.
B_0	1.437676078(29)	1.437676476(77)
D_0	$4.84178(14)\times10^{-6}$	$4.84256(63)\times10^{-6}$
H_0	$4.28(19)\times10^{-12}$	$2.80(16)\times10^{-12}$
λ_0	1.98475118(5)	1.984751322(72)
λ_0'	$1.9470(3)\times10^{-6}$	$1.94521(50)\times10^{-6}$
λ_0''	$9.70(3)\times10^{-12}$	$1.103(41)\times10^{-11}$
μ_0	–8.4253696(58)×10-3	$-8.425390(13)\times10^{-3}$
μ_0'	$-8.136(22)\times10^{-9}$	$-8.106(32)\times10^{-9}$
μ_0''	$-4.04(15)\times10^{-14}$	$-4.70(19)\times10^{-14}$

$b^1\Sigma_g^+$ state	This work	Rouillé et al.
ν_0	13122.0057456(89)	13122.00575(1)
B_0	1.39124922(11)	1.3912496(1)
D_0	$5.36909(28)\times10^{-6}$	$5.3699(3)\times10^{-6}$
H_0	$1.65(33)\times10^{-14}$	$-1.80(2)\times10^{-12}$

As described below, having accurate knowledge of the line positions (i.e., those given in Table 2) facilitated our efforts to unambiguously locate the electric quadrupole lines. This information, combined with accurate measurements of probe laser frequency, made it sufficient to interrogate the absorption spectrum over narrow spectral ranges centered on each expected line position.

TABLE 2. Calculated vacuum wave numbers (cm^{-1}) for the electric quadrupole transitions within the ${}^{N}O$, ${}^{P}O$, ${}^{R}S$, and ${}^{T}S$ branches of the $^{16}O_2$ A band using our lower and upper state rotational parameters given in Table 1. Transitions probed in this study are underlined. We use the designation ${}^{\Delta N}\Delta J(N'')$, such that ${}^{N}O(13)$ indicates the [(N' = 10)←(N'' = 13) , (J' = 12)←(J'' =14)] transition.

N''	${}^{N}O$	${}^{P}O$	${}^{R}S$	${}^{T}S$
1		13119.92145	13130.35305	13147.74429
3	13105.75288	13113.96544	13133.57572	13164.04113
5	13088.15293	13107.60461	13138.22862	13179.92388
7	13070.22159	13100.86413	13142.54086	13195.41358
9	13051.93672	13093.75012	13146.48617	13210.51223
11	13033.29479	13086.26481	13150.05690	13225.21793
13	13014.29577	13078.40910	13153.24888	13239.52744
15	12994.94055	13070.18320	13156.05889	13253.43688
17	12975.23027	13061.58694	13158.48395	13266.94194
19	12955.16606	13052.61982	13160.52106	13280.03801
21	12934.74895	13043.28109	13162.16713	13292.72019
23	12913.97982	13033.56974	13163.41892	13304.98336
25	12892.85936	13023.48451	13164.27298	13316.82215
27	12871.38808	13013.02394	13164.72571	13328.23096
29	12849.56627	13002.18633	13164.77328	13339.20396

5.3. Experiment

All measurements were made at the National Institute of Standards and Technology (NIST), in Gaithersburg, Maryland using the frequency-stabilized cavity ring-down spectroscopy (FS-CRDS) technique. This technique, which enables precise and accurate measurements of both the absorption coefficient and spectrum frequency axis, has been described previously [34,35]. See Figure 3(a) for a schematic of the setup. The

fundamental distinction between FS-CRDS and traditional cw-CRDS is that the cavity length is actively locked through the use of a co-resonant reference laser beam. In addition, the probe beam frequency is selectively locked to longitudinal modes of the TEM_{00} cavity mode.

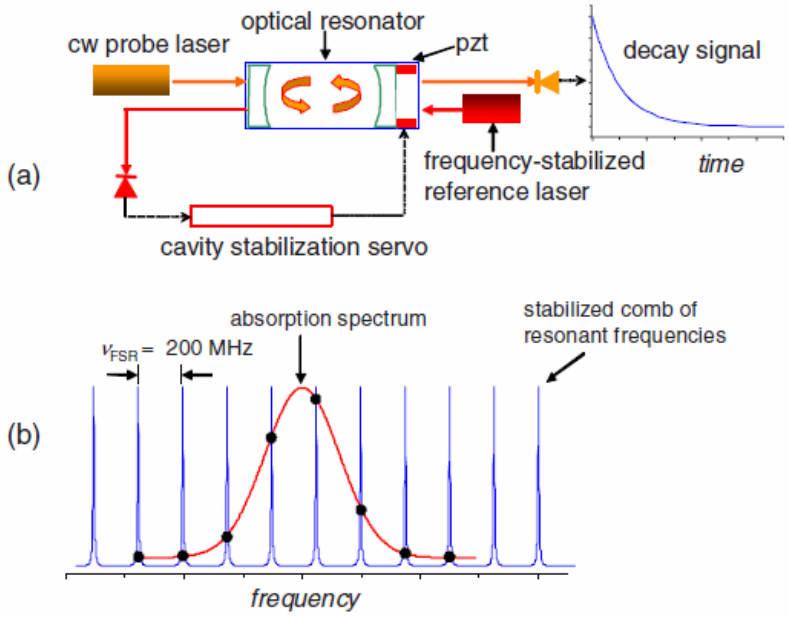

FIG. 3. Experimental configuration. (a) Principal components of the frequency-stabilized cavity ring-down spectrometer, including probe and reference lasers, ring-down cavity, and length-stabilization servo. (b) Spectral acquisition scheme illustrating how the probe laser is scanned over successive longitudinal modes of the resonant cavity. The equally spaced modes are separated by ~200 MHz and form a frequency axis whose long-term precision is limited by the stability of the reference laser. With this approach, the absorption spectrum is discretely sampled at fixed intervals as indicated by the solid circles.

5.3.1. Experimental Apparatus

The reference laser was a frequency-stabilized HeNe laser (λ = 633 nm) with a long-term (8 h time interval) frequency variation less than 2 MHz and output power of 1 mW. The probe beam was from a continuous-wave external-cavity diode laser (ECDL) with a Litmann-Metcalf resonator configuration. A Faraday isolator (−40 dB of isolation) was mounted directly on the probe laser housing. The ECDL output was single-mode and had a typical output power of 6–10 mW over the wavelength range λ = 759–771 nm. We used

custom-made, dichroic ring-down cavity mirrors with nominal transmission losses of 3×10^{-5} and 0.05 at λ = 765 nm and 633 nm, respectively. Losses at the probe wavelength corresponded to a cavity finesse, F~105,000, and the cavity length was 74 cm, yielding an effective optical path length of ~25 km. The mirror losses were ~7 times smaller compared to those of our previous FS-CRDS O_2 *A*-band studies [29,36]. However, the short-term detection limit (discussed below) was only ~4 times lower than previously demonstrated because of reduced signal intensity of the decay signals.

The internal volume of the ring-down cavity was ~0.2 L, and all internal surfaces (except for Cu gaskets used in vacuum-compatible knife-edge seals) were made of electro-polished stainless steel. We performed all experiments at room temperature and made no effort to control the temperature of the ring-down cell. The sample temperature, T, was measured using a NIST-calibrated 2.4 kΩ thermistor mounted in good thermal contact with an external wall of the ring-down cavity. Uncertainty in the measured sample temperature was limited by temperature gradients within the cavity and was estimated to be less than 0.2 K. Cell wall temperature varied by at most 0.2 K during the course of a day, and the average temperature for all spectra was 295.25±0.3 K. All measurements were made on O_2 with >99.9% purity and natural isotopic abundance. We measured gas pressure, p, using two NIST-calibrated capacitance diaphragm gauges with full-scale responses of 13.3 and 133 kPa, respectively. We estimated the relative combined standard uncertainty in the pressure measurement to be less than 0.2% of the reading over the entire pressure range.

Spectra were acquired by locking the probe laser frequency to successive longitudinal modes of the frequency-stabilized ring-down cavity as shown in Figure 3(b). As was previously demonstrated [29,33], this approach provides an exceptionally linear spectrum frequency axis with a step size given by ν_{FSR}, where FSR is the cavity free-spectral range. The spectral resolution was limited by the stability of the HeNe reference laser. To measure absolute frequencies and the cavity FSR, we used a commercial Michelson-interferometer wave meter having a precision of 30 MHz ($\Delta\tilde{\nu}$ = 0.001 cm^{-1}). We determined the mean cavity FSR to be 202.569(15) MHz by measuring the frequency

steps of nearly 1000 spectra, each spanning a range of 10 GHz. The 15 kHz uncertainty in FSR is due to variations in the effective path length of the ring-down cavity caused by concomitant changes in the sample index of refraction as the pressure was varied between 2.5 and 30 kPa. The wave meter was calibrated against the measured position of the $^{P}P(11)$ $^{16}O^{18}O$ A-band magnetic dipole transition. This line is within 0.15 cm^{-1} of the $^{N}O(5)$ electric quadrupole line, and its position was recently determined with an uncertainty of 4×10^{-5} cm^{-1} through the FS-CRDS method [37] by using hyperfine components of the D_1 and D_2 lines of ^{39}K as an absolute frequency reference [29].

We used a variable-frequency (200 MHz ± 10 MHz) acousto-optic modulator (AOM) to provide a first-order diffracted beam that was mode-matched into the ring-down cavity. A Si-PIN photoreceiver (bandwidth of 700 kHz and responsivity of 0.3 V W^{-1}) located at the cavity output measured probe beam transmission. Ring-down decay events were initiated by transmission bursts having amplitudes exceeding an adjustable threshold. These bursts triggered TTL pulses from a digital delay generator, switching off the AOM power (decay time <50 ns) and shifting the AOM frequency by 10 MHz. The resulting ring-down signals were digitized by a 12-bit analog-to-digital board at a rate of 25 M samples/s and had maximum decay times of 80 μs. The decays were acquired at a nominal acquisition rate, f_{acq} = 10 Hz. To obtain the decay time constant, τ, we fitted an exponential decay plus a DC baseline to each signal using the algorithm of Halmer et al. [38].

Spectra could be continuously measured over a 24 h interval without operator intervention. We employed two modes of laser tuning (coarse and fine). Coarse tuning was performed through the use of a stepper-motor-actuated grating (9 GHz minimum movement), while fine tuning was done via a piezoelectric transducer (PZT)-actuated mirror (full range of 60 GHz). The stepper motor, PZT, and wave meter were automatically used in combination to move the laser frequency to the desired starting point for an individual scan. Once this location was found, the PZT was employed to step the laser frequency over successive cavity longitudinal modes, q_m. A typical scan spanned a total of ~10 GHz, and took roughly ten to fifteen minutes. Fifty individual

ring-down time constants were averaged at each frequency step. The spectrum frequency axis was given by $\Delta q_{\mathrm{m}} v_{\mathrm{FSR}}$ where Δq_{m} was the number of mode steps through which the laser was tuned relative to the beginning of the scan. At least ten complete spectra were then co-added to produce a final averaged spectrum. The effects of these two separate averaging steps will be explored in detail in the next two sections

5.3.2. Short-Term Measurement Statistics and Signal Averaging

It is instructive to consider both short- and long-term averaging statistics to evaluate system performance and quantify detection limits and measurement precision. With regard to short times, we use the noise-equivalent absorption coefficient $\varepsilon_{\mathrm{NEA}}$ given by $\sigma_\tau / \left(c \bar{\tau}^2 f_{acq}^{1/2} \right)$. Here σ_τ represents the standard deviation of the observed time constant about its mean value, $\bar{\tau}$, and c is the speed of light. For a given averaging time, Δt_{av}, (corresponding to a set of ring-down signals acquired at fixed laser frequency) the uncertainty in the mean value of the base loss, $\bar{\alpha}$, is $u(\bar{\alpha}) = \varepsilon_{NEA} / (\Delta t_{av})^{1/2}$ $= \sigma_\tau / \left(c \bar{\tau}^2 n_d^{1/2} \right)$, where n_{d} is the total number of measured decay signals. We found that $\sigma_\tau / \bar{\tau}$ was typically less than 0.2%, leading to a $\varepsilon_{\mathrm{NEA}} = 2.5 \times 10^{-10}$ cm^{-1} Hz$^{-1/2}$. For the averaging time employed, $\Delta t_{\mathrm{av}} = 5$ s, this corresponded to an uncertainty in the absorption coefficient of $\alpha_{\mathrm{min,acq}} = 1.1 \times 10^{-10}$ cm^{-1}.

For sufficiently long averaging timescales, the noise-equivalent absorption coefficient cannot be used to predict detection limits because of slow drift in system variables. We observed that our system exhibited a nominally linear drift in $\bar{\tau}$ over a time span of several hours given by $\sigma_\tau^{-1} d\bar{\tau} / dt \sim 2 \times 10^{-5}$ s^{-1}. The Allan variance, which was originally formulated to quantify the performance of ultrastable clocks [39], provides a useful measure of long-term system stability and has been applied to analyze detection limits in laser absorption spectroscopy [40]. We measured the Allan variance under empty-cavity conditions. The results for our experiment are shown in Figure 4 and reveal an optimal averaging time of 150 s. For averaging timescales smaller than 150 s, the Allan variance varied inversely with Δt_{av} consistent with the definition of $\varepsilon_{\mathrm{NEA}}$, whereas

for longer averaging timescales, the Allan variance reached a minimum due to system drifts. When evaluated at the optimum averaging time, the Allan variance analysis yields a minimum uncertainty in the absorption coefficient of $\alpha_{min} = 4\times10^{-11}$ cm^{-1}, which corresponds to the peak loss from a self-broadened *A*-band line with an intensity $S\sim6\times10^{-31}$ cm^{-1} molec.$^{-1}$ at $p = 13.3$ kPa (100 Torr). Numerical simulations indicate that the optimal averaging time in our Allan variance is consistent with our observed drift rate.

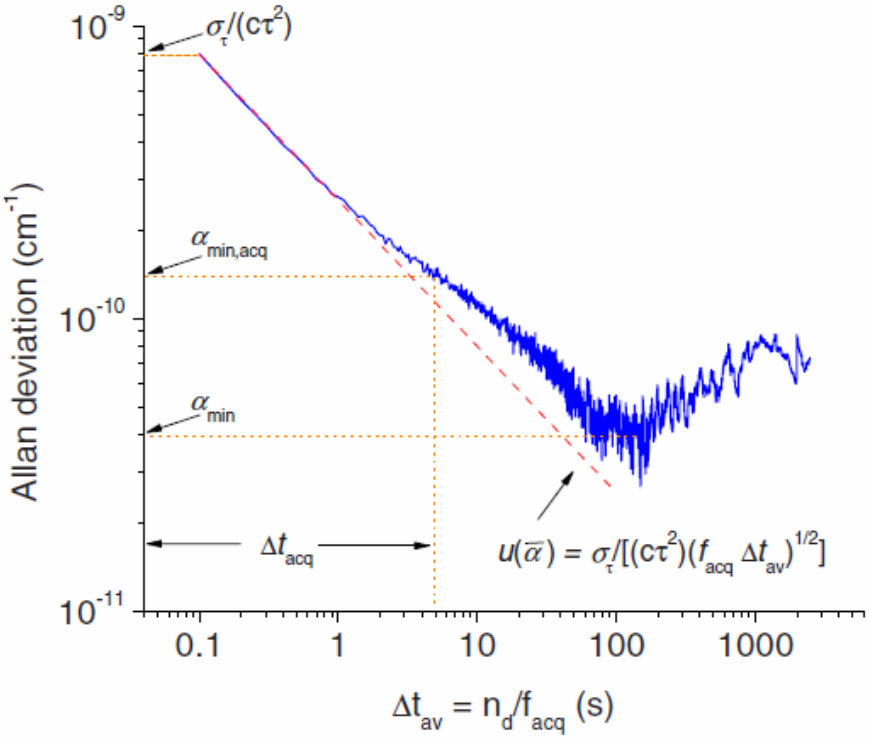

FIG. 4. Measured Allan deviation (square root of the Allan variance) of the cavity losses as a function of averaging time, Δt_{av}. The quantity n_d is the number of measured decay signals, and the ring-down signal acquisition rate is f_{acq}. The dashed line tangent to the Allan deviation corresponds to $\varepsilon_{NEA}=2.5\times10^{-10}$ cm^{-1} Hz$^{-1/2}$ and for short averaging times gives an uncertainty in $\overline{\alpha}$, $u(\overline{\alpha})$, which is proportional to $n_d^{-1/2}$.

5.3.3. Long-Term Averaging of Spectra

In addition to short-time averaging of successive ring-down time constants, ensembles of complete spectra were also averaged. It is important to note that this is a simple average; no baseline correction or other preanalysis was performed. It was found that, over time,

the broadband baseline absorbance drifted (as is to be expected due to thermo-mechanical drift); however, the integrated area of the relevant absorbance feature was independent of this drift. This is an important feature of FS-CRDS which allows spectra to be co-added, thereby reducing the amplitude of temporally uncorrelated residual features which vary on a timescale shorter than our single-spectrum acquisition time (10–15 min).

The base losses of ring-down spectrometers typically have a weak wavelength dependence that drifts slowly with time. The baseline spectrum of the empty cavity arises from λ-dependence in the mirror reflectivity and from secondary resonant cavities (etalons). Spectral and temporal variation in the base losses is a manifestation of coupling between cavities of low finesse and the main high-finesse ring-down cavity [41], and consequently the measured decay time τ is influenced by all resonant cavities along the optical axis of the probe beam. The most important secondary cavities are formed by pairs of surfaces where the first surface corresponds to one of the high-reflectivity ring-down cavity mirrors and the other corresponds to a normal-incidence surface in the probe beam path. Examples of the latter include: mode-matching lenses, view ports, detector faceplates, ring-down mirror input surfaces, etc. Note that a pair of coupled cavities will be mutually resonant at a given frequency, when the round-trip path difference is an integral multiple of $\lambda/2$. This effect gives rise to periodicity in the base losses as a function of optical frequency. Fourier analysis of ring-down spectra reveals the amplitudes and characteristic spatial frequencies (and hence path lengths) associated with these secondary resonators. Given that these etalons can involve optical elements external to the ring-down cavity, they are sensitive to slow thermo-mechanical variations in optical path length, therefore contributing to drift in the observed ring-down losses.

We evaluated the baseline noise of a composite spectrum by calculating the residuals to a quadratic fit in a region largely free of absorption features. The resulting rms baseline (in units of cm^{-1}) as a function of number of spectra averaged, n_s, can be found in Figure 5. The overall trend is a steady reduction in the rms baseline noise to a minimum value of 1.8×10^{-11} cm^{-1}. This trend persists for an averaging time of approximately 10 h and shows no evidence of leveling off, indicating that additional

gains could be achieved by further averaging. As shown in Figure 5, a power-law fit to the data gives a slightly smaller decay exponent of $\mu = 0.46$ than would be expected from an ergodic $n_s^{-1/2}$ dependence. Note the rms baseline for $n_s = 1$ is consistent with the single-spectrum $\alpha_{min,acq}$ value shown in Figure 4. Kassi et al. [42] similarly observed that co-adding cw-CRDS spectra reduced rms baseline noise in measurements made with a fibered distributed feedback (DFB) diode laser at 1.58 μm. However, they found a slightly faster decay of noise in their setup (μ = 0.61), which they assigned to the presence of slowly varying "interference fringes" whose movement was driven by thermo-mechanical drift.

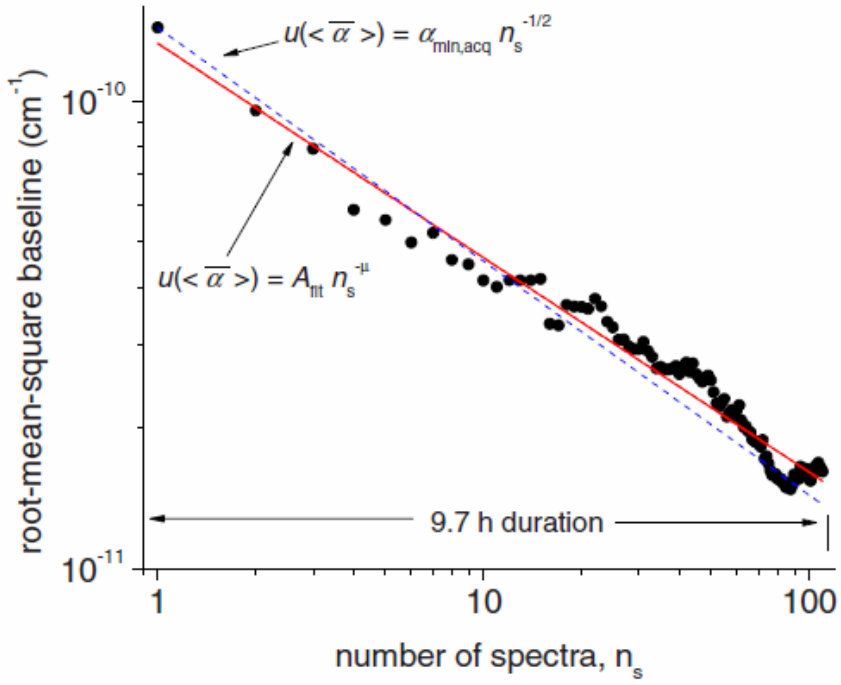

FIG. 5. Decrease in rms baseline noise (symbols) with increasing number of co-added spectra, n_s. The solid red line corresponds to a power-law fit yielding the decay exponent, μ=0.46 and the constant $A_{fit} \sim \alpha_{min,acq}$=1.1_$10^{-10}$ cm^{-1}. The dashed blue line represents an ergodic decay proportional to $n_s^{-1/2}$. The minimum value of the rms baseline corresponds to the peak loss of a self-broadened A band line with S~2.5×10^{-31} cm^{-1} molec.$^{-1}$ at p=13.3 kPa (100 Torr).

5.3.4. Effect of Long-Term Averaging on Observed Lineshape

One possible deleterious result of spectra averaging is that the averaged spectrum may exhibit a nonphysical line shape due to instrumental broadening. To examine instrumental broadening, we measured the $^{P}P(21)$ transition of $^{16}O_2$ at $\tilde{\nu}$ = 13,041.1236 cm^{-1} both with and without the frequency stabilization at p = 67 Pa. At this pressure the line shape was essentially Doppler broadened. The frequency-stabilized case is shown in Figure 6. A Galatry profile [43] was fit to the measured spectra to account for residual pressure broadening as well as collisional narrowing effects that were observable at the high SNR of these measurements. We used the recent line shape measurements of Robichaud et al. [36] for the broadening and narrowing coefficients of this line, which were 0.0118 and 0.0039 MHz Pa^{-1}, respectively.

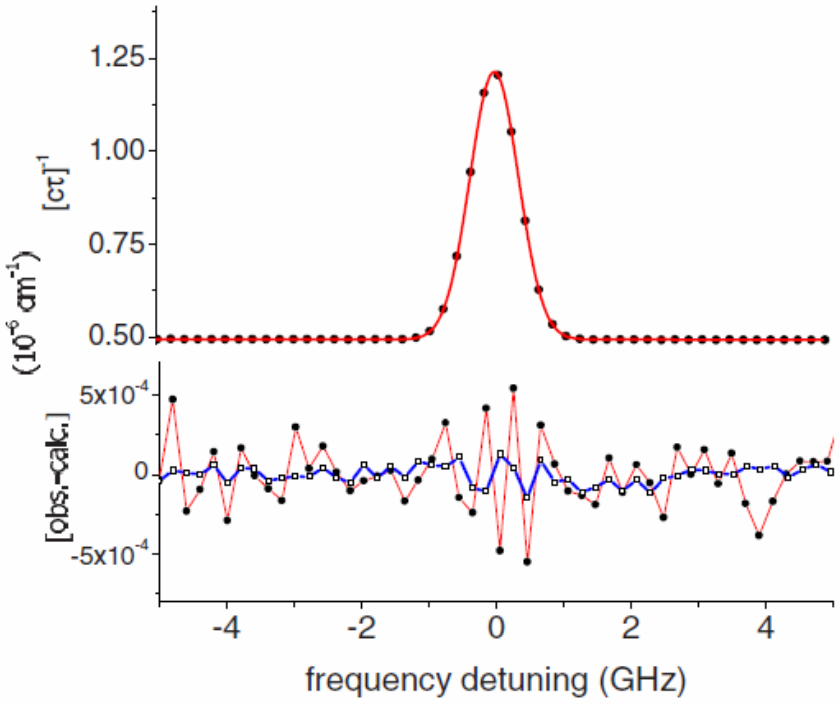

FIG. 6. Frequency-stabilized, Doppler-broadened spectrum of the $^{16}O_2$ $^{P}P(21)$ magnetic dipole transition at $\tilde{\nu}$ =13 041.1236 cm^{-1} for p=67 Pa, T=294.987(40) K, and an effective path length of 25 km. Upper panel shows the measured (symbols) and Galatry line shape fit (solid line) to a single spectrum. Lower panel shows the fit residuals for the single spectrum, and those corresponding to the fit of an averaged spectrum comprising 28 spectra (blue line with open symbols). SNR for the averaged spectrum was 18,000:1 with rms noise in the baseline absorption coefficient of 3.9×10^{-11} cm^{-1}.

We observed significant differences between the stabilized and unstabilized spectra with respect to the measured Doppler width and center frequency determinations. In the stabilized case, the mean difference between the measured Doppler width and the calculated value (~0.85 GHz) was 143 kHz, with a standard deviation of 329 kHz. In the unstabilized case, the difference was three times larger (379 kHz) and the measured standard deviation was six times larger (1.96 MHz). Apparent drifts in the transition center frequency as large as ~2 MHz min^{-1} were observed which resulted from continuous movement of the cavity modes over the 10 min duration of each spectrum acquisition. These effects of cavity drift were mitigated in the stabilized case, for which we measured a standard deviation in fit-derived center frequency of only 200 kHz. The residual scatter in center frequency for the stabilized case was driven in part by variations (occurring on the timescale of spectrum acquisition) in the HeNe laser reference frequency.

These results illustrate that with frequency stabilization of the ring-down cavity, the measured Doppler width and center frequency are stable to within 0.5 MHz. Therefore, co-adding multiple spectra obtained over time spans of several hours should introduce negligible instrumental broadening in the present experiment. We conclude that our measurements of the weak electric quadrupole lines, obtained by co-adding multiple spectra, can be readily modeled using standard line shapes [44].

5.3.5. Analysis of Measured Spectra

Higher-order line shape phenomena such as collisional narrowing [43] and speed-dependent effects [45] were not expected to be detectable for measurements of the ultraweak electric quadrupole lines. Therefore, we modeled all these lines as Voigt profiles. The observed spectra, given by the measured quantity $n_0(c\tau)^{-1}$, comprised absorption by O_2 and all other system losses. Here n_0 is the broadband (nonresonant) index of refraction of the cavity medium, which we assumed to be unity. The electric quadrupole lines were superimposed on a baseline (linear plus sinusoidal terms) to capture variations in the local loss arising from wings of other lines and etaloning effects.

The spectrum frequency axis was $\nu(q_m) = \nu_0 + q_m \nu_{FSR}$, where ν_0 was the starting frequency given by the wave meter. The electric quadrupole line intensities are given by $S = A/(nc)$, where A is the fitted area of the electric quadrupole peak, and n is the measured sample number density equal to $p(k_B T)^{-1}$, in which k_B is the Boltzmann constant. The Gaussian width, w_G, was calculated in terms of the measured temperature, transition frequency, and $^{16}O_2$ molecular mass. For the lines considered here, w_G, expressed as a full width at half-maximum (FWHM), was nominally 0.85 GHz.

Given the relatively low SNR of the electric quadrupole spectra, it was not possible to retrieve the Lorentzian width, w_L, from the fitting procedure with sufficient accuracy. Instead, we constrained w_L to be $2\gamma p$, where γ is the pressure broadening coefficient. This constraint also ensured self-consistency in the fit-derived areas for a given line as the sample pressure was varied. We used the empirical J-dependent correlation of Yang et al. [46] with the parameters found in the self-broadening measurements of O_2 A-band magnetic dipole P-branch spectra of Robichaud et al. [36] to calculate γ as

$$\gamma = A + \frac{B}{1 + c_1 J' + c_2 J'^2 + c_3 J'^4}, \tag{1}$$

where J' is the upper state angular momentum, A = 0.004481 MHz Pa^{-1}, B = 0.01269 MHz Pa^{-1}, and c_1, c_2, and c_3 equal 0.03723, -7.86×10^{-4}, and 1.05×10^{-6}, respectively. Note that these parameters are presently utilized to calculate the broadening coefficients found in HITRAN 2008 [47].

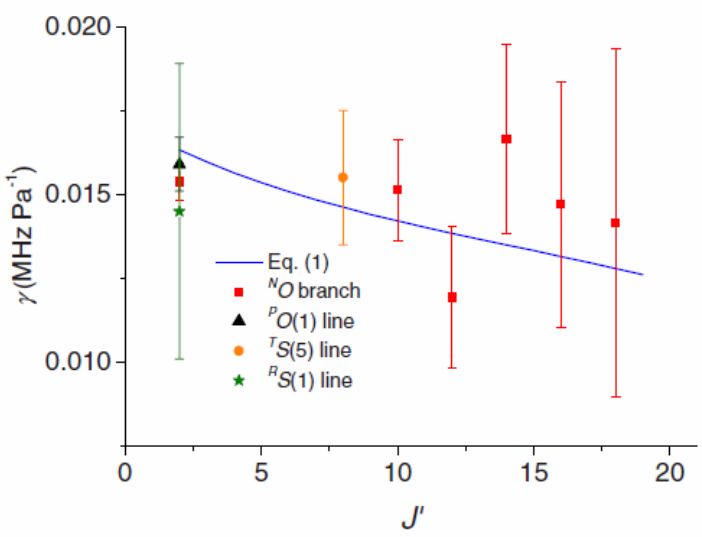

FIG. 7. Measured (filled symbols) and calculated (line) self-broadening coefficient, γ, vs. J'.

To test the applicability of Eq. 1, we relaxed the above constraint on w_L and subsequently retrieved γ from fits to the spectra. Figure 7 shows the results of these measured γ values and the predicted J'-dependent widths given by Eq. 1. Although the spread in the measurements is relatively large compared to the predicted variation with J', the mean γ values derived from the fits agrees well with the above correlation. The effect of uncertainty in γ on the uncertainty of the measured line intensities will be addressed in the Section 4.2.

5.4. Results and Discussion

5.4.1. Electric Quadrupole Line Intensity Measurements

We used FS-CRDS to measure six electric quadrupole transitions in the ^{N}O branch and one transition each in the ^{P}O, ^{R}S, and ^{T}S branches of the O_2 A-band. Except for the $^{T}S(5)$ transition, none of these transitions has previously been detected. We found good agreement between our observed and calculated line positions, with a mean deviation within the standard uncertainty of our calibrated frequency reference (60 MHz or 0.002 cm^{-1}).

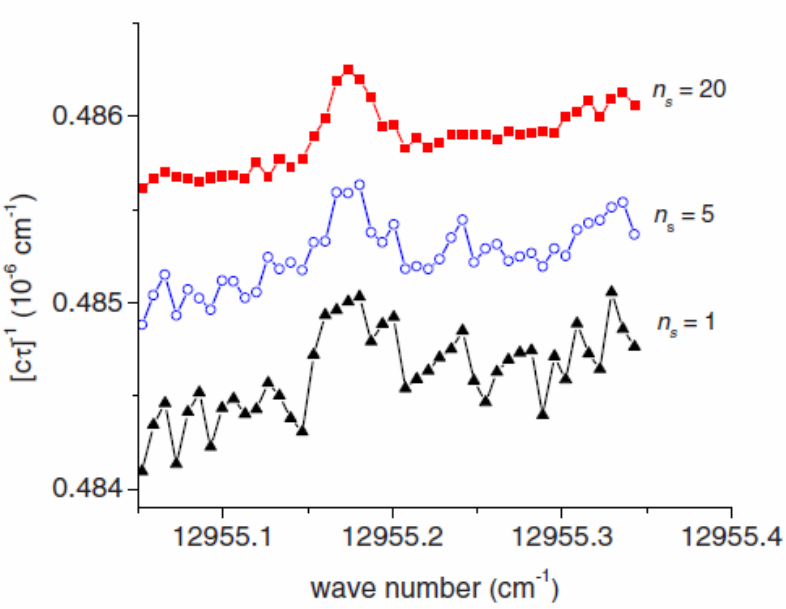

FIG. 8. Increase in SNR of average absorption spectrum with increasing number of averaged spectra. Central peak corresponds to the $^{N}O(19)$ electric quadrupole transition of $^{16}O_2$ ($\tilde{\nu}$ = 12,955.1661 cm^{-1}, S = 6.36×10^{-30} cm molec.$^{-1}$) at p = 12.7 kPa. The middle and top spectra are offset in the vertical direction by 0.0005 and 0.0010 units, respectively.

As discussed in the Experiment section, 50 ring-down acquisitions were averaged per frequency step within an individual spectrum. At least ten complete spectra were then co-added to produce a final averaged spectrum. The effect of the reduction in baseline noise level achieved by co-adding electric quadrupole spectra can be seen in Figure 8. It is apparent that a feature, which is only arguably observable in a single scan given the high noise level, is clearly visible with a SNR 10:1 after averaging twenty scans. Figure 9 shows the relatively isolated $^{T}S(5)$ transition, which was previously measured by Brault [5] and which we readily measured with a SNR of 50:1.

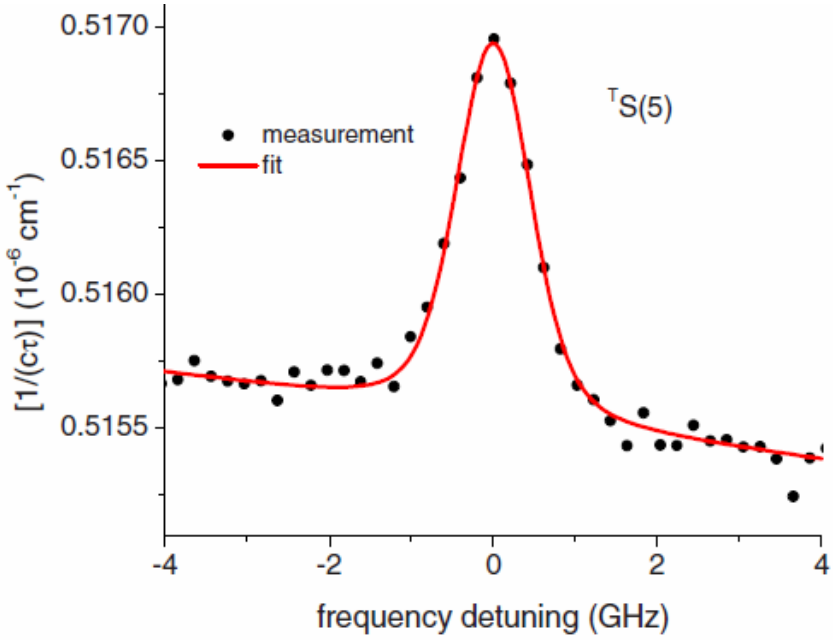

FIG. 9. $^{T}S(5)$ electric quadrupole line of $^{16}O_2$ ($\tilde{\nu}$ = 13,179.9239 cm^{-1}) at p = 12.7 kPa, T = 299.4 K. Symbols represent measured values and the line is a fit based on the Voigt line shape. The measurements correspond to the average of ten scans, giving a SNR~50:1.

The reduction in noise with signal averaging allows the quantitative observation of ultraweak absorption features within the wings of much stronger lines. The benefits of signal averaging are illustrated in Figure 10, which shows an average of 23 individual spectra, for the $^{N}O(21)$ electric quadrupole transition. This is the weakest line probed in the present study. Nevertheless, it can clearly be seen in the wings of a $^{16}O_2$ hot band line. The absorption peak of the electric quadrupole line is 3.4×10^{-10} cm^{-1} and the rms baseline is 2.1×10^{-11} cm^{-1}, giving a peak SNR of 16:1.

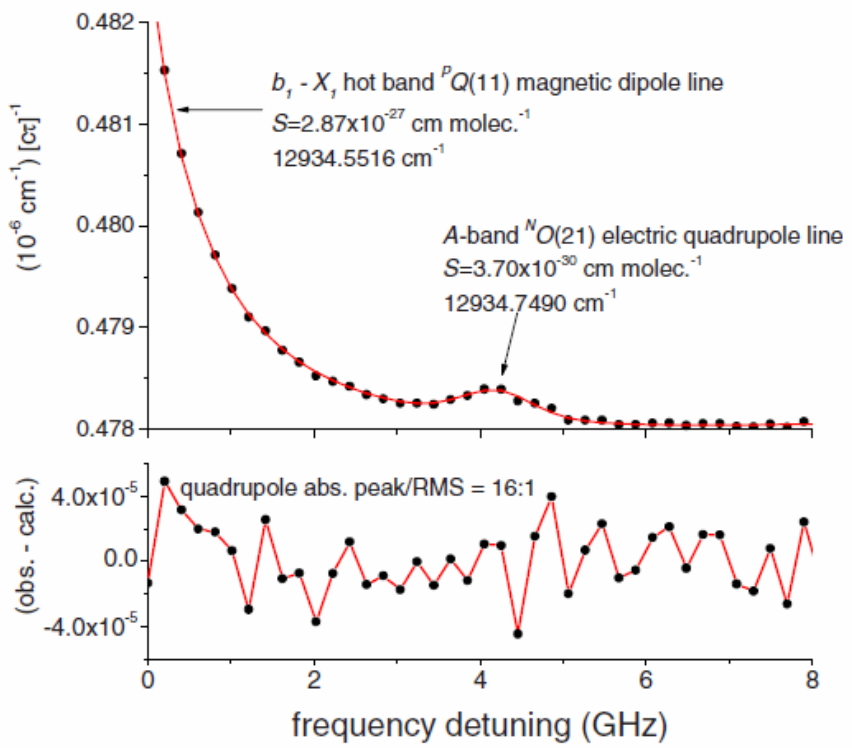

FIG. 10. Upper panel gives the $^{N}O(21)$ electric quadrupole line ($\tilde{\nu}$ = 12,934.7490 cm^{-1}, S = 3.70×10^{-30} cm molec.$^{-1}$) in the wings of the $^{P}Q(11)$ hot band, magnetic dipole transition of $^{16}O_2$ ($\tilde{\nu}$ = 12,934.5516 cm^{-1}, S = 2.87×10^{-27} cm molec.$^{-1}$). Symbols represent measured values and the lines are fitted Voigt line shapes. Bottom panel shows the fit residuals. The spectrum comprises an average of 23 files, taken at p = 12.7 kPa.

Averaged spectra were acquired at several pressures between 3.33 and 26.7 kPa, with each spectrum yielding a measurement of line intensity. The mean line intensity for each transition (see Table 3) was obtained by a weighted average over all measurements taken at various pressures. We used a normalized weighting factor proportional to $(n_j + \varepsilon_j^{-2})^{1/2}$, where n_j is the number of co-added spectra comprising the jth measurement, and $\varepsilon_j(p_j)$ is the fractional uncertainty in the jth measurement arising from systematic error in γ (as discussed below). We observed linearity between peak area, A_i, and O_2 number density, n, for all measured transitions. This result is illustrated in Figure 11, where the solid lines intersecting the origin correspond to the calculated peak areas based on the mean line intensity for each case (i.e., $A_{i,calc} = n\langle S_i \rangle c$).

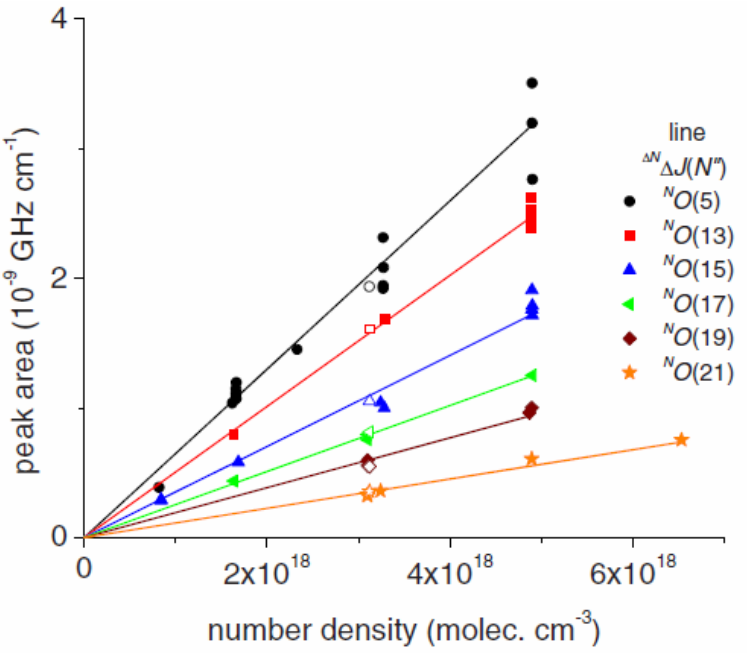

FIG. 11. Fit-derived peak areas (symbols), A_i, vs O_2 number density, n, for the ^{N}O branch electric quadrupole lines given in Table 2. The solid lines correspond to the expected areas based on the weighted mean line intensity for each case. The open symbols with abscissae near $n = 3.1\times10^{18}$ molec. cm^{-3}, are repeat measurements of the respective peak areas. The repeat data were obtained several weeks after the original data using another probe laser nominally identical to the original one.

For completeness, the measured intensities were also corrected to the standard reference temperature $T_r = 296$ K using the relation:

$$S(T_r) = S(T)\frac{Q(T)}{Q(T_r)}\frac{e^{-hcE''/(k_B T_r)}}{e^{-hcE''/(k_B T)}}, \qquad (2)$$

where E'' is the lower state energy, and $Q(T)$ is the total partition function for $^{16}O_2$. Lower state energies for the measured transitions are given in Table 3. Since most measurements were made within 1 K of 296 K, the corrections required to adjust the measured intensities to T_r were all less than 0.7%, far below our experimental measurement uncertainty.

TABLE 3. Measured electric quadrupole line intensities at 296 K (S in units of $10\times^{-30}$ cm molec.$^{-1}$), lower state energies (E'' in cm^{-1}) and standard relative uncertainties, [$u_{c,r}(S)$ in %] for the $^{16}O_2$ A band. The Type B uncertainties assume a 10% relative uncertainty in the self-broadening coefficient, γ. The quantities, n_T and $<n_s>$ represent the number of measurements of S and the corresponding average number of co-added spectra, respectively.

Transition	E''	S	$u_{c,r}(S)$	Type A	Type B	n_T	$<n_s>$
$^NO(5)$	42.2001	21.2	8.9	7.4	4.9	15	21
$^NO(13)$	260.6824	16.8	5.0	3.0	3.9	6	13
$^NO(15)$	343.9694	11.6	5.2	4.0	3.3	9	27
$^NO(17)$	438.7010	8.53	4.2	2.3	3.5	4	19
$^NO(19)$	544.8623	6.36	5.6	3.9	4.0	4	17
$^NO(21)$	662.4361	3.65	6.3	5.1	3.7	5	33
$^PO(1)$	2.0843	35.8	4.1	3.0	2.8	1	12
$^RS(1)$	0	3.83	11	9.9	4.7	1	45
$^TS(5)$	42.2240	20.5	4.4	3.0	3.3	1	10

5.4.2. Uncertainty Analysis

There are a number of observables in our experiment that do not make a significant contribution to the combined uncertainty in line intensity. These include measurements of the FSR, the spectrum frequency axis, and the sample temperature, pressure and number density. We estimate the relative combined uncertainty in S driven by uncertainties in these quantities to be less than 0.5%. There remain three dominant sources of uncertainty: (1) line shape effects influenced by collisional narrowing and self-broadening, (2) the base losses of the ring-down cavity, and (3) the total (base plus absorption) loss of the system. The first is a systematic (Type B) uncertainty, and the latter two can be treated as statistical uncertainties (Type A) that can be reduced by least-squares fits and signal averaging [48].

Our previous analysis of high SNR O_2 A-band spectra [36] revealed collisional (Dicke) narrowing line shape effects which we modeled using the Galatry profile [43]. In the present study, we estimated that our choice of the Voigt profile contributes a relative uncertainty of ~2% to S, with a larger uncertainty arising from our choice of broadening

parameter. We found the systematic uncertainty in S arising from uncertainty in γ by numerical evaluation of the sensitivity parameter, $d \ln S / d \ln \gamma$. This parameter represents the fractional change in line intensity per fractional change in broadening parameter and can be readily found by repeating the fits to the quadrupole transitions over a range of γ values. From this analysis we obtain $d \ln S / d \ln \gamma \sim \eta p$, where η is line dependent and ranges from 1.7 to 2.1 Pa^{-1}. Assuming a 10% relative uncertainty in γ, we find the relative uncertainty in S arising from error in γ to be less than 5% for all cases.

Variations in the base loss occurring on timescales that are comparable to the scan time can give rise to spurious structure in individual spectra. This type of effect may not be captured by a model that incorporates a simple linear or sinusoidal baseline. However, when taken over an ensemble of spectra, residual variations in base losses tend to diminish inversely with the square root of the number of spectra, consistent with a Type A uncertainty. Likewise, noise in the ring-down signals occurring in the photoreceiver and A/D systems, limits the precision with which the ring-down time constant can be measured. This effect is manifest as an intrinsic noisiness in the spectra that is apparent near the detection limit. It too tends to be uncorrelated from one scan to the next, and hence both effects can be reduced by signal averaging as illustrated in Figure 5.

The rms deviation in S about the ensemble mean $\langle S \rangle$ is a measure of the combined Type A uncertainty. For ^{N}O-branch lines (which are those for which several repeat measurements were made), Table 3 shows that this quantity ranges from 2.3% to 7.4%. We also repeated the peak area measurements as a further check on our measurement precision and reproducibility. These experiments were repeated for each line several weeks after the original data were taken (open symbols in Figure 11), and data were acquired using a different probe laser that was nominally identical to the first. We found an average relative difference between the new S and those based on previously determined $\langle S \rangle$ of 1.3% with a standard deviation of 4.1%. These differences are consistent with the rms deviations in S that were found in the original data set.

Combining, the Type A and Type B uncertainties in quadrature, we estimate the relative combined standard uncertainty for most of the ^{N}O-branch electric quadrupole line

intensities to be ~6%. By comparison, this relative uncertainty is only about 20 times greater than those of the O_2 *A*-band magnetic dipole lines [36]; despite the fact that the latter transitions are five orders of magnitude stronger than the former.

These data also indicate that it would be possible to detect much weaker lines using the present technique. Our weakest measured line had an intensity of 3.7×10^{-30} cm molec.$^{-1}$ with a Type A uncertainty of 5%. If we assume a best-case measurement precision of 2.5% (improved over the present case by a fourfold increase in signal averaging time or by a twofold reduction in mirror losses), we estimate a SNR of ~2:1 for a line having an intensity of 2×10^{-31} cm molec.$^{-1}$. This limit is approximately 100 times lower than the detection limit reported by Naus et al. [6] in their CRDS measurement of the $^{T}S(9)$ O_2 electric quadrupole line.

5.4.3. Electric Quadrupole Line Intensity Calculations

The SPCAT program [19] was modified to calculate the electric quadrupole matrix elements. Intensities for the $|\Delta N| = 1,3$ electric quadrupole transitions were calculated for $N'' = 1$ to 29 (with estimated values for M_1, Q_1, and Q_3). The values of Q_1 and Q_3 were determined in a least-squares fit of the predicted electric quadrupole intensities to those we measured. A similar procedure was used to determine M_1 from the previously measured magnetic dipole transition intensities [36]. The fitted transition moments were $M_1 = 6.369(8)\times10^{-25}$ J T^{-1} [0.06868(8) Bohr-magnetons], $Q_1 = 4.15(13)\times10^{-42}$ C m^2 [0.0124(4) D Å], $Q_3 = 2.61(8)\times10^{-42}$ C m^2 [0.00783(23) D Å], where the value in parentheses denotes the standard uncertainty in the last digit. We recalculated the predicted intensities for all four electric quadrupole branches using the fitted values of M_1, Q_1, and Q_3. The average absolute difference between the present electric quadrupole measurements and the calculations is ~5%, which is comparable to our reported average experimental uncertainty.

TABLE 4. Calculated intensities (at 296 K, in units of 10^{-30} cm molec.$^{-1}$) for the electric quadrupole transitions within the ${}^{N}O$, ${}^{P}O$, ${}^{R}S$, and ${}^{T}S$ branches of the ${}^{16}O_2$ *A* band. Fit uncertainties (mean absolute relative deviation between our measurements and calculated intensities) of these intensities are ~5%. Transitions observed in this study are underlined.

N''	${}^{N}O$	${}^{P}O$	${}^{R}S$	${}^{T}S$
1		<u>35.9</u>	<u>4.09</u>	6.09
3	11.4	76.5	51.2	14.0
5	<u>18.7</u>	102.3	80.9	<u>19.8</u>
7	21.8	114.0	96.6	22.7
9	21.9	112.3	98.9	22.8
11	19.7	100.4	90.9	20.7
13	<u>16.3</u>	82.4	76.2	17.2
15	<u>12.5</u>	62.7	58.8	13.2
17	<u>8.83</u>	44.4	42.1	9.46
19	<u>5.86</u>	29.4	28.2	6.32
21	<u>3.62</u>	18.2	17.6	3.95
23	2.11	10.6	10.3	2.31
25	1.15	5.78	5.68	1.27
27	0.60	2.97	2.93	0.661
29	0.29	1.44	1.42	0.318

The results of these intensity calculations for all four electric quadrupole branches can be found in Table 4. Figure 1 shows a stick spectrum based on the present calculations with all observed transitions indicated. Using the calculated transition moments, we calculated the transition band intensities: $S_{MD} = 2.25(2)\times10^{-22}$ cm molec.$^{-1}$ and $S_{EQ} = 1.8(1)\times10^{-27}$ cm molec.$^{-1}$. It is important to note that the $|\Delta N| = 1$ transitions (i.e., ${}^{P}O$ and ${}^{R}S$ branches) are four times stronger than the $|\Delta N| = 3$ transitions (i.e., ${}^{N}O$ and ${}^{T}S$ branches) as illustrated in Figure 1, thus confirming the 1934 prediction of van Vleck [49]. As a result, while the ratio of intensities between a $|\Delta N| = 3$ branch and a given magnetic dipole branch is 3×10^{-6} (as was reported by Brault [5]), the ratio of intensities for a $|\Delta N| = 1$ electric quadrupole branch is 12×10^{-6}. After summing intensities over all branches, we find that the ratio of electric quadrupole and magnetic dipole band intensities is 8×10^{-6}.

On average, the measurements of Brault [5] are systematically low by 15% compared to the present calculations for the ^{T}S electric quadrupole transition intensities, displaying increasing discrepancy with large J. A deviation of ~12% was observed between Brault's $^{T}S(5)$ measurement and our own. These disparities are consistent with the quadrature sum of the 10% uncertainty in effective path length reported by Brault and the uncertainties in our calculations and measurements.

5.5. Conclusions

We have reported laboratory observations, quantitative intensity measurements, and calculations of electric quadrupole transitions in the O_2 A-band. These measurements may serve as a benchmark for ultrasensitive spectroscopic techniques. The experiment exploited the high sensitivity, spectral fidelity, and long-term stability of frequency-stabilized cavity ring-down spectroscopy; a technique that enabled intensity measurements of ultraweak lines (S~3×10^{-30} to 2×10^{-29} cm molec.$^{-1}$) with unprecedented accuracy (4.4% to 11% relative combined uncertainty). Our calculations included the electric quadrupole line positions (uncertainties less than 3 MHz) and and line intensities. The line intensity calculations and measurements agreed to within our average experimental uncertainty of 6%. Our calculated positions and intensities are sufficiently accurate to model the electric quadrupole contribution to the O_2 A-band which may be observed in long-path atmospheric spectra. In addition, we have demonstrated how such high-sensitivity and low uncertainty measurements can add to our understanding of diatomic spectroscopy and provide a basis for comparison with present day computational models. Finally, the measurements of other ultraweak transitions in atmospherically relevant species may have possible future implications for increasingly sensitive remote sensing measurements.

Acknowledgements

David A. Long acknowledges the support of the National Defense Science and Engineering Graduate Fellowship. Daniel K. Havey received support from the National Research Council as a postdoctoral fellow at the National Institute of Standards and Technology (NIST). The research at the Jet Propulsion laboratory (JPL), California Institute of Technology, was performed under contract with National Aeronautics and Space Administration.

References

[1] J. F. Noxon, Can. J. Phys. **39,** 1110-1119 (1961).

[2] A. Goldman, J. Reid, L. S. Rothman, Geophys. Res. Lett. **8,** 77-78 (1981).

[3] E. Niple, W. G. Mankin, A. Goldman, D. G. Murcray, F. J. Murcray, Geophys. Res. Lett. **7,** 489-492 (1980).

[4] J. Reid, R. L. Sinclair, A. M. Robinson, A. R. W. McKellar, Phys. Rev. A **24,** 1944-1949 (1981).

[5] J. W. Brault, J. Mol. Spectrosc. **80,** 384-387 (1980).

[6] H. Naus, A. deLange, W. Ubachs, Phys. Rev. A **56,** 4755-4763 (1997).

[7] D. M. O'Brien, S. A. English, G. DaCosta, J. Atmos. Ocean. Technol. **14,** 105-119 (1997).

[8] R. A. Washenfelder, G. C. Toon, J. F. Blavier, Z. Yang, N. T. Allen, P. O. Wennberg, S. A. Vay, D. M. Matross, B. C. Daube, J. Geophys. Res.-Atmos. **111,** D22305 (2006).

[9] K. Chance, J. Quant. Spectrosc. Radiat. Transfer **58,** 375-378 (1997).

[10] S. Corradini, M. Cervino, J. Quant. Spectrosc. Radiat. Transfer **97,** 354-380 (2006).

[11] B. van Diedenhoven, O. P. Hasekamp, I. Aben, Atmos. Chem. Phys. **5,** 2109-2120 (2005).

[12] M. Yokomizo, Fujitsu Sci. Tech. J. **44,** 410-417 (2008).

[13] D. Crisp, R. M. Atlas, F. M. Breon, L. R. Brown, J. P. Burrows, P. Ciais, B. J. Connor, S. C. Doney, I. Y. Fung, D. J. Jacob, C. E. Miller, D. O'Brien, S. Pawson, J. T. Randerson, P. Rayner, R. J. Salawitch, S. P. Sander, B. Sen, G. L. Stephens, P. P. Tans, G. C. Toon, P. O. Wennberg, S. C. Wofsy, Y. L. Yung, Z. Kuang, B. Chudasama, G. Sprague, B. Weiss, R. Pollock, D. Kenyon, S. Schroll, In: *Trace Constituents in the Troposphere and Lower Stratosphere*, (Pergamon-Elsevier Science Ltd, Kidlington, 2004).

[14] C. E. Miller, L. R. Brown, R. A. Toth, D. C. Benner, V. M. Devi, C. R. Phys. **6,** 876-887 (2005).

[15] C. E. Miller, D. Crisp, P. L. DeCola, S. C. Olsen, J. T. Randerson, A. M. Michalak, A. Alkhaled, P. Rayner, D. J. Jacob, P. Suntharalingam, D. B. A. Jones, A. S. Denning, M. E. Nicholls, S. C. Doney, S. Pawson, H. Boesch, B. J. Connor, I. Y. Fung, D. O'Brien, R. J. Salawitch, S. P. Sander, B. Sen, P. Tans, G. C. Toon, P. O. Wennberg, S. C. Wofsy, Y. L. Yung, R. M. Law, J. Geophys. Res.-Atmos. **112,** D10314 (2007).

[16] C. E. Miller, D. Wunch**,** Unpublished.

[17] H. D. Babcock, L. Herzberg, Astrophys. J. **108,** 167-190 (1948).

[18] H. Lefebvre-Brion, R. W. Field, *The Spectra and Dynamics of Diatomic Molecules* (Elsevier, New York, 2004).

[19] H. M. Pickett, J. Mol. Spectrosc. **148,** 371-377 (1991).

[20] M. Y. Tretyakov, M. A. Koshelev, V. V. Dorovskikh, D. S. Makarov, P. W. Rosenkranz, J. Mol. Spectrosc. **231,** 1-14 (2005).

[21] G. Y. Golubiatnikov, A. F. Krupnov, J. Mol. Spectrosc. **217,** 282-287 (2003).
[22] Y. Endo, M. Mizushima, Jpn. J. Appl. Phys. 2 **21,** L379-L380 (1982).
[23] K. Park, I. G. Nolt, T. C. Steele, L. R. Zink, K. M. Evenson, K. V. Chance, A. G. Murray, J. Quant. Spectrosc. Radiat. Transfer **56,** 315-316 (1996).
[24] L. R. Zink, M. Mizushima, J. Mol. Spectrosc. **125,** 154-158 (1987).
[25] G. Rouille, G. Millot, R. Saintloup, H. Berger, J. Mol. Spectrosc. **154,** 372-382 (1992).
[26] G. Millot, B. Lavorel, G. Fanjoux, J. Mol. Spectrosc. **176,** 211-218 (1996).
[27] S. Brodersen, J. Bendtsen, J. Mol. Spectrosc. **219,** 248-257 (2003).
[28] K. W. Brown, N. H. Rich, J. W. Nibler, J. Mol. Spectrosc. **151,** 482-492 (1992).
[29] D. J. Robichaud, J. T. Hodges, P. Maslowski, L. Y. Yeung, M. Okumura, C. E. Miller, L. R. Brown, J. Mol. Spectrosc. **251,** 27-37 (2008).
[30] L. R. Brown, C. Plymate, J. Mol. Spectrosc. **199,** 166-179 (2000).
[31] A. J. Phillips, F. Peters, P. A. Hamilton, J. Mol. Spectrosc. **184,** 162-166 (1997).
[32] R. Schermaul, R. C. M. Learner, J. Quant. Spectrosc. Radiat. Transfer **61,** 781-794 (1999).
[33] D. J. Robichaud, J. T. Hodges, D. Lisak, C. E. Miller, M. Okumura, J. Quant. Spectrosc. Radiat. Transfer **109,** 435-444 (2008).
[34] J. T. Hodges, H. P. Layer, W. W. Miller, G. E. Scace, Rev. Sci. Instrum. **75,** 849-863 (2004).
[35] J. T. Hodges, R. Ciurylo, Rev. Sci. Instrum. **76,** 023112 (2005).
[36] D. J. Robichaud, J. T. Hodges, L. R. Brown, D. Lisak, P. Maslowski, L. Y. Yeung, M. Okumura, C. E. Miller, J. Mol. Spectrosc. **248,** 1-13 (2008).
[37] D. J. Robichaud, L. Y. Yeung, D. A. Long, M. Okumura, D. K. Havey, J. T. Hodges, C. E. Miller, L. R. Brown, J. Phys. Chem. A **113,** 13089-13099 (2009).
[38] D. Halmer, G. von Basum, P. Hering, M. Murtz, Rev. Sci. Instrum. **75,** 2187-2191 (2004).
[39] D. W. Allan, Proc. IEEE **54,** 221-230 (1966).
[40] P. Werle, R. Mucke, F. Slemr, Appl. Phys. B **57,** 131-139 (1993).
[41] D. Romanini, K. K. Lehmann, J. Chem. Phys. **99,** 6287-6301 (1993).
[42] S. Kassi, D. Romanini, A. Campargue, B. Bussery-Honvault, Chem. Phys. Lett. **409,** 281-287 (2005).
[43] L. Galatry, Phys. Rev. **122,** 1218-1223 (1961).
[44] P. L. Varghese, R. K. Hanson, Appl. Optics **23,** 2376-2385 (1984).
[45] P. R. Berman, J. Quant. Spectrosc. Radiat. Transfer **12,** 1331-1342 (1972).
[46] Z. Yang, P. O. Wennberg, R. P. Cageao, T. J. Pongetti, G. C. Toon, S. P. Sander, J. Quant. Spectrosc. Radiat. Transfer **90,** 309-321 (2005).
[47] L. S. Rothman, I. E. Gordon, A. Barbe, D. C. Benner, P. E. Bernath, M. Birk, V. Boudon, L. R. Brown, A. Campargue, J. P. Champion, K. Chance, L. H. Coudert, V. Dana, V. M. Devi, S. Fally, J. M. Flaud, R. R. Gamache, A. Goldman, D. Jacquemart, I. Kleiner, N. Lacome, W. J. Lafferty, J. Y. Mandin, S. T. Massie, S. N. Mikhailenko, C. E. Miller, N. Moazzen-Ahmadi, O. V. Naumenko, A. V. Nikitin, J. Orphal, V. I. Perevalov, A. Perrin, A. Predoi-Cross, C. P. Rinsland, M. Rotger, M. Simeckova, M. A. H. Smith, K. Sung, S. A. Tashkun, J. Tennyson, R.

A. Toth, A. C. Vandaele, J. Vander Auwera, J. Quant. Spectrosc. Radiat. Transfer **110,** 533-572 (2009).
[48] B. N. Taylor, C. E. Kuyatt, NIST Tech. Note **1297** (1994).
[49] J. H. van Vleck, Astrophys. J. **80,** 161-170 (1934).

CHAPTER 6

The Air-Broadened, Near-Infrared CO_2 Line Shape in the Spectrally Isolated Regime: Evidence of Simultaneous Dicke Narrowing and Speed Dependence

This chapter was submitted for publication as

D. A. Long, K. Bielska, D. Lisak, D. K. Havey, M. Okumura, C. E. Miller, and J. T. Hodges, *J. Chem. Phys.*, (2011).

Abstract

Frequency-stabilized cavity ring-down spectroscopy (FS-CRDS) was employed to measure air-broadened CO_2 line shape parameters for transitions near 1.6 μm over a pressure range of 6.7–33 kPa. The high sensitivity of FS-CRDS allowed for the first measurements in this wavelength range of air-broadened line shape parameters on samples with CO_2 mixing ratios near those of the atmosphere. The measured air-broadening parameters show several percent deviations from values found in the HITRAN 2008 database. Spectra were fit with a variety of models including the Voigt, Galatry, Nelkin-Ghatak, and speed-dependent Nelkin-Ghatak line profiles. Clear evidence of collisional narrowing was observed, which if unaccounted for can lead to several percent biases. Furthermore, it was observed that only the speed-dependent Nelkin-Ghatak line profile was able to model the spectra to within the instrumental noise level because of the concurrent effects of collisional narrowing and speed dependence of collisional broadening and shifting.

6.1. Introduction

Recent carbon dioxide remote sensing missions have set unprecedented precision targets as demanding as 0.3% [1-2] (change in atmospheric CO_2 mixing ratio of ~1 μmol mol^{-1}). These applications will require a detailed and thorough understanding of the near-infrared spectral line shapes of CO_2 and O_2 over a wide range of atmospherically relevant temperatures and pressures [3]. Of particular importance are higher-order effects such as collisional narrowing, speed-dependent effects and line mixing which are yet to be incorporated into the vast majority of atmospheric retrievals. These effects will play an even greater role in next generation, active sensing missions (such as NASA's Active Sensing of CO_2 Emissions over Nights Days and Seasons, ASCENDS) where individual transitions in the near-infrared spectral region will be employed, rather than entire bands.

While near-infrared CO_2 transitions have been extensively studied (for example see Refs. [4-20] and the references found therein), only recently have non-Voigt line profiles begun to be employed [9-14,19-20]. In a recent Fourier-transform spectroscopy (FTS) study, clear evidence of line narrowing was observed, and further it was found that the use of the Voigt profile (which does not include this effect) limited the accuracy of the measured spectroscopic parameters to ~1% [8]. These findings led to a reanalysis of the FTS measurements using a speed-dependent Voigt profile with line mixing which resulted in a ~2% increase in the measured broadening parameters [9-10].

More recently Casa et al. used a laser absorption spectrometer to measure low-pressure (<5 kPa), self-broadened CO_2 line shapes near 5,000 cm^{-1} [19]. Unlike previous FTS studies of CO_2 line shapes, they were able to clearly distinguish various line profiles because of the relatively high signal-to-noise ratio (~10,000:1) and spectral resolution (~1 MHz) of the measurements. However, they were unable to completely describe the observed line shapes with either the Voigt, Galatry, Nelkin-Ghatak, speed-dependent Voigt, correlated Galatry or correlated Nelkin-Ghatak profiles. Notably, none of these theoretical profiles incorporated both collisional narrowing and speed-dependent effects. This lack of consistency between experiment and theory motivated the present work in which we apply frequency-stabilized cavity ring-down spectroscopy (FS-CRDS) to the

measurement of near-infrared CO_2 line shapes. As previously demonstrated, the sensitivity and spectral fidelity of FS-CRDS make it an ideal technique for detailed study of subtle line shape effects [21-26]. Furthermore, the use of multispectrum fitting [24,27-28], which simultaneously fits spectra across a wide pressure range, can enable the collisional narrowing and speed-dependent effects to be separated and quantified. Below we present FS-CRDS pressure-dependent line shape measurements of an air-broadened near-infrared CO_2 transition near 6,360 cm^{-1}, and we compare our measured Lorentzian broadening parameters to literature values. We also show that both collisional narrowing and speed-dependent effects need to be taken into account to best describe the observed pressure dependence of the line shape.

6.2. Experiment

Measurements were made using the frequency-stabilized cavity ring-down spectrometer located at the National Institute of Standards and Technology in Gaithersburg, Maryland [29-30]. This particular FS-CRDS instrument has been described earlier [31], therefore, we will discuss only the most salient details herein.

FS-CRDS differs from traditional *cw*-CRDS in two fundamental ways. Firstly, the intracavity distance is actively stabilized with respect to a reference laser. This length stabilization in turn stabilizes the entire comb of ring-down cavity transmission modes, thus, providing an exceptionally linear, stable, and accurate frequency axis for our spectra. In addition, FS-CRDS is a single-mode technique which allows for quantitative ring-down measurements. FS-CRDS has been employed to measure ultraweak transitions [32-33], hyperfine structure [25], rare isotopes [22,31,34], and to produce ultraprecise spectroscopic reference data [21-22,26,34-35].

For the measurements described herein the probe laser was an external cavity diode laser with an output power of 15–18 mW and the reference laser was a frequency-stabilized HeNe laser with a long-term stability of 1 MHz (8 h). The ring-down mirrors had reflectivities of ~99.997% at the probe wavelength, corresponding to a finesse of ~105,000. Three hundred ring-down time constants were collected and averaged at each

frequency step leading to a minimum detectable absorption coefficient of 3.5×10^{-11} cm^{-1} (see Figure 1 of Chapter 7 for an Allan variance plot with the given system parameters).

For the wavelength region investigated here, the sensitivity of FS-CRDS enables high signal-to-noise-ratio CO_2 absorption spectra to be acquired on air samples with CO_2 mixing ratios close to the current atmospheric background value (~390 μmol mol^{-1}). This capability of FS-CRDS is in contrast to similar FTS measurements which require CO_2 mixing ratios at the several percent level. Therefore, air-broadening parameters can be directly measured with FS-CRDS. In the present study, measurements were made using NIST SRM 1676, a blend of carbon dioxide in air with a CO_2 mixing ratio of 367.81(37) μmol mol^{-1}. This dry gas sample contained nominally 20.8% oxygen and 0.98% argon.

At pressures above 40.0 kPa (300 Torr) line mixing (line coupling) became apparent. Therefore, at pressures near or exceeding 40.0 kPa it is no longer possible to treat the transitions as being spectrally isolated. The present study aimed to examine CO_2 line shape behavior in the spectrally isolated pressure regime, therefore, measurements were made over the pressure range 6.7–33 kPa (50–250 Torr). No evidence of line mixing was observed in these spectra. A future study is forthcoming which will utilize these low pressure results in combination with line mixing to model the CO_2 line shape at and above 101.325 kPa.

The sample pressure was measured using a NIST-calibrated diaphragm capacitance gauge having a full-scale response of 133.3 kPa (1,000 Torr) and a relative standard uncertainty below 0.1%. All measurements were made at room temperature with no attempt made to control the cell temperature. The cell temperature was monitored using a NIST-calibrated 2.4 kΩ platinum resistance thermistor. The combined standard uncertainty in the cell temperature has recently been shown to be ~30 mK [33].

The measured spectra were fit with a variety of line profiles including the Voigt profile (VP), the Galatry profile (GP) [36], the Nelkin-Ghatak profile (NGP) [37-38], the speed-dependent Voigt profile (SDVP) [39], and the speed-dependent Nelkin-Ghatak

profile (SDNGP) [38,40]. The physical basis and mathematical form of these line profiles is described in Refs. [23,41], therefore, this will be only briefly discussed herein.

The VP is a convolution of a Gaussian and Lorentzian line profiles and therefore accounts for Doppler and pressure broadening by treating these effects as statistically independent. The GP and NGP include the contribution of collisional (Dicke) narrowing [42], which makes the observed Gaussian width narrower than the classical Doppler width. In the case of a relatively light perturber, the GP is more applicable than the NGP because the former uses a soft-collision model, whereas the latter uses a hard-collision model of velocity-changing collisions. The SDVP does not include collisional narrowing, but generalizes the VP by taking into account the dependence of collisional width and shift upon absorber speed. These effects usually cause line narrowing and line asymmetry, respectively. Of the line profiles considered here, the SDNGP is the most complex, because it includes both collisional narrowing and speed dependence.

6.3. Results and Discussion

In the present study, we measured transitions within the (30012)←(00001) CO_2 band which is centered at wavelength λ = 1.576 nm. We focused upon the *R*16 transition which is located at wave number $\tilde{\nu}$ = 6,359.9673 cm^{-1} and which has been proposed for use in NASA's ASCENDS active sensing mission. The top panel of Figure 1 shows the measured absorption spectrum (symbols) and SDNGP fit (line) for the *R*16 transition, and the residuals obtained by individually fitting the VP, GP, SDVP, NGP, and SDNGP to the same measured spectrum are given in the bottom panels of this figure. Inspection of the VP residuals (note the unique y-axis scale for this residual panel) indicates that this profile underestimates the measured peak intensity and fails to capture the measured line shape. We attribute this lack of agreement to line narrowing. In contrast, the GP, NGP, and SDVP each model a mechanism of line narrowing (either collisional narrowing or speed dependence), and therefore fitting any one of these profiles to the measured spectrum leads to vastly reduced residuals when compared to the VP. However, only the SDNGP, which includes both collisional narrowing and speed-dependent narrowing, is

able to model the spectrum to within the instrumental noise level, resulting in a spectrum signal-to-noise ratio (ratio of peak absorption to standard deviation of fit residuals) of ~5,000:1.

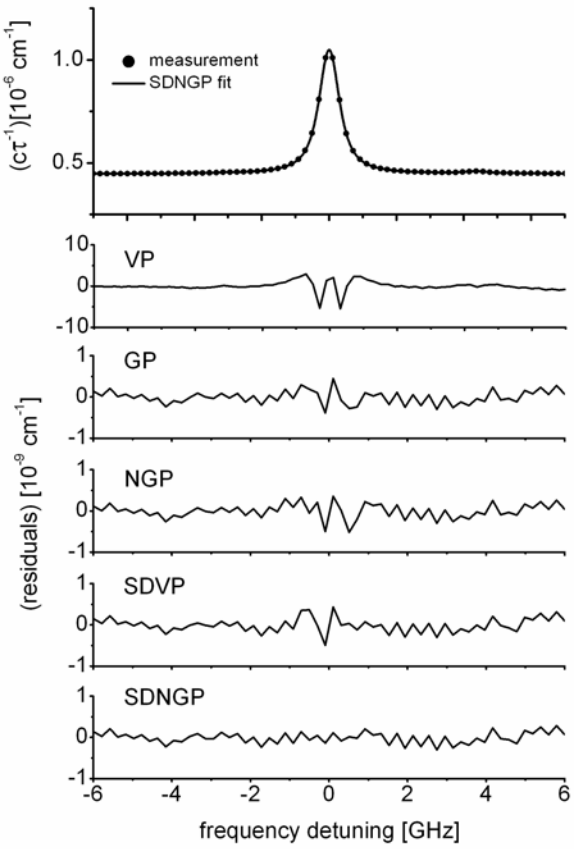

FIG. 1. Upper panel gives the measured FS-CRDS spectrum of the (30012)←(00001) *R*16 transition of CO_2 and the single-spectrum SDNGP fit to these data. The sample gas was air with a CO_2 molar fraction of 367.81(37) μmol mol^{-1} at a total pressure of 13.3 kPa. Bottom panels are the corresponding fit residuals for the indicated line profiles. Fitting the VP to the measured spectrum leads to large, systematic residuals which are attributed to collisional narrowing. Note the tenfold difference in the vertical axis scale between the VP residual plot and those of the other cases. Use of the GP, NGP, and SDVP reduces the spectrum residuals approximately tenfold, however, only the SDNGP is able to model the spectrum to within the instrumental noise level. The spectrum signal-to-noise ratio (ratio of peak absorption to standard deviation of the fit residuals) for the SDNGP fit is ~5,000:1.

The choice of line profile utilized to model the measured spectra can have a considerable impact on the fitted spectroscopic parameters obtained at a given pressure. As can be seen in Figures 2 and 3, fitting the VP to the measured spectra leads to significant deviations with respect to the measured Lorentzian width and spectrum area (proportional to line intensity). These deviations are especially large at low pressure (e.g., 6.7 kPa) where the Lorentzian width and spectrum area obtained through the fitting the Voigt profile deviate by as much as 6% and 2%, respectively from those obtained with the SDNGP fits. In addition, we note that the Lorentzian width and line area parameters obtained from VP fits do not converge with those obtained using the other line profiles

considered here, even at higher pressures. Furthermore, in the case of the VP, the fitted parameters have considerably larger uncertainties than those obtained with more advanced line profiles that are fit to the same data. Fitted parameters obtained with the GP, NGP, and SDVP are rather similar to those obtained with the SDNGP. Excluding the VP fits, we found that the maximum deviation in fitted Lorentzian width and spectrum area were at most 1.5% and 0.5%, respectively.

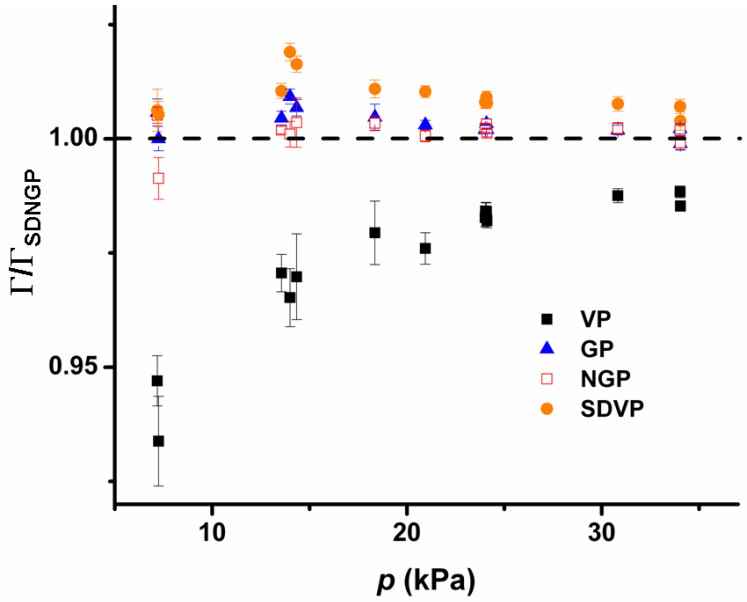

FIG. 2. Pressure dependence of the ratio of the air-broadened Lorentzian width, Γ, obtained by fitting various line profiles (VP, GP, NGP, SDVP) to that obtained with the SDNGP (denoted by Γ_{SDNGP}). These data correspond to the (30012)←(00001) *R*16 transition of CO_2. Fitting spectra with the VP systematically underestimates the Lorentzian width and at a pressure of 7 kPa leads to a deviation of as much as 6%. Although the ratio $\Gamma_{VP}/\Gamma_{SDNGP}$ increases with pressure, it does not converge to unity even at p = 40 kPa. In contrast, $\Gamma_{NGP}/\Gamma_{SDNGP}$ is insensitive to pressure and has a mean value of 1.0014(9).

Interestingly, for all the line profiles evaluated here the fitted Γ varies linearly with pressure, p, and as shown in Figure 4 the slope, $d\Gamma/dp$, is similar for all cases. Note that $d\Gamma/dp$ corresponds to the air-broadening parameter, γ. However, with regard to the set of $\Gamma(p)$ obtained from VP fits, we find that there is an unphysical, negative-valued, y-intercept, which implies the occurrence of a nonlinear relationship for $\Gamma(p)$ at low pressure. We attribute this result to pressure-dependent line narrowing effects that are not modeled by the VP. This mode of analysis may have a profound impact upon

laboratory and atmospheric determinations of γ. Specifically, when γ is evaluated as the ratio, Γ/p, where Γ is found by VP fits to a spectrum at a single pressure, then this measurement will tend to underestimate the true broadening parameter. In the present case, the magnitude of this effect is nominally 2%. Theoretical calculations using the GP to simulate line narrowing were performed and verify these experimental findings regarding the VP. For the air-broadened CO_2 transition considered here, it is expected that the value of $d\Gamma/dp$ observed at pressures below 6.7 kPa would diverge from the higher pressure value.

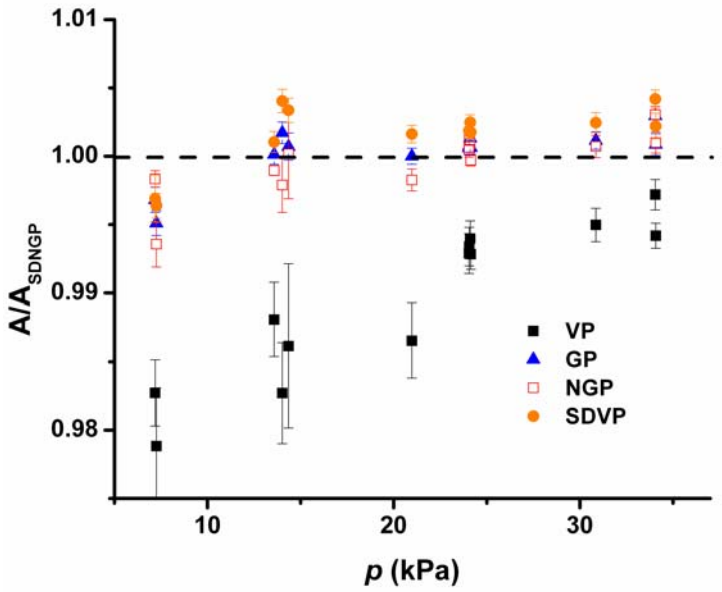

FIG. 3. Pressure dependence of the ratio of the spectrum area, A, obtained by fitting various line profiles (VP, GP, NGP, SDVP) to that obtained with the SDNGP (denoted by A_{SDNGP}). These data correspond to the air-broadened (30012)←(00001) $R16$ transition of CO_2. Fitting spectra with the VP systematically underestimates the spectrum area, and at a pressure of 7 kPa use of the VP leads to a deviation of as much as 2% from the SDNGP value. The SDVP-fitted areas are on average about 1.5% greater than A_{SDNGP}, whereas the GP and NGP fitted areas are within 0.02% and 0.04%, respectively, of A_{SDNGP}.

Regardless of the line profile employed, the air-broadening parameters obtained from the present measurements show large, several-percent deviations from those found in the HITRAN 2008 database [43] (see Figure 4). The HITRAN 2008 air-broadening parameters in this band are based upon FTS measurements of CO_2-air mixtures with several percent CO_2 [10]. As the self-broadening parameters of CO_2 are generally ~40%

larger than the air-broadening parameters [43], these results were extrapolated to natural abundance of CO_2. We speculate that either this extrapolation or other line shape effects (e.g., line mixing) are the source of this deviation. Note that the SDNGP-retrieved, air-broadening parameter for the *R*16 transition is 21.75(9) kHz Pa^{-1} (0.0735(3) cm^{-1} atm^{-1}) at T = 296 K. We observed similar deviations from the HITRAN 2008 air-broadening parameters for the *R*14, *R*18, *P*16, *P*18 transitions of CO_2; each of which was low from the HITRAN 2008 parameters by 0.9%–2.7%.

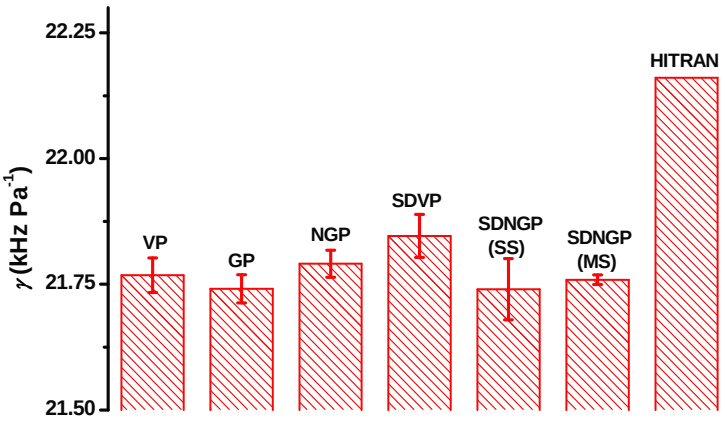

FIG. 4. Measured air-broadening parameter, γ, at T = 296 K for the (30012)←(00001) CO_2 *R*16 transition. The labels indicate the line profiles that were used, and SDNGP(SS) and SDNGP(MS) correspond to the single-spectrum fit and multi-spectrum fit cases, respectively for the SDNGP. Except for the multi-spectrum fit case, these results were obtained by fitting the profiles to FS-CRDS spectra over the pressure range 6.7–34 kPa and subsequently evaluating $\gamma = d\Gamma/dp$ from each set of fitted Γ values. The air-broadening parameter for the SDNGP(MS) case is 21.76(1) kHz Pa^{-1}. Note that each of the fitted values is ~2% lower than the HITRAN 2008 value, which is equal to 22.16 kHz Pa^{-1} [43]. The factor 1 cm^{-1} atm^{-1} ≡ 295.872 kHz Pa^{-1} can be used to convert these values into the conventional units for γ (cm^{-1} atm^{-1}).

The pressure dependence of the narrowing frequency obtained by fitting the GP to our measured spectra can be found in Figure 5. If collisional narrowing were the only source of line narrowing, we would expect to see a linear dependence on pressure. However, in the present case we observe a quadratic dependence on pressure (similar behavior is observed when the NGP is employed). This non-linearity is indicative of the simultaneous occurrence of collisional (Dicke) narrowing and speed-dependent narrowing (e.g., Refs. [23,44-47]).

The SDNGP accounts for both of these effects and is therefore the appropriate line profile for these measurements. However, since both collisional narrowing and speed dependence narrow the total line width, their fitted values can become correlated. Therefore, it is necessary to utilize multi-spectrum fitting [24] to simultaneously fit spectra across a given range of pressures, whereby the two sources of narrowing can be separated based on their different pressure dependencies. Specifically, the collisional narrowing frequency is given by $\nu_{nar} = \eta p$ in which η is the collisional narrowing parameter, whereas the quadratic approximation speed-dependent parameters a_w and a_s are independent of pressure [48]. This multispectrum fitting procedure produces a single value for each of the narrowing and asymmetry parameters (i.e., η, a_w, and a_s). With this approach, the SDNGP profiles were simultaneously fit to four spectra spanning the pressure range 14–34 kPa, to yield fitted values for these three parameters. The measured spectra, the fitted profiles, and the respective sets of fit residuals are shown Fig. 6. From this multi-spectrum fit of the SDNGP we find η = 6.18(21) kHz Pa^{-1}, a_w = 0.042(8) and a_s = 0.08(2). Note that the spectrum signal-to-noise ratio ranges from 2,150 to 3,600 and is not as high as that obtained with the SDNGP single-spectrum fit shown in Figure 1. We assign this reduction in fit quality to pressure-dependent variations in the spectrum baseline that cannot be fully taken into account with a fixed baseline model.

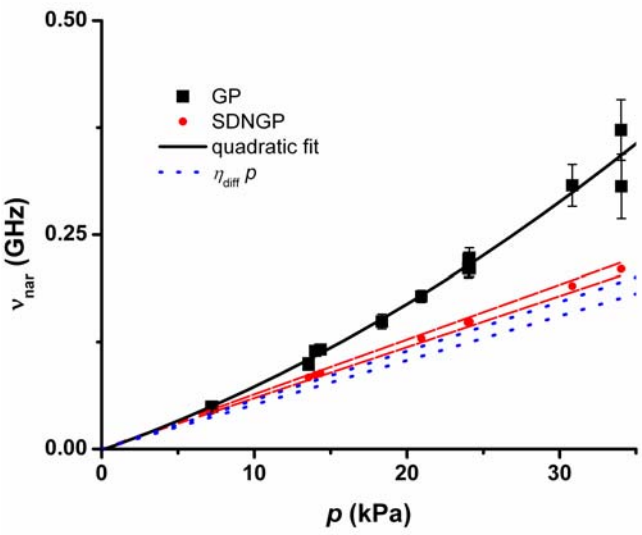

FIG. 5. Collisional narrowing frequency, ν_{nar}, as a function of pressure for the air-broadened (30012)←(00001) *R*16 CO_2 transition. For single-spectrum fits of the GP (square symbols) the ν_{nar} values have an unphysical, quadratic pressure dependence caused by the concurrence of collisional (Dicke) narrowing and speed-dependent narrowing. The indicated narrowing frequencies (red circles) are obtained when the same spectra are simultaneously fit over the entire pressure range with the SDNGP. This multi-spectrum analysis uses the SDNGP subject to the constraint that $\nu_{nar} = \eta_{SDNGP} p$. Importantly, the fitted collisional narrowing parameter (the slope of the line formed by the red circles, shown with its standard uncertainty in dashed red lines), agrees well with the diffusion-based value, η_{diff} [49]. We find that η_{SDNGP} = 6.18(21) kHz Pa^{-1} and η_{diff} = 5.44(27) kHz Pa^{-1}.

When all velocity changing collisions contribute to the line narrowing, the collisional narrowing parameter can be calculated based on the mass diffusion coefficient of the absorber, D, and pressure and temperature, as $\eta_{diff} = k_B T/(2\pi m_a D p)$. For dilute mixtures of CO_2 in air we estimate that η_{diff} = 5.44(27) kHz Pa^{-1} (0.0184(9) cm^{-1} atm^{-1}) [49], and as can be seen in Figure 5, the collisional narrowing parameter, η_{SDNGP} which was obtained from the multi-spectrum fit agrees well (relative difference of <15%) with η_{diff}. This agreement supports our use of the SDNGP for describing the collisional narrowing effect [45] in the present case and is consistent with the underlying assumption (required also for the GP and NGP) that all velocity changing collisions fully contribute to the line narrowing. Therefore, it appears unlikely that models accounting for correlations between velocity- and phase-changing collisions such as the CNGP [38] or the CSDNGP [50] are required to describe our measured CO_2 line shapes in this pressure range.

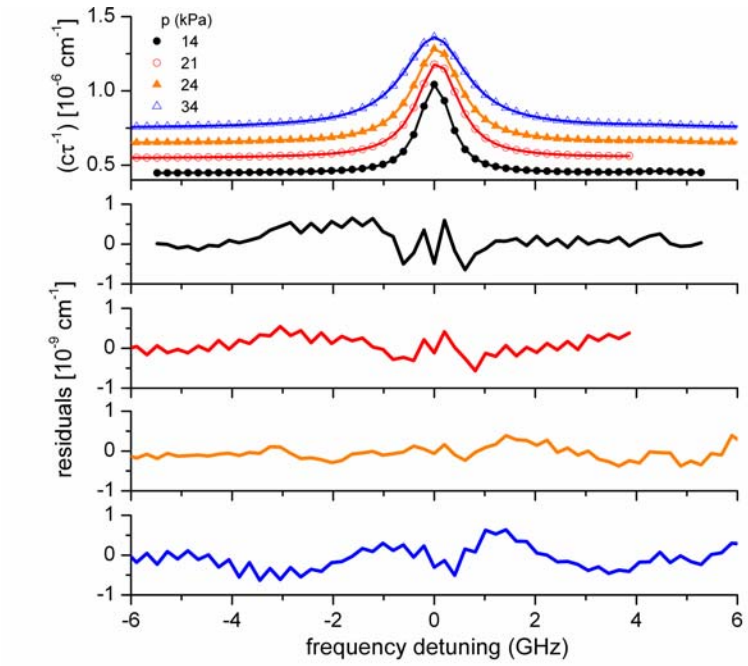

FIG. 6. Measured and modeled absorption spectra of air-broadened (30012)←(00001) *R*16 CO_2 transition. The top panel shows the measured spectra (symbols) and multi-spectrum SDNGP fit (lines). For clarity, the three highest-pressure spectra are successively offset in the vertical direction in increments of 2.5×10^{-7} cm^{-1}. The bottom four panels (increasing pressure from top to bottom) give the residuals of the SDNGP global fit (measured spectrum – fitted profile) for each pressure. Prior to implementing the multi-spectrum fit, each individual spectrum is corrected for a baseline etalon.

Casa et al. recently observed that fitting the GP to self-broadened CO_2 spectra (near $\lambda = 2.0$ μm) over the range $p = 0.7$–4.0 kPa led to collisional narrowing parameters that exceeded η_{diff} by roughly a factor of two [19]. This discrepancy between measured and calculated narrowing parameters can be explained by the simultaneous occurrence of collisional narrowing and speed-dependent effects, as found in the present study. We anticipate that a multi-spectrum fit of the SDNGP to their measured spectra, equivalent to that presented here, would yield a physically consistent collisional narrowing parameter that is either equal to or less than η_{diff}.

6.4. Conclusions

Air-broadened near-infrared CO_2 transitions were measured with frequency-stabilized cavity ring-down spectroscopy (FS-CRDS) at CO_2/air mixing ratios close to those in the atmosphere. Special emphasis was placed upon the *R*16 transition within the (30012)←(00001) band (located near 6360 cm^{-1}) which has been proposed for use in NASA's ASCENDS active sensing mission. For the measured transitions, these were the

first measurements of the air-broadening parameters at near-atmospheric mixing ratios. We find that our measured broadening parameters differed by up to several percent relative to those in the HITRAN 2008 database.

The measured spectra showed unambiguous evidence of collisional narrowing. Failure to account for this narrowing (i.e., through the application of the commonly used Voigt line profile) led to biases of several percent in the measured broadening parameters and intensities and to relatively large uncertainties by comparison to those obtained with more complex line profiles. In addition, it was found that both collisional narrowing and speed dependence of collisional broadening and shifting played a significant role in this pressure range (6.7–33 kPa). Of the profiles considered here, the SDNGP (which includes both of these effects) was the only one that modeled the spectra to within the instrumental noise level. Finally, excellent agreement was observed between the fitted and mass diffusion-based narrowing parameters when SDNGPs were simultaneously fit to spectra acquired over a range of pressure. This result indicated that the use of correlation line profile models such as the correlated-NGP or correlated-SDNGP is likely unnecessary in the present case. For the pressure range considered, we found no evidence of line mixing, although in general, we expect that more comprehensive models which include line mixing effects will be required to accurately predict the evolution of CO_2 absorption spectra for pressures exceeding ~40 kPa.

Acknowledgements

David A. Long was supported by the National Science Foundation and National Defense Science and Engineering Graduate Fellowships. Daniel K. Havey was supported by a National Research Council postdoctoral fellowship at the National Institute of Technology (NIST), Gaithersburg, MD. Part of the research described in this paper was performed at the Jet Propulsion Laboratory, California Institute of Technology, under contract with the National Aeronautics and Space Administration (NASA). Additional support was provided by the Orbiting Carbon Observatory (OCO) project, a NASA Earth System Science Pathfinder (ESSP) mission; the NASA Upper Atmospheric Research

Program grants NNG06GD88G and NNX09AE21G; the NASA Atmospheric Carbon Observations from Space (ACOS) grant 104127-04.02.02; and the NIST Greenhouse Gas Measurements and Climate Research Program. Research was also supported by the Polish MNISW Project No. N N202 1255 35.

References

[1] D. Crisp, R. M. Atlas, F. M. Breon, L. R. Brown, J. P. Burrows, P. Ciais, B. J. Connor, S. C. Doney, I. Y. Fung, D. J. Jacob, C. E. Miller, D. O'Brien, S. Pawson, J. T. Randerson, P. Rayner, R. J. Salawitch, S. P. Sander, B. Sen, G. L. Stephens, P. P. Tans, G. C. Toon, P. O. Wennberg, S. C. Wofsy, Y. L. Yung, Z. Kuang, B. Chudasama, G. Sprague, B. Weiss, R. Pollock, D. Kenyon, S. Schroll, In: *Trace Constituents in the Troposphere and Lower Stratosphere*, (Pergamon-Elsevier Science Ltd, Kidlington, 2004).

[2] C. E. Miller, D. Crisp, P. L. DeCola, S. C. Olsen, J. T. Randerson, A. M. Michalak, A. Alkhaled, P. Rayner, D. J. Jacob, P. Suntharalingam, D. B. A. Jones, A. S. Denning, M. E. Nicholls, S. C. Doney, S. Pawson, H. Boesch, B. J. Connor, I. Y. Fung, D. O'Brien, R. J. Salawitch, S. P. Sander, B. Sen, P. Tans, G. C. Toon, P. O. Wennberg, S. C. Wofsy, Y. L. Yung, R. M. Law, J. Geophys. Res.-Atmos. **112,** D10314 (2007).

[3] C. E. Miller, L. R. Brown, R. A. Toth, D. C. Benner, V. M. Devi, C. R. Phys. **6,** 876-887 (2005).

[4] C. E. Miller, L. R. Brown, J. Mol. Spectrosc. **228,** 329-354 (2004).

[5] R. A. Toth, L. R. Brown, C. E. Miller, V. M. Devi, D. C. Benner, J. Mol. Spectrosc. **239,** 221-242 (2006).

[6] R. A. Toth, L. R. Brown, C. E. Miller, V. M. Devi, D. C. Benner, J. Mol. Spectrosc. **239,** 243-271 (2006).

[7] R. A. Toth, C. E. Miller, V. M. Devi, D. C. Benner, L. R. Brown, J. Mol. Spectrosc. **246,** 133-157 (2007).

[8] R. A. Toth, L. R. Brown, C. E. Miller, V. M. Devi, D. C. Benner, J. Quant. Spectrosc. Radiat. Transfer **109,** 906-921 (2008).

[9] V. M. Devi, D. C. Benner, L. R. Brown, C. E. Miller, R. A. Toth, J. Mol. Spectrosc. **245,** 52-80 (2007).

[10] V. M. Devi, D. C. Benner, L. R. Brown, C. E. Miller, R. A. Toth, J. Mol. Spectrosc. **242,** 90-117 (2007).

[11] A. Predoi-Cross, A. Unni, W. Liu, I. Schofield, C. Holladay, A. R. W. McKellar, D. Hurtmans, J. Mol. Spectrosc. **245,** 34-51 (2007).

[12] A. Predoi-Cross, W. Liu, C. Holladay, A. V. Unni, I. Schofield, A. R. W. McKellar, D. Hurtmans, J. Mol. Spectrosc. **246,** 98-112 (2007).

[13] T. Hikida, K. M. T. Yamada, M. Fukabori, T. Aoki, T. Watanabe, J. Mol. Spectrosc. **232,** 202-212 (2005).

[14] T. Hikida, K. M. T. Yamada, J. Mol. Spectrosc. **239,** 154-159 (2006).

[15] I. Pouchet, V. Zeninari, B. Parvitte, G. Durry, J. Quant. Spectrosc. Radiat. Transfer **83,** 619-628 (2004).

[16] S. Nakamichi, Y. Kawaguchi, H. Fukuda, S. Enami, S. Hashimoto, M. Kawasaki, T. Umekawa, I. Morino, H. Suto, G. Inoue, Phys. Chem. Chem. Phys. **8,** 364-368 (2006).

[17] B. V. Perevalov, A. Campargue, B. Gao, S. Kassi, S. A. Tashkun, V. I. Perevalov, J. Mol. Spectrosc. **252,** 190-197 (2008).

[18] B. V. Perevalov, S. Kassi, V. I. Perevalov, S. A. Tashkun, A. Campargue, J. Mol. Spectrosc. **252,** 143-159 (2008).
[19] G. Casa, R. Wehr, A. Castrillo, E. Fasci, L. Gianfrani, J. Chem. Phys. **130,** 184306 (2009).
[20] L. Joly, F. Gibert, B. Grouiez, A. Grossel, B. Parvitte, G. Durry, V. Zeninari, J. Quant. Spectrosc. Radiat. Transfer **109,** 426-434 (2008).
[21] D. J. Robichaud, J. T. Hodges, L. R. Brown, D. Lisak, P. Maslowski, L. Y. Yeung, M. Okumura, C. E. Miller, J. Mol. Spectrosc. **248,** 1-13 (2008).
[22] D. J. Robichaud, L. Y. Yeung, D. A. Long, M. Okumura, D. K. Havey, J. T. Hodges, C. E. Miller, L. R. Brown, J. Phys. Chem. A **113,** 13089-13099 (2009).
[23] D. Lisak, J. T. Hodges, R. Ciurylo, Phys. Rev. A **73,** 012507 (2006).
[24] D. Lisak, P. Maslowski, A. Cygan, K. Bielska, S. Wojtewicz, M. Piwinski, J. T. Hodges, R. S. Trawinski, R. Ciurylo, Phys. Rev. A **81,** 042504 (2010).
[25] D. A. Long, D. K. Havey, M. Okumura, C. E. Miller, J. T. Hodges, Phys. Rev. A **81,** 064502 (2010).
[26] D. A. Long, D. K. Havey, M. Okumura, C. E. Miller, J. T. Hodges, J. Quant. Spectrosc. Radiat. Transfer **111,** 2021-2036 (2010).
[27] D. C. Benner, C. P. Rinsland, V. M. Devi, M. A. H. Smith, D. Atkins, J. Quant. Spectrosc. Radiat. Transfer **53,** 705-721 (1995).
[28] D. Lisak, D. K. Havey, J. T. Hodges, Phys. Rev. A **79,** 052507 (2009).
[29] J. T. Hodges, H. P. Layer, W. W. Miller, G. E. Scace, Rev. Sci. Instrum. **75,** 849-863 (2004).
[30] J. T. Hodges, R. Ciurylo, Rev. Sci. Instrum. **76,** 023112 (2005).
[31] D. A. Long, M. Okumura, C. E. Miller, J. T. Hodges, Appl. Phys. B**,** Accepted (2011).
[32] D. A. Long, D. K. Havey, M. Okumura, H. M. Pickett, C. E. Miller, J. T. Hodges, Phys. Rev. A **80,** 042513 (2009).
[33] D. K. Havey, D. A. Long, M. Okumura, C. E. Miller, J. T. Hodges, Chem. Phys. Lett. **483,** 49-54 (2009).
[34] D. A. Long, D. K. Havey, S. S. Yu, M. Okumura, C. E. Miller, J. T. Hodges, J. Quant. Spectrosc. Radiat. Transfer**,** Submitted (2011).
[35] D. J. Robichaud, J. T. Hodges, P. Maslowski, L. Y. Yeung, M. Okumura, C. E. Miller, L. R. Brown, J. Mol. Spectrosc. **251,** 27-37 (2008).
[36] L. Galatry, Phys. Rev. **122,** 1218-1223 (1961).
[37] M. Nelkin, A. Ghatak, Phys. Rev. **135,** A4 (1964).
[38] S. G. Rautian, I. I. Sobelman, Sov. Phys. Usp. **9,** 701-716 (1967).
[39] P. R. Berman, J. Quant. Spectrosc. Radiat. Transfer **12,** 1331-& (1972).
[40] B. Lance, G. Blanquet, J. Walrand, J. P. Bouanich, J. Mol. Spectrosc. **185,** 262-271 (1997).
[41] J. M. Hartmann, C. Boulet, D. Robert, *Collisional Effects on Molecular Spectra* (Elsevier, Amsterdam, 2008).
[42] R. H. Dicke, Phys. Rev. **89,** 472-473 (1953).
[43] L. S. Rothman, I. E. Gordon, A. Barbe, D. C. Benner, P. F. Bernath, M. Birk, V. Boudon, L. R. Brown, A. Campargue, J. P. Champion, K. Chance, L. H. Coudert,

V. Dana, V. M. Devi, S. Fally, J. M. Flaud, R. R. Gamache, A. Goldman, D. Jacquemart, I. Kleiner, N. Lacome, W. J. Lafferty, J. Y. Mandin, S. T. Massie, S. N. Mikhailenko, C. E. Miller, N. Moazzen-Ahmadi, O. V. Naumenko, A. V. Nikitin, J. Orphal, V. I. Perevalov, A. Perrin, A. Predoi-Cross, C. P. Rinsland, M. Rotger, M. Simecková, M. A. H. Smith, K. Sung, S. A. Tashkun, J. Tennyson, R. A. Toth, A. C. Vandaele, J. Vander Auwera, J. Quant. Spectrosc. Radiat. Transfer **110,** 533-572 (2009).

[44] D. Lisak, G. Rusciano, A. Sasso, J. Mol. Spectrosc. **227,** 162-171 (2004).

[45] P. Duggan, P. M. Sinclair, A. D. May, J. R. Drummond, Phys. Rev. A **51,** 218-224 (1995).

[46] J. F. D'Eu, B. Lemoine, F. Rohart, J. Mol. Spectrosc. **212,** 96-110 (2002).

[47] D. Lisak, G. Rusciano, A. Sasso, Phys. Rev. A **72,** 012503 (2005).

[48] P. Duggan, P. M. Sinclair, R. Berman, A. D. May, J. R. Drummond, J. Mol. Spectrosc. **186,** 90-98 (1997).

[49] W. J. Massman, Atmos. Environ. **32,** 1111-1127 (1998).

[50] D. Robert, J. M. Thuet, J. Bonamy, S. Temkin, Phys. Rev. A **47,** R771-R773 (1993).

CHAPTER 7

Frequency-Stabilized Cavity Ring-Down Spectroscopy Measurements of Carbon Dioxide Isotopic Ratios

This chapter was published as

D. A. Long, M. Okumura, C. E. Miller, and J. T. Hodges, *Appl. Phys. B*, In press: doi: 10.1007/s00340-011-4518-z.

Abstract

Carbon dioxide (CO_2) isotopic ratios on samples of pure CO_2 were measured in the 1.6 μm wavelength region using the frequency-stabilized cavity ring-down spectroscopy (FS-CRDS) technique. We present CO_2 absorption spectra with peak signal-to-noise ratios as high as 28,000:1. Measured single-spectrum signal-to-noise ratios were as high as 8,900:1, 10,000:1, and 1,700:1 for $^{13}C/^{12}C$, $^{18}O/^{16}O$, and $^{17}O/^{16}O$, respectively. In addition, we demonstrate the importance of utilizing the Galatry line profile in the spectrum analysis. The use of the Voigt line profile, which neglects the observed collisional narrowing, leads to large systematic errors which are transition dependent and vary with temperature and pressure. While the relatively low intensities of CO_2 transitions near λ = 1.6 μm make this spectral region non-optimal, the sensitivity and stability of FS-CRDS enabled measurement precision comparable to those of other optical techniques which operate at far more propitious wavelengths. These results indicate that a FS-CRDS spectrometer designed to probe CO_2 bands near wavelengths of 2.0 or 4.3 μm could achieve significantly improved precision over the present instrument and likely be competitive with mass spectrometric methods.

7.1. Introduction

For over half of a century, stable isotope measurements have been utilized to quantify sources and sinks of CO_2 [1]. Recent simultaneous measurements of $^{18}O/^{16}O$ and $^{17}O/^{16}O$ isotopic ratios in CO_2 have elicited considerable interest due to their use as a tracer of stratospheric dynamics through the observed mass-independent isotope effect [2]. In addition, isotopic fractionation measurements are important in partitioning CO_2 emissions between natural and anthropogenic sources and deducing exchange between the biosphere, ocean, and atmosphere [3].

Isotope-ratio mass spectrometry (IR-MS) is the standard for isotope fractionation measurements. Commercial, dual-inlet IR-MS instruments routinely achieve measurement precisions better than 0.1‰ for measurements of $^{13}C/^{12}C$ and $^{18}O/^{16}O$ isotopic ratios (e.g., [4]). Unfortunately, IR-MS has a number of technical limitations: it is expensive, bulky, time intensive, sample destructive, and requires careful sample pre-concentration to remove isobaric interferences. In addition, IR-MS analysis is incompatible with molecules such as H_2O and SO_2 which have a tendency to stick to surfaces. Thus, isotopic analysis of these species requires an initial chemical conversion which increases the complexity and overall uncertainty of the measurement. Finally, measurements of $^{17}O/^{16}O$ ratios in CO_2 by IR-MS are greatly complicated by the presence of the $^{16}O^{13}C^{16}O$ isobar. This necessitates an initial conversion of CO_2 to O_2 which introduces an uncertainty of approximately ±0.1‰ and precludes a simultaneous measurement of the $^{13}C/^{12}C$ ratio [5].

These difficulties with IR-MS have motivated the development of isotope ratio measurements based on laser absorption spectroscopy [6]. These new laser-based spectroscopic techniques have significant potential for inexpensive, *in situ* measurements. In addition, since individual isotopologues exhibit distinct spectra, unlike IR-MS methods they are not susceptible to isobaric interference. As these techniques have recently been reviewed [6,7], we will only discuss a few recent developments in laser-based isotope ratio measurements of CO_2. For measurements of $^{13}C/^{12}C$ ratios, laser-based

spectroscopic techniques have begun to rival IR-MS, with commercially available instruments offering precisions better than 0.3‰. For $^{18}O/^{16}O$, precisions as high as 0.05‰ have been achieved through the use of quantum cascade lasers which can probe the CO_2 fundamental band at $\lambda \sim 4.3$ μm [8]. The low isotopic abundance of $^{16}O^{12}C^{17}O$ presents a significant challenge to spectroscopic measurements (see Table 1 for natural isotopic abundances). As a result, only three previous studies have measured the $^{17}O/^{16}O$ isotopic ratio of CO_2 [9,10,11]. The highest precision was achieved by Castrillo et al. [11] who measured samples of 2% CO_2 in exhaled breath. They utilized wavelength-modulation spectroscopy with a liquid-nitrogen-cooled quantum cascade laser emitting at $\lambda \sim 4.3$ μm. Short term precisions of 0.5‰ and 0.6‰ were achieved for the $^{18}O/^{16}O$ and $^{17}O/^{16}O$ isotopic ratios, respectively. Unfortunately, the measurements exhibited large, systematic deviations of 11.5‰ and −13.0‰ for the two isotopic ratio measurements, respectively. These were attributed to either non-linearity in the second-harmonic detection (as they were operating outside of the linear Beer's law regime) or non-linearity in their HgCdTe detector.

TABLE 1. CO_2 isotopologue (Iso.) transitions utilized in this study. Positions, intensities (at near-natural isotopic abundance as given in Ref. [12], n_a, and T = 296 K), and lower state energies (E'') are from the HITRAN 2008 database [12]. The shown Type A (random) uncertainties capture the Galatry fit uncertainty as calculated based upon the spectral signal-to-noise ratio (SNR). The uncertainty in the corresponding ratio measurement due to temperature, u_δ, is a Type B (systematic) uncertainty which was calculated as shown in Eq. 1. Note that the uncertainties in p and the ring-down cavity free spectral range are not present as these will cancel in the isotopic ratio measurements. The quantity $A_{Diff} = 1000(A_{GP}/A_{VP}-1)$, where A_{GP} and A_{VP} are the spectral areas derived using the GP and VP, respectively.

Iso.	n_a	Trans.	Band	Position (cm^{-1})	E″ (cm^{-1})	Intensity (cm/molec.)	Type A unc. (‰)	u_δ (‰)	SNR	A_{Diff} (‰)
626	0.98420	*R*66	(30013)←(00001)	6263.369778	1722.9412	3.156E-26	0.03	-	28000:1	10
636	0.01106	*R*50	(30012)←(00001)	6270.249101	994.2387	8.48E-27	0.11	0.33	8900:1	20
628	0.0039471	*R*22	(30012)←(00001)	6269.931712	186.271	1.938E-26	0.09	0.69	10000:1	20
627	0.000734	*P*37	(30012)←(00001)	6265.793803	532.0822	1.403E-27	0.59	0.54	1700:1	40

We have recently constructed a frequency-stabilized cavity ring-down spectrometer in order to perform ultrasensitive, high-resolution lineshape studies of CO_2 combination bands near λ = 1.6 μm [13]. These laboratory measurements will assist

remote sensing measurements of atmospheric CO_2 concentrations [14,15]. We have taken this opportunity to evaluate the potential of frequency-stabilized cavity ring-down spectroscopy (FS-CRDS) for measurements of CO_2 isotopic ratios. While this wavelength range is non-optimal due to the relative weakness of these transitions (two orders of magnitude weaker than the transitions at $\lambda \sim 2.0$ μm and five orders of magnitude weaker than those of the fundamental band at $\lambda \sim 4.3$ μm), this study allows us to compare FS-CRDS to other optical methods in the determination of isotopic ratios. In addition, the results of this study enable us to estimate the precision and accuracy of a FS-CRDS measurements made at more advantageous wavelengths.

7.2. Experimental Apparatus

Measurements were made using the frequency-stabilized cavity ring-down spectrometer located at the National Institute of Standards and Technology (NIST) in Gaithersburg, Maryland. The FS-CRDS spectrometer utilized herein is similar to that which was previously employed to measure the O_2 *A*-band at $\lambda \sim 0.762$ μm [16,17,18,19,20,21,22,23]. In the present experiment we used a different external-cavity diode laser with an output centered near $\lambda = 1.6$ μm, thus enabling us to probe near-infrared CO_2 transitions. Measurements in this spectral region also required a different set of highly reflective cavity ring-down mirrors and an InGaAs in place of a Si-PIN detector. All other aspects of the present FS-CRDS experiment including the cavity and probe laser frequency locking and data collection methods were identical to those employed for our previous O_2 *A*-band studies. Because of the similarities of the two sets of experiments, in this chapter we will only present the most pertinent details.

FS-CRDS differs from traditional cw-cavity ring-down spectroscopy in two fundamental ways [24,25]. Firstly, the optical cavity length is actively stabilized to an external frequency reference, in our case a frequency-stabilized HeNe with a long-term stability of ~1 MHz (3×10^{-5} cm^{-1}) over 8 h. Secondly, FS-CRDS is a single-mode cavity ring-down technique. Individual resonances of the fundamental transverse mode (TEM_{00}) of the ring-down cavity are selectively excited, allowing for accurate, quantitative

measurements of the total cavity losses. During a spectral scan, the probe laser frequency is locked to successive longitudinal modes with ring-down time constants collected at each frequency step. This leads to an extremely stable, accurate, and linear frequency axis. We have recently demonstrated the capability to measure line positions with uncertainties less than 0.5 MHz (1.5×10^{-5} cm^{-1}) [16], Doppler (Gaussian) widths to better than 1 part in 6,000 [21], and line intensities with relative uncertainties less than 0.3% [18,23]. Importantly, the FS-CRDS spectrometer is completely automated such that spectra can be taken over a broad spectral region without operator intervention [25].

The probe source was an external-cavity diode laser with a wavelength tuning range of 1.57–1.63 μm and an output power of 15–18 mW. The ring-down cavity mirrors had nominal reflectivities of 99.997%, corresponding to a finesse of ~105,000 and an effective path length of ~25 km. The relative standard deviation of the measured ring-down time constant was ~0.05%, which for these mirrors and cavity length leads to a relative standard deviation in the absorption coefficient of 2.1×10^{-10} cm^{-1}. The cavity's free-spectral range was determined to be 203.097(22) MHz via the procedure of Lisak and Hodges [26].

The FS-CRDS system stability was assessed through a measurement of the Allan variance [27], a measure which was originally derived as a performance metric for atomic clock standards. Figure 1 shows that as successive ring-down time constants are averaged the Allan deviation (square-root of the Allan variance) decreases roughly in proportion to $n_d^{-1/3}$, where n_d is the number of decays in an averaging bin. This result differs from the frequently observed $n_d^{-1/2}$ dependence of Allan deviation on bin size. For a 1 s averaging time (corresponding to $n_d = 30$ obtained at an acquisition rate of 30 Hz), the minimum detectable absorption (MDA) was 8×10^{-11} cm^{-1}. After averaging ~3,000 ring-down time constants the Allan variance reaches a minimum, indicating the presence of system drifts on the ~100 s timescale. Averaging over 3,000 successive decay events leads to an MDA of 1.4×10^{-11} cm^{-1}, which is a fifteen-fold decrease relative to the single-shot case. For the measurements discussed herein 300 averages were employed, corresponding to an MDA of 3.5×10^{-11} cm^{-1}.

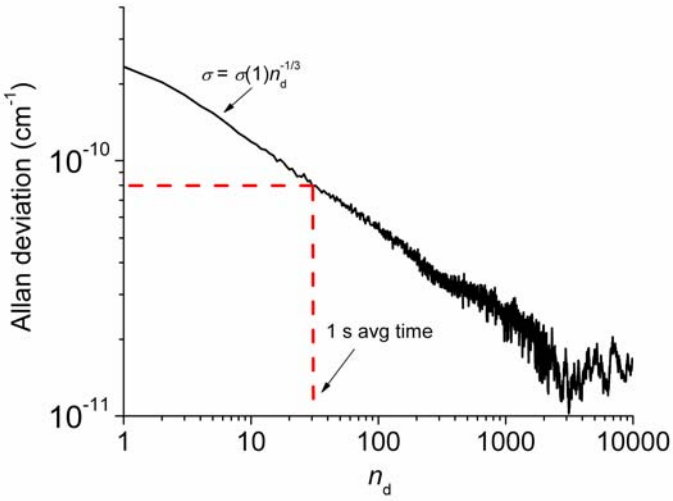

FIG. 1. Allan deviation σ (square-root of the Allan variance) of the empty cavity losses as a function of the number of measured ring-down decays, n_d, in an averaging bin. For $n_d < 3{,}000$ the Allan deviation of these data is proportional to $\sim n_d^{-1/3}$. Averaging for 1 s, which at an acquisition rate of 30 Hz corresponds to an average over 30 ring-down time constants, reduces the standard uncertainty in the absorption coefficient from 2.1×10^{-10} cm^{-1} to 8×10^{-11} cm^{-1}. The minimum in the Allan deviation occurs at $n_d \sim 3{,}000$ (100 s averaging time) and yields an MDA of 1.4×10^{-11} cm^{-1}. Note that this Allan deviation corresponds to an ensemble of ring-down decay time measurements obtained at a single data-point in the absorption spectrum.

Measurements were made on a sample of pure CO_2 at natural isotopic abundance and a nominal pressure of 6.67 kPa (50 Torr). We measured the sample pressure with a NIST-calibrated capacitance diaphragm gauge having a relative standard uncertainty of less than 0.1% and a full-scale response of 133 kPa (1,000 Torr). The ring-down cavity cell wall temperature was measured with a NIST-calibrated 2.4 kΩ thermistor. Spectra were collected at room temperature (298.60–299.22 K) with no attempt made to actively control the cell temperature.

7.3. Results and Discussion

Measurements were made in the 6,263–6,271 cm^{-1} wave number region (see Fig. 2). We selected this spectral region because it provides transitions from multiple isotopologues with comparable absorption strengths. This approach allows us to make the most precise measurements of the isotopic ratios [28,29,30], although one disadvantage is that

isotopologue transitions of comparable absorption typically have very different lower state energies and, therefore, different temperature dependencies. The uncertainty in the measured isotopic ratio, u_δ, caused by the temperature uncertainty, u_T, can be calculated as [29]:

$$u_\delta \approx \frac{\Delta E''}{kT}\frac{u_T}{T} \quad (1)$$

where $\Delta E''$ is the difference in lower state energies of the pair of transitions probed, T is the temperature, and k is the Boltzmann constant. It has been shown that the temperature uncertainty in these FS-CRDS measurements is ~28 mK [20]. For the $^{16}O^{13}C^{16}O$, $^{16}O^{12}C^{18}O$, and $^{16}O^{12}C^{17}O$ isotopologue transitions utilized in the present study (see Table 1), this temperature uncertainty leads to Type *B* (systematic) uncertainties in the isotopic ratio measurements of ~0.47‰, ~0.83‰ and ~0.70‰, respectively.

Figure 2 shows a spectral survey of the 6,263–6,271 cm^{-1} wave number region and a spectrum which was calculated using the Voigt line profile parameters found in the HITRAN 2008 database [12]. Approximately 170 transitions were observed in this survey representing the $^{16}O^{12}C^{16}O$, $^{16}O^{13}C^{16}O$, $^{16}O^{12}C^{18}O$, $^{16}O^{12}C^{17}O$, $^{16}O^{13}C^{18}O$ isotopologues with intensities ranging from 7.8×10^{-26} to 3.6×10^{-29} cm molec.$^{-1}$. All observed transitions are in the HITRAN 2008 database with the exception of the $^{16}O^{13}C^{16}O$ (14411)←(00001) *R*38 transition. This transition is listed in the database of Perevalov et al. [31] with an intensity of $S \sim 3.04\times10^{-28}$ cm molec.$^{-1}$.

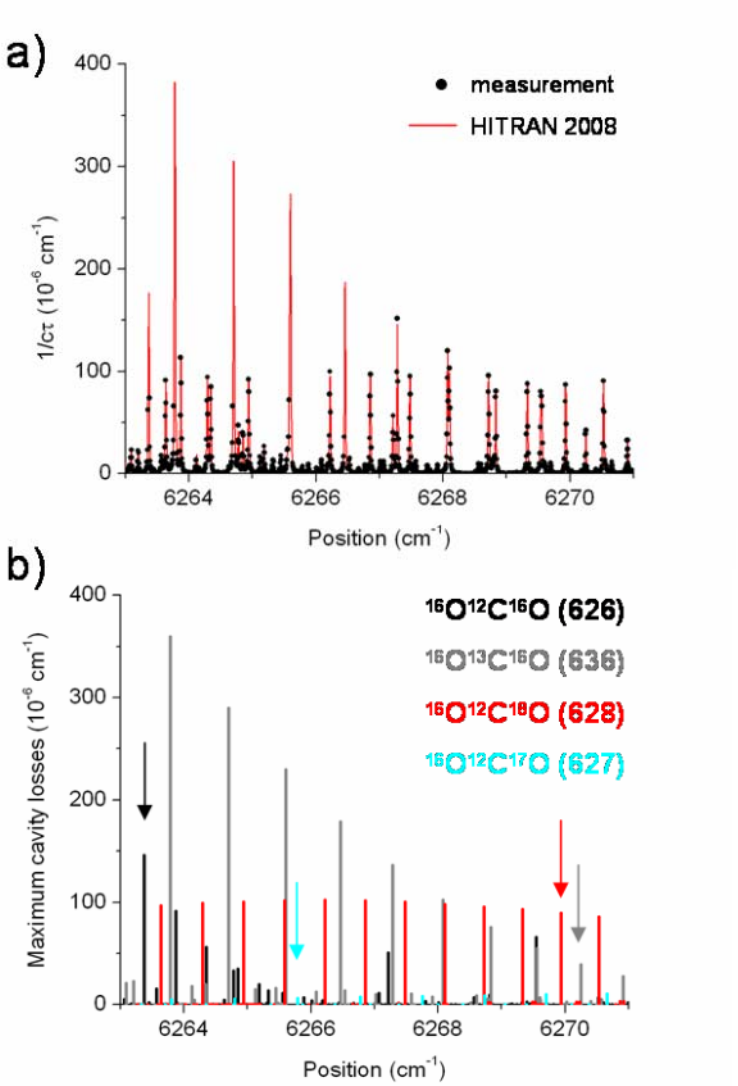

FIG. 2. Survey of the 6,263–6,271 cm^{-1} wave number region. a) FS-CRDS measurement (symbols) and calculated HITRAN 2008 spectrum [12] (lines) using the Voigt line profile for a pure CO_2 sample at natural isotopic abundance, a pressure of 6.67 kPa (50 Torr), and a temperature of 298.733 K.
b) Corresponding stick spectrum of the four dominant isotopologues calculated through the use of HITRAN 2008. This spectral region was chosen to minimize the absorption difference between isotopologue transitions. Transitions utilized in the present study to determine isotopic ratios are marked by arrows. The $^{16}O^{13}C^{18}O$ transition is unmarked but it is located at 6270.3543 cm^{-1} [12].

All measured transitions (including interfering transitions) were fit with a Galatry profile (GP) [32] which accounts for Dicke (collisional) narrowing [33]. The Doppler width was constrained to the theoretical value based upon the measured temperature and molecular mass, while the other parameters (e.g., transition area, Lorentzian width,

narrowing frequency) were floated during the resulting fit. Because the measured spectra exhibit collisional narrowing, we find that fitting the Voigt profile (VP) to our data incurs large, systematic residuals (see Fig. 3). Thus, use of the GP (as opposed to the commonly used VP) is critical for the present application. More specifically, the use of the VP also results in a measured area (and therefore CO_2 number density) which is on average ~20‰ lower than with the GP, an error which is far greater than our experimental imprecision. However, the difference in transition areas measured using the two profiles is not identical for the isotopologue transitions considered here but rather varies between 10‰ and 40‰, thus, removing the possibility of a constant correction factor. This is not surprising as collisional narrowing parameters are known to exhibit *J*-dependence (e.g., [23,34,35]). In addition, this deviation is expected to be both pressure and temperature dependent.

An example spectrum of the $^{16}O^{12}C^{16}O$ *R*66 (30013)←(00001) transition (at natural isotopic abundance in a pure CO_2 sample at 6.67 kPa and 298.929 K) and the corresponding Galatry fit is shown in Fig. 3. This transition is located at a wave number of 6,263.369778 cm^{-1} with an intensity of 3.156×10^{-26} cm molec.$^{-1}$ [12]. The signal-to-noise ratio (SNR, defined as the ratio of peak absorption to root-mean-square fit residuals) is 28,000:1, leading to a precision in the area measurement of 0.03‰. The highest SNR previously reported was ~10,000:1 by Casa et al. [34] who utilized an intensity-stabilized diode laser absorption spectrometer to probe transitions at $\lambda \sim 2.0$ μm. Note that the transition shown in Fig. 3 is ~40,000 times weaker than the transitions probed in the Casa et al. study.

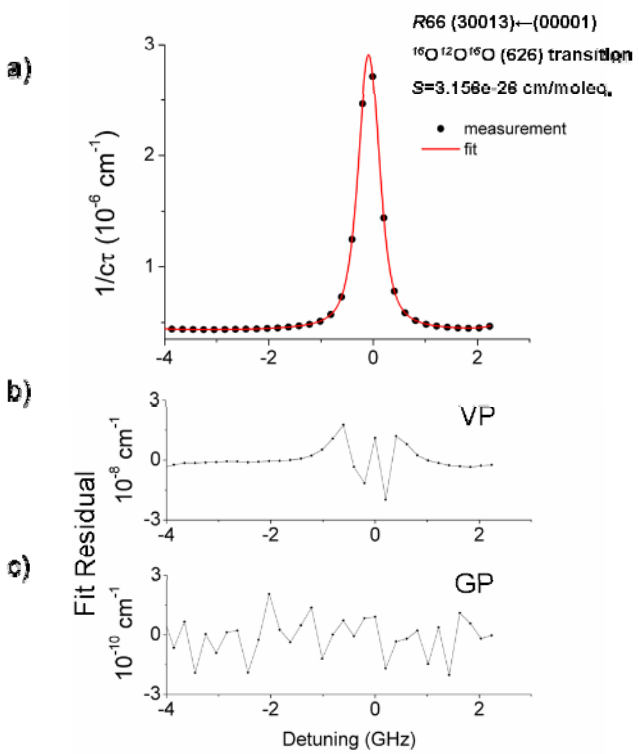

FIG. 3. a) Measurement and Galatry line profile (GP) fit of the $^{16}O^{12}O^{16}O$ (30013)←(00001) *R*66 transition. Sample conditions are at T = 298.929 K, p = 6.67 kPa (50 Torr) for pure CO_2 at natural isotopic abundance. This transition is located at wave number 6,263.369778 cm^{-1} with an intensity of 3.156×10^{-26} cm molec.$^{-1}$ [12]. b) Voigt line profile (VP) fit residual. All line profile parameters were floated except for the Doppler width which was fixed. The presence of collisional narrowing leads to a large systematic residual which is ~100 times greater than the instrumental noise level. c) GP fit residual. All line profile parameters were floated except for the Doppler width which was fixed. Note the difference in scale between the GP and VP fit residuals. The GP accounts for collisional narrowing leading to a signal-to-noise ratio of 28,000:1 with a precision in the area measurement of 0.03‰. The root-mean-square of the Galatry residual is 1×10^{-10} cm^{-1}. The fitted areas determined using the two line profiles differ by 9‰, which is far greater than the measurement precision.

Figure 4 shows an example spectrum of one of the doubly-substituted CO_2 isotopologues, $^{16}O^{13}C^{18}O$, with a SNR of 20:1. The interfering transitions have been fitted and subtracted from the shown spectrum. This transition is located at 6,270.3543 cm^{-1} with an intensity of only 3.588×10^{-29} cm molec.$^{-1}$ at natural isotopic abundance [12]. The Type A (random) uncertainty of the measured area resulting from the Galatry fit is ~50‰, demonstrating the capability of FS-CRDS to make quantitative measurements of ultraweak absorption features. This transition is eleven orders of magnitude weaker than $^{16}O^{12}C^{16}O$ fundamental transitions in the mid-infrared and is one of the weakest

transitions to be quantitatively measured in the laboratory. Unfortunately, this precision pales in comparison to modern IR-MS measurements, which can achieve external precisions as high as 0.01‰ for this isotopologue through the use of large, pre-concentrated samples and long averaging times (~24 h) [36].

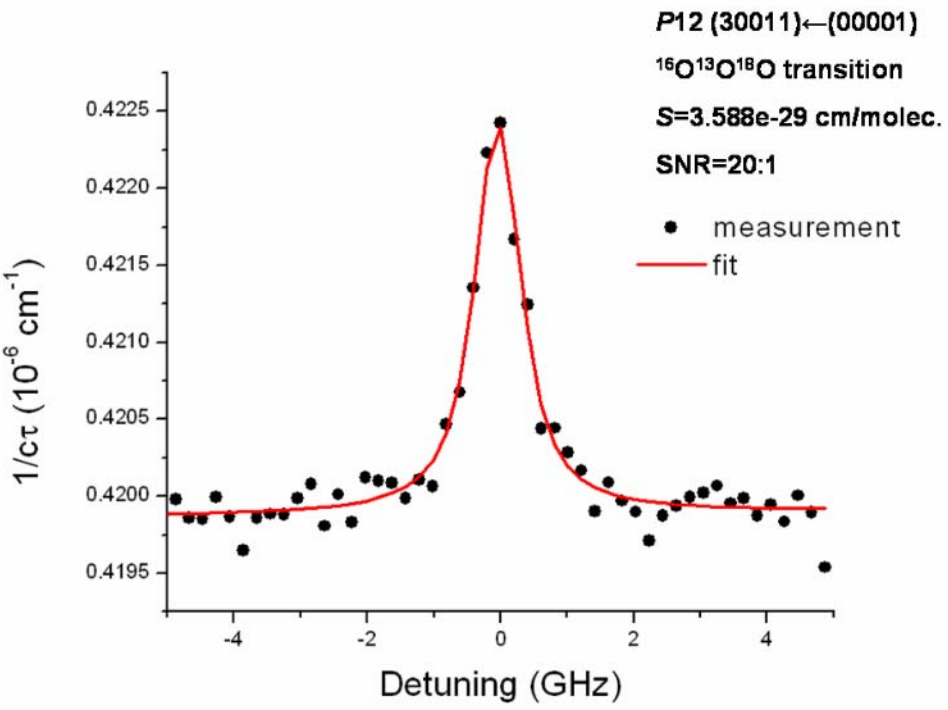

FIG. 4. Measurement and Galatry fit of the $^{16}O^{13}O^{18}O$ (30011)←(00001) *P*12 transition at T = 298.814 K and p = 6.67 kPa (50 Torr) of CO_2 at natural isotopic abundance. This doubly-substituted isotopologue transition is located at a wave number of 6,270.3543 cm^{-1} with an intensity of 3.588×10^{-29} cm molec.$^{-1}$ [12]. In this background-subtracted spectrum the signal-to-noise ratio is 20:1.

We found single-spectrum fit precisions of 0.11‰, 0.09‰ and 0.59‰ for the $^{13}C/^{12}C$, $^{18}O/^{16}O$ and $^{17}O/^{16}O$ ratios, respectively. These single-spectrum precisions are given by the inverse of the SNR of the fitted spectra and therefore do not include systematic uncertainties. They represent the highest precision which could be achieved with the present instrument, for transitions of the given line intensities, in the absence of confounding effects such as temperature uncertainties and interfering transitions. The corresponding uncertainties due to temperature can be calculated, as shown in Eq. 1.

Once added in quadrature with the shown single-spectrum fit precisions, the corresponding uncertainties are 0.35‰, 0.70‰ and 0.80‰ for the $^{13}C/^{12}C$, $^{18}O/^{16}O$ and $^{17}O/^{16}O$ ratios, respectively.

The presence of interfering transitions, which leads to additional unconstrained fit parameters and a more weakly constrained area determination, can degrade the reproducibility of the isotope ratio measurement. In order to quantify the magnitude of this effect, several repeated measurements of the chosen isotopologue transitions were performed to measure the distribution of fitted areas. During these fits, the pressure broadening and collisional narrowing parameters were fixed to our previously measured values. For the $^{16}O^{13}C^{16}O$, $^{16}O^{12}C^{18}O$ and $^{16}O^{12}C^{17}O$ transitions the relative standard deviations of the ensemble of measured areas were 4‰, 0.5‰, and 10‰, respectively. These values were comparable to the estimated relative uncertainties in the fitted areas, yet much larger than the single-spectrum fit precisions. This indicates that uncertainties from interfering transitions, temperature effects, etalons etc. dominate the uncertainty in the spectrum area determination. For the $^{16}O^{12}C^{18}O$ transition this uncertainty is lower than the previously estimated precision, indicating that neighboring transitions play a negligible role in this measurement. This was to be expected as all neighboring transitions are orders of magnitude weaker than the $^{16}O^{12}C^{18}O$ transition in this spectral region. However, for the $^{16}O^{13}C^{16}O$ and $^{16}O^{12}C^{17}O$ transitions, it is clear that neighboring transitions significantly impact the reproducibility of the isotopic ratio. Thus, the dominant uncertainty in the $^{18}O/^{16}O$ measurement is due to temperature while for the $^{13}C/^{12}C$ and $^{17}O/^{16}O$ measurements it is due to the presence of interfering transitions.

This suggests two areas in which the precision of a future FS-CRDS-based isotope ratio measurement could be improved. Firstly, the introduction of active temperature control to minimize the temperature gradient is needed if the $^{18}O/^{16}O$ measurement is to be improved. For example, by reducing the temperature uncertainty to the few millikelvin-level, the uncertainty in the isotopic ratio measurement due to temperature, u_δ, could be reduced below the single-spectrum fit precision. Secondly, by moving to a more optimal wavelength range, we could access transitions which are orders

of magnitude stronger (two orders of magnitude for $\lambda \sim 2.0$ μm or five orders of magnitude for $\lambda \sim 4.3$ μm). Distributed-feedback diode lasers are readily available at $\lambda \sim 2.0$ μm and external-cavity quantum-cascade lasers (which operate without cryogenic cooling) are now available at $\lambda \sim 4.3$ μm. By moving to $\lambda \sim 2.0$ μm, the stronger transitions would allow us to utilize a lower pressure in our measurements, where the relevant isotopologue transitions would be significantly more isolated. This would eliminate the dominant uncertainty in the $^{13}C/^{12}C$ and $^{17}O/^{16}O$ measurements. In addition, the spectral SNRs for the $^{16}O^{12}C^{17}O$ and $^{16}O^{13}C^{18}O$ transitions would be significantly higher due to the increased intensities in this range. It is worth noting that this would not be the case for the $^{16}O^{12}C^{16}O$ and $^{16}O^{12}C^{18}O$ transitions where we are already utilizing nearly the complete dynamic range of the instrument. The use of the fundamental band at λ~4.3 μm would lead to an additional three orders of magnitude increase in spectral intensity and allow for CO_2 isotope ratios to be measured at natural abundance (i.e., ~385 ppm) with precisions similar to those predicted for pure CO_2 at $\lambda \sim 2.0$ μm.

7.4. Conclusions

We employed frequency-stabilized cavity ring-down spectroscopy (FS-CRDS) on pure samples of CO_2 to optically measure CO_2 isotopic ratios at $\lambda \sim 1.6$ μm. Although this spectral region is non-optimal, the sensitivity and stability of FS-CRDS led to single-spectrum fit precisions (based on spectrum SNR) of 8,900:1, 10,000:1 and 1,700:1 for the $^{13}C/^{12}C$, $^{18}O/^{16}O$ and $^{17}O/^{16}O$ ratios, respectively. $^{16}O^{12}C^{16}O$ transitions were measured with SNRs as high as 28,000:1. We found that fitting Voigt profiles to the measured spectra significantly compromises the accuracy of the measured isotopic ratios. This is a result of collisional narrowing of the observed lineshapes; an effect which can be modeled using the Galatry profile. The fitted areas derived using Voigt and Galatry profiles differ by 10‰–40‰ for the measured transitions, which is far greater than the experimental precision. We will focus future developments upon the $\lambda \sim 2.0$ μm band. These transitions are about two orders of magnitude stronger than those discussed herein and are readily accessible through the use of distributed feedback diode lasers. With the

temperature stability demonstrated here, this should enable simultaneous measurements of $^{13}C/^{12}C$, $^{18}O/^{16}O$, and $^{17}O/^{16}O$ on pure CO_2 samples with precision at the sub–0.5‰ level.

Acknowledgements

David A. Long was supported by the National Science Foundation and National Defense Science and Engineering Graduate Fellowships. Part of the research described in this paper was performed at the Jet Propulsion Laboratory, California Institute of Technology, under contract with the National Aeronautics and Space Administration (NASA). Additional support was provided by the Orbiting Carbon Observatory (OCO) project, a NASA Earth System Science Pathfinder (ESSP) mission; the NASA Upper Atmospheric Research Program grant NNG06GD88G and NNX09AE21G; and the NIST Greenhouse Gas Measurements and Climate Research Program.

References

[1] M. H. Thiemens, Science **283,** 341-345 (1999).

[2] D. Krankowsky, F. Bartecki, G. G. Klees, K. Mauersberger, K. Schellenbach, J. Stehr, Geophys. Res. Lett. **22,** 1713-1716 (1995).

[3] P. Ghosh, W. A. Brand, Int. J. Mass Spectrom. **228,** 1-33 (2003).

[4] W. Brand, In: *Handbook of Stable Isotope Analytical Techniques*, P.A. de Groot (Elsevier, Amsterdam, 2004).

[5] S. K. Bhattacharya, M. H. Thiemens, Z. Naturfors. **44,** 435-444 (1989).

[6] E. Kerstel, L. Gianfrani, Appl. Phys. B **92,** 439-449 (2008).

[7] E. R. T. Kerstel, In: *Handbook of Stable Isotope Analytical Techniques*, P.A. de Groot (Elsevier, Amsterdam, 2004).

[8] B. Tuzson, J. Mohn, M. J. Zeeman, R. A. Werner, W. Eugster, M. S. Zahniser, D. D. Nelson, J. B. McManus, L. Emmenegger, Appl. Phys. B **92,** 451-458 (2008).

[9] B. Lehmann, M. Wahlen, R. Zumbrunn, H. Oeschger, Appl. Phys. **13,** 153-158 (1977).

[10] K. P. Petrov, R. F. Curl, F. K. Tittel, Appl. Phys. B **66,** 531-538 (1998).

[11] A. Castrillo, G. Casa, L. Gianfrani, Opt. Lett. **32,** 3047-3049 (2007).

[12] L. S. Rothman, I. E. Gordon, A. Barbe, D. C. Benner, P. F. Bernath, M. Birk, V. Boudon, L. R. Brown, A. Campargue, J. P. Champion, K. Chance, L. H. Coudert, V. Dana, V. M. Devi, S. Fally, J. M. Flaud, R. R. Gamache, A. Goldman, D. Jacquemart, I. Kleiner, N. Lacome, W. J. Lafferty, J. Y. Mandin, S. T. Massie, S. N. Mikhailenko, C. E. Miller, N. Moazzen-Ahmadi, O. V. Naumenko, A. V. Nikitin, J. Orphal, V. I. Perevalov, A. Perrin, A. Predoi-Cross, C. P. Rinsland, M. Rotger, M. Simecková, M. A. H. Smith, K. Sung, S. A. Tashkun, J. Tennyson, R. A. Toth, A. C. Vandaele, J. Vander Auwera, J. Quant. Spectrosc. Radiat. Transfer **110,** 533-572 (2009).

[13] D. A. Long, D. K. Havey, K. Bielska, M. Okumura, C. E. Miller, J. T. Hodges**,** In preparation (2010).

[14] D. Crisp, R. M. Atlas, F. M. Breon, L. R. Brown, J. P. Burrows, P. Ciais, B. J. Connor, S. C. Doney, I. Y. Fung, D. J. Jacob, C. E. Miller, D. O'Brien, S. Pawson, J. T. Randerson, P. Rayner, R. J. Salawitch, S. P. Sander, B. Sen, G. L. Stephens, P. P. Tans, G. C. Toon, P. O. Wennberg, S. C. Wofsy, Y. L. Yung, Z. Kuang, B. Chudasama, G. Sprague, B. Weiss, R. Pollock, D. Kenyon, S. Schroll, *Trace Constituents in the Troposphere and Lower Stratosphere* (Pergamon-Elsevier Science Ltd, Kidlington, 2004, 700-709).

[15] M. Yokomizo, Fujitsu Sci. Tech. J. **44,** 410-417 (2008).

[16] D. J. Robichaud, J. T. Hodges, P. Maslowski, L. Y. Yeung, M. Okumura, C. E. Miller, L. R. Brown, J. Mol. Spectrosc. **251,** 27-37 (2008).

[17] D. J. Robichaud, J. T. Hodges, D. Lisak, C. E. Miller, M. Okumura, J. Quant. Spectrosc. Radiat. Transfer **109,** 435-444 (2008).

[18] D. J. Robichaud, J. T. Hodges, L. R. Brown, D. Lisak, P. Maslowski, L. Y. Yeung, M. Okumura, C. E. Miller, J. Mol. Spectrosc. **248,** 1-13 (2008).

[19] D. J. Robichaud, L. Y. Yeung, D. A. Long, M. Okumura, D. K. Havey, J. T. Hodges, C. E. Miller, L. R. Brown, J. Phys. Chem. A **113,** 13089-13099 (2009).
[20] D. K. Havey, D. A. Long, M. Okumura, C. E. Miller, J. T. Hodges, Chem. Phys. Lett. **483,** 49-54 (2009).
[21] D. A. Long, D. K. Havey, M. Okumura, H. M. Pickett, C. E. Miller, J. T. Hodges, Phys. Rev. A **80,** 042513 (2009).
[22] D. A. Long, D. K. Havey, M. Okumura, C. E. Miller, J. T. Hodges, Phys. Rev. A **81,** 064502 (2010).
[23] D. A. Long, D. K. Havey, M. Okumura, C. E. Miller, J. T. Hodges, J. Quant. Spectrosc. Radiat. Transfer **111,** 2021-2036 (2010).
[24] J. T. Hodges, H. P. Layer, W. W. Miller, G. E. Scace, Rev. Sci. Instrum. **75,** 849-863 (2004).
[25] J. T. Hodges, R. Ciurylo, Rev. Sci. Instrum. **76,** 023112 (2005).
[26] D. Lisak, J. T. Hodges, Appl. Phys. B **88,** 317-325 (2007).
[27] D. W. Allan, Proc. IEEE **54,** 221-231 (1966).
[28] J. F. Becker, T. B. Sauke, M. Loewenstein, Appl. Opt. **31,** 1921-1927 (1992).
[29] P. Bergamaschi, M. Schupp, G. W. Harris, Appl. Opt. **33,** 7704-7716 (1994).
[30] G. Gagliardi, A. Castrillo, R. Q. Iannone, E. R. T. Kerstel, L. Gianfrani, Appl. Phys. B **77,** 119-124 (2003).
[31] B. V. Perevalov, V. I. Perevalov, A. Campargue, J. Quant. Spectrosc. Radiat. Transfer **109,** 2437-2462 (2008).
[32] L. Galatry, Phys. Rev. **122,** 1218-1223 (1961).
[33] R. H. Dicke, Phys. Rev. **89,** 472-473 (1953).
[34] G. Casa, R. Wehr, A. Castrillo, E. Fasci, L. Gianfrani, J. Chem. Phys. **130,** 184306 (2009).
[35] R. Wehr, R. Ciurylo, A. Vitcu, F. Thibault, J. R. Drummond, A. D. May, J. Mol. Spectrosc. **235,** 54-68 (2006).
[36] K. W. Huntington, J. M. Eiler, H. P. Affek, W. Guo, M. Bonifacie, L. Y. Yeung, N. Thiagarajan, B. Passey, A. Tripati, M. Daeron, R. Came, J. Mass Spectrom. **44,** 1318-1329 (2009).